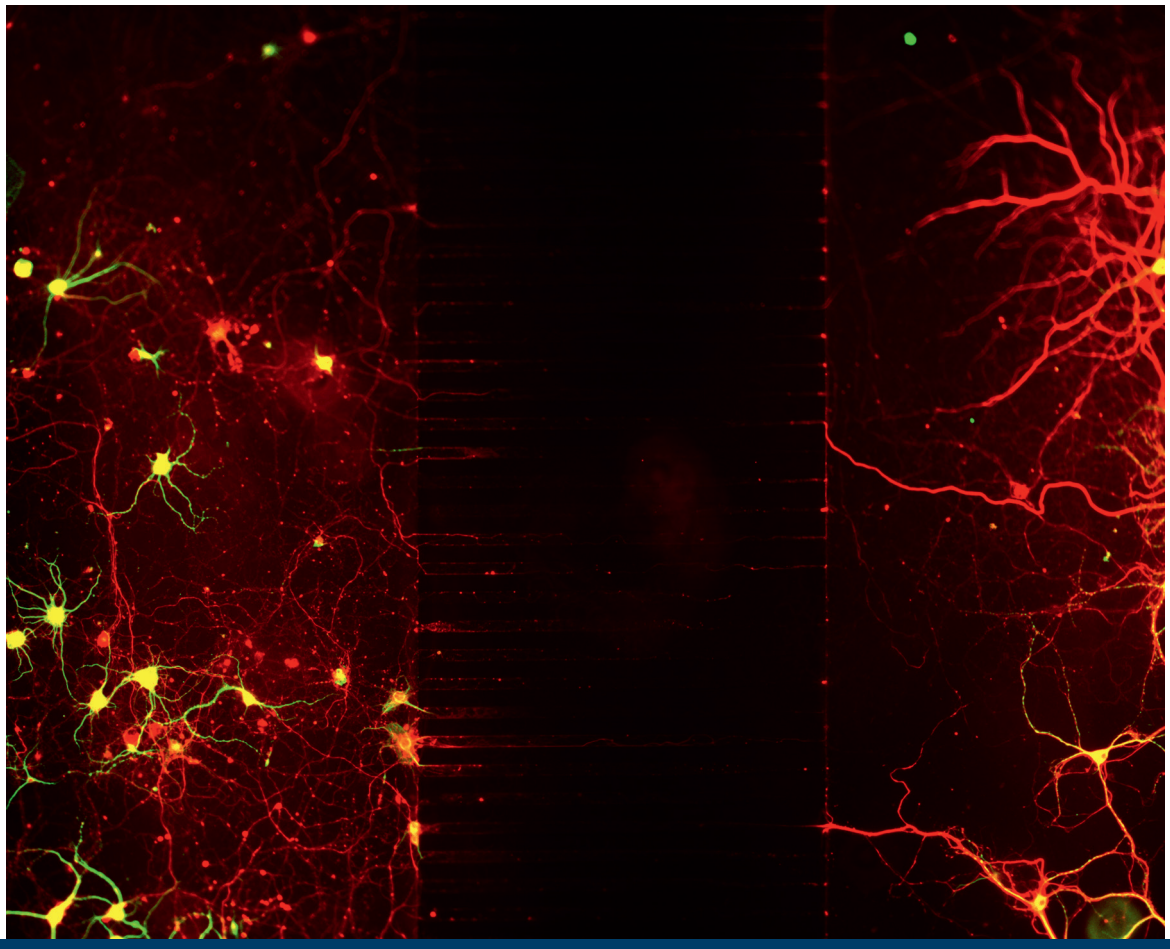

Microfluidic-MEA hybrid systems for electrophysiological recordings of neuronal co-cultures

Jelena Stevanović

Schlüsseltechnologien / Key Technologies
Band / Volume 295
ISBN 978-3-95806-831-5

Mitglied der Helmholtz-Gemeinschaft

JÜLICH
Forschungszentrum

Microfluidic-MEA hybrid systems for electrophysiological recordings of neuronal co-cultures

Von der Fakultät für Mathematik, Informatik und Naturwissenschaften der RWTH Aachen University zur Erlangung des akademischen Grades einer Doktorin der Naturwissenschaften genehmigte Dissertation

vorgelegt von

Jelena Stevanović, M.Sc.

aus

Belgrad, Serbien

Berichter: *Prof. Dr.-Ing. Laura De Laporte*

Prof. Dr. Andreas Offenhäusser

Tag der mündlichen Prüfung: *20.03.2025*

“My brain is only a receiver, in the Universe there is a core from which we obtain knowledge, strength and inspiration. I have not penetrated the secrets of this core, but I know that it exists.”

Nikola Tesla

Forschungszentrum Jülich GmbH
Institut für Biologische Informationsprozesse (IBI)
Bioelektronik (IBI-3)

Microfluidic-MEA hybrid systems for electrophysiological recordings of neuronal co-cultures

Jelena Stevanović

Schriften des Forschungszentrums Jülich
Reihe Schlüsseltechnologien / Key Technologies Band / Volume 295

ISSN 1866-1807 ISBN 978-3-95806-831-5

Bibliografische Information der Deutschen Nationalbibliothek.
Die Deutsche Nationalbibliothek verzeichnet diese Publikation in der
Deutschen Nationalbibliografie; detaillierte Bibliografische Daten
sind im Internet über http://dnb.d-nb.de abrufbar.

Herausgeber und Vertrieb:	Forschungszentrum Jülich GmbH Zentralbibliothek, Verlag 52425 Jülich Tel.: +49 2461 61-5368 Fax: +49 2461 61-6103 zb-publikation@fz-juelich.de www.fz-juelich.de/zb
Umschlaggestaltung:	Grafische Medien, Forschungszentrum Jülich GmbH
Druck:	Grafische Medien, Forschungszentrum Jülich GmbH
Copyright:	Forschungszentrum Jülich 2025

Schriften des Forschungszentrums Jülich
Reihe Schlüsseltechnologien / Key Technologies, Band / Volume 295

D 82 (Diss. RWTH Aachen University, 2025)

ISSN 1866-1807
ISBN 978-3-95806-831-5

Vollständig frei verfügbar über das Publikationsportal des Forschungszentrums Jülich (JuSER)
unter www.fz-juelich.de/zb/openaccess.

Abstract

The study of brain development and degeneration is frequently observed in the scope of *in vivo* studies. However, newly developed *in vitro* models offer better precision and specificity in the investigation of neuronal networks. For example, the use of microfluidic microchannels, which have proven to be a successful method of isolating axons and directing their growth. Building upon the axon diode microchannel shape initially proposed by Peyrin et al. in 2011, I developed a µFluidic-MEA device with integrated microchannel structures on a recording platform. The microchannels were fabricated using photostructurable polymer, i.e. HD-8820, with the goal of improving the precision of aligning the compartmentalized microfluidic on top and facilitating the co-culturing of cortical and striatal neuronal cells.

The primary objective of this thesis was to characterize the electrophysiological activity of a cortico-striatal co-culture in a µFluidic-MEA device, with variation of axon diode microchannel lengths. A secondary objective was to enhance the unidirectionality of the device and recordable activity yield by modifying the microelectrode array layout and the number of electrically active microchannels. The co-culture is then observed in a newly proposed design µFluidic-r16MEA device following the same conditions of reversible (RB) and irreversible (IRB) final device assembly. The analysis of recorded electrophysiological activity was focused on action potential spike shapes classification, microchannel amplification effect, and measuring of the signal propagation velocities over the long-term cell culture maintenance (up to DIV 35).

One of the main findings in this thesis is the definition and characterization of small in peak-to-peak amplitude monophasic spike shapes that, to the best of our knowledge, have not been reported previously. The significance of these results lies in the comprehensive understanding of axonal dynamics within the microchannel area. The occurrence of this shape is associated with the boundary microchannel electrodes, indicating that the axon-electrode coupling is less effective and results in a less visible signal.

Depending on the electrode pair and the length of the microchannel observed for this type of analysis, the signal propagation velocities range from 0.14 to 1.7 m/s. The size of the microchannels allows multiple axons to pass through, making it challenging to determine with certainty whether a given spike pair is correct. This can be observed in recordings where the

directionality of signal propagation is atypical, with both forward and backward spike pairs being detected in a train of spikes that are labeled as belonging to the same axon.

In conclusion, the successful application of a novel fabrication approach for microchannels on top of an MEA has been demonstrated. The following effects of final device assembly (RB vs. IRB) were observed on electrophysiological activity from cortico-striatal co-culture. The introduced changes in the overall microfluidic design have brought benefits in terms of microchannel activity yield and unidirectionality of axonal growth.

Zusammenfassung

Die Untersuchung der Entwicklung und Degeneration des Gehirns wird häufig im Rahmen von *In-vivo*-Studien durchgeführt. Neu entwickelte *In-vitro*-Modelle bieten jedoch eine bessere Präzision und Spezifität bei der Untersuchung von neuronalen Netzwerken. Zum Beispiel die Verwendung von mikrofluidischen Mikrokanälen, die sich als erfolgreiche Methode zur Isolierung von Axonen und zur Steuerung ihres Wachstums erwiesen haben. Aufbauend auf der ursprünglich von Peyrin et al. 2011 vorgeschlagenen Axon Dioden Mikrokanalform habe ich ein µFluidic-MEA-Gerät mit integrierten Mikrokanalstrukturen auf einer Aufnahmeplattform entwickelt. Die Mikrokanäle wurden unter Verwendung von photostrukturierbarem Polymer, d.h. HD-8820, hergestellt, um die Präzision der Ausrichtung der kompartimentierten Mikrofluidik auf der Oberseite zu verbessern und die Ko-Kultivierung von kortikalen und striatalen neuronalen Zellen zu erleichtern.

Das primäre Ziel dieser Arbeit war die Charakterisierung der elektrophysiologischen Aktivität einer kortiko-striatalen Co-Kultur in einem µFluidic-MEA-Gerät, wobei die Länge der Axon Dioden Mikrokanäle variiert wurde. Ein sekundäres Ziel war es, die Unidirektionalität des Geräts und die aufzeichenbare Aktivitätsausbeute zu verbessern, indem das Layout des Mikroelektroden-Arrays und die Anzahl der elektrisch aktiven Mikrokanäle verändert wurden. Die Co-Kultur wird dann in einem neu vorgeschlagenen µFluidic-r16MEA-Gerät unter den gleichen Bedingungen der reversiblen (RB) und irreversiblen (IRB) Endmontage des Geräts beobachtet. Die Analyse der aufgezeichneten elektrophysiologischen Aktivität konzentrierte sich auf die Klassifizierung von Aktionspotential-Spike-Formen, den Mikrokanal-Verstärkungseffekt und die Messung der Signalausbreitungsgeschwindigkeiten während der Langzeit-Zellkulturpflege (bis zu DIV 35).

Eines der wichtigsten Ergebnisse dieser Arbeit ist die Definition und Charakterisierung von monophasischen Spike-Formen mit geringer Spitze-zu-Spitze-Amplitude, über die unseres Wissens bisher noch nicht berichtet worden ist. Die Bedeutung dieser Ergebnisse liegt in einem umfassenden Verständnis der axonalen Dynamik im Bereich der Mikrokanäle. Das Auftreten dieser Form ist mit den Grenzmikrokanalelektroden verbunden, was darauf hindeutet, dass die Kopplung zwischen Axon und Elektrode weniger effektiv ist und zu einem weniger sichtbaren Signal führt.

Je nach Elektrodenpaar und Länge des Mikrokanals, der für diese Art der Analyse beobachtet wird, liegen die Signalausbreitungsgeschwindigkeiten zwischen 0,14 und 1,7 m/s. Aufgrund der Größe der Mikrokanäle können mehrere Axone durchlaufen, was es schwierig macht, mit Sicherheit zu bestimmen, ob ein bestimmtes Spike-Paar korrekt ist. Dies kann bei Aufzeichnungen beobachtet werden, bei denen die Richtung der Signalausbreitung atypisch ist, wobei sowohl vorwärts als auch rückwärts gerichtete Spike-Paare in einer Folge von Spikes erkannt werden, die als zum selben Axon gehörig gekennzeichnet sind.

Zusammenfassend lässt sich sagen, dass die erfolgreiche Anwendung eines neuartigen Herstellungsverfahrens für Mikrokanäle auf einer MEA demonstriert wurde. Die folgenden Auswirkungen der Endmontage des Geräts (RB vs. IRB) wurden auf die elektrophysiologische Aktivität von kortiko-striatalen Co-Kulturen beobachtet. Die eingeführten Änderungen im gesamten mikrofluidischen Design haben Vorteile in Bezug auf die Ausbeute der Mikrokanalaktivität und die Unidirektionalität des axonalen Wachstums gebracht.

Abbreviations

AC	alternating current
ADC	analog to digital converter
AP	action potential
APTES	(3-aminopropyl) triethoxysilane
Au	gold
BSA	bovine serum albumin
BioMAS	bioelectronic multifunctional amplifier system
Ca^{2+}	calcium ion
Cal-AM	calcein-acetoxymethylester
Cl^{-}	chloride ion
CMOS	complementary metal oxide semiconductor
Comp -	compartmentalized
CMD	compartmentalized microfluidic devices
CNS	central nervous system
CNT	carbon nanotubes
DA	dopaminergic (neurons)
DIV	days in vitro
EAP	extracellular action potential
ECF	extracellular fluid
EIS	electrochemical impedance spectroscopy
EtHD	ethidium homodimer
EtOH	ethanol
EPSP	excitatory postsynaptic potential
GABA	gamma-aminobutyric acid
HBSS	Hank's balanced salt solution
HDMEA	high density microelectrode array
IPA	isopropanol
IPSP	inhibitory postsynaptic potential
IRB	irreversible bonding
K^{+}	potassium ion
LoC	lab-on-a-chip

MAD	median average distribution
MEA	microelectrode array
MEMS	micro-electromechanical systems
µFluidic	microfluidic
µTAS	miniaturized total analysis systems
N_2	nitrogen
Na^+	sodium ion
NB	neurobasal (medium)
OOC	organ-on-a-chip
PBS	phosphate buffered saline
PBO	polybenzoaxole
PDMS	polydimethylsiloxane
PEDOT	poly(3,4-ethylenedioxythiophene)
PLL	poly-L-lysine hydrobromide
PNS	peripheral nervous system
PSP	postsynaptic potential
PVD	physical vapor deposition
p2p	peak-to-peak
RB	reversible bonding
SCG	cervical ganglion
SDS	sodium dodecyl sulfate
SNR	signal-to-noise ratio
STA	spike triggered averaged (footprints)
TMAH	tetramethylammonium hydroxide
UV	ultraviolet

Table of Contents

Introduction

The human brain is a complex organ that has long inspired scientists in their investigations into its mechanisms of storing and processing information. The underlying concepts have significant value in understanding neural diseases, providing the key for improved brain-machine interfaces, and revolutionizing the domain of machine learning (Aebersold et al., 2016). There are two major approaches in studying the brain: top-down and bottom-up. The first approach entails observing the nervous system as a whole and subsequently examining it at increasingly smaller scales through the lens of stimulation-based behavioral changes. The second begins by studying the elementary functions of individual neurons and small circuits and extrapolate them to higher-level systems. The fundamental principles of neuronal mechanisms of action serve as a foundational understanding of the concepts of information processing in complex neuronal circuits. The electrophysiological activity of neuronal cells can be recorded, and this is where the connection of current technological development connects to nature itself. The microfluidic technique, in combination with an MEA technique, is a bottom-up approach in investigating neural circuits by recording their spatiotemporal activity. In this thesis, I refined and optimized this technique for controlling the direction of growth of axons and analyzed the spontaneous activity of co-cultured neuronal networks.

There are various approaches that can be employed to regulate and direct the growth of neurons in a culture. One of the most common methods utilized at our institute is microcontact printing. In this method, the surface is chemically patterned in a manner that attracts or repels cell bodies placed on that surface (Perl et al., 2009). Upon seeding, the neurons migrate in such a way as to only cover the cell-adhesive regions, thereby creating the pre-defined network that has been engineered on the stamp. An alternative method is to engineer the geometric features onto or into the substrate, which further controls the placement of cell bodies in small cages and entraps them on top of the electrodes (Erickson et al., 2008). One of the most widely used methods is also a soft lithography technique, which enables the application of removable structures. These are most commonly produced from polydimethylsiloxane (PDMS), a material that is easily handled and therefore a very suitable choice for engineering different types of microenvironments for controlled neuronal growth. Structures with through-holes can be used for cell immobilization and investigation of

networks with a single cell resolution (Li et al., 2014). Moreover, microfluidic PDMS structures can also be utilized for cell delivery, localization, or chemical screening (Millet and Gillette, 2012). Depending on the design, it is also possible to polarize the growth of axons by physically isolating the soma and dendrites, thereby enabling the analysis of specific regions of the neuronal cell components (Taylor et al., 2005). The potential applications are numerous. Given the simplicity and creative potential of the last approach, it was selected as a tool for a more detailed examination of neuronal co-cultures in this thesis.

The thesis is structured as follows: **Chapter 1** presents the fundamentals on the topic of basic concepts of electrophysiology of neuronal cells, electronic interfaces for recording their activity, and the history and application of compartmentalized microfluidic devices. In **Chapter 2**, detailed information on the materials, methods, measurements, and cell culture is provided. The section of Results and Discussion is divided into a total of three separate chapters. **Chapter 3** is devoted to the fabrication and characterization of the µFluidic-MEA devices employed in this study. It also addresses the initial and adapted designs of these devices, as well as the steps involved in acquiring each component of the final product. The results of reversible and irreversible device assembly are presented and discussed in the context of final device characterization through electrochemical impedance spectroscopy. The two main sections of **Chapter 4** address the adaptations of microfluidic design for successful cell culture development and the comparison of proposed axon-guiding shapes and axon-trap shapes for improving unidirectional axonal growth in these microenvironments. **Chapter 5** is focused on the analysis of electrophysiological recordings obtained in previously developed µFluidic-MEA hybrid interfaces. The results pertaining to unidirectionality, action potential spike shapes, the amplification effect of microchannels and signal propagation velocities are discussed in greater detail.

Chapter 1

Fundamentals

1.1 The Nervous System and Neuron Doctrine

The study of the brain has fascinated humans since ancient times, and this interest persists today. The evolution of neuroscience knowledge throughout history is as impressive as the field itself. Evidence of the first brain surgeries dates to prehistoric times, as seen at the Stone Age burial site of Enisheim, Alsace in France (Alt et al., 1997). Trepanation, the process of boring holes in the skull, was used 7000 years ago to treat headaches or mental disorders. It is interesting to note that 5000 years ago, ancient Egyptians did not give significant attention to the brain. Instead, they believed that the heart was the organ of highest importance for storing memories and the human soul. As a result, the brain was not preserved like the rest of the body for the afterlife but rather scooped out through the nostrils and discarded. Beliefs about the brain's involvement in sensations and intelligence began only in the times of Hippocrates in ancient Greece. Two centuries later, Galen gained a more detailed understanding of brain structure through dissections of animal brains. He identified the distinct central regions of the cerebrum, cerebellum, and ventricles. These observations formed the basis of the *fluid-mechanical theory* of brain function, which was strongly supported by Rene Descartes in the 17th century. According to this theory, the fluid is forced out of the ventricles through the nerves, causing movement in the body (Donaldson, 2009). In the following century, scientists extensively analyzed the nervous system, gaining a better understanding of the gray and white matter, as well as the patterns of grooves on the brain's surface.

During the 19th century, Luigi Galvani and Emil du Bois-Reymond made a significant discovery regarding the connection between nerves and electricity. They caused muscles to twitch with electrical stimulation of nerves, demonstrating that the brain can generate electricity. Galvani described nerve conduction as a consequence of the flow of electric fluid in an unbalanced condition (Piccolino, 2002). In the same century, Marrie-Jean-Pierre Flourens gained insight into function localization in the brain by systematically injuring animal brains. The development of microscopy techniques allowed Theodor Schwann to distinguish a single cell as a unit of tissue and propose *cell theory*. However, it remained unclear whether the nerve cell was a basic unit of the brain or part of a continuous *nerve net*.

By the end of the 19th century, Camillo Golgi, and Santiago Ramón y Cajal played crucial roles in examining the question of nerve cell-cell communication. Golgi invented the histological method of staining tissues in a silver chromate solution called Golgi stain, and Santiago used it

to its full potential. These contemporaries represented opposing ideas on the nature of nerve cell-cell communication. Golgi believed that the nerve net acts similarly to the blood vessels of the circulatory system. Ramón y Cajal (Garcia-Lopez et al., 2010) claimed that neurons communicate by contact, supported by a series of remarkable staining and drawings of different brain circuitries (Figure 1.1). Through his artistic and scientific skills, Ramón y Cajal significantly contributed to a better presentation of neuroanatomy in a functional context and is considered the father of modern neuroscience (Llinás, 2003). Cajal's hypothesis, known as the ***neuron doctrine***, posits that neuron is the fundamental unit of the nervous system. This idea was ultimately confirmed with the advent of the electron microscope in the 1950s.

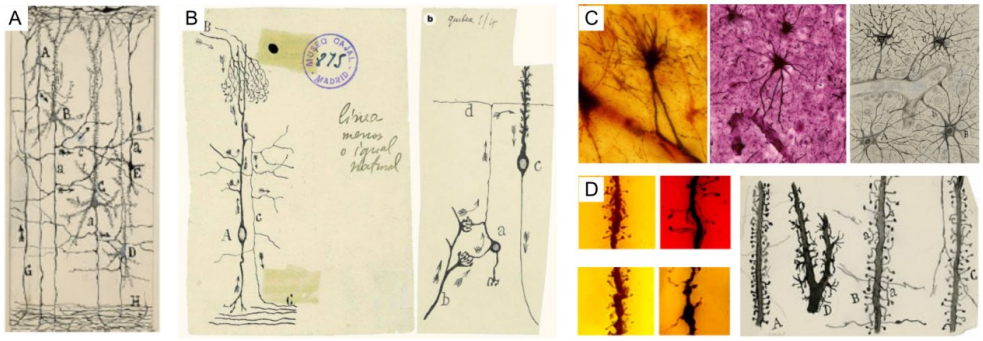

Figure 1.1 – Ramón y Cajal´s histological slides and drawings. **(A)** Drawing of pyramidal cells from a 15-year-old boy's brain (Garcia-Lopez et al., 2010). **(B)** Drawings of the directionality of "nervous current", indicating that the nervous impulse is conducted from the cell body towards the axon and then to the next neuron (Llinás, 2003). **(C)** An example of histological slides (on the left) and corresponding drawings (on the right) of fibrous astrocytes and **(D)** dendritic spines in pyramidal cells of the frontal cortex (Garcia-Lopez et al., 2010).

Other contemporaries of Cajal who made significant contributions to the understanding of neuronal electrophysiology were Herman von Helmholtz and Julius Bernstein. Helmholtz correctly hypothesized that complex electrical molecular rearrangements were the cause of nervous conduction, while Bernstein partially understood the negative intracellular potential by connecting it with the potassium electrochemical equilibrium and the selective permeability of the membrane to this ion (Piccolino, 2002). These are fundamental building blocks for further research in neuroscience. Since then, we have learned much more about the nervous system, including its structure and complex functions in the human body. In the following paragraphs, I will review the structure and electrophysiological nature of neuronal cells, the mechanism of action potential generation, and cell-cell communication.

1.1.1 Neuronal Cell

The nervous system is composed of two types of cells: glial cells and nerve cells, also known as glia and neurons (Kandel et al., 2013a). Both types are present in approximately equal numbers (around 85 billion cells of each type). Although they are similar in number, these cells differ significantly in morphology and function. Glial cells play critical roles in maintaining the functionality of the nervous system. Astroglia distribute nutrients, microglia respond to neuronal immune response, and oligodendrocytes isolate neurons. These functions are essential for the proper functioning of the nervous system (Benjamin Kacerovsky and Murai, 2016). Although both types are important, neuronal cells can be considered the smallest functional units of the nervous system. They are responsible for most of the brain's unique functions in information processing.

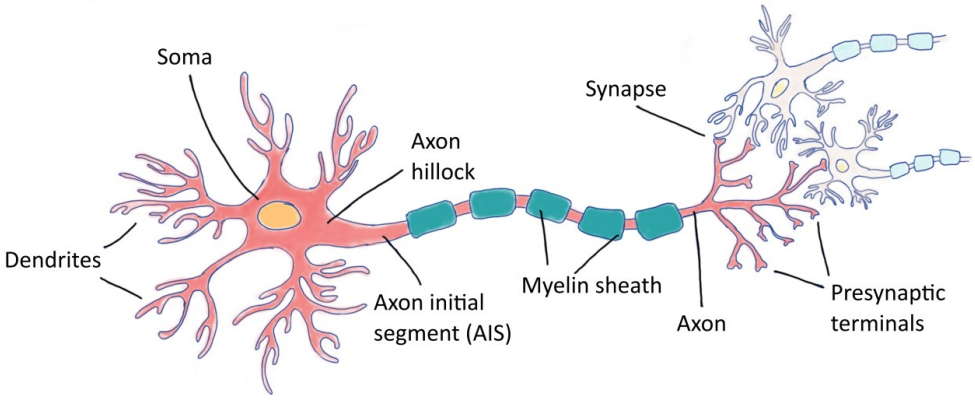

Figure 1.2 – **The structure of a neuron**. The neuron's metabolic center responsible for synthesizing necessary proteins and metabolites for information processing is the cell body or soma. Dendrites receive signals from other neurons, while the axon arises from the axon hillock and extends to greater lengths. The action potential is initiated in the axonal initial segment (AIS) and propagates down the axon to the presynaptic terminals. Here, information is transmitted across synapses. Additionally, the insulation provided by the myelin sheath improves the conduction of axon potentials.

A typical mature neuron morphology has four defined regions: the cell body (soma), dendrites, axon, and presynaptic terminals (Figure 1.2). The cell body, usually about 20 µm in diameter, contains organelles typical of a eukaryotic cell (Bear er al., 2015a). including the nucleus, endoplasmic reticulum, Golgi complex, and mitochondria. Dendrites are shorter, branching structures that receive signals from upstream neurons. Meanwhile, an axon sends electrical signals downstream from the soma over distances ranging from 0.1 mm to 2 m, also known as action potentials. Action potentials are initiated in the initial segment of the axon and propagate down the axon at speeds ranging from 1 to 100 m/s (Kandel et al., 2013b). More

information on action potential will be provided in the following paragraphs. The conduction speeds of action potentials are influenced by the insulating lipid sheath, or myelin, which is spread at regular intervals around the axon. Presynaptic terminals are specialized regions of axonal branches where signals are transmitted.

1.1.2 Resting Potential

As briefly mentioned, neuron cells exhibit their function by conducting a particular type of signal – **action potential**. These nerve impulses refer to the change in potential or, in other words, to the separation of electrical charge across the membrane. This means that the neuronal cell membrane is excitable, and the mechanism of action potential will be explained in the next section 1.1.3. The membrane of the excitable cell is *at rest* when the cell is not generating impulses. At rest, there is a specific distribution of electrical charge, being negative along the inside compared to the outside surface of the cell membrane. The difference in this electrical charge across the membrane is called the **resting potential** (Bear et al., 2015b).

Ion	Concentration outside [mM]	Concentration inside [mM]	Equilibrium potential [mV]
K^+	5	100	-80
Na^+	150	15	62
Ca^{2+}	2	≤0.0002	123
Cl^-	150	13	-65

Table 1.1 – **Approximate ion concentrations and equilibrium potentials**. Each ion is present inside and outside the neuronal cell and influence the membrane potential (adapted from Bear et al., 2015c).

The membrane plays an important role in separating the electrical charge between the intra- and extracellular sides. As in any animal cell, the characteristic feature of the membrane is the phospholipid bilayer, accompanied by a large variety of transmembrane proteins that provide a high functionalization property for successful interaction with the environment. The intra- and extracellular fluids are water-based environments and, therefore, effective solvents for charged or polar molecules and ions. The ions carrying the principal role for the neuronal cell membrane potential characteristics are cations: Na^+ (sodium), K^+ (potassium), Ca^{2+} (calcium), and anions: Cl^- (chloride). At rest, the concentration of these ions is approximately constant in the intra- and extracellular region (Bear et al., 2015b).

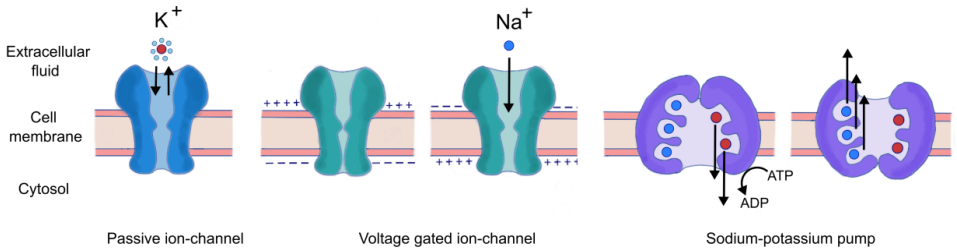

Figure 1.4 – Transmembrane proteins in charge of transferring ions across the cell membrane. The figure shows the most common ion channels and a pump responsible for the rest state of the membrane and action potential. Passive ion channels are highly selective and permeable to the specific hydrated ion. Voltage-gated ion channels are activated upon the change in membrane potential and present one of the crucial actors in the depolarization phase of an action potential. Sodium-potassium pump is an example of the active transport of these ions against the concentration gradient, intending to maintain the ionic concentration gradients that drive Na^+ and K^+ through their channels during the action potential. Figure adapted from Kandel et al. (2013b) and Bear et al. (2015c).

Ion channels and ion pumps, the specialized transmembrane proteins, mediate the movement of ions across the membrane (Figure 1.4). Ion channels are passive transporters and can be ion-specific or gated channels. The ion-specific channels work mainly on the principle of diffusion down the concentration gradient of one specific ion, while the changes in the local microenvironment of the membrane regulate the gated-ion channels. These changes can include electrical, mechanical, or chemical signaling. On the other hand, active ion

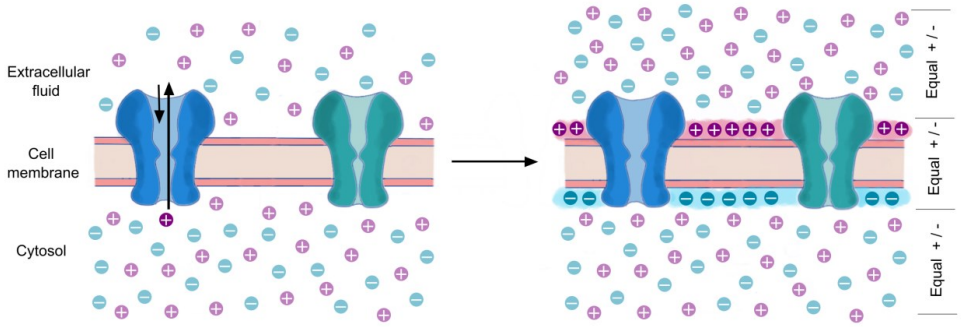

Figure 1.3 – Establishing equilibrium in a selectively permeable membrane and capacitive properties of the phospholipid bilayer. Potassium ions are shown in purple, while blue spheres present negatively charged ions. Due to the concentration difference, potassium ions diffuse down the concentration gradient via potassium-selective ion channels (in this case, from inside to the outside). Upon the equilibrium formation between the diffusion and electrostatic force, the slight imbalance between the positive and negative charge on the opposing sides of the membrane yields a potential difference. In the case of K^+, it is equal to -80 mV (Table 1.1). The positive and negative charges are equally distributed across the membrane (right), giving the phospholipid bilayer capacitive properties. Figure adapted from Bear et al. (2015b).

transporters, or ion pumps, work on the principle of using energy in order to transport specific ions across the membrane, usually against the concentration gradient (Kandel et al., 2013b; Bear et al., 2015c).

Ion channels' roles in electrical signaling, establishing, and maintaining the membrane rest state make them a key factor in the physiology of the nervous system. Because of their crucial functions, many neurological diseases are associated with the malfunction of these channels. K^+ ions are drawn by diffusion to the outer region through potassium-specific ion channels to balance the difference in concentration across the membrane. As this happens, the net charge of the cell interior becomes negative because the positive charge is exported. Because the phospholipid bilayer is only 5 nm thick, the charge distribution localizes on both sides of the membrane. Hence, the neuronal cell membrane is said to store electrical charge and thus exhibit capacitive properties (Figure 1.3). Likewise, the neuronal membrane dynamics can be represented via the equivalent electric circuit (Figure 1.5).

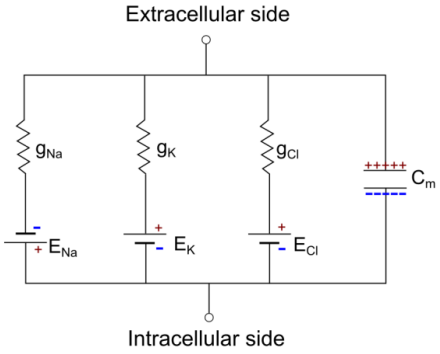

Figure 1.5 – An equivalent circuit of the neuronal membrane. The movement of ions across the cell membrane assigns important electrical properties to neuronal cells. These properties can be illustrated by the mode derived from electrical circuits. The phospholipid bilayer does not have conductive properties, but its ability to separate electrical charge gives the equivalent to a capacitor. Each ion channel that contributes to the distribution of ions across the membrane can be considered a resistor or a conductor of ionic current. Figure adapted from Kandel et al. (2013c).

Now, negatively charged chloride ions from the inside start attracting the potassium ions that have diffused to the outside. At some point, this electrostatic force perfectly counterbalances the force of diffusion, making the potassium ion net movement at equilibrium. This equilibrium can be defined as the electrical potential difference that balances against an ionic concentration gradient and is called **ionic equilibrium potential E_{ion}** (Bear et al., 2015b). Each

ion has its ionic equilibrium potential, which can be calculated with the use of the Nernst equation (Bear et al., 2015b):

$$E_{ion} = 2.203\ \frac{RT}{zF} log_{10} \frac{[ion]_{out}}{[ion]_{in}} \tag{1.1}$$

Where **R** is the gas constant, **T** is the temperature, **z** is the charge of the ion, **F** is Faraday's constant, and $\mathbf{[ion]_o}$ and $\mathbf{[ion]_i}$ are the concentrations of the given ion outside and inside the cell. At body temperature (37 °C), the ionic equilibrium potential depends only on the ionic concentrations on either side of the membrane. The term $2.303\ \mathrm{RT}/z\mathrm{F}$ can be calculated as 61.54 mV for K^+ and Na^+, -61.54 mV for Cl^-, and 30.77 mV for Ca^{2+}. The inside concentration of potassium ions is twenty times higher than on the outside (Table 1.1), giving the final calculation on ionic equilibrium potential for potassium ions:

$$E_K = 61.54\ mV\ \times log \frac{1}{20} = -80\ mV \tag{1.2}$$

Ionic concentration gradients are highly dependent on the actions of ion pumps, the proteins that actively transport the ions across the membrane (Figure 1.3). The essential pumps are the sodium-potassium pump and the calcium pump. The sodium-potassium pump is an enzyme that uses the chemical energy derived from the ATP dephosphorylation for the internal Na^+ exchange with the external K^+. By transporting these ions against the concentration gradient, this pump ensures that K^+ concentrates inside and Na^+ concentrates outside the cell. This process is of great importance for neuronal functioning and takes up as much as 70% of the overall ATP molecules used by the brain (Bear et al., 2015c). The calcium pump actively transports Ca^{2+} ions outside of the cell, keeping the internal concentrations of Ca^{2+} at a low level (≤ 0.0002 mM). The ionic equilibrium potentials present the values of membrane potential that would exist exclusively if the membrane was selectively permeable entirely to that exact ion of interest. However, the reality of the cell membrane dynamics is different, as it is concurrently permeable to various types of ions but at distinct levels. When calculating the resting membrane potential, these facts must be considered, and they are found in the modified Nernst equation, the Goldman equation. With respect to the minor influence of Ca^{2+} and Cl^- ions, the membrane potential depends mainly on the K^+ and Na^+ concentrations and relative membrane permeability to these ions. In conclusion, the Goldman equation takes on the following appearance:

$$V_m = 61.54\ mV\ log_{10} \frac{P_K[K^+]_{out} + P_{Na}[Na^+]_{out}}{P_K[K^+]_{in} + P_{Na}[Na^+]_{in}} \tag{1.3}$$

Where P_K and P_{Na} represent the relative permeability of potassium and sodium ions. As the membrane is 40 times more permeable to K^+ than Na^+ (P_{Na} = 1 and P_K = 40) the calculated membrane potential at rest is -65 mV (Bear et al., 2015). This value is closer to the ionic equilibrium potential of potassium (E_K = -80 mV), due to the higher permeability of the membrane to this ion.

1.1.3 Action Potential and Axonal Conduction

1.1.3.1 Generation of An Action Potential

An **action potential (AP)** is a signal that conveys information between neurons and over long distances. Compared to the cell membrane at rest, an action potential is a rapid event that reverses the charge distribution inside and outside the membrane. It happens when a neuron receives a stimulation strong enough to depolarize the membrane to a **threshold** voltage, usually around -50 mV (Figure 1.6). If the depolarization reaches this threshold value, voltage-gated Na^+ channels open, and sodium ions from the

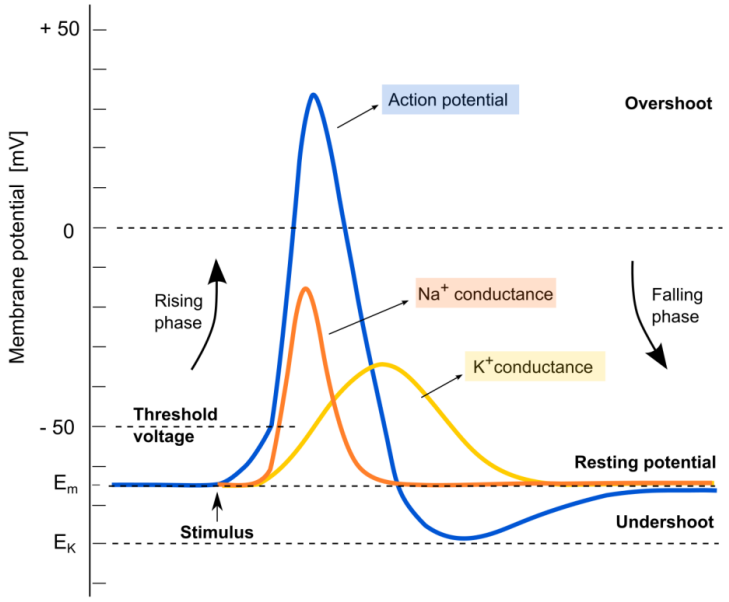

Figure 1.6 – The neuronal action potential. The action potential consists of separate components that attribute to the opening of Na^+ and K^+ channels, described by Hodgin and Huxley's model. The graphic depicts the relationship between potassium and sodium ion channels. The undershooting phase of the action potential occurs due to the temporal difference between Na^+ and K^+ channel activities. Namely, as the sodium conductance decreases, potassium conductance is still present due to the open voltage-gated potassium channels adding up to this ion's already high membrane permeability. Figure adapted from Kandel et al. (2013d) and Bear et al. (2015e).

outside are streamed inside the cell by a driving force of concentration gradient and electrostatic attraction. This event causes further rapid depolarization of the membrane, also called **the rising phase**, up to about 40 mV. This positive part of the action potential is the **overshoot**, where the charge reversal is established, and the inner side becomes positively charged. At this moment, the membrane potential is closer to the value of sodium equilibrium potential (Table 1.1).

This depolarization causes the inactivation of voltage-gated Na^+ channels and triggers the opening of voltage-gated K^+ channels. The strongly depolarized membrane causes the K^+ ions to stream out of the cell, repolarizing the membrane to a negative potential, seen on the graph as the **falling phase**. The voltage-gated potassium channels add up to already high K^+ permeability, and since the sodium channels are closed, the membrane is experiencing hyperpolarization close to the value of E_K. This phase of the action potential is called **undershoot**, as it is more negative than the resting membrane potential. The membrane is hyperpolarized while the voltage-gated potassium channels are open. Then, the channels are again closed with sequential membrane depolarization. During these rapid changes of ions influx and efflux, the previously mentioned sodium-potassium pump works all the time to maintain the concentration gradients of Na^+ and K^+ that will drive these ions through their channels during the next action potential. Typically, the action potential lasts about 2 ms (Kandel et al., 2013c; Bear et al., 2015d).

In 1952, Hodgin and Huxley introduced a mathematical conductance-based **H-H model** that describes the initiation and propagation of action potentials in neurons. This model was a leading scientific breakthrough, proving that neuronal membranes behaved nonlinearly (Meunier and Segev, 2002). The model for the generation of action potential in its single-compartment form can be defined by the following equation that defines the membrane current as a sum of a leakage current, a delayed-rectified K^+ current, and a transient Na^+ current (Hodgkin and Huxley, 1952):

$$I_m = g_{leak}(V_m - E_{leak}) + g_K n^4 (V_m - E_K) + g_{Na} m^3 h (V_m - E_{Na}), \qquad (1.4)$$

where $\mathbf{1/g_{leak}}$ is the passive membrane resistance $\mathbf{R_{leak}}$, $\mathbf{g_K}$ and $\mathbf{g_{Na}}$ are the conductances of the respective ion channels, $\mathbf{E_{leak}}$ is the resting potential of the membrane, $\mathbf{E_K}$ and $\mathbf{E_{Na}}$ are the reversal potentials of the ion channels, and **n**, **m**, and **h** are the gating variables. Although it has a significant historical achievement, the H-H model had to be adapted over time due to several weaknesses. The most prominent is the inaccurate prediction of the inactivation kinetics of the sodium channels. Namely, later it has been shown that the inactivation of

sodium channels occurs only after their activation (Bezanilla and Armstrong, 1977), which matches the findings of a second open state for sodium channels (Chandler and Meves, 1970). The equation also includes only two voltage-dependent ionic currents, which is why researchers preferably use H-H-like models by adding new currents according to the observed situation (Dayan and Abbott, 2005; Meunier and Segev, 2002). The H-H model provides undoubtful usefulness at the single-cell level, but it has no use in observing the collective phenomena in neural networks, like the collective synchronization of activity (Meunier and Segev, 2002). In describing the behavior of neural networks, integrate-and-fire (I-F) type models (Abbott, 1999) and phase-oscillator models (Hansel et al., 1993) are finding better applications.

1.1.3.1 Axonal Conduction

Usually, the AP propagates towards the tip of the axon, but some studies also report back-propagation of action potential into dendrites (Sakmann and Stuart, 1994; Rapp et al., 1996; Mateus et al., 2021). The AP is generated at the axon hillock (Figure 1.2), where the density of voltage-gated Na^+ channels is the highest. The membrane behind the generated action potential is in the refractory phase because of the inactivated sodium channels (Kandel et al., 2013c). This means that depolarization spread is driven by the difference in potential between the axonal membrane's active and resting regions and thus dictates propagation direction. Neuronal conduction velocity is a significant property of neuronal activity, as precise regulation is needed to utilize complex nervous system activities correctly. Conduction velocity depends on various aspects, but the most significant evolutionary solution in vertebrates for increasing the velocity is the development of a myelin sheath that serves as an insulation layer wrapping the axon and preventing the current leakage. Myelination of axons was for the first time described in the 19th century (Virchow, 1854) as a lipid-based multiple-layer sheath provided by oligodendrocytes in the central nervous system (CNS) and Schwann cells in the peripheral nervous system (PNS) (Seidl, 2014). This sheath is interrupted in regular intervals called nodes of Ranvier (Figure 1.2), where the density of voltage-gated sodium channels is high, and the action potentials are reactivated. Conduction velocity depends on many parameters, such as the thickness of myelin sheath, ion channels distribution, kinetics, internodal distance, varicosities, branching points and geometry, extracellular accumulations of neurotransmitters and ions, or axonal coupling through gap junctions and ephaptic interactions (Debanne, 2004).

The acceleration of conduction velocity is not the most important evolutionary achievement, as all mentioned properties contribute to a complex coordinated regulation of axonal conduction, with the aim of isochronic conduction to different target locations. Axonal branches can show a decreased conduction or even backward propagation, depending on the defined purpose of the activity. This occurrence is different from the traditional representation of axons as reliable transmission cables in which the action potential steadily propagates once it has been generated. Later studies of single-neuron extracellular recordings on custom CMOS technology show a significant dynamics of conduction velocities occurring locally within single axons (Bakkum et al., 2013).

1.1.4 Cell-Cell Communication via Synaptic Transmission Mechanisms

Neuronal cells transfer information to each other via synaptic transmission, described for the first time in the nineteenth century by English physiologist Charles Sherrington (Bear et al., 2015f). The histological description of this site was done for the first time by Ramon y Cajal, although opposing scientific opinions regarding information transmission were still present at the time. The nature of these sites of contacts named synapses was discovered in more detail years later when the hypothesis of chemical transmission was supported in 1921 by Otto Loewy, and the hypothesis of electrical transmission was proven in 1959 by Edwin Furshpan and David Potter (Bear et al., 2015f). Concrete numbers vividly describe the importance and prevalence of these connections: in the human brain that contains at least 10^{11} neuronal cells, an average neuron forms and receives 1000 to 10 000 synaptic connections. This means there are 10^{14} to 10^{15} synaptic connections in the brain, equivalent to a number 1000-fold higher than the 100 billion stars in our galaxy (Kandel et al., 2013e)!

1.1.4.1 Electrical Synapse

The electrical synapse has a site of connection called a gap junction, where the cell membranes of two cells are only 3 nm apart. At each side of this narrow gap, special clusters of proteins called **connexins** form two channels, **connexons**. When combined, two connexons create a **gap junction channel**. This complete physical connection of two communicating cells enables the direct passage of ions from one cell to another (Figure 1.7). The gap junction channel allows the passage of ions in either direction, making these synapses bidirectional in their

nature of signal propagation direction. Action potential from the presynaptic cell causes the ionic current to flow through the channel, depolarizing the postsynaptic cell and evoking a postsynaptic potential (PSP). The time delay between these potentials is remarkably short, measured in a fraction of a millisecond. In contrast to later described chemical synapses, the postsynaptic cell gets depolarized even in the case of a subthreshold depolarizing current in the presynaptic cell (Kandel et al., 2013d). The exceptionally rapid transmission across electrical synapses carries different benefits and importance in the nervous system and vertebrate brain. Speed is useful for escape responses or for orchestrating the actions of large groups of neurons (Kandel et al., 2013e). However, this property is not the main advantage compared to chemical synapses because the chemical synaptic delays are insignificantly low. The more significant specialty of gap junctions is bidirectionality and interconnection of mutually similar neurons in the brain, whereas chemical synapses are usually unidirectional.

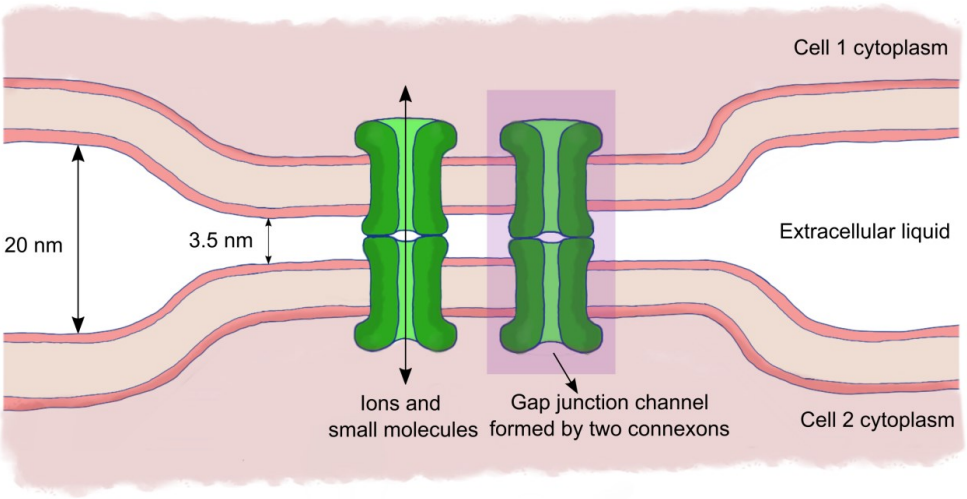

Figure 1.7 – Electrical synapse. Two connexon proteins (green) from different cells form a tight bidirectional connection called gap junction. Figure is adapted from Bear et al. (2015f).

This symmetrical coupling simultaneously strengthens communication in multiple cells, thus providing a coordinated act as one large cell (Connors and Long, 2004). Gap junctions are commonly formed during brain development when they transmit both types of signals, electrical and chemical, responsible for cell maturation and growth (Bear et al., 2015f). Their role is not entirely electrical, as they can also transport metabolic signals by conducting different ions like Ca^{2+}, which acts as a second messenger or allow moderate-sized organic

compounds or peptides to rapidly reach a target cell (Kandel et al., 2013e). Gap junctions are also present in non-neural cells, like glia, epithelial cells, liver cells, or cardiac cells.

1.1.4.1 Chemical Synapse

The mechanism of chemical transmission is more complex than in electric synapses. The notable difference is the non-existence of any structural continuity that would enable direct communication, but communication is carried via specific chemical substances – **neurotransmitters** (Bear et al., 2015f). Neurotransmitters released from the presynaptic axon terminals diffuse across the 20-50 nm wide synaptic cleft and bind to the receptors in the postsynaptic cell membrane of the target cell (Figure 1.8).

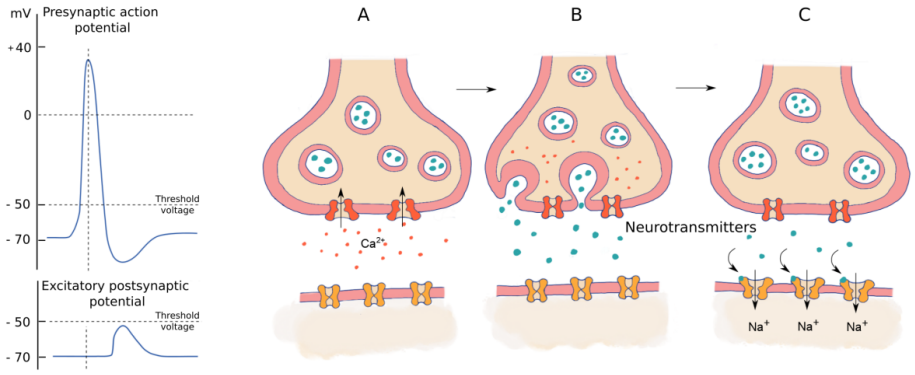

Figure 1.8 – Chemical synaptic transmission. Several complex steps in the chemical synaptic transmission cause a delay between the presynaptic and postsynaptic potential. The figure shows an example of the EPSP that starts approximately with a 1 ms delay compared to the action potential in the first cell. This is a clear difference from electrical synapses, where communication happens instantaneously. **(A)** Calcium voltage-gated channels open in response to the incoming action potential, and Ca^{2+} rushes from the outside to the cell's interior. **(B)** The rise of the inside concentration of Ca^{2+} initiates exocytosis of the vesicles containing neurotransmitters. **(C)** Neurotransmitters diffuse across the synaptic cleft and finally bind to the corresponding postsynaptic membrane receptors. This causes the change in ion channel activity, thus modulating their conductivity. In this example, receptors are opening for the influx of Na^{+}, causing the generation of EPSP.

Most neurotransmitters belong to one of three chemical categories: amino acids, amines, and peptides. Some simple neurotransmitters like glutamate and glycine are readily available, as they are abundant in all cells of the body. At the same time, gamma-aminobutyric acid (GABA) and amines have to be synthesized in the neuronal cell that releases them. This synthesis takes place in the axon terminal, where they are also packed into synaptic vesicles. The peptide neurotransmitters are synthesized from amino acids strung together by the ribosomes in the endoplasmic reticulum and then further processed through the Golgi apparatus. Further, they

are transported within the secretory granules to the axonal terminal (Bear et al., 2015f). With a slight difference, both synaptic vesicles and secretory granules release their neurotransmitters in the process of exocytosis triggered by the arrival of action potential to the axon terminal and consequential activation of voltage gated Ca^{2+} channels. This is followed by a large inward driving force on Ca^{2+}, due to a very low resting concentration of calcium ions (see Table 1.1). This influx of Ca^{2+} ions signals for the rapid neurotransmitter release into the synaptic cleft. Exocytosis of secretory granules is also a calcium-dependent event. However, their different position relative to the active zone requires high-frequency trains of action potential to reach the necessary inner calcium concentration for the peptide release (Bear et al., 2015f).

Chemical nature does not determine the activity of a neurotransmitter, but it is entirely dependent on the binding receptor properties. Thus, the same neurotransmitter can act inhibitory or excitatory on the postsynaptic cell. Receptors perform an effector function in the target cell by responding to a stimulus, such as a neurotransmitter binding. The typical role of the receptor is the opening or closing of ion channels. In case when open channels are permeable to Na^{+}, the postsynaptic cell gets transiently depolarized towards the threshold potential for initiating the action potential. This depolarization is called an **excitatory postsynaptic potential** (EPSP), and the effect of neurotransmitter binding is **excitatory**. On the other hand, when the net effect is **inhibitory**, the postsynaptic cell is experiencing hyperpolarization due to the ion channel permeability to Cl^{-} (chloride equilibrium potential is negative, see Table 1.1). A transient hyperpolarization of the postsynaptic membrane potential is called **inhibitory postsynaptic potential** (IPSP) (Bear et al., 2015f). The binding of a neurotransmitter can control the opening of ion channels either directly or indirectly. Ionotropic receptors are concurrently serving as ion channels that open directly by undergoing conformational change upon the transmitter binding (therefore, also called transmitter-gated ion channels). In contrast, activated metabotropic receptors stimulate the production of second messengers that, in a cascade of events, finally modulate ion channel activity. The duration of synaptic actions drastically differs between these two types of receptors. For example, the ionotropic lasting in milliseconds is common in mediating rapid behaviors like stretch or reflex, while the metabotropic measured in seconds to minutes reinforces pathways in learning (Kandel et al., 2013e).

1.2 Electrophysiological Recording of Neuronal Cells

At the beginning of the electrophysiological research of electrogenic cells in 1950s, scientists used the squid axon or giant snail neurons because of their large size and easier technical manipulation (Hodgkin and Huxley, 1952; Huxley, 2002). With the rise of technological development, measuring electrical neuronal activity has become more and more sophisticated. This is a rapidly developing field with wide applications in diagnostics and medical treatment of various neurological diseases. In this section, I will focus on two basic techniques of electrophysiological recordings – the patch-clamp technique and microelectrode arrays (MEA), used for intracellular and extracellular recordings, respectively. The activity of primary cortical and striatal cell cultures in this thesis was investigated with microelectrode arrays, however, understanding the differences between these two techniques is important for interpretation of recording results.

All these approaches are valuable in studying ion channel behavior in various conditions and providing very high signal-to-noise ratio recordings, including the subthreshold potentials. However, the patch-clamp technique is limited to the investigation of single neurons, and its invasive approach cannot support the studies of developing neuronal networks or change over extended periods.

1.2.1 Intracellular vs. Extracellular Recordings

1.2.1.1 Intracellular Recording

A widely used technique from the 1950s was the ***voltage clamp*** attributed to Kenneth C. Cole, which presents a feedback system to control the potential difference across the membrane (Bear et al., 2015g). By controlling the membrane potential at the set value, they were able to measure the currents flowing across the membrane and deduce the changes in membrane conductance on different membrane potentials.

However, due to the robustness of this technique, they could not study mammalian cells, which are much smaller and more challenging to handle. An advancement in this direction happened through the development of the **patch-clamp** technique by Sakmann and Neher (1984). In principle, they used this technique to resolve the current contributions of individual

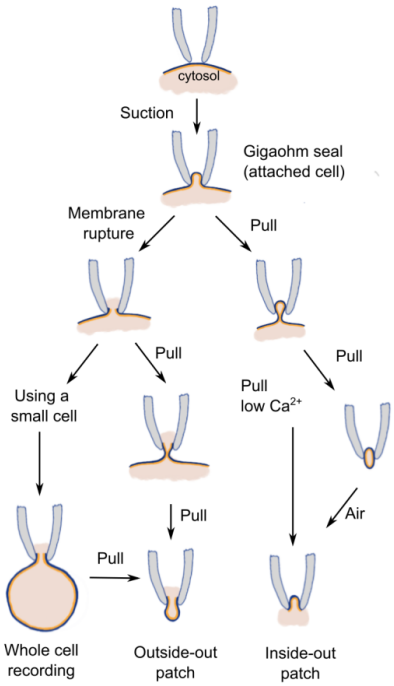

Figure 1.9 – Schematic representation of different patch-clamp configurations. After obtaining the gigaohm seal between the pipette and membrane patch, different experimental configurations are possible. For a more straightforward observation of the specific steps, the cell membrane is simplified into two layers, representing the outer (in dark blue) and inner (in orange) sides of the cell membrane. The figure is adapted from (Hamill et al., 1981).

ionic channels in an electrogenic cell membrane. During a patch-clamp recording, a glass micropipette filled with electrolytes and attached to a conductive wire as an electrode is brought in close contact with the cell membrane. The potentials are measured with respect to an Ag/AgCl reference electrode. The crucial technical step is establishing an electrical seal between the pipette and membrane. By achieving this seal, the current flowing through the pipette is identical to the current flowing through the selected piece of the membrane. By applying a slight suction through the pipette, this small piece of membrane, or *a patch*, is sucked into the pipette interior, creating a semivesicle in the shape of an omega (Figure 1.9). This step provides a tight seal of the patched membrane to the inner pipette wall, and the electrical resistance across the seal reaches the order of 10-100 gigaohms. The high seal resistance enables high-resolution current measurements and the application of voltages across the membrane. Different measurement configurations can be obtained by further manipulating the sealed membrane patch, as shown in Figure 1.9 (Hamill et al., 1981). In the

case of the *whole cell recording*, the pipette establishes an electrical connection with the cell interior after rupturing the membrane patch. Although this ensures an improved signal amplitude, direct mixing of the electrolyte and cytosol can have a negative impact on the cell. This access of the pipette interior to the intracellular space makes it possible to study the direct effects of drugs on cells in real-time. When the pipette is slowly withdrawn from the cell, the fragments of the pulled-out cell membrane fuse together, creating the *outside-out* configuration. This configuration can be used in studying ionic channels controlled by externally located receptors. For studying the intracellular surface of the membrane with the *inside-out* configuration, the pipette and the cell membrane form a gigaseal without rupturing the membrane, after which the selected membrane patch is pulled out from the rest of the cell. The ends of the patch membrane can fuse and form a vesicle, which has to be opened by air exposure or solutions free of divalent ions. Consequently, the interior of the cell membrane faces the solution used for various influence on membrane currents.

1.2.1.2 Extracellular Recordings

The challenges facing the patch clamp technique became solvable with the development of **microelectrode arrays (MEAs)** in the 1960s and 1970s (Pickard, 1979). Microelectrode arrays (Figure 1.10) are devices for extracellular recordings of electrogenic cells, either from dissociated cultures or explants and tissue slices (Weidlich, 2017). The principle of their work is sensing the voltage drop in the cleft between the cell membrane and a recording electrode. The voltage drop happens because cellular ionic current changes during an action potential

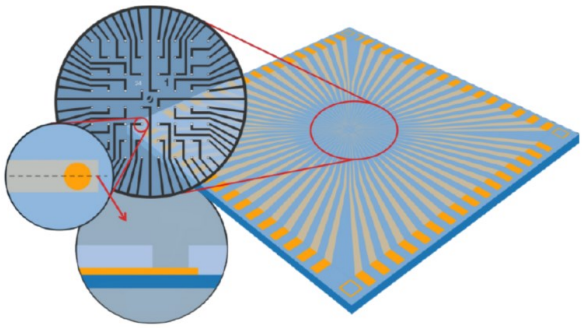

Figure 1.10 – **Microelectrode array.** Schematic representation of a 64-electrode MEA. Electrodes are placed in a regularly spaced grid of 8 x 8 electrodes in the center of an MEA. The metal layer (yellow) is insulated with a passivation layer (light blue) with openings for electrodes and contact pads that are supposed to be in contact with electrogenic cells and the measuring device, respectively. Figure adapted from Weidlich (2017).

(Bear et al., 2015g). The first successful recordings of cultured cardiac myocytes on MEAs were reported by Thomas et al. (1972). The following reports included the use of MEAs in studying ganglion cells from the snail *Helix pomatia* and cultured neonatal rat superior cervical ganglion cells (Gross, 1979; Pine, 1980). The MEA fabrication technology advanced in 1986, when flexible MEAs were used for elongated recordings of extracellular field potentials from brain slices (Novak and Wheeler, 1986; Boppart et al., 1992). This enabled thorough studies of neural networks by simultaneous stimulation or recording multiple sites of neural circuits *in vitro*. Its non-invasive cell-electrode interface and spatiotemporal measurement platform allow recordings and stimulation over prolonged periods (Kim et al., 2014). The fabrication process is relatively simple: a conductive layer is deposited on a planar substrate, and the photolithography technique is used to structure the electrode positions, contact feedlines, and contact pads. Subsequently, the MEA is insulated by a passivation layer of the desired material, and only contact pads and electrodes are opened in additional photolithography or etching process. One of the significant aspects of achieving a good signal coupling is ensuring a low impedance of the microelectrodes (more in section 1.2.2).

Decades of technological advancements resulted in various ways of improving and overcoming the MEA challenges. For example, a limiting feature of MEAs is that the number and length of contact feedlines define the number of available electrodes. In order to play around this issue, one has to compromise between losing the spatial resolution if increasing the array size and increasing the noise due to the prolonged contact feedlines (Eick, 2009). A different complementary metal oxide semiconductor (CMOS) technology approach is partially overcoming this issue. CMOS improves spatial resolution by integrating active electronic components on the same substrate as the actual electrodes. This kind of co-integration improves signal amplification due to significantly fewer parasitic capacitances and resistances than classic MEA (Hierlemann et al., 2011). These devices may contain hundreds to thousands of electrodes that map electrical activity at sub-cellular resolution. In this manner, Bakkum et al. (2013) observed the change in axonal conduction along a single axon, and Abbott et al. (2020) used a newly developed CMOS chip for recording direct synaptic signals.

Electrode impedance is another factor to consider for improving recording quality, as it directly affects the signal-to-noise ratio (SNR) (Guo et al., 2012). Electrode surface area and impedance are reversely proportional; thus, the impedance can be lowered by increasing the effective

surface area of the electrode (Kim et al., 2014). For achieving this, porous materials like platinum black show promising applications (Chang et al., 2000; Heim et al., 2012a) however, the problem of mechanical stability remains. The use of carbon nanotubes (CNTs) also effectively increases the roughness of the recording electrodes (Heim et al., 2012b; Keren and Hanein, 2012) and, with certain modifications of the surface represents a promising tool for *in vivo* applications (Foremny et al., 2021) also in conjugation with conductive polymers (Castagnola et al., 2015) like poly(3,4-ethylenedioxythiophene) (PEDOT). Another possible way to increase the cell-electrode contact area while preserving the low impedance is by introducing nanocavities between the electrode and insulation layer. This nanocavity space allows for keeping a large electrode area for lower impedance while maintaining a single-cell resolution with limited geometrical access to an electrode on the surface of the MEA (Hofmann et al., 2011; Czeschik et al., 2014, 2015). Indirectly, the SNR can be improved by introducing microfluidic microchannels over the electrodes that serve as **axon signal amplifiers** (FitzGerald et al., 2008). As this is closely related to the topic of this thesis, more words on this effect are written in section 1.3.3.

1.2.2 Relationship Between Intra- and Extracellular AP Shape

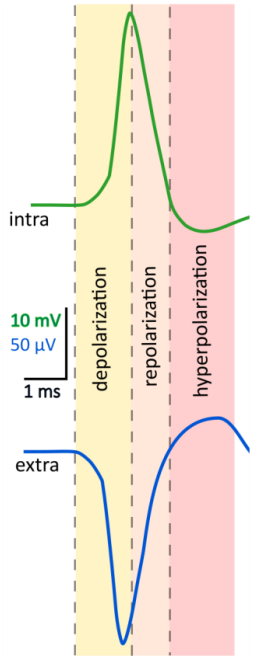

Figure 1.11 — Approximate illustration of intra- and extracellular temporal and waveform relationship. Figure adapted from Henze et al. (2000).

Extracellular action potentials (EAPs) arise in response to transmembrane currents and concurrent changes in intracellular membrane potential (Henze et al., 2000). Studies done in the middle of the last century (Brooks and Eccles, 1947; Fatt, 1957; Terzuolo and Araki, 1961) suggested that the resistive and capacitive properties of the cell membrane cause the resemblance of the extracellular unit waveform to the first derivative of the intracellular action potential (Figure 1.11). Later *in vivo* experimental (Buzsáki et al., 1996; Henze et al., 2000; Anastassiou et al., 2015) and computational modelling studies (Gold et al., 2006; Anastassiou et al., 2013) supported the idea of this approximation, with additional observance that the late positive component of the EAP is slower than expected from the intracellular first derivative (Henze et al., 2000). This divergence arises because only the capacitive component of EAP current is proportional to the intracellular first derivative, while the total sum of the *leak* current that causes the arising of EAP includes all active ionic currents and the capacitive current (Hodgkin and Huxley, 1952; Henze et al., 2000). The importance of waveform correlation between extra- and intracellular action potentials lays in the possibility of using the parameters of AP temporal variations for differentiation between different neuronal classes (Henze et al., 2000; Sun et al., 2021). A lot of work has already been done in systematization of *in vivo* extracellularly recorded spike waveforms through various spike-sorting tools; however, this data cannot be equated to the ones found from *in vitro* studies (Sun et al., 2021).

1.2.3 Point Contact Model, Impedance, and Sealing Resistance

The nature of electrical contact with the cell is of crucial importance for recording the action potential signals. As described before, in the case of the patch-clamp technique (see section 1.2.1), a tight seal between the cell and the glass pipette enables an instantaneous and direct electrical coupling of the cell's electrical activity and the recording electrode. In the case of planar sensing devices, the mechanism of electrical coupling between the cell and electrode is more complex and depends on several parameters. The standard model for describing the electrical characteristics of the cell-electrode interface is **the point contact model** (Fromherz, 2003), depicted in Figure 1.12. Based on this model, the cell and electrode are not in direct contact, but there is a cleft filled with the electrolyte and a typical thickness of 40-150 nm (Wrobel et al., 2007; Spira and Hai, 2013; Toma et al., 2014). The contact is simplified to one single point in the cleft where the junctional membrane is facing the sensing pad (Figure 1.12) and exhibits the junction potential $V_j(t)$ upon the occurrence of action potential from the cell $V_m(t)$. The cell membrane and the electrode are represented as capacitors in parallel with corresponding resistors, connected over the cleft. An indispensable element of the cleft that dictates the quality of the signal recording is the **sealing resistance** (R_{seal}). While the tight connection in the patch clamp gives the R_{seal} up to 1 GΩ, a larger gap of the cleft usually provides the R_{seal} values in the range of 100 kΩ to 1 MΩ– 150 (Spira and Hai, 2013). Therefore, it influences the SNR of the recorded extracellular potential changes. Membrane current consists of both – capacitive and resistive components (Nam and Wheeler, 2011), and the Na^+ and K^+ leakage currents are described by Hodgkin-Huxley elements (Hodgkin and Huxley, 1952)

that are taking in account the specific properties of ion channels in the contact region, like different densities or opening properties.

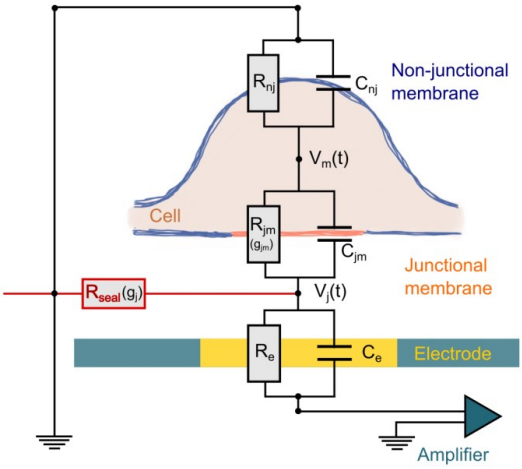

Figure 1.12 – **Neuroelectronic hybrid.** The point contact model depicts the electric circuit analog of the spatial relationships of the neuron-electrode interface. The cell membrane can be subdivided into a junctional membrane (orange) that faces the electrode and a free non-junctional membrane (dark blue). A junctional membrane and an electrode form the cleft filled with the ionic solution, serving as a charge dispersal of extracellular currents originating from a propagating action potentials or synaptic potentials. Both, the cell membrane and electrode exhibit resistive and capacitive characteristics. The cleft generates the sealing resistance (R_{seal}) to the ground and represents the direct determinant of the amplitude and shape of the recorded signals by the device. Figure adapted from Spira and Hai (2013).

All these characteristics of the membrane's current can be put together in the equation solved via Kirchhoff´s law (Ingebrandt et al., 2005; Kireev, 2017) which gives a perspective in the relation of all observed components:

$$g_j V_j(t) = i_c + i_{jm} + \sum_{channel=1}^{n} i_{channel} = C_{jm}\frac{d(V_m(t) - V_j(t))}{dt} + g_{jm}V_m(t) + \sum_{channel=1}^{n} g_{jm}(V_m(t) - V_j(t) - E_{ion}) \quad (1.5)$$

where the observed current of the recorded signal $\mathbf{g_j V_j(t)}$ can be viewed as a sum of: $\mathbf{i_c}$ – capacitive membrane current, $\mathbf{i_{jm}}$ – the ohmic current as the leakage currents over the junctional membrane, $\mathbf{i_{channel}}$ – the ionic current through each ion channel. $\mathbf{C_{jm}}$ stands for the junction-membrane capacitance, $\mathbf{V_m(t)}$ is the membrane potential, and $\mathbf{E_{ion}}$ is the electrochemical driving force of the specific ion (or ionic equilibrium potential, see section 1.1.2). As the potential at the point contact $\mathbf{V_j(t)}$ is very small compared to the membrane

voltage **$V_m(t)$** it can be neglected from the capacitive component of the membrane current and the current of the specific ionic flows (Ingebrandt et al., 2005):

$$V_j(t) \ll V_m(t) \rightarrow V_m(t) - V_j(t) \approx V_m(t) \tag{1.6}$$

As the conductance is in reverse proportion to the resistance value, the corresponding resistances can be incorporated into the equation, giving the following:

$$V_j(t) = \left(C_{jm} \frac{V_m(t)}{dt} + \frac{V_m(t)}{R_{jm}} + \sum_{channel=1}^{n} \frac{i_{channel}}{R_{channel}} \right) R_{seal} \tag{1.7}$$

Where R_{seal} stands for the sealing resistance, R_{jm} is the resistance of the junctional membrane, and $R_{channel}$ is ion-channel resistance. In the case of the cell–MEA interface, the coupling primarily occurs capacitively, which means that the ionic current flow in the junction membrane can be neglected entirely, further giving the following simplification of the previous equation:

$$V_j(t) = \left(C_{jm} \frac{dV_m(t)}{dt} \right) R_{seal} \tag{1.8}$$

From here, it is evident that the extracellular potential is proportional to the first derivative of the intracellular signal, which affects the action potential shapes typically seen in the actual recordings (see section 5.2.1). In case when no voltage-gated ion channels are present in the junction membrane, the leakage currents $g_{jm}V_m(t)$ will dominate over the capacitive component, giving the following simplification of the equation 1.5:

$$g_j V_j(t) \approx g_{jm} V_m(t) \tag{1.9}$$

In this case, the extracellular potential is directly proportional to the intracellular voltage, directly affecting the shape of the recorded signal, which is very similar to the typical intracellular action potential (Fromherz, 2003).

According to the point contact model, the recorded signal at the junction $V_j(t)$ is directly dependent on the sealing resistance R_{seal}, which is why increasing the sealing resistance is another important aspect for improving the SNR via closer contact between the cell and electrode. Many different approaches were introduced in developing MEA technology in this direction. For example, the previously mentioned approach of nanocavity microelectrodes for decreasing the electrode impedance also enables improvement of the sealing resistance, as cellular protrusion into the nanocavity area between the electrode and insulation layer develops a tight cell-electrode sealing. Furthermore, different surface modification methods

are also used to increase the R_{seal}. For example, self-assembled monolayers with specific functional groups form covalent bonds with immobilized biomolecules that enhance the interaction between the cell and electrode (Nam and Wheeler, 2011).

1.3 Compartmentalized Microfluidic Devices

Microfluidics itself is a broad field of various applications for studying and manipulation of fluids at the submillimeter length scale. The potential of microfluidics as a tool gives a rise in diagnostics application in medicine, as well as in cell biology and neurobiology experimental research (Sackmann et al., 2014). Its biggest application can be found in the field of micro-electromechanical systems (**MEMS**) also referred to as miniaturized total analysis systems (**μTAS**), compartmentalized-microfluidic devices (**CMDs**), or lab-on-a-chip (**LoC**) devices (Sackmann et al., 2014). In convergence with cell biology techniques, it develops further towards more and more complex studies of human physiology in microenvironments of so-called organ-on-a-chip (**OOC**) devices. Designs of compartmentalized microfluidic platforms mainly depend on their purpose of investigation and various designs mimicking *in vivo* environments have been developed so far. In this section, I will focus on the first historical developments of CMDs, and special integration of microchannels used for neuroscience research.

1.3.1 Development of CMDs

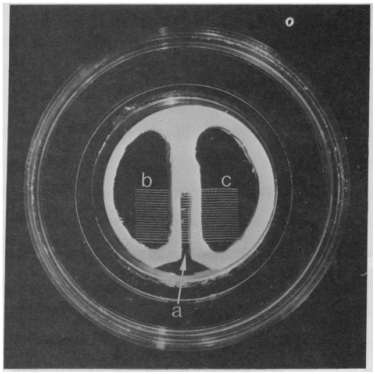

Figure 1.13 – Robert B. Campenot's three-chamber device for local control of neurite development by nerve growth factor. (a) – Central chamber in which neurons were plated. **(b)** and **(c)** – side chambers where the neurite growth is guided by a series of parallel scratches on the underlying collagen surface (from Campenot, 1977).

The first compartmentalized microfluidic device (CMD) was created in 1977, by Robert B. Campenot, who used this device for investigating the dependence of growth and survival of neurites upon nerve growth factor (Campenot, 1977; Kimpinski et al., 1997; Sackmann et al., 2014). This device was constructed on a Falcon petri dish with a polystyrene coverslip floor, coated with a film of dried collagen. Twenty evenly distanced insect pins were used to make parallel scratches about 200 µm apart on the collagen surface. A Teflon divider with three separate open chambers was placed above, creating three compartments interconnected by the scratches that served as guidelines for neurite growth from dissociated neurons plated in the middle chamber (Figure 1.13). This construction was truly a breakthrough for culturing neuronal cells as it served later as an inspiration for more sophisticated compartmentalized microfluidic platforms widely used nowadays in neurobiological research.

The design of these devices allows isolation of the axon and cell body, axonal guidance via construction of microchannels, controlled interaction of different cell populations growing in different compartments and even pharmacological manipulation and screening for potential drug development for neurological disorders. However, over the years it has been going through numerous adaptations and changes and is still evolving in accordance with technological development. The main materials in use for fabrication of these devices were silicon and glass, all until 1980s, when the micromoulding techniques found its first application in cell biology (Masuda et al., 1989) after being developed by Bell Labs a decade earlier (Aumiller et al., 1974). The method of *soft lithography* in the microfluidic field was significantly advanced with introducing polydimethylsiloxane (PDMS), used for the first time at Harvard, by Whitesides and his group in 1998 (Duffy et al., 1998). They described this novel approach of creating microfluidic systems as beneficial for numerous reasons, as its optically transparent,

gas- and vapor-permeable properties make it a candidate for versatile use also with biological systems (Sackmann et al., 2014). Nevertheless, the biocompatibility of PDMS remains a debatable description, as there are limitations to its implementation in biomedical research (Kim et al., 2007). Some of the main issues with this material are leaking uncross linked oligomers into solution, absorption of small molecules that can affect cell signaling dynamics, permeation of potentially harmful gases or evaporation of the medium, leading to detrimental effects to the cell culture (Yun et al., 2007; Sackmann et al., 2014). Other thermoplastic materials like polymethyl methacrylate and polycarbonate can be used as an alternative to PDMS, although the fabrication methods are more difficult and expensive than those of PDMS (Sackmann et al., 2014).

In terms of studying neuronal connectivity, there are several outstanding designs to be mentioned, as they were also a point of inspiration for the workflow of this thesis. Different microfluidic platform designs have a goal of creating an *in vitro* microenvironment suitable for mimicking a highly complex *in vivo* requirements for proper cellular development and function. The complexity of this task considers cells' sensitivity to patterns, factor concentrations, mechanical changes of the substrate, sheer stress, chemical properties, and spatiotemporal gradient cues (Neto et al., 2016). Microchannel size is an important geometrical aspect of microfluidic platforms; larger sizes 100 - 1000 µm are more suitable for cell culture, while smaller sizes in order of tens of microns are usually used in chemical applications, single cell analyses or cell sorting and manipulation (Van Den Berg et al., 2010). The constant fluid replacement and nutrient replenishment in perfusion systems can be achieved by external pumps via access ports and tubing. Passive pumping is a less complicated approach of fluid replacement as it relies on a flow induced by a differential pressure between ports of a microchannel. This is a more favorable method for biological applications, due to its simplicity and congruence with other techniques (Van Den Berg et al., 2010).

1.3.2 Microfluidic Devices for Axonal Guidance

With the establishment of soft lithography techniques and the use of PDMS, the initial idea of Campenot´s chambers (Campenot, 1977) was given more possibilities for refining and more complex application in neurobiological research. One of the first papers describing and characterizing a novel neuronal culture device was published by Taylor et al., in 2003 (Figure

1.14 (a)). The device was created in PDMS, containing two separate compartments connected by micron-size grooves of 150 µm length. The master mold was created by photolithography technique in double layer SU-8, giving the negative pattern for creating 3 µm × 10 µm (H × W) microchannels and 100 µm × 1500 µm (H×W) culture chambers. These dimensions served as a starting point for various future applications of similar devices. In addition to isolation of soma from neurites, Taylor et al. were able to successfully combine microcontact printing to micropattern the substrate inside the device, for controlled neuronal attachment and orientation of axonal growth. The same group followed up with experiments, showing the potential of the described platform in examining multiple aspects of axonal biology, such as axonal RNA localization, injury, and regeneration (Taylor et al., 2005).

A significant improvement of the device was achieved by Peyrin et al. (2011) with modification of microchannel architecture. The **axon-diode** asymmetrical design of the microchannels enabled the reconstruction of oriented neuronal networks, by predefining the axonal growth in a specific direction (Figure 1.14 (b)). This approach presents a step closer to realistically mimicking the neuronal networks observed *in vivo* in a controlled microenvironment. In their work, Peyrin et al. successfully reconstructed the cortico-striatal unidirectional connectivity that occurs in the mammalian brain. This gave an important concept of interest with various potential applications in studying neuronal development, synaptic transmission, and neurodegenerative disorders. This design was also a starting point of interest for this thesis. The nature of examined cells highly influences the adaptation of the microfluidic design for successful outcome of an *in vitro* model. For example, dissociated dorsal root ganglion cells (DRGs) and entire DRG explants from adult origin, require precise site of adherence in the soma compartment for sufficient neurite density in the axonal side. In the original microfluidic model device, Neto et al. (2014) have solved this by adding a chamber in the DRG soma compartment, centrally aligned with the microchannel array (Figure 1.14 (c)). Meanwhile, Takeuchi et al. (2011) used adapted design of compartmentalized microfluidic device (Figure 1.14 (d)) in combination with a MEA for co-culturing cervical ganglion (SCG) neurons and ventricular myocytes (VMs). Their microfabrication process approach allows the construction of micrometer-sized cell compartments for holding a very small number of cells, enabling observation of electrophysiological relationship activities between a small number of SCG neurons and VMs. The Jeon lab microfluidic device design (Figure 1.14 (a)) highly contributed to further research of the axon trafficking, directly connected with investigation of

neurodegenerative diseases such as Parkinson´s disease (Taylor et al., 2005). Lu et al. (2012) adjusted the design of enclosed soma compartment into a microdevice with a large open compartment (Figure 1.14 (e)), more suitable for survival of dopaminergic (DA) neurons. The open compartment of this design enabled improved cell viability and axon growth, and parallel microchannels made it possible to track anterograde and retrograde movements of labeled mitochondrial along DA axons. For improving the localized control of biomolecular environments, Park et al. (2014) improved the conventional microfluidic device design used until then. Their compartmentalized microfluidic device (Figure 1.14 (f)) makes it possible to perform a quantitative axonal growth analysis, a goal that is hardly achievable with previously

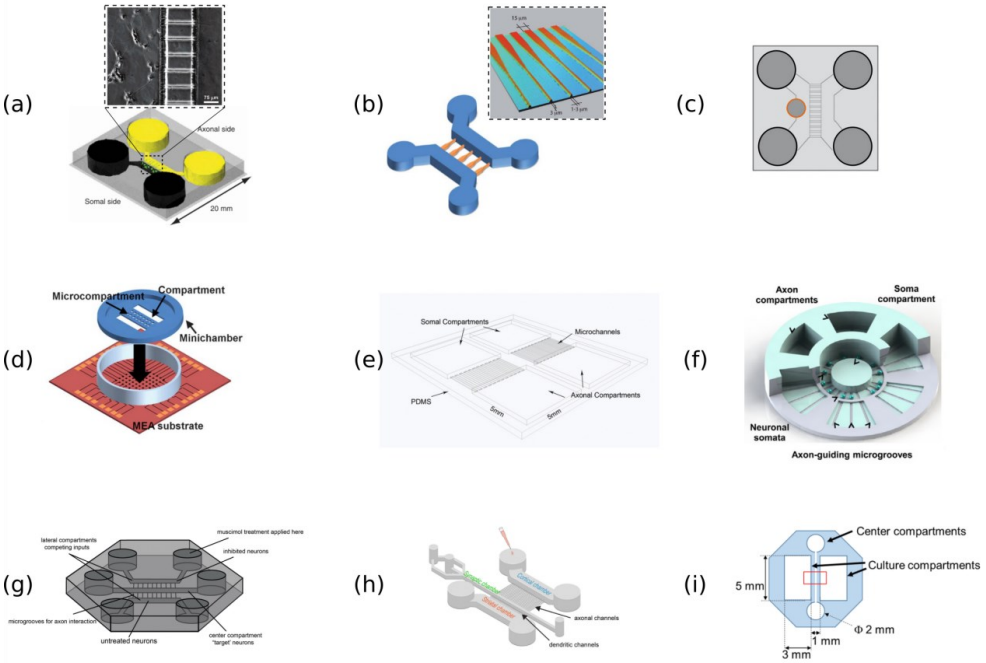

Figure 1.14 – Different Comp-microfluidic Platforms used in neuroscience research. (a) Conventional design for the CMD developed by modern soft-lithography techniques by Taylor et al. (2003). **(b)** Axon diode microchannel design introduced by Peyrin et al. (2011). **(c)** Adaptation of the conventional design with additional seeding chamber for DRG cells (Neto et al., 2014). **(d)** Micrometer-sized cell compartments for precise alignment of cell bodies with the microelectrode array underneath (Takeuchi et al., 2011). **(e)** Device with open somal compartments suitable for dopaminergic neurons (Lu et al., 2012). **(f)** Radial array of multiple compartment configuration for simultaneous drug screening (Park et al., 2014). **(g)** 3-compartment microfluidic device for evaluation of synaptic competition in a 3-cell culture system network (Coquinco et al., 2014). **(h)** 3-compartment microfluidic device with a synaptic chamber of a cortico-striatal network (Virlogeux et al., 2018). **(i)** 3-compartment microfluidic device with open cell culture compartments and central compartments for introduction of pharmacological treatments (Shimba et al., 2021).

reported designs. Additionally, multiple axonal compartments distributed cylindrically around the soma compartment carry a potential for higher-throughput screening microchip platform, as different localized axonal treatments can be applied within a single device. A three-compartment design where the central compartment is connected via microchannels to the lateral (Figure 1.14 (g)), found its application in different study approaches. As it has been described before (Park et al., 2006; Whitesides, 2006) the hydrostatic forces between compartments allow the creation of distinct chemical environments and manipulation of separate cell cultures. This simple, yet effective model carries high potential for studying activity dependent synaptic plasticity (Coquinco et al., 2014). In this case, an additional central compartment was used for a cell culture that was forming different number of synaptic connections with cultures in lateral compartments, depending on the inhibition of one input's activity. In a similar design from Saudou's group (Figure 1.14 (h)) the central compartment served as a synaptic chamber of a cortico-striatal network for investigating pathogenic mechanisms of synaptic transmission in Huntington's disease (Virlogeux et al., 2018). In combination with MEAs, Shimba et al. (2021) used a three-compartment design for measuring changes in axonal conduction properties, depending on the pharmacological treatment conducted through the central compartment of the device (Figure 1.14 (i)).

1.3.3 Amplification Effects of Microchannel Structures

In previous sections about types of electrophysiological recordings of neuronal action potentials (see section 1.2) I described the difference between intra- and extracellular

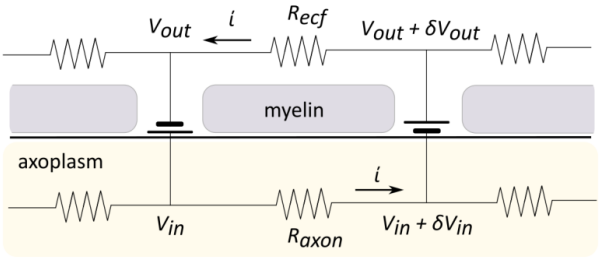

Figure 1.15 – Local currents during depolarization of an axonal membrane. Adapted from Fitzgerald et al. (2008). Intra- and extracellular current flow is equal and opposite and dependent on the resistances of extracellular fluid (R_{ecf}) and the axon (R_{axon}). The extracellular fluid resistance has direct influence on the amplitude of extracellularly recorded voltage (V_{out}). The Fitzgerald's model predicts amplification of the signal by increased extracellular fluid resistance.

recording techniques. Some of the most prominent differences in these approaches are invasiveness and signal to noise ratio of recorded potentials. As explained in the same chapter, increased sealing resistance has the main effect on achieving a good signal-to-noise ratio and is one of the biggest challenges to achieve in extracellular recordings. Therefore, the amplitudes of extracellular action potentials are significantly smaller in comparison to intracellular (Figure 1.11) and more difficult to interpret. In addition to concepts for overcoming the challenge of sealing resistance (see section 1.2.2), this section focuses on the amplification effect of microfluidic channels. This effect was first described in the late 1960s by Clark and Plonsey (1968), later studied in detail by FitzGerald et al. (2008), and observed during this thesis. The finite-element model proposed by Fitzgerald examines electrical behavior of axons in microchannels by observing a myelinated axon with the membrane voltage V_m defined as $\mathbf{V_m = V_{in}-V_{out}}$ (Figure 1.15). The current flow in internal and external side of the membrane is equal and opposite, with the dependence on the resistances of extracellular fluid ($\mathbf{R_{ecf}}$) and the axon ($\mathbf{R_{axon}}$):

$$\delta V_{out} = i\, R_{ecf}$$
$$\delta V_{in} = -i\, R_{axon}$$
$$\frac{\delta V_{out}}{\delta V_{in}} = -\frac{R_{ecf}}{R_{axon}}$$

Axon resistance is dependent on the axon diameter, length, and resistivity, while the R_{ecf} is more complex due to its inhomogeneous nature. Consequentially, FitzGerald et al. are suggesting considering the radial and longitudinal component on that matter. This distinction is particularly important for examining the radial decay of axonal signals. From the relation in the equation above, the δV_{out} can be amplified in case of increase of R_{ecf}. One way of doing so is the increase of extracellular fluid (ECF) resistivity by changing ECF composition, but this can easily lead to a negative effect on the viability of the cell culture. The other way of achieving this is by reducing the ECF volume, which can be done by confining it to a small space like a microchannel. The model predicts the amplification of V_{out} amplitude with the increase of axon diameter, and with the decrease of channel cross-section area, as Clark and Plonsey presented in their calculations (Clark and Plonsey, 1968; FitzGerald et al., 2008). The following in vitro experiments from the same research group verified the amplification effect of microchannels with recorded extracellular potentials up to 0.5 mV of L5 ventral roots nerves from adult rat (FitzGerald et al., 2009). The model also predicts that the microchannel provides almost purely

longitudinal extracellular current flow, which enables the recording of V_{out} regardless of the axon position relative to the electrode. This brings obvious amenities, but at the same time makes a challenge in obtaining spatial selectivity for distinguishing specific neuronal axons. However, this can somewhat be overcome by distribution of axons between many different channels (FitzGerald et al., 2008, 2009). In a more commercialized setup, Pan et al. (2014) confirmed the microchannel amplification effects, reporting the values up to 4.5 mV of spontaneously active unmyelinated rat cortical neurons. They also examined further the origins of these effects in correlation with the electrode and microchannel impedances, stating that the latter plays the main role in amplification.

Chapter 2

Materials and Methods

2.1 Device Fabrication Processes

The fabrication of a Microfluidic-MEA-hybrid device involves two distinct stages for each segment of the final device. The microelectrode arrays are fabricated entirely in a clean room environment using standard techniques such as electron beam metal deposition and photolithography. The final microfluidic structures are created using the soft lithography technique, which does not necessarily require cleanroom conditions. The SU-8 molds are constructed using similar techniques and conditions as MEAs. This section describes all the techniques used and the chemical properties of the polymers used to construct the final device.

2.1.1 Metal Deposition by Electron Beam Evaporation

Thin films can be deposited through physical or chemical processes, depending on the procedure used (Fotovvati et al., 2019; Bashir et al., 2020). In this work, a conductive layer was deposited using the electron beam evaporation process (Figure 2.1). Two key processes occur during physical vapor deposition (PVD): evaporation and sputtering. The source material transitions to a vapor phase and then back to its original phase, forming a thin film on the substrate. Evaporation can be a thermal or electron beam, depending on the melting point of the material in use. Electron beam evaporation is more suitable for metals with a high melting point, such as gold, which is used in my fabrication process. This method involves evaporating the source material using high-energy electrons in the form of an intense beam (Bashir et al., 2020). Evaporation rate can be controlled, allowing for a wide range of deposition rates, from 0.1 nm/s up to 100 nm/s (Seshan, 2002).

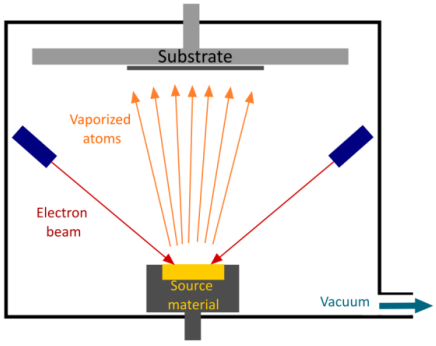

Figure 2.1 – Electron beam physical vapor deposition. The source material is evaporated by high intensity electron beam. Vaporized atoms reach the substrate where they are deposited in a thin film. Figure is adapted from Fotovvati et al.

2.1.2 Photolithography

Photolithography, also known as optical lithography, is a process used in manufacturing to produce patterned thin films of desired materials on a substrate. (Jaeger, 2002). The process involves using a photosensitive polymer (resist) that is spin-coated onto a wafer and then exposed to high-intensity ultraviolet light (UV). The desired pattern design is defined via a photomask, which is structured in an absorption chromium layer on a UV transparent substrate, such as quartz. Passing UV light alters the chemical structure of the exposed areas in a photoresist, creating a predefined pattern on a substrate after the development step (Figure 2.2). Prior to exposure, a crucial step is *soft baking* (or *prebaking*), which enhances adhesion and eliminates solvent from the photoresist (Jaeger, 2002). There are two types of photoresists: positive and negative. When exposed to UV light, positive resists become soluble to a photoresist developer and are therefore removed. In the case of negative resist, the UV light initiates cross-linking of the polymer, making it insoluble to the developer, while the unexposed area is dissolved. Figure 2.2 illustrates the basic difference between UV exposure of positive and negative photoresists. In this thesis, both types of photoresists were used, depending on their purpose. The MEA fabrication process utilized negative photoresists LOR-3B and AZ nLOF-2020 (Microchem Corp., USA) to define conductive feedlines and contact pads.

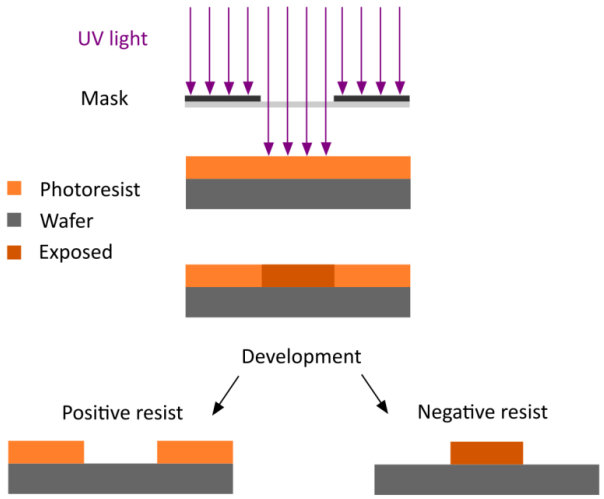

Figure 2.2 – UV exposure of positive and negative photoresist. A photomask is used to allow UV light to pass through transparent regions without a chromium layer. The photoresist is then exposed and chemically altered in the corresponding area. After development, the exposed area is removed in the case of positive resist and remains insoluble in the case of negative resist.

A positive photoresist, polymer HD-8820 (HD MicroSystems), was used to passivate the MEAs and structure microchannels on top. Macromolds were created using negative photoresist SU-8 of varying density.

2.1.3 Soft Lithography

Soft lithography is a widely used technique in micro- and nanofabrication processes for the fabrication of microfluidic devices. It presents a non-photolithographic set of microfabrication methods based on using a patterned elastomer as a stamp (Xia and Whitesides, 1998). Elastomers such as poly(dimethylsiloxane) (PDMS), polyurethanes, and polyimides are commonly used in soft lithography. The process of preparing the elastomeric stamp involves cast molding: a prepolymer of the elastomer is poured over a master with a desired microstructure on its surface, cured, and then peeled off (Xia and Whitesides, 1998). The master mold is fabricated by using some of the microlithographic techniques, such as photolithography, micromachining, e-beam writing, or structures etched in metals or silicon (Manz and Becker, 1998). The elastomer PDMS is the most widely used and is also used in this thesis. Figure 2.3 illustrates the procedure for fabricating PDMS stamps.

Commercially available PDMS Sylgard™ 184 is a two-part kit consisting of a liquid silicon rubber base and a catalyst or curing agent, is mixed in a desired ratio. The resulting mixture is then poured over a master mold and heated to elevated temperatures. The liquid mixture solidifies due to the hydrosilylation reaction between vinyl ($SiCH=CH_2$) groups and hydrosilane (SiH) groups, which initiates polymer cross-linking (Manz and Becker, 1998; Xia and Whitesides, 1998). This process results in the formation of a solidified elastomer that can be easily released from the rigid master used to mold the previously designed three-dimensional structures.

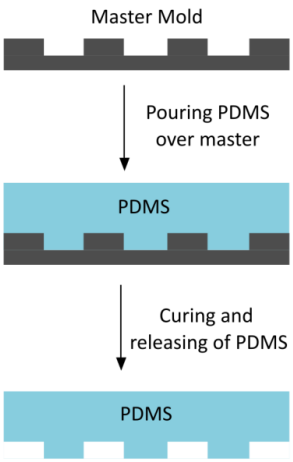

Figure 2.3 – Soft lithography technique. PDMS, a liquid elastomer, is poured over the master mold and allowed to cure. The cured PDMS is then released, revealing a structured relief.

2.1.4 Polymers Used in Device Fabrication

2.1.4.1 SU-8 Photoresist

SU-8 (Microchem Corp., USA) is an epoxy-based negative photoresist that is widely used in microelectronic applications for high-aspect-ratio and three-dimensional lithographic patterning (Del Campo and Greiner, 2007). Its chemical structure is based on Bisphenol A Novolak epoxy oligomer (Figure 2.4). The oligomer contains eight highly reactive epoxy sites that allow for a high degree of cross-linking. Activation of these moieties occurs upon protonation of epoxides by hexafluoroantimonic acid, which is created after the decomposition of the photoacid generator. Protonated epoxides are available to react with neutral epoxides, causing a series of cross-linking reactions after photothermal activation (Del Campo and Greiner, 2007). The portions of the film that are exposed to UV and subsequently thermally cross-linked become insoluble to liquid developers, giving this resist a negative tone. Commercially available formulations can cover a film thickness range of 2 to 300 µm in a single coating process or up to 3 mm by multicoating processes. This enables the construction of various height layers and three-dimensional structures that can be used as a master mold in the process of soft lithography.

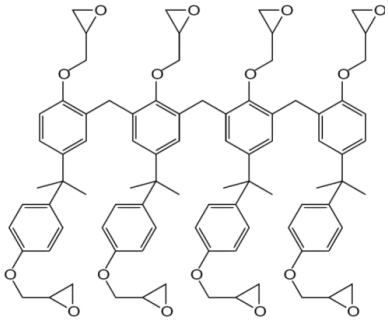

Figure 2.4 – Chemical structure of SU8 oligomer. The SU8 oligomer comprises eight highly reactive epoxy moieties that enable cross-linking reactions upon photothermal activation.

2.1.4.2 Polydimethylsiloxane PDMS

Polydimethylsiloxane (PDMS) is an elastomeric polymer that is extensively used in biomedical applications due to its desirable properties. These properties include biocompatibility, chemical stability, gas permeability, good mechanical properties, excellent optical

transparency, and simple fabrication by replica molding (Mata et al., 2005; Miranda et al., 2021).

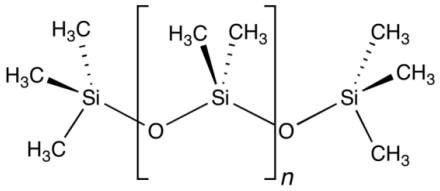

Figure 2.5 – Polydimethylsiloxane (PDMS) chemical structure. The polymer is hydrophobic due to the presence of two methyl groups. To achieve hydrophilicity, surface modification and addition of silanol groups via plasma oxidation are necessary.

Soft lithography technology has enhanced the use of PDMS in various microelectromechanical systems (MEMS) applications, including microcontact printing, and microfluidic components (Raj M and Chakraborty, 2020; Miranda et al., 2021). The manufacture of microfluidic devices is a common use of PDMS, which is employed in the development of systems such as drug delivery, DNA sequencing, clinical diagnostics, point of care testing, and chemical synthesis (Shakeri et al., 2021). Surface chemical modifications such as plasma treatment, ultraviolet radiation and silanization enhance the versatility of PDMS applications. Although PDMS has a highly hydrophobic chemical structure (Figure 2.5), its surface can be easily modified by introducing polar functional groups (SiOH) through plasma treatment (Raj M. and Chakraborty, 2020). This approach was also employed in this study, as hydrophilicity is critical for the successful operation of the microfluidic system. Silanization of the surface facilitates easy removal during soft lithography. Additionally, the network polymer structure of PDMS can absorb certain materials and small molecules, which can have both positive and negative effects depending on the application (Toepke and Beebe, 2006). The absorption of small molecules may significantly impact the outcome of drug screening studies or affect the availability of micronutrients in cell cultures.

2.1.4.3 HD-8820 Polymer

HD-8820 (HD MicroSystems) is a positive photodefinable polybenzoxazole (PBO) precursor used for creating micro-scale patterns with controlled side-wall profiles (Process Guide, 2009). During the development step, the exposed areas are washed away, while the unexposed areas remain (Figure 2.2).

Although colloquially referred to as “polyimide”, the chemical structure of HD-8820 does not correspond to it[1]. The exact chemical structure of the HD-8820 monomer unit is not publicly available information. Typical photosensitive polybenzoxazole (PBO) undergoes ring closure during the curing process, as illustrated in Figure 2.6 (Gotro, 2017). The polymer backbone's aromatic rings confer rigid properties and excellent thermal and chemical stability.

PBOs are typically positive-acting and aqueous-developable materials that are soluble in alkaline developers such as 2.38% tetramethylammonium hydroxide (TMAH) (Thapa, 2020). PBO has several advantages over polyimides (PI), including lower curing temperatures, a lower modulus, higher elongation, and good electrical insulation (Nishimura et al., 2015).

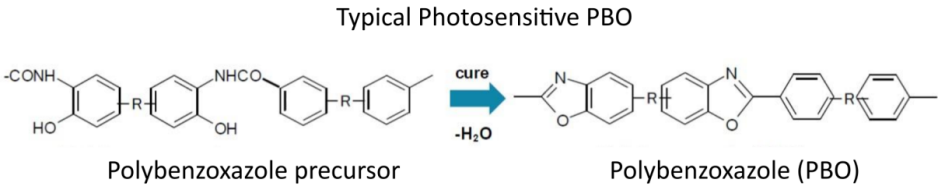

Figure 2.6 – **Typical photosensitive polybenzoxazole.** During the curing process, ring closure occurs which causes the polymer layer to harden. Figure adapted from Gotro et al. (2017).

[1] Polyimides are commonly used in microfabrication technology for creating insertion probes, which is probably where this name confusion comes from. To ensure clarity and accuracy of the chemical name and structure, I contacted the manufacturer directly and obtained additional details.

2.1.5 Cleanroom Fabrication Processes

The fabrication of the final device consists of the following fabrication processes: **(1)** fabrication of MEAs (see section 2.1.5.1), **(2)** fabrication of SU-8 molds (see section 2.1.5.2), **(3)** fabrication of PDMS-based Comp-microfluidic devices by soft lithography (see section 2.1.5.3), **(4)** structuring of microchannels on top of MEAs (see section 3.1.3), and **(5)** assembly of the final µFluidic-MEA device (see section 3.2.3). The first three processes mentioned above have already been established protocols, while the last two are the newly developed protocols and are therefore presented in detail in the Results and Discussion section 3.1 of Chapter 3. All fabrication steps figures are presented within the corresponding sections in Chapter 3 to provide a better overview of the specific adaptations and changes introduced within each process. Protocols of all processes are summarized in Appendix A.

2.1.5.1 Microelectrode Arrays Cleanroom Fabrication Process

The microelectrode arrays were fabricated using classical photolithography techniques at the Helmholtz Nanoelectronic Facility (HNF) of the FZJ in an ISO 1 cleanroom on a 4" quartz wafer (Plan Optik AG, Germany). The first batches of MEAs with short microchannels on top were fabricated by technician Marko Banzet, while the rest of the iMEA200 batches with all microchannel lengths and r16MEA were fabricated by me (for layout representation of MEA devices, see section 3.1.1). The fabrication process is shown schematically in section 3.1.2 (see Figure 3.3) After the initial dehydration step, a double layer of negative photoresists LOR-3B and AZ nLOF-2020 (both Microchem Corp., USA) was spin coated. The feedline areas were defined by photolithography using 350 nm UV light (55 mJ/cm^2). The wafer then underwent post-exposure bake at 110 °C for 1 minute and was developed in AZ MIF-326 (Microchem Corp., USA) for 35 seconds, followed by a water cascade. The metal deposition process was performed by electron-beam evaporation (Pfeiffer PLS 570, Pfeiffer Vacuum, Asslar, Germany) of Ti (10 nm, deposition rate 0.3 nm/s) and Au (100 nm, deposition rate 0.5 nm/s). The lift-off process was performed in acetone for at least 12 hours, followed by AZ MIF-326 for 10 minutes to remove the excess photoresist covered with the metal layer. After the dehydration step, the MEAs were coated with an adhesion promoter VM-652, followed by passivation with a layer of HD-8820 (HD MicroSystems) spun at 5000 rpm for 45 seconds. The soft baking on a proximity hotplate at 120°C for 4 minutes with a ramp speed of 0.1 mm/s, starting from 10

mm height, is followed by the UV exposure with a power density of 400 mJ/cm^2 for the construction of electrode apertures and contact pads. The development step was performed in a double puddle of AZ MIF-326, with each puddle lasting 60 seconds while the wafers were shaken and rotated, followed by a water cascade, and drying. The curing process for full polymerization was carried out in a furnace with a nitrogen purge of 20 L/min. The temperature gradually increased at a rate of 4 °C/min to 200°C, where it was held for 30 minutes. The temperature was then ramped up to 350°C at a rate of 2.5°C/min and held for 30 minutes before the furnace gradually cooled.Microchannels are then structured directly on top of the MEA, in a developed process explained in detail in section 3.1.3 and Appendix A1. The wafers were then coated with 4 mL of AZ-5214e resist (Microchem Corp., USA), spin-coated at 3000 rpm with the lid closed for 45 s, and soft-baked at 100°C for 1 min. This layer acts as a protective layer during the dicing process. Each wafer is diced into nine MEAs, each with a side length of ~ 24 mm. The resist is then removed by incubation in AZ-100 Remover (Microchem Corp., USA) for 15 minutes with occasional stirring, followed by rinsing in acetone, then IPA, and drying with N_2.

2.1.5.2 SU-8 Molds Fabrication

The desired SU-8 mold is constructed in a 2-layer process on a 0.6 mm thick dehydrated silicon wafer (4" diameter, MEMC Electronic Materials, USA). The wafer is first dehydrated on a hotplate at 200°C for 5 minutes to properly prepare the resist spincoat. The molds were fabricated at the Helmholtz Nanoelectronic Facility (HNF) of the FZJ in an ISO 1 cleanroom on a 4" silicon wafer by technician Marko Banzet. The complete protocol is available in Appendix A2.

The first SU-8 layer

The first layer is constructed by spincoating SU-8 2005 (Microchemicals, USA) at 5000 rpm for 45 s, followed by a soft bake at 95 °C for 150s. To define the microchannel walls, the wafer is then optically exposed through a mask aligner (7.0 mWcm^2, hard contact, 9 s) and then baked at 95 °C for 150 s. The first-layer structures are then developed in two steps with MR-dev600. In the first step, the wafer is waved for 30 s, followed by rinsing with IPA and intensive drying with N_2. In the second step, the wafer is waved for 15 seconds in the same developer, again followed by rinsing with IPA and intensive drying with N_2. The development time may need to

be adjusted for each specific sample, as actual dissolution rates can vary widely as a function of agitation rate, temperature, and resist processing parameters (Process Guide, 2014). The hardbake is performed in the furnace at 200 °C for 30 min with 20 L/min nitrogen purge. After gradual cooling down of the wafers, the samples are ready for further processing. The wafers are cleaned in acetone, then in IPA in ultrasonic to remove any possible residual of SU-8 after development. The final microchannel thickness of the first SU-8 layer is approximately 3 µm.

The second SU-8 layer

The second, thicker layer of SU-8 defines the macrochannel compartments and seeding chambers. After dehydration bake, a thin layer of adhesion promoter (SU-8 2001, 3.5 mL) is applied, spincoated with an open lid at 3000 rpm, followed by a softbake step at 95 °C for 1 min. Subsequently, a modified high UV-absorbing SU-8 2050 is spin-coated at 2000 rpm for 35 s (first 5 s at 500 rpm with an acceleration of 100 rpm/second). After spincoating, it is important to clean the bottom of the wafer from any excess SU-8 that may cause further uneven wafer leveling. It is also recommended to manually remove the resist in the area over the alignment markers to make them visible in the subsequent exposure steps. A softbake is performed in two steps, at 65 °C for 2 min, then directly at 95 °C for 10 min. Due to the chemical changes induced during photoactivation, the absorption of UV light progressively increases during exposure, and there is a gradual decrease in light intensity across the film thickness, with the decrease becoming more pronounced during exposure. Since the UV absorption spectrum of the unexposed SU-8 resist shows a much higher absorbance at shorter wavelengths than at longer wavelengths, and since the absorbance change during exposure is more pronounced at short wavelengths, it is recommended to filter out the wavelengths below 365 nm during exposure. The wafer is then optically exposed through a mask-aligner (7.0 mWcm2, hard contact, 60 s). It is recommended to leave the wafer overnight in a closed dark container to ensure proper degassing of the thick layer. The post-exposure bake is performed in two steps by gradually increasing the temperature for 8 min to 65°C, hold for 5 min, and then again gradually increasing the temperature for 8 min to 95°C, hold for 12 min, followed by a gradual decrease in temperature to at least 50°C. This ramping process is necessary for the thicker layer of SU-8 to keep it intact and uniform and avoid the cracking in sudden temperature changes. The development is done in two steps in the same developer (mr-Dev600), including rinsing with IPA between the steps as described above. The first step is done in 5 min with smooth waving and rotating, and the second step is done in 2 min with

waving the wafer. As previously described, the development times may need to be adjusted slightly for each new wafer. After rinsing the wafer in IPA, the final step of hardbaking is performed in the furnace at 200°C for 30 min with 20 L/min nitrogen purge with gradual cooling of the wafer when the hardbaking is complete.

2.1.5.3 PDMS Comp-µFluidic Device Fabrication

The PDMS (SYLGARD 184, DOW Corning) is prepared by mixing the base and the curing agent in a 10:1 ratio and degassing the mixture overnight in a freezer at -20°C. The SU-8 mold with the desired structures is cleaned with IPA, rinsed with Milli-Q water, and dried with N_2. To increase hydrophobicity, the wafer can be incubated in 2% SDS for 15 minutes, but this step was not necessary each time the wafer was used. SU-8 wafers are then clamped in custom made Teflon holders, with a steel plate the size of the wafer underneath it. The steel plate ensures the position of the wafer and prevents leakage of PDMS while in the liquid state. The degassed PDMS is heated to room temperature and then poured onto the SU-8 mold wafer from the center to avoid bubbles in the mixture. The Teflon holder is placed in a flat container protected with aluminum foil and covered to protect from dust. PDMS is cured at 60°C for at least 12 hours. After curing, the ~5 mm high elastomeric polymer prints are removed from the SU-8 mold by pulling in the direction of the microchannels from the wide end to the narrow end. Each print contains 9 comp-µFluidic devices, which are extracted using a custom-made circular steel punch with an inner diameter of 14 mm (Figure 3.7). Subsequently, four reservoirs/seeding chambers were punched for each device using a 3.5 mm diameter biopsy puncher. The resulting comp-µFluidic devices are then cleaned in an ultrasonic bath with acetone and IPA, 3 minutes each, with individual rinsing of each device with IPA as it is transferred from one beaker of solvent to another. After US cleaning, each device is rinsed with absolute EtOH, followed by 70% EtOH, Milli-Q water, and finally dried with N_2.

The protocol is also available in Appendix A3.

2.2 Characterization Methods

The device was characterized by topographical surface examination of SU-8 molds and MEAs. The aim was to provide a detailed description of the dimensions of the microfluidic compartments and the passivation thickness of the MEA. Electrodes were characterized using electrode impedance spectroscopy and their size was observed microscopically.

2.2.1 Dek-Tak

The DekTak profilometer (Stylus Profilometers) was utilized to characterize the topography of the MEA and SU-8 mold surfaces. The profilometer measures height variations by moving a stylus across the sample. The styluses are typically made of diamond or other hard materials to ensure accuracy and reliability of the measurements. This tool is capable of measuring surface variations on a nanometer scale, making it a powerful tool for surface topography characterization.

2.2.2 Electrode Impedance Spectroscopy (EIS)

Section 1.2.3 describes the electrical properties of a neuroelectronic hybrid, which exhibit resistive and capacitive characteristics in both the cell membrane and the electrode. The electrode impedance defines the response of an electrical circuit to alternating current (AC) or voltage as a function of frequency. This is the parameter of interest for MEA characterization, as it determines the signal loss during electrophysiological recordings. The impedance of electrodes was measured before MEAs usage and was taken as a measure of MEA quality.

The potentiostat VSP-300 (BioLogic Science Instruments) was used to obtain impedance measurements. During EIS measurements, an electrolyte solution of adjusted phosphate-

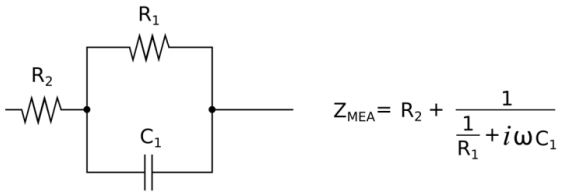

Figure 2.7 – Neuroelectric hybrid electric circuit equivalent. Equivalent circuit is based on the single element model, and corresponding circuit equation by applying Kirchoff's law.

buffered saline (PBS; Sigma Aldrich, Germany) with comparable resistivity to the cell culture medium was used.

The Figure 2.7 shows the electrochemical cell of a neuroelectronic hybrid (cell-electrode interface) and its equivalent electric circuit equation, which was derived by applying Kirchoff's law. Applying Ohm's law, EIS yields the impedance of the entire electrochemical cell. The contact between the electrode (an electronic conductor) and the electrolyte (an ionic conductor) creates a separation of charges at the interface that behaves as a capacitor (C1). A 10 mV sinusoidal voltage is applied in a frequency spectrum of 10 Hz to 10^6 Hz to measure the current created along this capacitor. The movement of charges is described by R_1, and capacitance (C_1) created by the electronic-ionic conductor contact. R2 represents the elements external to the electrode, mainly the resistance of PBS. After measuring the impedance of an electrode using EIS, capacitance C_1 is calculated by the EC-Lab V11.30 software (Claix, France) by fitting the EIS data to the circuit via non-linear least squares fitting. The capacitance measurement is then compared to the expected, theoretical capacitance based on the electrode characteristics such as material and size. For instance, the specific capacitance of gold is 0.4 pF/µm^2, which results in theoretically calculated impedance values of 0.88 MΩ for 24 µm electrode diameter and 3.52 MΩ for 12 µm electrode diameter.

2.2.3 Optical Characterization

The fabricated samples were optically validated using the Leica INM 300 digital microscope. The microscope was utilized to verify all steps during the fabrication process. Commercial software measurement tools were used to characterize the final electrode diameters and microchannel lengths and widths in specified parts of the cured structures.

2.3 Cell Culture

The compartmentalized devices investigated in this study are a valuable tool for replicating the neuronal pathways of the brain. This thesis utilizes the primary cortico-striatal co-culture as an in vitro model to mimic the neuronal pathway and investigate signal propagation through electrically active microchannels.

2.3.1 Preparation of Primary Cortical and Striatal Cells

Cell preparation was performed by technician Bettina Breuer. Embryonic cortical and striatal neurons from pregnant E18 Wistar rats were isolated by dissecting the cortex and digesting it in 0.05% Trypsin for 10 minutes at 37°C and 5% CO_2. The suspension was swiveled once after 5 minutes of incubation. The digestion was halted by transferring the cortices into a reaction tube containing fresh Neurobasal (NB) medium (Life Technologies, Carlsbad, CA, USA) supplemented with 1% (v/v) B27 (Thermo Fisher Scientific (Gibco) USA), 0.5 mM L-glutamine (Thermo-Fisher Scientific (Gibco), USA), and 0.05 mg/mL Gentamicin (Sigma Aldrich, Germany). After washing the cells three times with NB medium, they were mechanically dissociated using an Eppendorf pipette with a 100-1000 µL tip and left to settle for 1 minute. This procedure enables glia cells to attach to the reaction tube. The supernatant is then diluted and used to seed the cells at an appropriate density, depending on the substrate used for seeding. For glass coverslips, the density was 60k cells/mL, and for microfluidic devices, the cell density was 1.5×10^6 cells/mL.

The protocol details are also listed in Appendix B1.

2.3.2 Viability Assay

The samples were washed 2-3 times with preheated phosphate-buffered saline (PBS; Sigma Aldrich, Germany). A staining solution of calcein-acetoxymethylester (cal-AM) and ethidium homodimer (EtHD; both from Thermo Fisher Scientific (Gibco), USA) in a 1:1000 dilution was added to the cell cultures after one-time wash with the same solution and incubated for 15 minutes on a hot-plate at 37 °C. The samples were then washed with PBS 2-3 times and analyzed using fluorescence microscopy.

For the complete protocol, see Appendix B2.

2.3.3 Fluorescent Immunocytochemistry

The immunostaining technique allows for the visualization of specific parts of the cell body through fluorescent microscopy. This is achieved by fluorescently labeling proteins and large molecules in cells. The primary antibody binds to a specific antigen/target, and a secondary antibody couples to a fluorophore that amplifies and visualizes the bound primary antibodies.

After rinsing the samples twice with 1×PBS, the cells were fixed with pre-warmed (37°C) 4% paraformaldehyde at room temperature for 10 minutes. The samples were then washed with PBS three times. Depending on the experiment, PDMS µFluidic structures were either removed from the samples before or after this step or left intact with the substrate. The fixed samples were permeabilized with 0.3% Triton X-100 (Sigma Aldrich, Germany) in PBS for 10 minutes at room temperature. After rinsing the samples twice with 1×PBS, unspecific protein binding sites were blocked with a blocking buffer (1% BSA and 0.3% Triton X-100 in PBS) for 30 minutes at room temperature. The primary antibody was applied in a 0.5% blocking buffer dilution overnight at 4°C. After rinsing the samples three times with 1×PBS, a complementary secondary antibody was applied in a 0.5% blocking buffer dilution and incubated for 3 hours in the dark, at room temperature. The final steps before imaging involved a one-time wash with 1×PBS, followed by rinsing with Milli-Q water to prevent PBS crystallization on the dry samples. The mounting medium solution (Agilent Dako, USA) was then applied. After the mounting solution dried overnight at room temperature, a clean glass coverslip was placed on top of the sample in the case of samples with removed PDMS µFluidic structures. All samples were stored at 4°C for imaging. Imaging was performed using an AxioImager Z1 microscope (Zeiss, Germany) and an HXP metal halide light source with suitable optical filters. Primary and secondary antibodies were used as shown in the Table B.3 depending on availability and the experiment. Fr the complete protocol, see Appendix B3.

2.3.4 Phase Contrast Microscopy

Phase contrast microscopy is a type of optical microscopy in which the contrast of the imaged tissue can be modulated for improved visualization. In this work, the routine imaging of the culture samples was performed using a ZEISS Axiovert 200 (Carl Zeiss AG, Oberkochen, Germany) inverted microscope equipped with phase contrast objectives and using transmitted light. Neuronal cell cultures were regularly monitored for the viability and development of axonal growth within the microchannels.

2.4 MEA Recordings and Data Analysis

2.4.1 Bioelectronic Multifunctional Amplifier System (BioMAS)

All electrophysiological recordings were performed with a custom amplification system designed and developed at our institute (Figure 2.8). This system consists of a headstage with a 10.1× preamplification connected to a Bioelectronic Multifunctional Amplifier System, BioMAS (Krause et al., 2000; Ecken et al., 2003; Eick, 2009), which serves as the main amplifier.

Figure 2.8 – BioMAS recording setup: the main amplifier, headstage, and MEA chip with a growing cell culture. This custom amplification system was designed and developed at the institute as a part of a doctoral thesis (Eick, 2009).

The maximum output range of this amplifier is ± 10V and a built-in gain of 1×, 10×, or 100× is available, and the amplifier was operated with an analog 3 kHz low-pass filter, and a high-pass filter with cut-off frequencies of 0.1 Hz, 1 Hz, 10 Hz or 72 Hz. The coupling can be switched between AC and DC mode and the system can record up to 64 channels with an additional 16 channels for external sources. The system also allows voltage-controlled stimulation by connecting a current measurement board to record the injected current. The analog amplified voltage traces are transferred to a computer via an AD converter (Texas Instruments, USA). LabView 2016 software (version BioMAS-dev_2018-10-16) was used to control the amplifier. The options provided by the software include channel selection, stimulation pulses, and control of the above-mentioned functions such as gain and high-pass filter. The raw data was written and saved as a *.dat* file with a corresponding *.xml* file containing metadata about the recording.

2.4.2 Extracellular Measurements of Neuronal Activity

The cell culture medium was changed approximately 1-2 hours before the recording session. During the recording session, MEA samples from the same petri-dish were kept closed on the hot plate at 37 °C. MEAs with cortico-striatal co-cultures were placed on the headstage in a BioMAS setup. An Ag/AgCl pellet electrode was used as a reference electrode, which was carefully immersed in the cell culture medium in one of the seeding chambers, without damaging the cell network. Recordings were made in AC coupling mode with appropriate gain and high-pass filtering depending on the noise of the recording. Depending on the experiment, recordings were either performed without the addition of any external chemical stimulant for recording the spontaneous activity of the co-cultures, or the cells were treated with 8 mM caffeine to induce the bursting activity and verify the cellular origin of the voltage changes. After spontaneous activity was recorded, the cells were maintained under cell culture conditions.

2.4.3 Raw Data Processing and Peak Detection Algorithm

Successful recordings of co-culture activities were saved as the raw data in a *.dat* file with a corresponding *.xml* file containing metadata about the recording. These were further converted to *.csv* files for the sake of easier manipulation of the data and further processing as needed.

The analysis pipeline was developed by a colleague PhD student, Bogdana Čepkenović. Firstly, Butterworth band-pass filter (lowcut: 100 Hz; highcut: 4000 Hz) was applied to raw data recordings, followed by detection of negative peaks of extracellular axonal action potentials. Peak detection was using the **find_peaks** algorithm of the SciPy Python library. Following the automatic detection, the found spikes were inspected, and the height threshold was adjusted

accordingly to yield the most accurate spike finding. The parameters for find_peaks are summarized in Table 2.1.

Spike-finding parameter	Value used
Height threshold	Trace median + 4 (or 5) SD
Minimal width	0.5 ms
Minimal between-spike distance	2 ms

Table 2.1 – Parameters used for detection of extracellular action potentials (find_peaks algorithm). Main parameters taken into consideration are height threshold, minimal width, and minimal between-spike distance. The height threshold was varied between 4 and 5, depending on the observed recording.

The electrode with the highest number of events crossing the defined threshold is used as a reference for identifying spikes in all other electrodes. In other electrodes, the algorithm then finds the nearest corresponding spikes in the time window of [-10, +10] milliseconds around each spike detected in the reference electrode. Two main analyses were performed: **(1)** spike shape analysis and **(2)** signal propagation analysis. Specific details of each approach and parameters are given in section 5.2.2 and section 5.4.2 respectively.

2.4.4 Cleaning of MEAs after Recording

The cells were incubated in 0.05% trypsin-EDTA for 15 minutes at 37 °C to detach from the surface, aspirated and rinsed with sterile Milli-Q water. Removal was checked by light microscopy and trypsin digestion was repeated if necessary. The glass rings and reversibly bound PDMS µFluidic structures were then gently removed manually from the MEA by applying uniform pressure over the entire MEA. Any PDMS residue was gently removed with a Q-tip and the MEAs were thoroughly rinsed in a water stream for at least 1 hour. The MEAs were then dried and stored in a clean box. Prior to the next use, the MEAs were cleaned as previously described in acetone, isopropanol, ethanol, and Milli-Q, respectively. For MEAs with irreversibly bound PDMS µFluidic structures, the purification procedure is slightly different. The first step is to disrupt the cells as described above and rinse with sterile Milli-Q. There is no removal of the ring and PDMS, so rinsing with any organic solvent is not recommended due to the high absorbency of the PDMS material. If rinsing the interior with 70% EtOH is necessary, it should be done in ≤ 15 seconds and immediately rinsed with a stream of sterile water. After

thorough rinsing through the water stream, multiple aspirations and rinsing with sterile Milli-Q are recommended. To store the devices for the next use, it is recommended to aspirate all the liquid from the macro and micro channels and to start preparing the devices for the next cell culture by activating the interior with oxygen plasma. However, all these steps do not guarantee perfect cleaning and non-absorption of small molecules by PDMS, which could later affect the health of the cell culture. Therefore, it is recommended to use these types of devices only once in cell culture or to completely switch to reversibly bound devices for all experiments.

Results and Discussion

Chapter 3

Device Fabrication and Characterization

The complex structure of a MEA-µFluidic hybrid device requires a thoughtful and systematic approach to the overall design and fabrication steps. In this thesis, two main groups of devices are observed, depending on the MEA layout used: (1) iMEA200 or (2) r16MEA.

In the first group, a variation of microchannel lengths is introduced, while the second group focuses on the efficacy of supporting axon-trap shape structures to promote the unidirectionality of a device. The unique approach in the fabrication process of proposed microelectrode arrays is the use of photodefinable PBO polymer HD-8820, which allows direct and convenient manipulation of the MEA surface and provides a wide spectrum of creative solution possibilities.

This chapter gives a detailed description of the proposed MEA and microfluidic designs and elaborates on the fabrication steps and expected results within the scope of the experimental setup. Finally, a characterization by EIS gives an additional analysis of the electrode quality and possible effects of material selection for device fabrication.

3.1 MEAs Design and Fabrication Adaptation

Two different MEA designs were used to analyze neuronal network activities in the final µFluidic-MEA hybrid device. The difference in designs was mainly introduced to accompany the proposed microfluidic structures designed for successful unidirectional connectivity of two sub-compartments. The following sections focus mainly on microelectrode array designs and established cleanroom fabrication processes.

3.1.1 Original (iMEA200) and Modified (r16MEA) Layouts

3.1.1.1 iMEA200 Layout

The initial design was **iMEA200**, which had an electrode layout already established in the institute. This design features 64 electrodes (including two reference electrodes) distributed in an 8 × 8 grid layout with an interelectrode distance of 200 µm. The round-shaped electrodes have diameters of either 12 or 24 µm. Each 4" wafer can accommodate 9 square MEAs with a length of 24 mm. The MEAs are numbered, with even numbers indicating electrodes of 12 µm diameter and odd numbers indicating electrodes of 24 µm diameter. Figure 3.1 (A) displays the iMEA200 layout. The MEA layout incorporates axon diode designed microchannels, proposed by Peyrin et al. (2011), to create a confined space over a subsequent number of electrodes. In this work, two different microchannel lengths were observed, compared to the originally described short length microchannels. The total number of microchannels is 120, with variations in length as follows: 576 µm (**short/S**), 864 µm (**medium/M**), and 1152 µm (**long/L**). The microchannel contains a varying number of electrodes depending on its length: 2 electrodes for short channels, 4 electrodes for medium channels, and 6 electrodes for long channels. Figure 3.1 (C-D) illustrates a comparison of all three channel lengths.

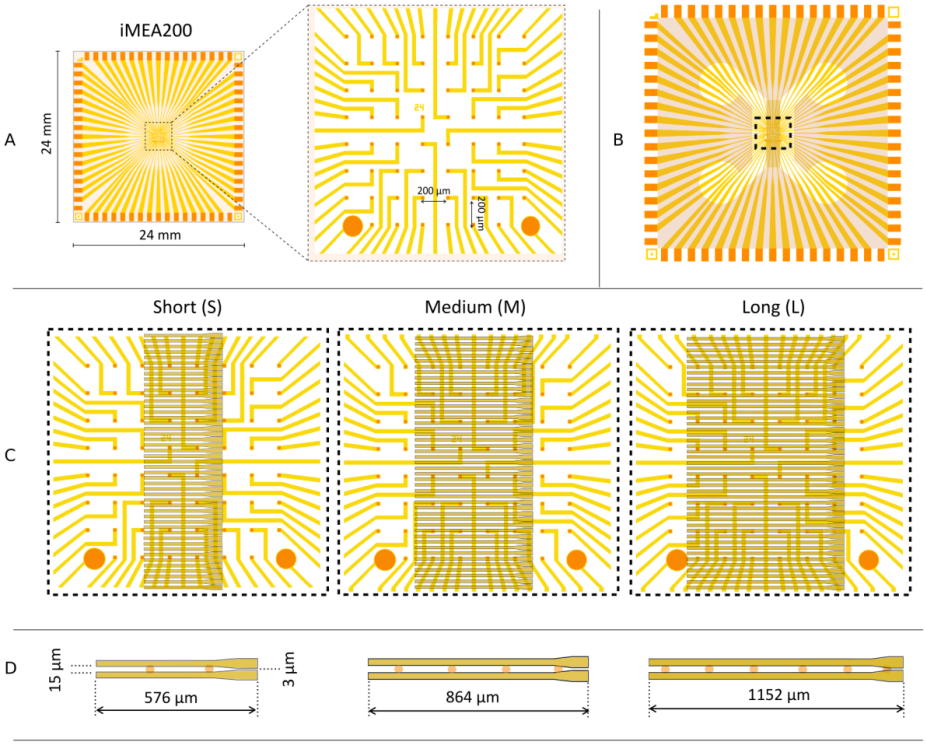

Figure 3.1 – An iMEA200 electrode layout and axon diode microchannels of different lengths. (A) The iMEA200 microelectrode arrays consist of 64 electrodes arranged in an 8×8 grid layout with an interelectrode spacing of 200 µm. **(B)** A total of 120 microchannels are patterned on an MEA connecting the left and right compartments. **(C)** The microchannels vary in length (S, M, L) and the number of electrodes within them (2, 4, 6). **(D)** In all three microchannel lengths, the dimensions of the axon diode entrance and exit are consistent: 15 µm and 3 µm, respectively.

The device presented in this text has a noteworthy feature of constructing microchannels directly on top of the MEA, which is described in detail in the following section. All 120 microchannels in the left compartment of the device are available for axonal growth of neuronal cells. However, only eight microchannels, which are placed over subsequent electrodes, are electrically active. Electrophysiological recordings can only be made within these eight microchannels. The probability of axonal growth through these channels depends on several parameters, such as the number of cells, successful axonal development, axonal bundle creation, and topographical influences on axonal growth direction. As described later in section 5.1, some of the eight microchannels are not consistently active, indicating a lack of axon growth. In addition, the recording capability of the electrodes is highly dependent on their position in relation to the microchannel. Recording was only possible with electrodes

inside the microchannels where signals were amplified due to the increased sealing resistance within the confined extracellular space in this area. The overall result of the design was a high number of low SNR signals recorded outside the microchannels, which is undesirable.

3.1.1.2 r16MEA Layout

To address the problem of many electrodes recording with low SNR, a new MEA microchannel design was proposed. The electrodes were rearranged to ensure that all were able to record with good SNR by placing them all inside the microchannels. I also limited the total number of microchannels to only those that were electrically active. I chose to use four electrodes per channel, as this is a sufficient number to accurately measure action potential propagation velocities and provides 16 microchannels for axonal growth. Figure 3.2 shows the **r16MEA**

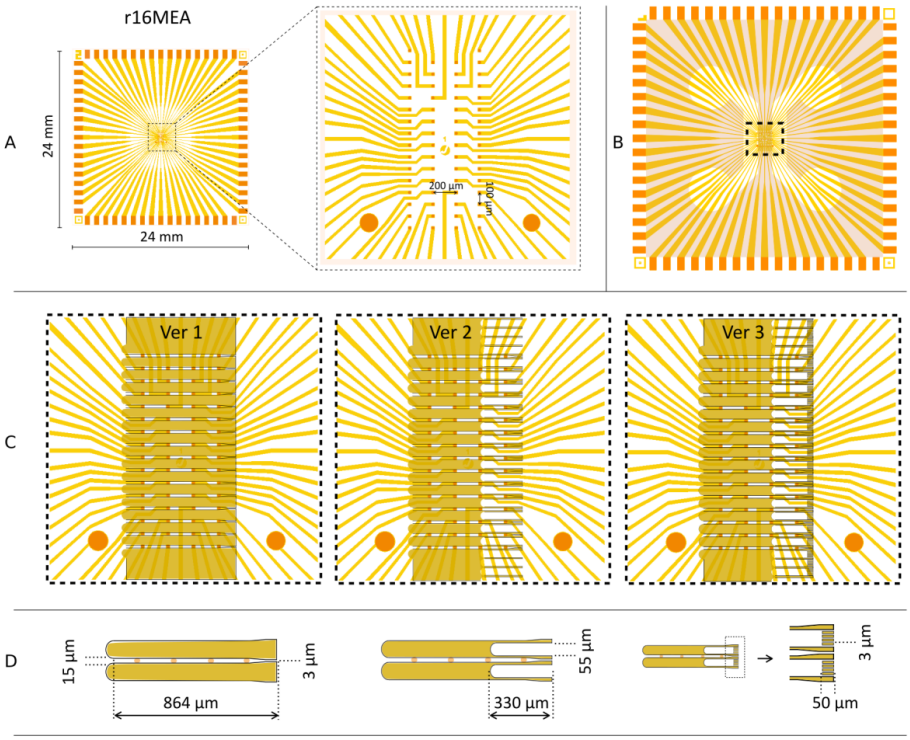

Figure 3.2 – A r16MEA electrode layout and trap-shape structures designs. (A) The r16MEA microelectrode arrays contain 64 electrodes distributed in 16 × 4 grid. Interelectrode space is 200 µm in horizontal, and 100 µm vertical distance. **(B)** A total of 16 axon diode shaped microchannels are structured on top of a MEA, with additional trap-shape structures **(C)** in the right compartment of a device. **(D)** Microchannel lengths are constant in all three versions (Ver1, 2, and 3) with 'U'-trap shapes present in design Ver2 and Ver3.

layout, which consists of 16 rows of electrodes. Each row, except the first, contains four electrodes spaced 200 µm apart. The first row has only two electrodes because two large reference electrodes were placed at a distance from the later integrated microchannel recording area. The vertical interelectrode spacing is 100 µm, which was chosen to limit the connection space and increase the likelihood of electrode coverage by growing axons. The r16MEA is accompanied by structures known as **axon-trap shapes** (see Figure 3.2, C-D), while the microchannel design is the previously described axon diode shape. The main purpose of the additional 'trap-shapes ' is to reduce the likelihood of microchannel occupation by axons growing out of the right subcompartment of a device. More details on these structures and their effectiveness in this regard is presented in section 4.2.2.

3.1.2 MEA Fabrication Process Adaptations

The MEA fabrication process is described in detail in section 2.1.5 in Material and Methods. The schematic of the process is presented in Figure 3.3, and consists of three main parts:

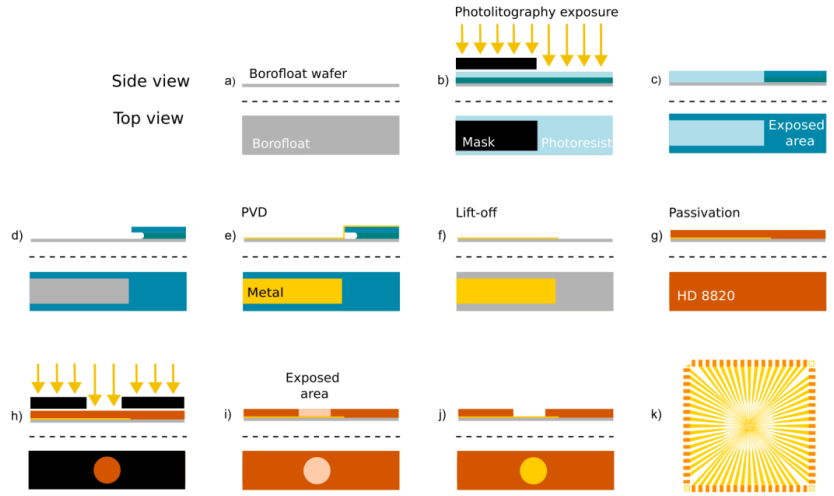

Figure 3.3 – MEA fabrication process: Negative photoresists LOR-3B and AZ nLOF-2020 are spin-coated on the dehydrated borofloat wafer **(a)** and exposed by photolithography **(b-c)**. After development **(d)**, metal is deposited by physical vapor deposition (PVD) **(e)**, followed by lift-off and definition of metal feedlines **(f)**. The samples are passivated with the photodefinable polymer HD-8820 **(g)**, then exposed to UV **(h)** and developed to define the electrode openings and contact pads **(i-j)**. The final product is a microelectrode array **(k)**, which is subjected to further construction of microchannel structures on top.

metallization (a-f), passivation (g-h), and development (i-j) for final structuring of electrode openings and contact pads. The passivation layer (g) was created by spin coating the HD-8820 resist at higher speed (at 5000 rpm) than the predicted span found in the process guide, with a goal of achieving thinner passivation thickness.

The passivation thickness achievable under these conditions is 2.4 ± 0.4 µm. The available information in the Photoresist Process Guide only provides expected thickness values up to 4000 rpm (Figure 3.4). However, the portion of the graph (in orange) showing the trend from 2000 to 4000 rpm is consistent with the process guide data, although the thickness difference is acceptable due to the dependence of the results on various conditions throughout the process.

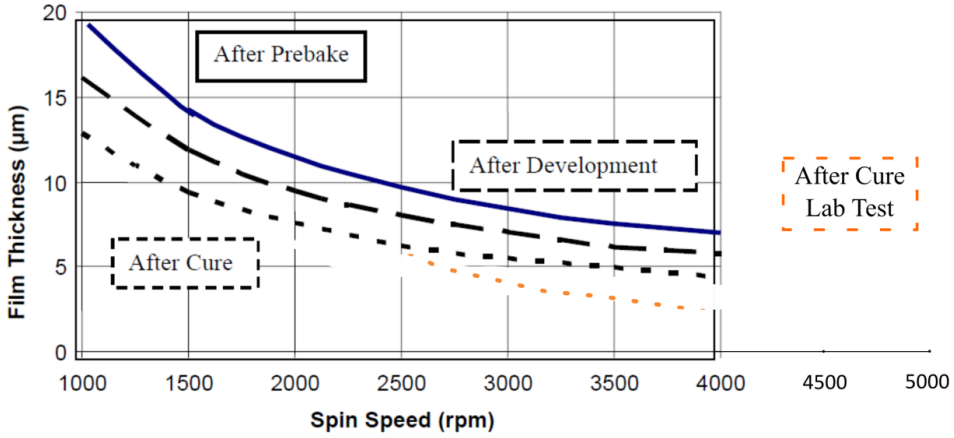

Figure 3.4 – Spin-speed curve for HD-8820. The orange dashed line represents tested thickness values for spin speeds ranging from 2000 to 5000 rpm. The graph is scaled to the figure from the Process Guide for HD-8820 aqueous positive PBO, for comparison.

The diameter of electrodes structured by the described process varied slightly depending on the positioning of the MEA on the wafer. The diameters were measured using microscope software tools, taking into account the 'inner circle' of the electrode micrograph (see Figure 3.5). However, it is important to note that this evaluation may be subjective, leading to potential biases and inaccuracies. The measured diameters of the large electrodes were 25.6 ± 0.7 µm, while those of the small electrodes were 13.4 ± 0.8 µm. These values are slightly wider than the corresponding mask dimensions predicted by the photolithography process, which were 24 µm and 12 µm, respectively. However, the overdevelopment of the electrode structures is still considered necessary to achieve a thinner overall passivation layer thickness.

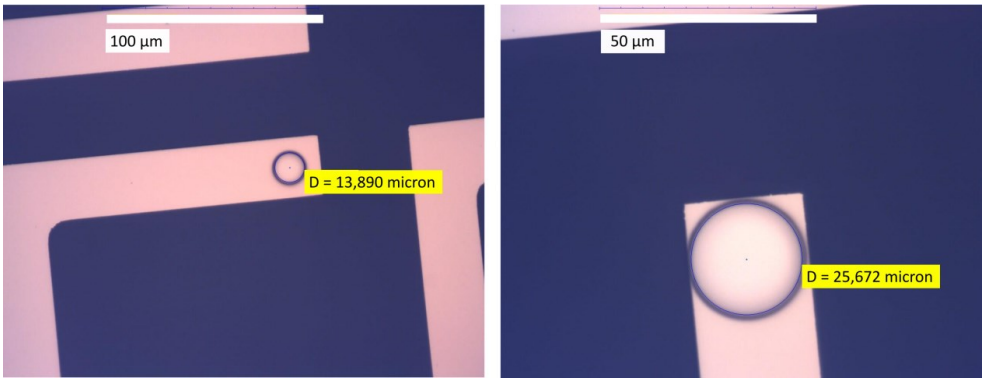

Figure 3.5 – **Electrode diameters after curing.** The electrode diameters after curing were found to be slightly larger than expected based on the measurement tool available in the visualization software. An example of an electrode belonging to MEA 8 is shown on the left, while an electrode from MEA 9 is shown on the right. The scale bars are 100 µm and 50 µm.

3.1.3 Structuring of Microchannels on Top of MEAs

Microchannels of the desired shape were structured from the same polymer as the MEAs. The process is illustrated in Figure 3.6. Before starting the process, the wafers were dehydrated,

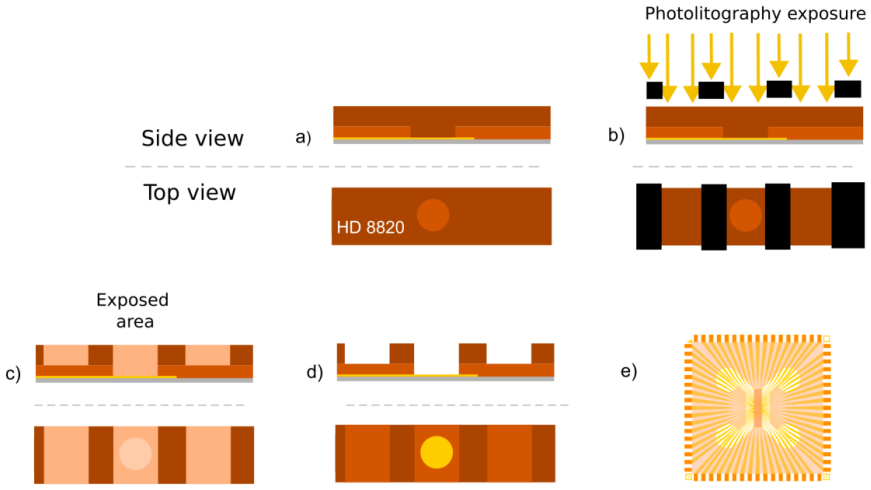

Figure 3.6 – **Microchannel structuring on top of MEA: (a)** The microchannels are structured directly on the MEA by spin-coating the second layer of HD-8820. **(b)** The exposed layer is exposed to UV light with a mask that corresponds to the desired microchannel design. The exposed area is developed **(c-d)**, creating the desired structure shape on the MEA **(e)**.

and an adhesion promoter was applied. In this work, HD-8820 was spin-coated at 2500 rpm with the lid closed for 45 seconds. A soft bake was performed as previously defined, followed by UV exposure at the same power. The development process involved using AZ MIF-326 in a double puddle process. The wafers were waved and rotated for 2 minutes before being transferred to fresh developer and waved and rotated for another minute. The microchannel layer of the wafers was polymerized in the furnace using the curing process parameters described above. After a water cascade and drying, the process was complete. The microchannel height under these conditions is 4.9 ± 0.3 µm, which corresponds to the spin-speed curve for HD-8820 (Figure 3.4). Longer development times of 2 min followed by 1 min 30s double puddle structured lower microchannel heights ranging from 3.3 to 4.4 µm.

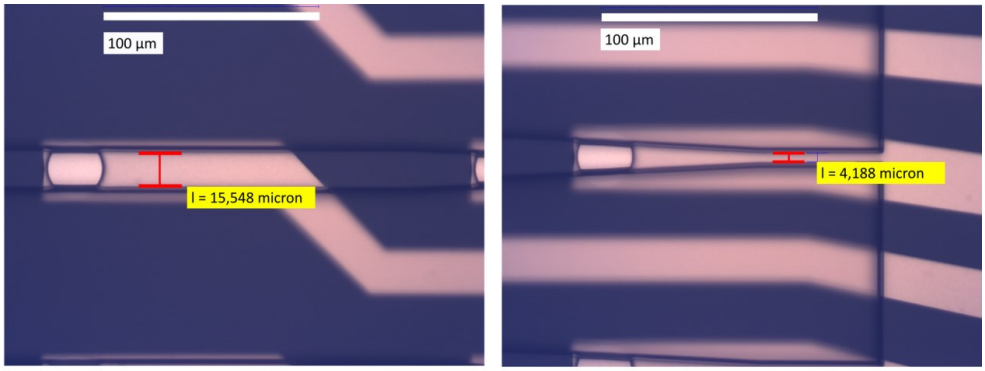

Figure 3.7 – **Microchannel widths after curing.** Microchannel widths were measured using distance measurement software. The left micrograph shows the width of the wider microchannel area, while the right micrograph shows the narrower emitting part of the axon diode shape. Scale bars are 100µm.

The microscope software tool was used to estimate the widths of the entrance and exit sides of the axon diodes (Figure 3.7). The entrance side of the microchannel has an average width of 15.7±0.5 µm, while the exit side has an average width of 4.1±0.5µm.

3.2 µFluidic Fabrication and Final Device Assembly

The second part of the device consists of a PDMS-based microfluidics that is fabricated by a soft lithography technique. Microfluidics corresponds to the MEAs by matching dimensions and designs that serve the purpose of creating a suitable environment for a successful development of neural networks in interconnected sub compartments.

3.2.1 SU-8 Molds Fabrication Process Adaptations

The detailed fabrication process is given in Material and Methods, in section 2.1.5.2. Fabrication of the final SU-8 mold is achieved in a two-layer process, by firstly constructing the microchannels (Figure 3.8, (A), a-e), followed by a thicker layer for construction of macrochannels and seeding chamber areas (f-i). The final macrochannel thickness depends on the SU-8 viscosity and spin coating rate used. The listed protocol in Material and Methods assumes the use of SU-8 2050, spin-coated at 2000 rpm for 35. The final thickness of constructed macrochannels described in this process is ~80 µm. For thicker macrochannel structures, a different type of SU-8 was used by changing the spin coating, exposure, and development parameters. When using the more viscous SU-8 2100, the spincoating parameters for the final thickness results are as follows:

SU-8 2100 spin coating	final layer thickness
3000 rpm | open lid | 45 s	95 - 100 µm
2500 rpm | closed lid | 45 s	120 µm
2000 rpm | closed lid | 45 s	150 µm

Development is done in the same developer for 15min or 5 min with ultrasound for 1 min. The thickness of the structures varied from sample to sample, but was in the range of 80-120 µm, depending on the availability of the SU-8 photoresist.

The procedure described was used in the case of mold fabrication to study cell co-cultures on coverslips or IBIDI dishes. In the case of MEAs, the procedure includes the flat first layer (~ 3µm height) instead of the microchannels (Figure 3.8 (B)). This construction then serves as PDMS *lids* that come on top of already structured HD-8820 microchannels on MEAs.

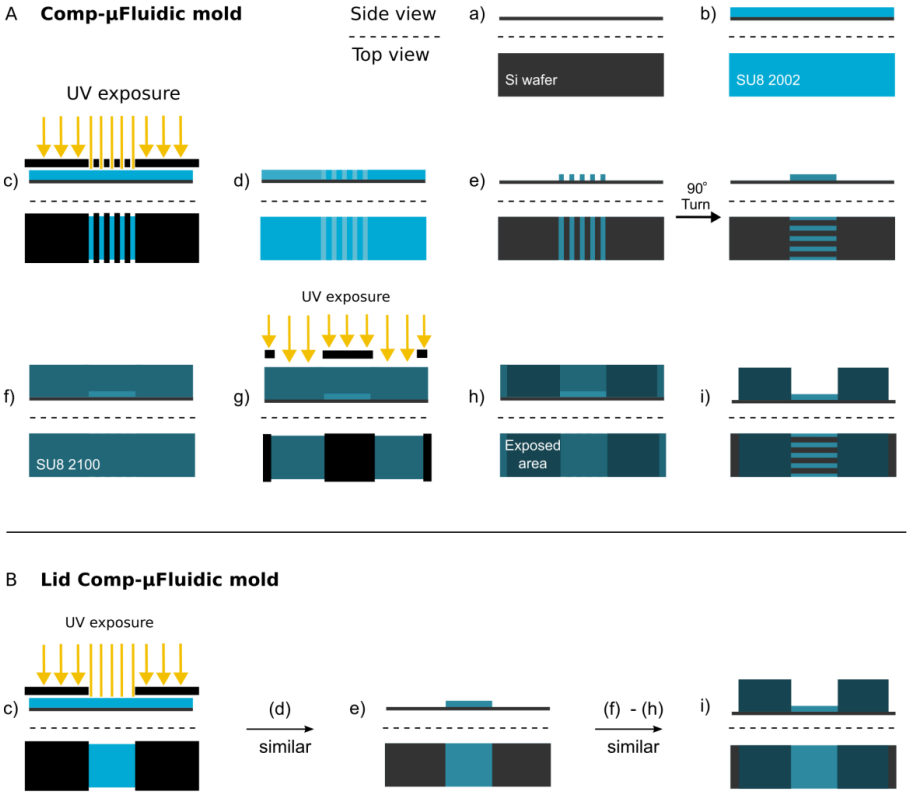

Figure 3.6 – SU-8 mold fabrication: (A) On the dehydrated silicon wafer **(a)**, a first layer of SU8 2002 is spin-coated and UV-exposed using a photolithography technique **(b-d)**. The unexposed area is removed in a development process **(e)**, leaving the microchannel structures on the silicon wafer. A second layer of SU8-2100 or 2050 is spin-coated onto the sample **(f)**, followed by UV exposure of the corresponding macrochannel areas **(g-h)**. The final two-layer structure for microfluidic molding is obtained after development and curing **(i)**. **(B)** The Lid Comp-µFluidic molds are created in the same process with the use of different mask pattern: **(c)** depict the difference in UV-exposed area. **(f-h)** are the same steps with the different pattern, resulting in the **(i)** final Lid Comp-µFluidic mold.

3.2.2 (Lid) Comp-µFluidic Structures Fabrication

The final compartmentalized microfluidic device (**Comp-µFluidic device**) is constructed from a silicon-based organic polymer PDMS. The SU-8 mold is cast in a custom-made Teflon holder (Figure 3.9), and the PDMS mixture is poured over. After overnight curing, the comp-µFluidic structures are isolated and prepared for further device assembly and cell culture.

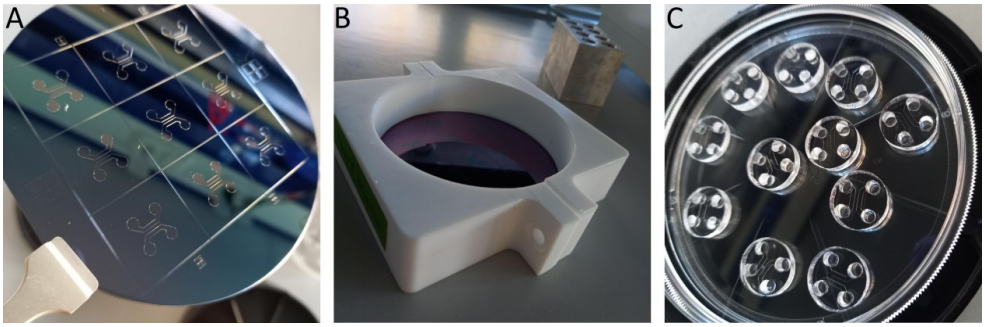

Figure 3.7 – Soft lithography process for the fabrication of PDMS-based comp-µFluidic devices. (A) SU-8 mold with a desired microchannel design. Structures are arranged at equal intervals across the mold. **(B)** The mold is clamped in a Teflon casting ring and 10:1 PDMS is poured. **(C)** After curing, the comp-µFluidic structures are isolated and cleaned.

A detailed illustration of this process is depicted in Figure 3.8 and detailed protocol can be found in section 2.1.5.3. Figure 3.10 depicts two comp-µFluidic structures used for experiments. The original design incorporates microchannels and is used for cell culture experiments performed on a glass surface or IBIDI-dish. An additional design was created for the purpose of utilizing comp-µFluidic devices in conjunction with MEAs that had already been structured with microchannels. Namely, the lid-µFluidic structure serves to merely cover the top of the microchannels. This approach simplifies the assembly of a comp-µFluidic and MEA devices, while ensuring that the microchannels provide a uniform microenvironment for axonal growth.

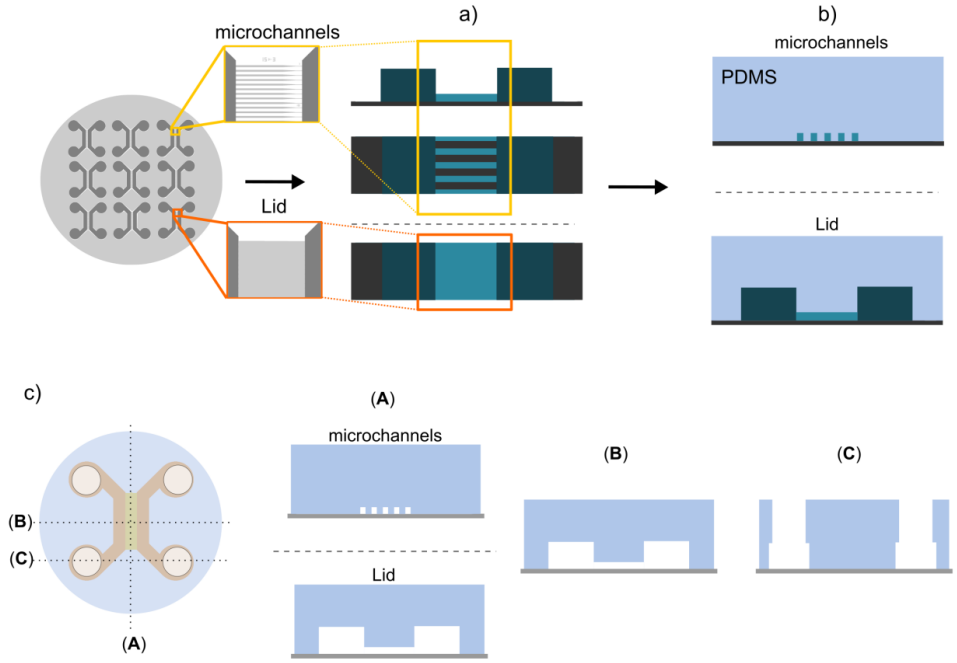

Figure 3.8 – Compartmentalized-microfluidic device fabrication: An SU-8 mold with a desired microchannel design **(a)** is clamped in a Teflon casting ring and PDMS is poured over the structure at a ratio of 10:1 **(b)**. After curing of the PDMS, the desired PDMS stamps are obtained using the soft-litography technique **(c)**. Cross-sections of a device are labeled (A) longitudinal cross section of microchannels/lid, (B) lateral cross section of microchannels/lid and macrochannels, and (C) lateral cross section of seeding chambers.

3.2.3 MEA and Comp-µFluidic Hybrid Device Assembly

In this thesis, two main methods were used to assemble the final device: **irreversible** (**IRB**) and **reversible** (**RB**) bonding. The irreversible bonding protocol allows a covalent bond between PDMS and HD-8820, mediated by (3-aminopropyl) triethoxysilane (APTES), while the

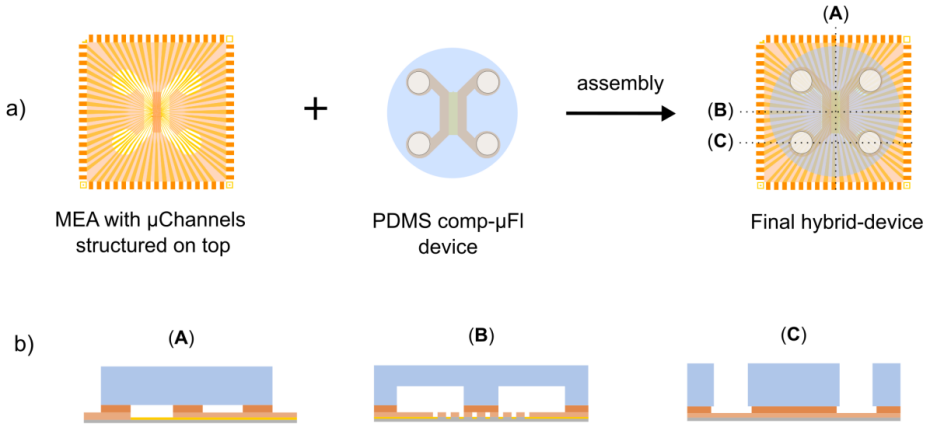

Figure 3.9 – MEA and PDMS comp-µFluidic device assembly: An MEA with top-structured microchannels and a PDMS comp-µFluidic device are assembled by aligning the corresponding structures and bonding in a desired manner **(a).** Cross-sections of a device **(b)** are labeled (A)-longitudinal cross section of the microchannels. The sketch shows an example of only two adjacent mmicrochannels, where the left microchannel is electrically active and the other is not; (B) – lateral cross of microchannels and macrochannels and (C) – lateral cross of seeding chambers in combination with an MEA at the bottom.

reversible bonding relies on the attachment of hydrophobic surfaces and allows the detachment and reuse of the MEA with another freshly prepared comp-µFluidic device. The assembly and cross-section of the final device are depicted in Figure 3.11.

3.2.3.1 Irreversible APTES Bonding

After proper cleaning of the MEA and comp-µFluidic device, the corresponding surfaces of both samples were activated by oxygen plasma. MEAs were activated at 0.4 W, 0.8 mbar for 1 min and PDMS comp-µFluidic devices were activated at 0.7 W, 0.8 mbar for 1 min. Samples are then placed on aluminum foil with activated surfaces facing up. The activated surfaces are then treated with 30% aqueous APTES solution and covered with a Petri dish lid to prevent drying. After 10 minutes of incubation, the MEAs and PDMS devices are thoroughly rinsed with

Milli-Q water and dried with N_2. The PDMS structures were aligned over the MEAs using a FINEPLACER® Lambda (Finetech GmbH & Co. KG, Germany) as shown in Figure 3.10 (A), or manually under the microscope.

The alignment of the structures and the final assembly of the two parts must be done in a short time after the incubation period for a successful bonding procedure. In the case of longer time, APTES tends to dry out on both surfaces, creating a sticky film without any possibility of bonding or removal. The choice of alignment method depends on the skill of the operator and can be done correctly either way. After alignment, the hybrid device is placed on a hot plate at 110°C for 10 minutes. After this step, Milli-Q water is added to the system to prevent the loss of hydrophilicity in macro- and microchannels. Glass rings are bonded by spreading the 10:1 PDMS on the ring edge and placing the ring around the comp-µFluidic device on the MEA (Figure 3.10 (B)). Rings are bound on the hot plate for an additional 10-15 minutes.

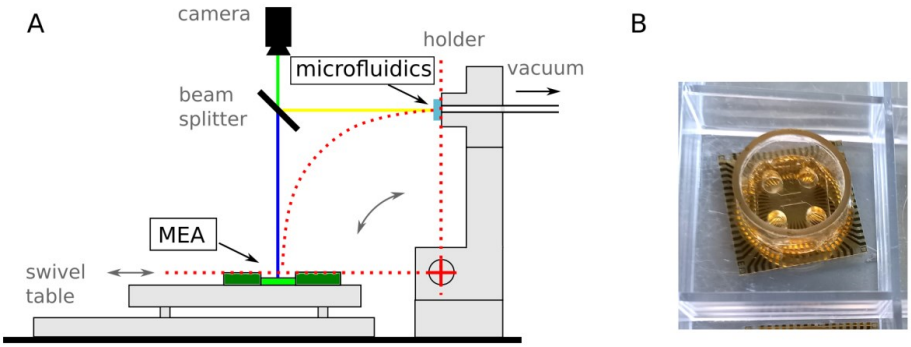

Figure 3.10 – Assembly procedure of MEA and comp-µFluidic device. (**A**) Sketch of a FINEPLACER® application for MEA and comp-µFluidic assembly. (**B**) Final MEA-µFluidic hybrid device with a glass ring attached.

3.2.3.2 Reversible Binding

In this process, MEAs and comp-µFluidic devices are aligned directly after the previously described cleaning protocol. After alignment with a FINEPLACER® or under a microscope, the PDMS comp-µFluidic structures are gently pressed onto the MEA to ensure that any air bubbles between the surfaces are released. The hybrid devices are then heated at 90 °C for 10 minutes, while the outer rings are reversibly bonded. The devices are then activated by oxygen plasma at 0.5 W, 0.8 mbar for 1 min.

3.3 MEA-µFluidic Hybrid Device Characterization

To evaluate the quality of the final hybrid device, parameters such as electrochemical impedance of the electrodes (EIS), noise, and signal-to-noise ratio (SNR) were observed. The impedance directly affects the baseline noise of the electrodes, which is crucial in determining signal loss during electrophysiological recordings. The SNR is then calculated as the ratio between the peak-to-peak (p2p) amplitude of a recorded potential and the electrode's baseline. The amplitude of the signal depends on several parameters and is closely related to the amplification effect of the microchannels. Chapter 5 discusses this relation and the observed effect in hybrid devices in more detail.

3.3.1 Electrochemical Impedance Spectroscopy (EIS)

Electrochemical characterization of the electrodes was performed by electrochemical impedance spectroscopy (EIS). EIS measurements were performed in a three-electrode setup, consisting of an Ag/AgCl reference electrode (Science Products GmbH, Germany), a Pt wire as counter electrode and each electrode of the MEA (Au) as working electrode. A VSP-300 potentiostat (BioLogic Science Instruments, France) was used for these measurements, and simultaneous measurements of two channels were possible. Therefore, the measurements were performed by short-circuiting the reference and counter electrodes of each channel. Consequently, the potential is given with respect to the Ag/AgCl electrode. The measurements were performed in 1×PBS at room temperature, applying a 10-mV sinusoidal waveform with 51 measurement points, sampling frequencies from 10 Hz to 10^6 Hz, and the impedance of the device was defined at 1 kHz frequency. Measurements were performed on the planar MEAs with pre-structured HD-8820 microchannels on top. A theoretically calculated impedance is used as a reference to characterize the quality of the MEA. The experimental impedance values varied significantly depending on the device production batch. Table 3.1 summarizes the expected and evaluated mean impedance values for the samples presented measured at 1 kHz:

Electrode diameter	Expected Impedance |Z| [MΩ]	iMEA200 |Z| [MΩ]	r16MEA |Z| [MΩ]
12 µm	3.52	5.76 ± 0.96	3.66 ± 1.08
24 µm	0.88	5.79 ± 1.79	4.00 ± 2.53

Table 3.1 – The mean value electrochemical impedance measured at 1kHz for different electrode diameters. The impedance is measured prior to µFluidic-MEA device assembly. The higher values than theoretically expected may be due to the polymer microchannel structures on top of the MEAs.

One of the reasons for the increased impedance is the presence of HD-8820-based microchannel structures on the MEAs. The width of the microchannels is approximately 15 µm and 3 µm, which means that the electrodes are partially covered within this area. This physically reduces the effective electrode area and changes the impedance of the electrode. Another possible reason for this phenomenon is the passivation thickness and hydrophobic nature of HD-8820. As mentioned in the sections above, the passivation thickness is approximately 2.4 µm and the microchannel height ranges from 3.3 to 4.9 µm. This makes the total walls surrounding some electrodes up to 7.3 µm high. The hydrophobic nature of the polymer may cause poor electrolyte-electrode contact by repelling the aqueous PBS molecules. Despite the high impedance measured, the MEAs showed a very good recordability of propagating action potentials along isolated axons. These results are discussed in more detail in sections 5.2, 5.3, and 5.4.

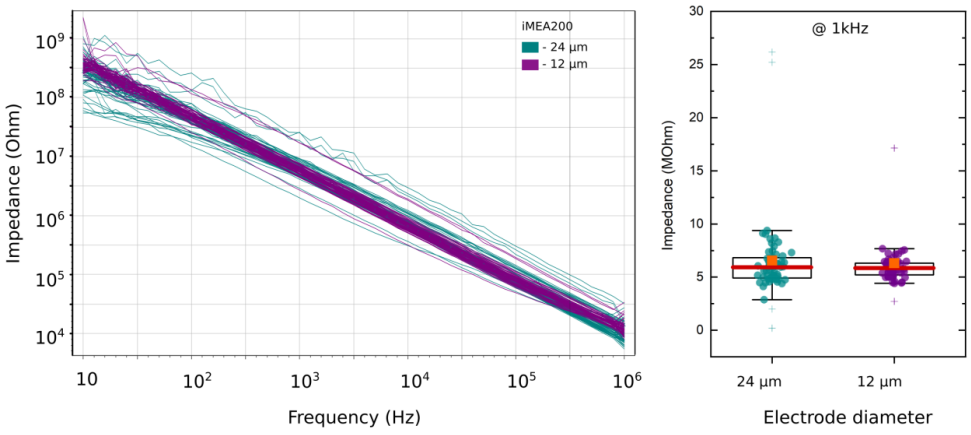

Figure 3.11 – EIS data of the iMEA200s of 24 (teal) and 12 (purple) µm electrode diameter. The bode impedance plot (left) presents scan frequencies from 10 Hz to 10^6 Hz. Presented are data sets from two MEAs with structured microchannels on top. Box plots present impedance values scanned at 1 kHz. Data points are plotted in teal (24 µm) and purple (for 12 µm) circles.

Figure 3.11 and Figure 3.12 show examples of impedance measurements for single MEAs with 24 and 12 µm electrode diameter. Sixty electrodes of each iMEA200 device with different electrode diameters (Figure 3.11) are measured in the frequency range 10-10^6 Hz. The impedance of the 24 µm electrode diameter (median: 5.93 MΩ, *Q1*: 4.92, *Q3*: 6.82) is not significantly different from the measured impedance of the 12 µm electrode diameter (median: 5.85 MΩ, *Q1*: 5.25, *Q3*: 6.32).

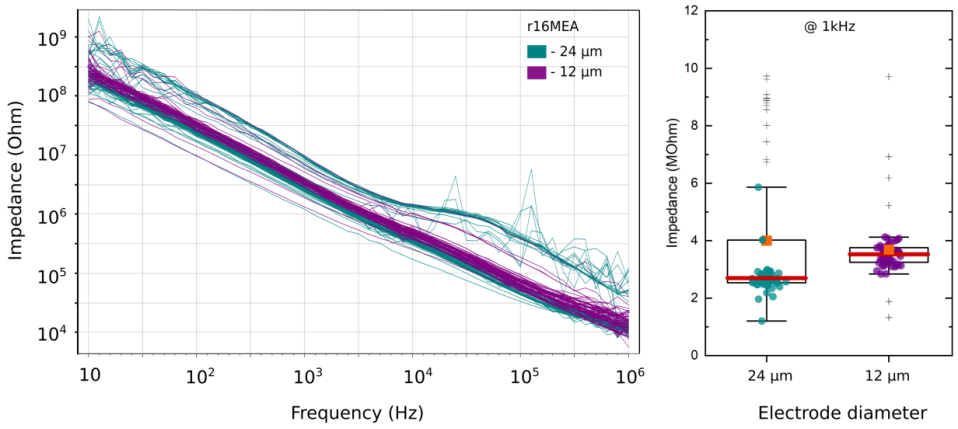

Figure 3.12 – EIS data of the r16MEAs of 24 (teal) and 12 (purple) µm electrode diameter. The bode impedance plot (left) presents scan frequencies from 10 Hz to 10^6 Hz. All electrodes are located beneath structured microchannels on top of the r16MEAs. Box plots present impedance values scanned at 1kHz.

In the case of r16MEA samples (Figure 3.12), 62 electrodes of each electrode diameter were subjected to electrochemical impedance spectroscopy measurement. A range of measured values for 24 µm diameter electrodes was larger compared to the sample with 12 µm electrode diameter.However, there was no significant difference in impedance between the sample with 24µm (median: 2.70 MΩ, *Q1*: 2.54, *Q3*: 3.76) and 12µm electrode diameters (median: 3.53 MΩ, *Q1*: 3.25, *Q3*: 3.76).

The final assembly of a MEA-µFluidic device significantly affects the EIS measurement of the electrodes within the microchannel area. In Figure 3.13, the Bode plot shows a comparison of 24 µm diameter electrodes on the same MEA before final device assembly (teal markers) and after PDMS microfluidic is attached to the MEA (orange lines). The box plots show the measured impedances at 1 kHz on a device without (w/o) and with microfluidics with respect to the reference electrode positioning (w/L – with on left side; w/R – with on right side). There

is a significant difference between the impedance values on the MEA without and with microfluidics on top of it (determined by paired two sample for means *t-test*; $p < 0.0001$). Average values with standard deviation are given in a table within the same Figure 3.13. After microfluidics assembly, the impedance increases significantly from MEA (median: 1.10 MΩ, *Q1*: 1.04, *Q3*: 1.25) and shows no significant difference whether recorded with a reference electrode on the left (median: 2.24 MΩ, *Q1*: 2.11, *Q3*: 2.43) or right (median: 2.24 MΩ, *Q1*: 2.09, *Q3*: 2.37) compartment of the device.

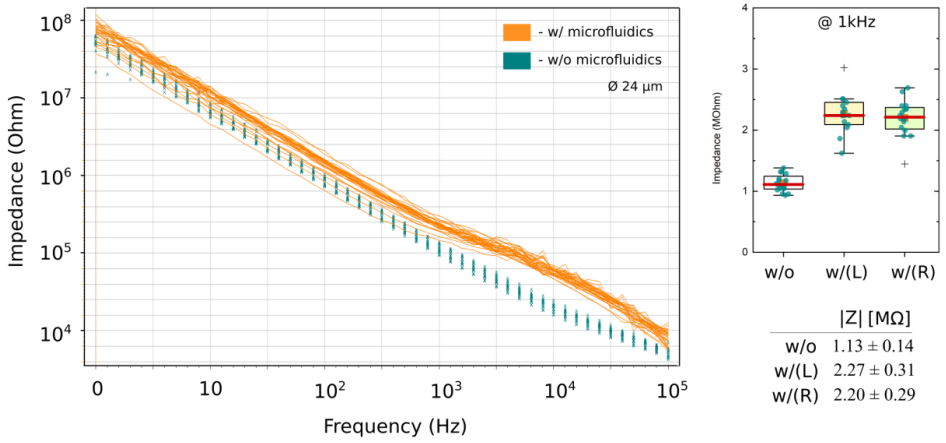

Figure 3.13 – EIS measurements of a MEA with and without microfluidics on top. A significant increase of impedance is evident upon microfluidic assembly. Box plots correspond to data evaluation at 1 kHz. The table gives mean values with standard deviation of the sample without (w/o) and with microfluidics on top, with respect to the position of the reference electrode left (w/L) or right (w/R) compartment.

3.3.2 Electrode Noise in The Final Device

Directly related to the electrode impedance discussed above is noise, which can be caused by unwanted electrical signals or fluctuations that can interfere with the accurate recording of neural activity. Here I present the noise distribution in devices with all three microchannel lengths. The noise levels at each electrode are calculated as twice the median average distribution (2×MAD). The noise distribution depends on the electrode position relative to the microchannel. For all three microchannel lengths, the noise inside the microchannel is greater than the noise outside the microchannel. This has already been reported by (Pan et al., 2011),

who claim that microchannel confinement increases the sensitivity to weak current sources, whether noise or signal.

Noise values vary with electrode position and electrode diameter. Figure 3.14 shows the median noise distribution as a function of electrode diameter and microchannel length. In all three examples, the result is consistent with the expected increase inside and decrease outside the microchannels. Depending on the electrode diameter, the noise levels are slightly higher for the 12 µm diameter compared to the 24 µm diameter. The mean values tend to be consistent and in line with the expectations already described, therefore the quality of the MEAs is accepted as satisfactory for cell culture experiments.

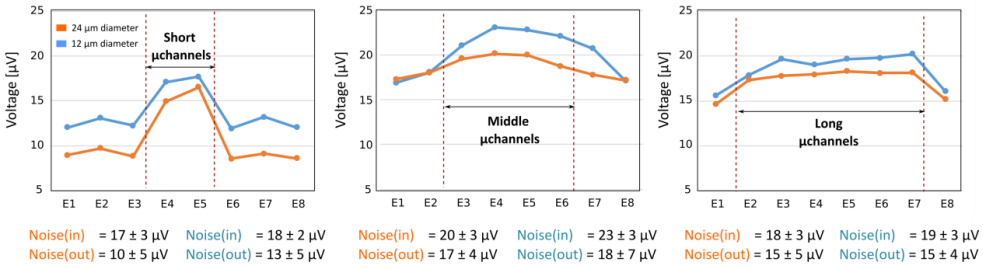

Figure 3.14 – Noise levels inside and outside microchannels. Plots represent the change in median noise levels observed at each electrode position relative to the microchannel. Orange plots represent MEAs with 24 µm electrode diameter and blue plots represent MEAs with 12 µm electrode diameter. Mean noise values with standard deviation for electrodes inside (in) and outside (out) the microchannels are highlighted in the corresponding color below each figure.

They also report consistent SNR values whether recorded inside or outside of microchannels. However, this consistency was not observed in the recordings with µFluidic-MEA hybrids presented in this thesis because the action potentials were almost always recorded only within the microchannels. The SNR for each electrode with recorded action potentials was analyzed as the ratio between peak-to-peak amplitude values and the corresponding baseline. The mean value and standard deviation of the SNR are calculated by averaging the data set of each electrode. SNR is only calculated for recordings within microchannels. The data belonging to the same MEA is grouped by electrode positioning and averaged to approximate the SNR trend along the microchannel. The original data is double step averaged, resulting in slightly different final values, but still within the range of standard deviation. This approximation is accepted.

This section presents only the SNR results of two different MEAs with long microchannels and different device assembly approaches, both measured at DIV 14. One noticeable difference is

the trend of the SNR along the microchannel depending on the assembly procedure. The irreversibly bonded (IRB) sample shows an increase in SNR with a final drop at the narrowed side of the microchannel, while the reversibly assembled (RB) sample shows a more consistent distribution of median SNR values along the microchannel. In the observed IRB sample, the maximum reaches SNR = 14, while in the RB sample, it goes up to SNR=11 (see Figure 3.15). Section 5.3 will provide a detailed discussion of the microchannel amplification effect that results in a high SNR. The distribution of SNR values varies depending on the assembly procedure of each sample, which can be explained by the same effect. This section focuses solely on confirming the quality of recorded signals through the electrically active microchannels.

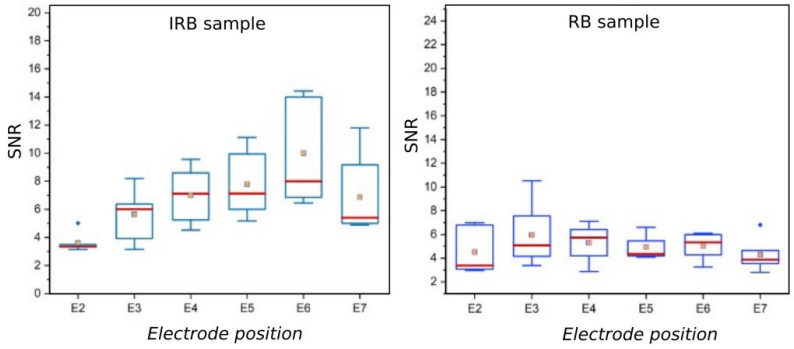

Figure 3.15 – Signal to noise ratio in IRB and RB sample at DIV 14. SNR box plots calculated for each electrode position as averaged value of corresponding electrodes in those positions along the microchannel.

3.4 Conclusions and Outlook

The main challenges in achieving an ideally controllable comp-µFluidic system are good spatial resolution and manipulation of axonal growth. The incorporation of micro-sized channels allows isolation of axons and control over the direction of axon growth, facilitating precise neural circuit formation and connectivity studies. Several groups have already incorporated such devices into their investigative studies (Park et al., 2006; Lewandowska et al., 2015; Sakai et al., 2017; Lopes et al., 2018). An important technical advance proposed in this work is the direct construction of microchannels on top of MEAs using a photodefinable polymer HD-8820. This approach greatly facilitates the final construction of the device by ensuring precise axonal guidance over the recording electrodes. The microchannel dimensions achieved in the experiments are 5×16 | 4 µm (H×$W_{entrance}$ | W_{exit}).

The electrode layout variations used are 8×8 (in iMEA200) and 16 × 4 (in r16MEA) grids. The permutation of electrode positions doubles the number of electrically active microchannels while maintaining good spatial resolution required for signal propagation analysis.

The quality of the recordings is highly dependent on the design and material of the electrodes and their physicochemical properties. Gold was used to construct electrodes in all MEAs characterized by EIS measurements. Electrodes with diameters of 25.6 ± 0.7 µm and 13.4 ± 0.8 µm showed higher impedance than theoretically expected. The exact value ranges were highly dependent on the production batch, so I decided to present the values of individual MEAs used in the experiments (Table 3.1). This did not affect the functionality of the recording electrodes (see Chapter 5).

Possible improvements to the proposed device include varying the material used for microchannel patterning on MEAs and exploring other electrode materials and designs for lower impedance values.

Chapter 4

Axonal Growth in Comp-µFluidic-Microchannel Systems

Various compartmentalized microfluidic microchannel systems have been proposed in the literature (Neto et al., 2016; Sim et al., 2017; Brofiga et al., 2021). One of the desired properties of such a device for neuroscience research is the high unidirectional selectivity of microchannels. This allows us to reliably mimic the unidirectional neuronal networks found in the mammalian brain. Therefore, I found the initial inspiration in choosing an axon diode microchannel design first described by Peyrin et al. in 2011. In the first part of the chapter, I point out all the technical difficulties that might arise when using this type of microfluidic system, and I give reasonable solutions to solve possible problems of cell seeding and uniform distribution in the macrochannel area. I then examine the unidirectional selectivity of such devices without successfully reproducing the results in available publications. This leads to the second part of the chapter, where I propose changes in the design of microfluidic systems and investigate their effect on unidirectional selectivity.

4.1 Cell Culture Challenges in the Comp-µFluidic Device

4.1.1 Sterilization and Homogeneous Coating of Substrates

The final assembly of the device is previously described in section 3.2.3. The assembly procedures described are either irreversible or reversible. For the successful development of neuronal cells in the microenvironment, it is necessary to provide sterile conditions to reduce the possibility of contamination by various pathogens. Since the comp-µFluidic-MEA device has specific requirements for its functionality, an appropriate procedure has been developed to ensure that all requirements are met. After the final assembly, the devices are activated by oxygen plasma, to create a hydrophilic environment within the macro- and microchannel areas. This step also provides additional cleaning of the interior of the devices. The devices are then further sterilized under UV light for 1 hour, in an open Petri dish. This step ensures that the exterior of the device is free of pathogens. The same Petri dishes, or new sterile dishes can be used for further maintenance of the devices with cell culture. After UV sterilization, the interior of the device is filled with sterile Milli-Q water to maintain the hydrophilicity achieved by oxygen plasma activation. The devices are then completely sterilized and stored in a Petri dish sealed with parafilm to prevent water evaporation.

One hour before seeding, the devices are dried with an aspirator and rinsed with prepared PLL/HBSS coating solution. Coating solution (20 µg/mL PLL in HBSS (Sigma Aldrich, Germany) is then applied in an amount sufficient to fill the microfluidic device. The device is then incubated at 37°C for 1 hour. An important step is to ensure that no air bubbles are created in the macro- or microchannels, as this will disrupt uniform cell distribution and axonal growth along the microchannels. After the incubation with the coating solution, the devices are ready for the cell seeding procedure.

4.1.2 Achieving a Uniform Distribution of Cells in Cell Compartments

4.1.2.1 Challenges in Keeping Cells in Microchannel Compartments

Achieving a uniform distribution and successful connection of cells is a very challenging step in using the comp-µfluidic-MEA hybrid system. In Figure 4.1, I illustrate this issue by comparing cortical cells cultured on the glass coverslip (control) and in a microfluidic device on a glass substrate, imaged at DIV 7.

A cell seeding suspension density of 60k cells/mL is applied in control samples and 1.5×10^6 cells/mL in microfluidic samples. Multiple observations confirmed that cells seeded in the microfluidic device don't occupy the macrochannel area but rather tend to concentrate in the seeding chambers and around their edges. This is a major problem when using comp-µFluidics as it prevents the recording of cell activity with the microelectrode array located in the microchannel area.

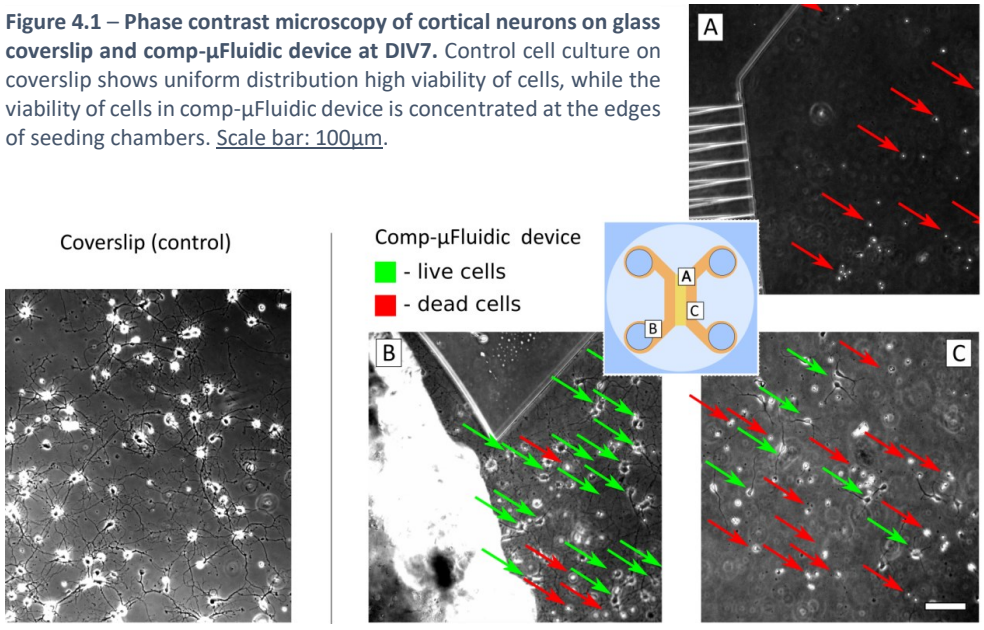

Figure 4.1 – Phase contrast microscopy of cortical neurons on glass coverslip and comp-µFluidic device at DIV7. Control cell culture on coverslip shows uniform distribution high viability of cells, while the viability of cells in comp-µFluidic device is concentrated at the edges of seeding chambers. Scale bar: 100µm.

4.1.2.2 Additional and Wider Seeding Chambers as a Potential Solution

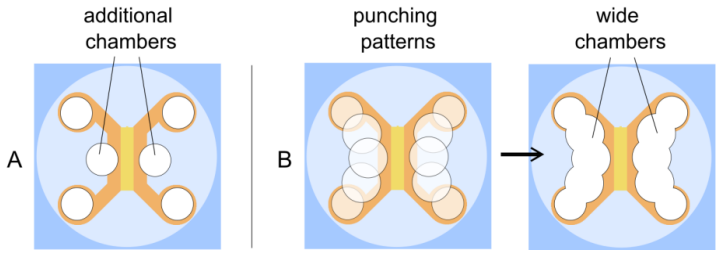

Figure 4.2 – Adapting a microfluidic device design for more successful cell seeding. (A) Microfluidic device with additional chambers added in the areas of the cell compartments, right next to the microchannels. **(B)** Microfluidic device with wide chambers, created by opening a large area along the cell compartments.

The first proposed solution to overcome the problem described above was to add an extra chamber next to the microchannels (Figure 4.2 (A)). This approach allowed better accessibility of microchannels to the growing axons. However, cells were localized only in the area where the **additional chamber** was created. This means that axons occupy only a limited number of microchannels near this chamber, leaving the rest empty and unused. To have complete occupation of all electrically active microchannels by axons, another design of **wide chambers** was introduced, which presents a large open space around both sides of the microchannels (Figure 4.2 (B)).

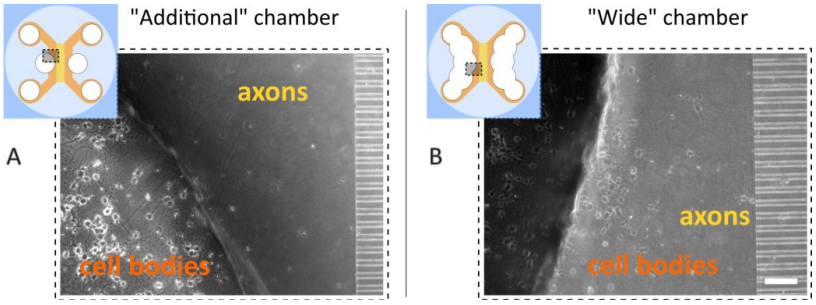

Figure 4.3 – Additional vs. wide seeding chambers. Sketches and phase-contrast microscopy images show the distribution of cells within each seed chamber design. **(A)** In *additional* chambers, cell bodies tend to be primarily localized within the chamber, and axon extension toward microchannels starts from this area. **(B)** In the case of a *wide* seeding chamber, cell bodies also occupy the microchannel area of a device Scale bar: 100 µm.

When seeded in a device with additional chambers, cells tend to be highly localized in the open space of the additional chamber, without access to the rest of the cell compartment (Figure 4.3 (A)). In the case of the wide chamber device, cells are mostly localized in the open area but also position themselves in the compartment area beyond the seeding chamber (Figure 4.3

(B)). This results in a more uniform distribution of cells along the microchannel area, allowing for better occupancy of the microchannels by outgrowing axons. Fluorescence microscopy images of the cortico-striatal co-culture (Figure 4.4) confirm that cells grow near the microchannels and extend axons through the microchannels. The goal of the presented experiments was to overcome the problem of cell positioning during the seeding protocol, and the modification of the chambers allowed the creation of a successfully connected co-culture.

However, the proposed solution was less than ideal, as the original concept of a device design was lost, and instead of growing in a uniform microfluidic environment, the cells grow in open space without fully controlled conditions due to faster evaporation of the medium and exposure to possible contaminants.

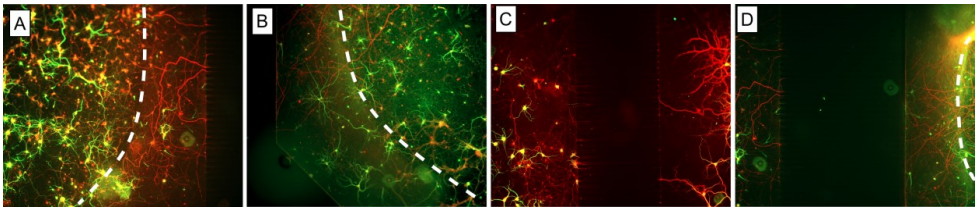

Figure 4.4 – Fluorescence micrographs of immunostained cortico-striatal co-culture in wide chambers comp-µFluidic devices at DIV 28. Neurons were fixed and fluorescently labeled for: MAP-2 (green) and NFH (red). Dashed white lines outline the shape of the wide chambers in the imaged region. **(A)** Left compartment with cortical cell culture. **(B)** Right compartment with striatal cell culture. **(C)** Short microchannels (576 µm) and **(D)** medium microchannels (976 µm) connecting cell compartments and guiding axonal growth. Scale bar: 200 µm.

4.1.2.3 Optimization of The Cell Seeding in The Original Comp-µFluidic Device

To find an optimal solution, I decided to modify and adapt the cell seeding protocol in the original device design. Since the area of a cell compartment is a tunnel shape of small volume structured by PDMS material on the HD-8820 substrate, the coating distribution is different from that applied on a flat surface. In addition, the absorption properties of PDMS also affect the final concentration of the coating solution. Therefore, the first changes introduced were to double the concentration of the PLL/HBSS coating solution to ensure sufficient coverage of the substrate surface and cell adherence. Second, the method of cell seeding was modified.

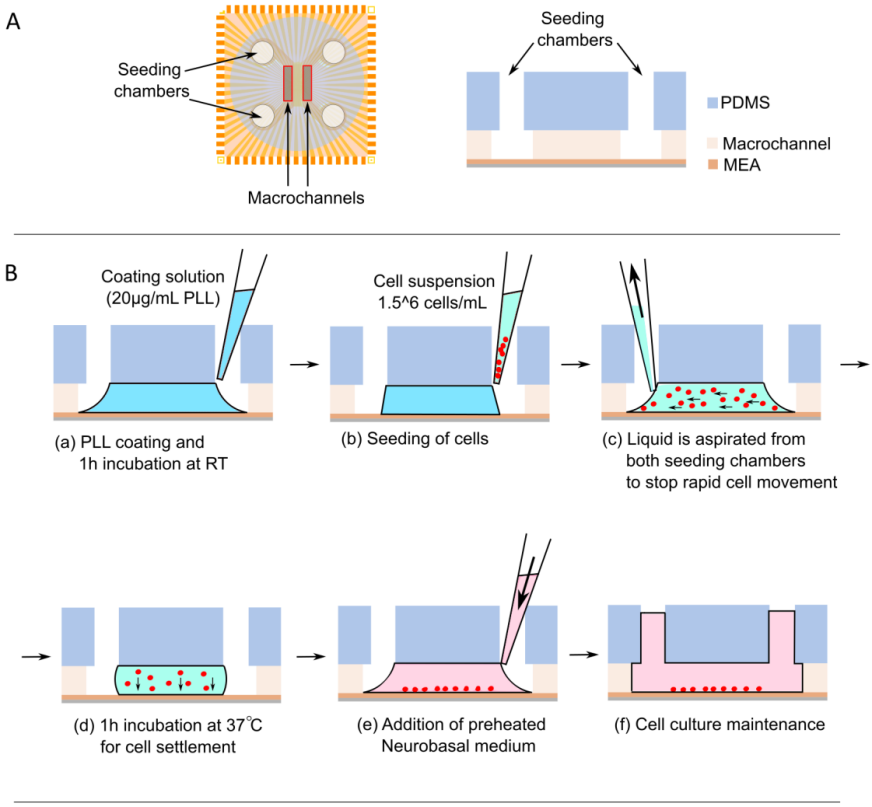

Figure 4.5 – Seeding procedure sketch. (A) Top and side views of microfluidic seeding chambers and macrochannels. **(B)** Sequence of cell seeding protocols: The µFluidic-MEA system is incubated with 20µg/mL PLL coating solution for 1h **(a)**. Cell seeding **(b)** causes an imbalance of fluid levels in both chambers, thus cells tend to move rapidly with the liquid movement **(c)**. Liquid is aspirated from both chambers, so that only the area covered by PDMS is filled with cell suspension **(d)**. The devices are incubated for 1h at 37 ˚C. During this time, the cells settle and attach to the coated MEA surface. Finally, pre-heated Neurobasal medium is added to the device, and culture is maintained for several days **(e-f)**.

Figure 4.5 illustrates a step-by-step description of the modified seeding procedure after coating the device (a). First, the embryonic cortical and striatal cell suspension is kept on ice prior to seeding to avoid coagulation of highly concentrated cells ($1{,}5\times10^6$ cells/mL). The suspension is gently pipetted up and down to develop uniform cell distribution and 10 µL is added to one of the seeding chambers on each side of a device (b). Due to an imbalance of fluid levels in both chambers, the cells tend to move rapidly with the fluid movement. Therefore, seeding chambers are then immediately dried by aspiration of any remaining fluid, leaving only the macro- and microchannel areas filled with liquid (c-d). After one hour of incubation under sterile conditions at 37˚C (d), Neurobasal medium is added to fill the rest of the device (e-f).

The modified procedure yielded better results in terms of uniform distribution of cells, as presented in phase-contrast microscopy images in Figure 4.6.

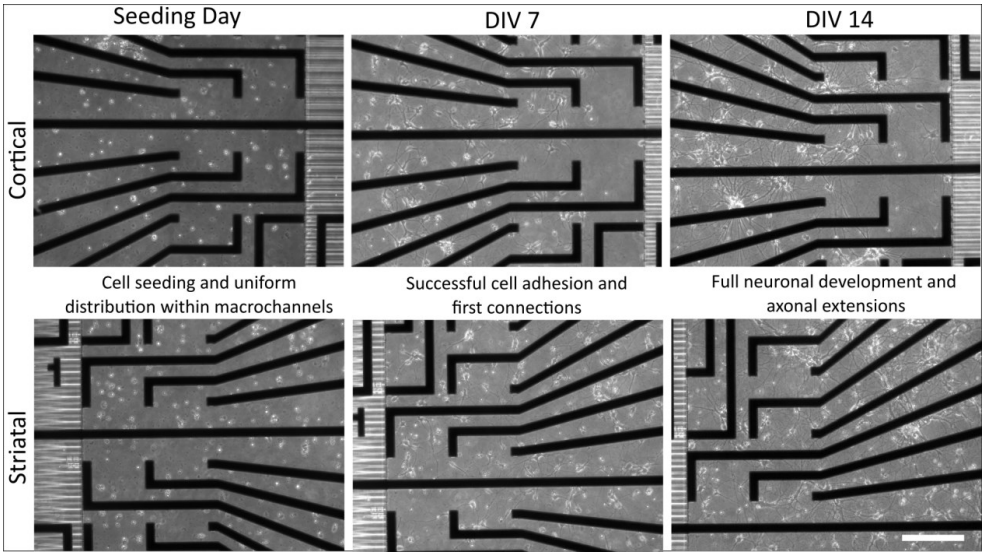

Figure 4.6 – Uniform cell distribution and development of cortical and striatal neurons at DIV 7 and DIV 14. Optimized cell seeding procedure results in uniform cell distribution, successful adherence, and fully functional cell development over time. Scale bar: 200µm.

The viability of the cells and their interconnection through the microchannels is confirmed by immunocytochemistry, as shown in Figure 4.7. The proposed process of cell seeding was used throughout the rest of the experiments for electrophysiological evaluation of neuronal activity.

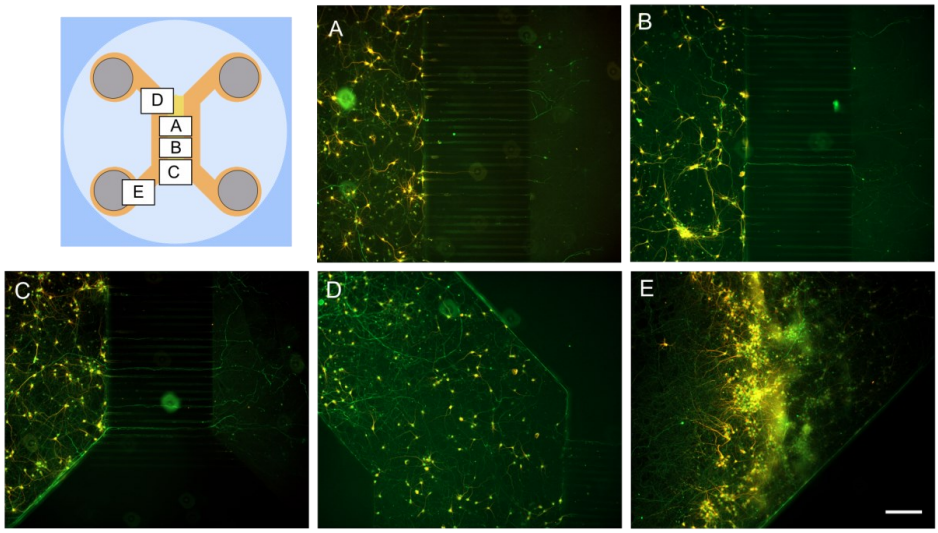

Figure 4.7 – Cortical neurons in a comp-µFluidic device with axon diode microchannels, at DIV 15. Neurons were fixed and fluorescently labeled for: MAP-2 (orange) and NFH (green). The positions of the acquired images are labeled on the sketch of a microfluidic device. **(A-C)** Cortical neurons growing in the left cell compartment and axons growing through microchannels to the opposite side of the device. **(D)** Cells are evenly distributed throughout the cell compartment area. **(E)** The highest density of cells remains in the region of the chamber edges, where cell bodies stay coagulated from the day of seeding. Scale bar: 200µm.

4.1.3 Axon Diodes and Unidirectionality of Axonal Growth

The initial design of a microfluidic device used in this thesis was the one first introduced by Peyrin et al. (2011). The general concept of this design is shown in Figure 4.8. The device consists of two cell compartments connected by asymmetric microchannels, called *axon diodes*, with 15 µm and 3 µm wide openings on opposite sides of the microchannel (Figure 4.8 (d)). The purpose of an asymmetric microchannel design is to provide unidirectional growth of axons, videlicet in the direction from left to right compartment. The cell compartments designated as left (**L-**) and right (**R-**) (Figure 4.8 (b)) are used for the cultivation of different cell culture types. Experiments co-culturing cortical neuronal cells in the L-compartment and

striatal neuronal cells in the R-compartment are a reconstruction of a cortico-striatal directional network found naturally in the mammalian brain. Seeding chambers are positioned at each end of the cell compartments (Figure 4.8 (a)).

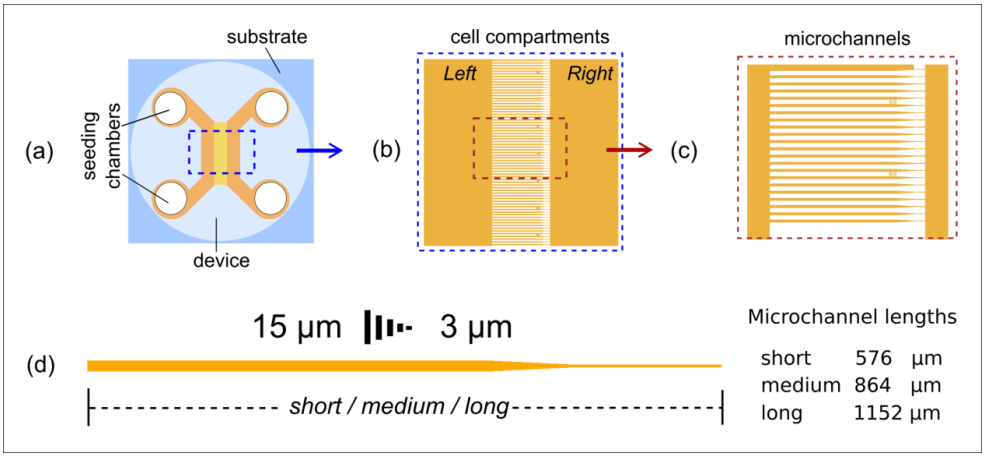

Figure 4.8 – **Axon diode microchannel design. (a)** Illustration of a microfluidic device attached to a substrate (glass/polymer/MEA) with four chambers used for cell seeding and medium exchange. The rectangle area **(b)** is an illustration of the left (*L*) and right (*R*) cell compartments, each 1000 µm wide, connected by microchannels **(c).** The distance between the microchannels is 15 µm. **(d)** Illustration of a single axon diode microchannel first introduced by Peyrin et al. and the dimensions of widths and lengths. **Note**: Orange colored space corresponds to the area where neurons are cultured, and axons are extended through the microchannel shape.

The microchannel length in the original design proposed by Peyrin et al. is 500 µm and 3 µm high. In the same study, they report a significant decrease in axonal growth in the direction from the R- to the L-compartment, which is important for accurate reconstruction of unidirectional neuronal co-cultures. Furthermore, they claim that the proposed design imposes unidirectional connectivity with 97% selectivity (Peyrin et al., 2011). A detailed description of the microchannels is unfortunately not available in the publication but seen from the micrographs presented in the same publication, the constriction of the microchannels starts in the second half of the microchannel length, leaving 50% of the length with a 15 µm width and 50% of the length with a constricted 3 µm width. However, this poses a challenge for integrating the device with an MEA for electrophysiological studies of neuronal co-culture activity. To integrate a series of electrodes with a minimum spacing of 200 µm and to keep the length of the microchannels in the range of the developing axon under *in vitro* conditions, Peyrin's design was adapted by creating a ratio of 70% length with 15 µm width to 30% length with 3 µm width constriction. The total length of the *short* microchannels used in this work is 576 µm. As already described in section 3.1.1, short microchannels are

accompanied with two electrodes, as a minimum for detection of action potential signal propagation. The advantage of highly selective unidirectionality of the axon diode design was the main reason for choosing this type of structure for integration with an MEA. Nevertheless, the 97% unidirectional selectivity could not be reproduced by our research group (Figure 4.9). One of the reasons could be a described adjustment of the asymmetric ratio of the microchannels. However, I decided not to compromise the goal of integrating microchannels with a series of electrodes. With the intention of improving the unidirectional selectivity of the axon diodes used in this thesis, I proposed and investigated a variety of shape designs described in the following sections.

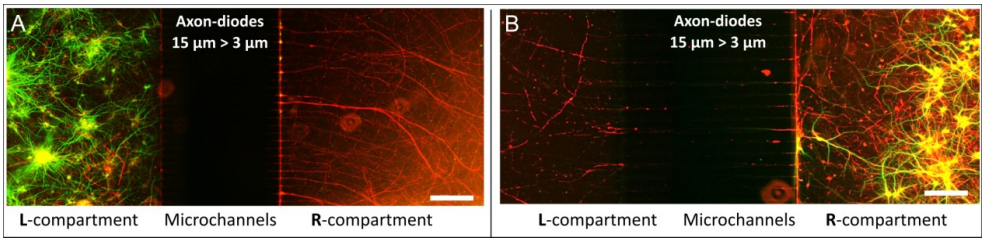

Figure 4.9 – Unidirectional selectivity of axon diode microchannels fabricated in our research group. Previously studied cortical **(A)** and striatal **(B)** cultures at DIV 21; done by Haberkorn B., and Zobel K. Immunostaining labels: MAP2 (green) for cell bodies and NFH (red) for axons. Scale bars: 200 µm.

4.2 Changes in the Design of Microfluidic Systems

The microchannel design of the axon diode, inspired by Peyrin et al. (2011), was utilized in all samples created for this thesis. To enhance its ability to promote unidirectional axonal growth, I modified the number of available microchannels and their architectural surroundings. In the first attempt, I created the so-called *axon-guiding shapes* with a focus on the receiving end of the microchannels. Subsequently, I designed the *axon-trap shapes* on the emitting side of the microchannels to capture any axons that may grow in the opposite direction of the axon diode microchannels.

4.2.1 Axon-Guiding Shapes

The first approach to addressing the previously described low unidirectional selectivity of the axon diodes was to reduce the total number of available microchannels connecting the left and right compartments. The chosen number of 16 is adapted to the previously described r16MEA layout by creating a system of fully electrically active microchannels. This choice was made with two goals:

1) By reducing the number of microchannels from 120 to 16, the expected occupancy density of microchannels with axons growing from the left compartment should increase, resulting in a lower probability of axonal growth in the opposite direction.

2) The electrical activity of the µFluidic-MEA system would be improved by doubling the number of electrically active microchannels and eliminating electrically inactive microchannels.

In addition, several other changes were introduced in the design of the receiving (left) and emitting (right) sides of the microchannel areas. The proposed designs are depicted in Figure 4.10 (b) and (c). On the left compartment, or *receiving* side, three different guiding shapes were created with the goal of successful agglomeration of axons and redirection into the microchannel. Structures L1 and L2 are characterized by a triangular shape and additional

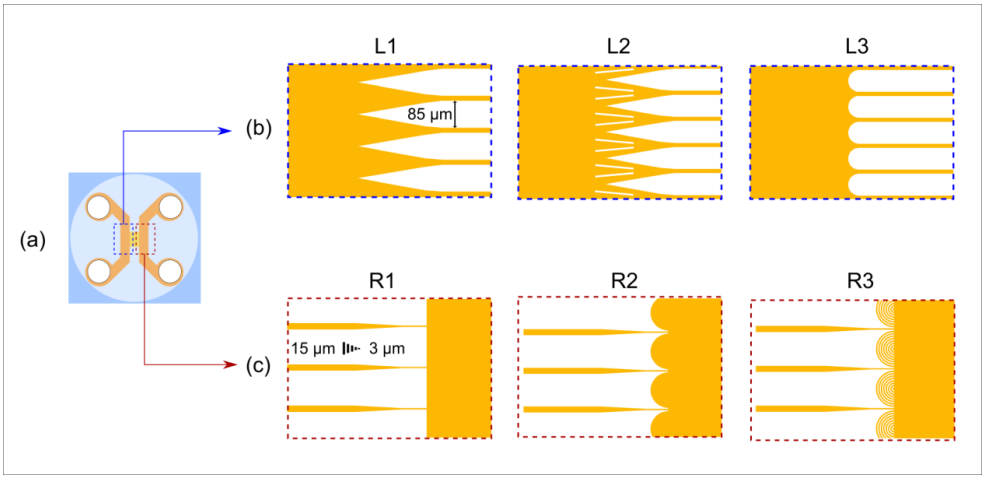

Figure 4.10 – Axon-Guiding shapes microfluidic designs. (a) Illustration of a microfluidic device attached to a substrate with four chambers used for cell seeding and medium exchange. Dashed rectangles represent left, and right cell compartments connected by 16 microchannels. **(b)** Different designs of the receiving side in the left compartment of a device; the microchannel spacing is 85 µm. **(c)** Different designs of the emitting side in the right compartment of a device; microchannels are in the previously described axon diode shape, with 15 µm wide entrance and 3 µm wide exit.

directional lines in the case of L2, while L3 has a simpler design with outwardly facing oval-shaped walls between each of the microchannels. On the right or *emitting* side, the axon diode microchannel design is maintained, with the addition of distinct shapes in structures R2 and R3.

The purpose of the proposed shape designs is to redirect axons extending from neuronal cells growing in the same compartment. R2 characterizes an inward oval shape of 45.5 µm radius, and R3 consists of circular microchannels, each 3 µm wide. Devices are fabricated on HD-8820 substrates by directly constructing microchannels and axon guiding shapes on the surface using the process of photolithography (see section 3.1.3). PDMS lid-comp-µFluidic devices are reversibly attached to substrates (described in section 3.2.3.2), and cortical cells are cultured on only one side of each device. Neurons are immunostained for MAP2 (orange) and tau (green) at DIV 15 (Figure 4.11) or DIV 20 (Figure 4.12). Figure 4.11 shows that the proposed structure L1 does not improve axonal clustering and redirection into the microchannel, rather cells tend to grow over these structures.

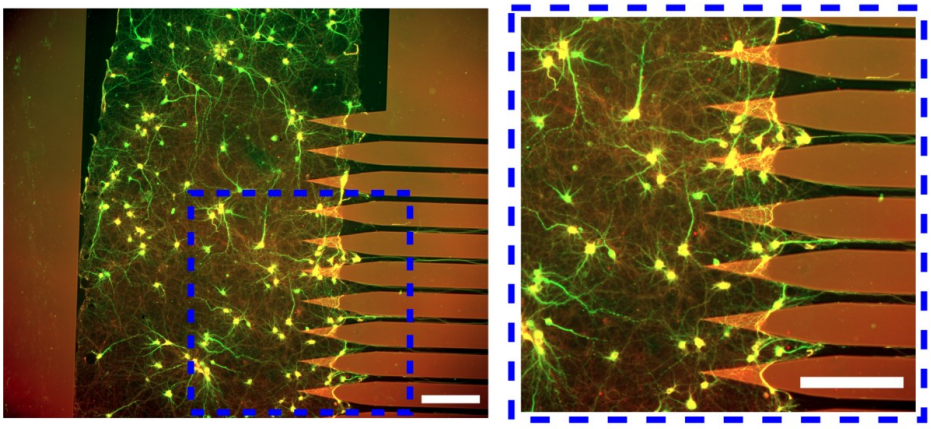

Figure 4.11 – Cortical neurons cultured in a left compartment of a microfluidic device with axon-guiding shapes towards axon diode microchannels, at DIV 15. Neurons were fixed and fluorescently labeled for: MAP2 (orange) and Tau (green). Blue square area in the original image (left) is magnified (right), showing that cells are growing over the triangle axon-guiding shapes. Axons are growing through microchannels to the opposite side of a device. Scale bars: 200 µm.

This is most likely due to the lower height of the structures, as they are more susceptible to overdevelopment in the fabrication process due to their location and sharp triangular shape. For these reasons, I have chosen R3 as the optimal shape to continue the optimization of a design. This shape has no edges that can be overdeveloped, and the oval shape guides the axons into the microchannels instead of them growing along the walls and skipping the

microchannel entrance, as has been shown to happen occasionally in previous experiments (Figure 4.11).

Figure 4.12 shows examples of samples in which cortical cells were cultured only in the R-compartment of a device. By fluorescently labeling cell bodies and axons, I wanted to observe the behavior of axonal outgrowth in the adapted emitting side of a microfluidic device with the previously described designs R1, R2, and R3. In all three examples, I observed that axons still successfully find a way to grow along the microchannels to the opposite side (Figure 4.12 (B)). In the initial R1 structure, axons tend to grow along the polymer wall and then redirect their growth into the microchannel. In the R2 designs, axons tend to be collected and redirected back into the same compartment, while the R3 design allows only redirection of their growth through circularly structured microchannels (Figure 4.12 (A)). From this point of view, R2 design seemed to be a more promising design for further optimization and implementation in a device to reduce axonal growth in unwanted direction.

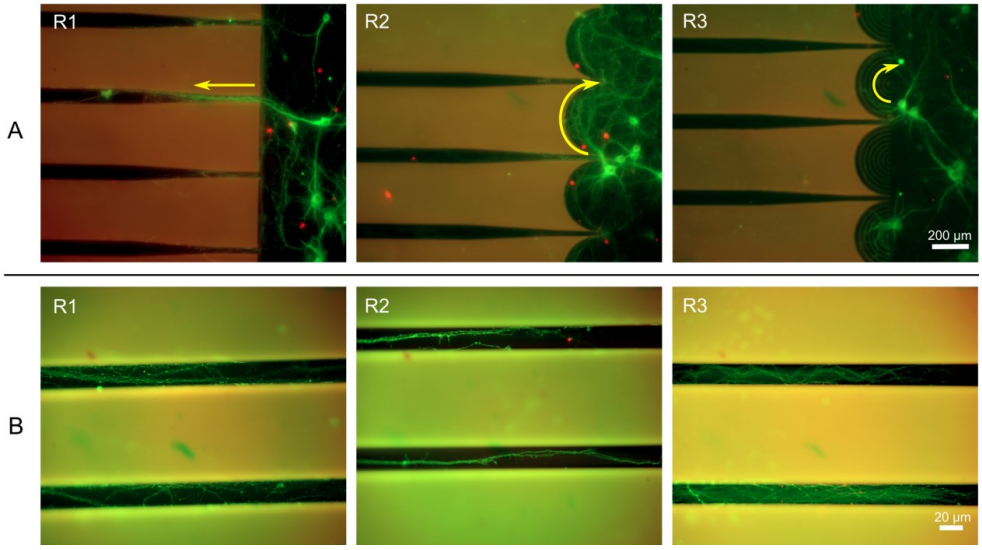

Figure 4.12 – Cortical neurons cultured in an R-compartment of a microfluidic device with axon-guiding shapes, at DIV 20. Neurons were fixed and fluorescently labeled for: MAP-2 (orange) and Tau (green). **(A)** Cells growing in the emitting side of a device with previously described designs R1, R2 and R3. Yellow arrows guide the eye in the direction of axon growth. Scale bar: 200 µm. **(B)** Magnified images of axons growing through microchannels from right to left in corresponding devices with design R1, R2 and R3, respectively. Scale bar: 20 µm.

4.2.2 Axon-Trap Shapes

Further optimization of the microfluidic design focuses on the emitting side of the microchannel area. The number of microchannels was kept at 16, as described in a section above. The receiving side of the microchannels was kept in an outward oval shape (guiding shapes L3). The emitting structure was kept to an axon diode shape with the addition of inward oval shapes in between the microchannels that serve to trap and redirect axons growing from the right compartment of the device (Figure 4.13 (d)). Throughout the text, the design variations will be referred to as *Ver1, Ver2* and *Ver3*, with Ver1 serving as the control design without new shape integration. In Ver2, the shape of the axon trap is an open channel 55 µm wide and 327 µm long, while in Ver3 the shape of the axon trap contains five evenly distributed channels of 50 µm length each, mimicking the environment of the original microfluidic design before the number of microchannels connecting the two compartments was reduced. The main difference between Ver2 and Ver3 is therefore the size of the surface area where axons could grow (Figure 4.13 (d)).

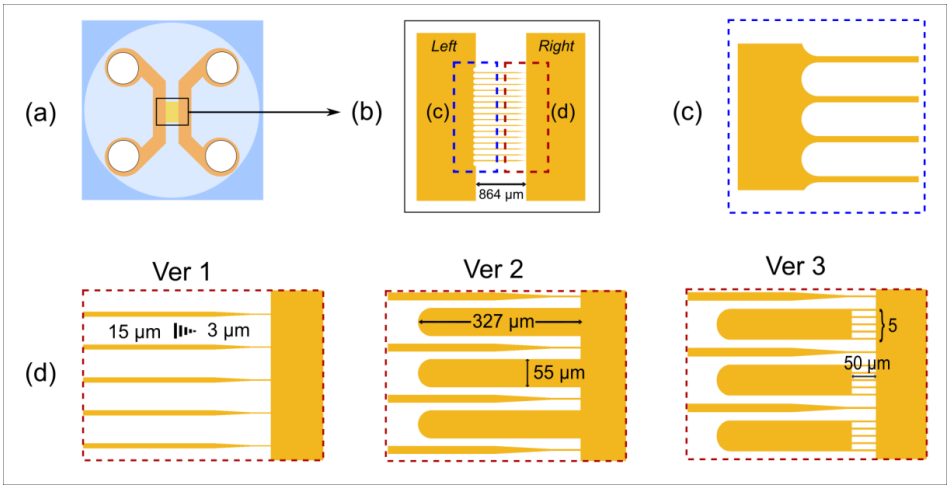

Figure 4.13 – **Axon-Trap microfluidic designs. (a)** Illustration of a microfluidic device attached to a substrate (glass/polymer/MEA). The microchannel area occupies a smaller area than in the original design, because the number of microchannels is reduced to 16. The rectangular area **(b)** shows a total of 16 microchannels, each 864 µm long and 85 µm apart. **(c)** Left compartment with outward oval shapes that widen the receiving side of the microchannels. **(d)** Three different versions (Ver-version) of axon trap shapes in the right compartment of a device. In each version, the microchannels retain the axon diode shape, with additional axon trap shapes areas between the microchannels in Ver2 and Ver3. **Note**: Orange colored space corresponds to the area where neurons are growing and extending axons.

4.2.2.1 The Effectiveness of Axon Trap Shapes in Improving Unidirectionality

To evaluate the effectiveness of the proposed designs in improving the unidirectionality of the microfluidic design used, cortical cells were seeded in the right compartment while the left side was left empty. The number of transmitted axons is determined by immunostaining for NFH (green, Figure 4.14). Because HD-8820 is an autofluorescent material, it is difficult to clearly visualize immunostained cells on this substrate. For this reason, experiments were performed on commercially available dishes with sterile glass bottoms and lids that prevent evaporation of the medium (µ-Dish 35mm, iBiDi GmbH, Germany). Detailed quantitative analysis was not possible due to the small number of experiments. However, qualitative observation of the fluorescence micrographs presented (Figure 4.14) reveals a difference in the number and length of axons exiting the microchannels in the left compartment is notable. In *sample_1* from group Ver2, the axon length is significantly shorter than in all other samples, not exceeding 600 µm and averaging 400 µm after exiting the microchannel (Figure 4.14 (A)). Furthermore, *sample_4* from group Ver3 shows the longest axonal extension of almost 1000 µm in length (Figure 4.14 (B)). The density of axonal transmission is difficult to estimate without proper computational analysis of the fluorescence intensity, but my own judgement

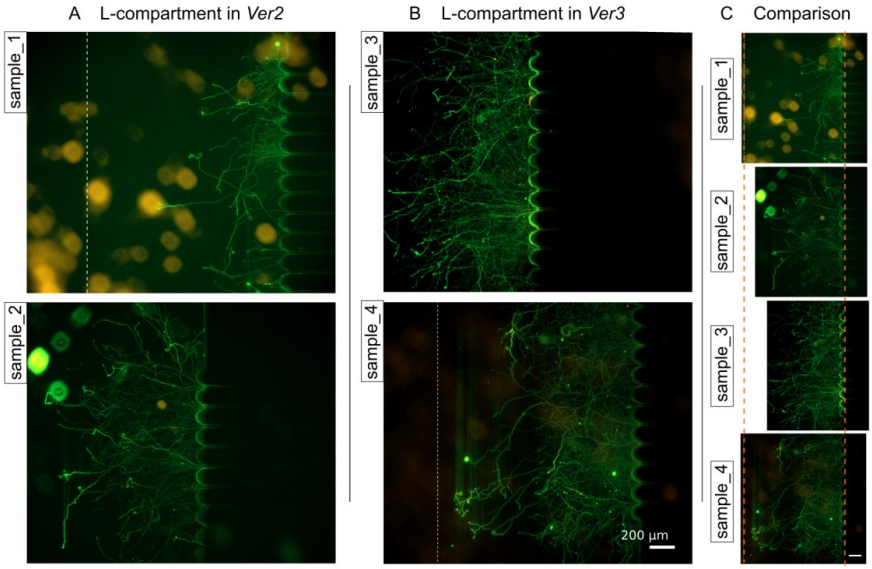

Figure 4.14 – Fluorescence micrographs of the comp-µFluidics axon-trap immunostaining axonal transmission in the right-to-left direction at DIV 29. Axons growing toward the L-compartment of the device with **(A)** Ver2 (samples _1 and _2) and **(B)** Ver3 (samples _3 and _4) axon-trap shape design in the R-compartment of the device. **(C)** Alignment of micrographs for better comparison of outgrowth axon density and length. Immunostaining: MAP2 (orange) and NFH (green). Scale bars: 200 µm.

is that *samples _3* and *_4* show a denser network of outgrowing axons. This is consistent with intuitive expectations given the difference in proposed designs. Namely, the size of the open access area of the axon-trap shape is larger in Ver2 than in Ver3, consequently allowing a higher number of axons to grow in this direction than towards the emitting opening of the axon diode microchannels. The presence of 5 additional microchannels within axon-trap shape in Ver3 reduces the size of the entrance area and therefore the actual probability of axons being trapped. However, despite the proposed explanation for the results presented, cell culture itself may play an important role in the density and distribution of axonal outgrowth. In the absence of more successful experiments that would undoubtedly give a better picture of the influence of shape variations on this matter, I decided to examine the number of cell bodies in the right compartment of each sample in the window area of 1 mm^2. The observation is shown in Figure 4.15. Remarkable dark areas of irregular oval shapes are present in all four micrographs and may be due to either the dead cells or areas of uneven coating where cells were never originally attached. Due to the age of the cell culture at DIV 29, it is likely that cells have begun to die and detach from certain areas of the substrate. Cell counts were performed manually by counting all visible stained cell bodies within the selected observation window. The number of cells counted was as follows: 132, 102, 86, and 138 in *samples_1*, *_2*, *_3*, and *_4*, respectively. It is obvious that *sample_1* and *sample_4* do not differ

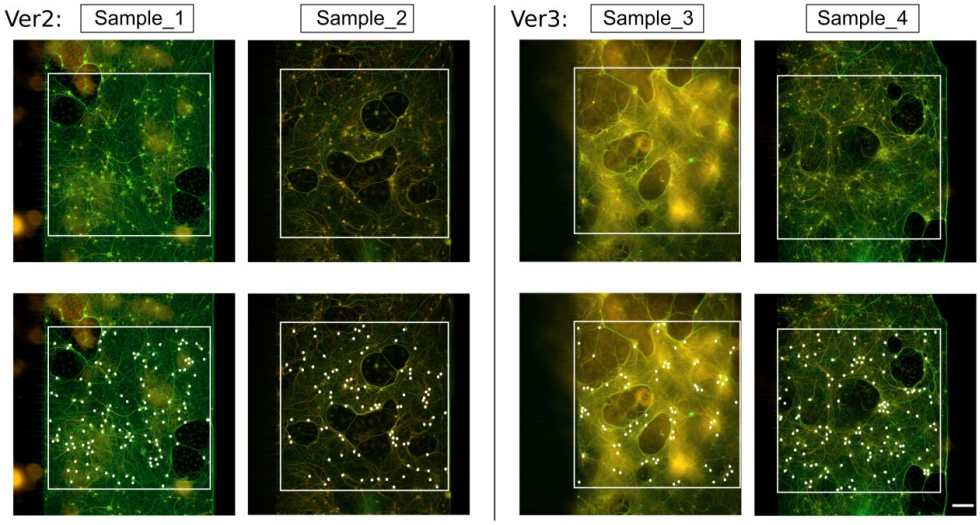

Trap Shape:	VER2		VER3	
Sample:	S_1	S_2	S_3	S_4
Cell count:	132	102	86	138

Figure 4.15 – Cell count in fluorescence micrographs of immunostained cortical neuronal network in the right compartment of the devices. Cells are counted manually in an area of 1 mm^2 (square). Scale bar: 200 µm.

much in the number of cell bodies counted, but there is a significant difference in the observed length and density of axons in the left compartments of the devices (Figure 4.14). Similarly, the number of cells in *sample_3* is significantly lower than in *sample_1* or *sample_4*, but the situation in the left compartment is more like *sample_4*, with significantly higher density and length of immunostained axons compared to *sample_1* and *sample_2*. This leads me to conclude that the difference between the Ver2 and Ver3 designs may have a significant influence in reducing the number of axons growing in the unwanted direction, in favor of the Ver2 design. More data would be needed to confirm these results.

4.2.2.2 Behavior of Axons within Axon Trap Shapes

Another obstacle to characterizing the trap-like structures was the inability to successfully visualize axons within these microstructures and microchannels (Figure 4.16). Due to the small volume of these areas, it is difficult to uniformly immunostain the axon along the entire length of the microchannels and trap shapes. Therefore, visualization was only successful in the limited length of less than 200 µm near the beginning of the microchannels on the left side of

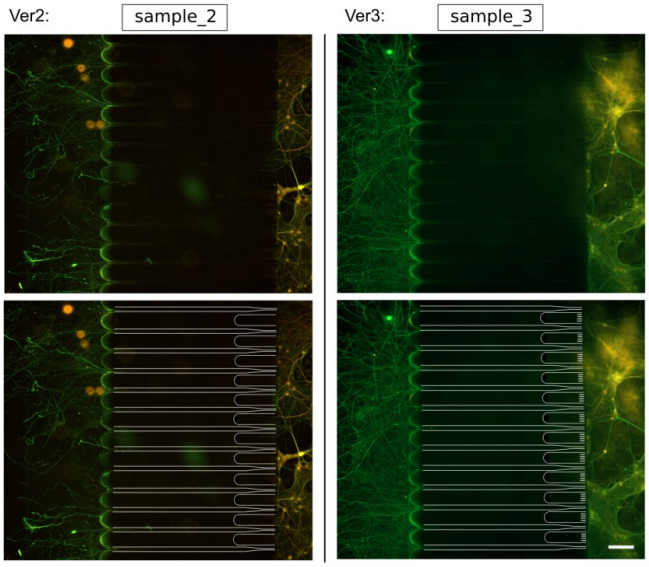

Figure 4.16 – Fluorescence micrographs of the central area in microfluidic devices with axon-trap shapes Ver2 and Ver3. Original images of the microchannel area in Ver2 *sample_2* (top left) and Ver3 *sample_3* (top right). Below the original images are manually sketched microchannels and axon-trap-shape structures with their approximate dimensions and positions. Immunostaining: MAP2 (orange) and NFH (green). Scale bar: 200 µm.

the devices. To overcome this problem and to be able to visualize the behavior of axonal growth within the proposed trap-shape designs, I approached the process of immunostaining in the devices in a slightly different way. In the following experiments, I first chose to reversibly attach the microfluidics to the glass substrates (see sections 3.2.3.2 and 2.3.3). Phase contrast microscopy after cell fixation and removal of the microfluidics revealed some cracking around microchannels and trap shapes (Figure 4.17).

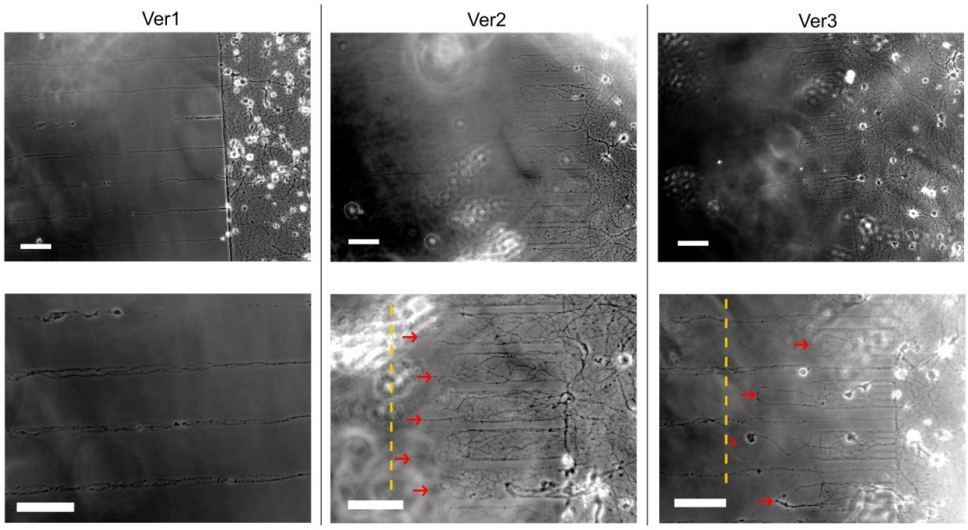

Figure 4.17 – **Phase contrast images of cortical neuronal cultures after fixation and after removal of microfluidic devices with corresponding axon-trap designs: Ver1, Ver2 and Ver3.** Original images of each sample are shown in the top row, while corresponding magnified areas of interest are shown in the bottom row. Ver1 sample with microchannels being occupied by axons belonging to the cells growing on the right compartment of the device. A magnified image shows axonal rupture in one of the microchannels and multiple axons occupying each of the rest of microchannels. Ver2 and Ver3 samples with axons occupying the corresponding trap-shapes. In magnified images, the yellow dashed line represents the full length of the structures within the microfluidic device, while the red arrows point to the longest extension of the axons reaching into each of the observed shapes. Scale bars: 100µm.

However, this was a sporadic occurrence and was expected to be less severe due to the robustness of manual microfluidic removal. Nevertheless, most of the axonal extension and branching remained intact, and the immunostaining procedure was continued with the same choice of antibodies as in a previously discussed experiment. As can be seen from the phase-contrast microscopy images, axons occupy Ver2 trap-shapes to a greater extent than in the case of Ver3. The red arrows in Figure 4.17 represent the degree of axonal elongation in each of the observed structures, while the yellow dashed line marks the actual length expected

from the structures in a microfluidic device. The density of axons in Ver2 occupies almost the entire area of the structure, while in Ver3, however, the trap shapes are irregularly occupied with most density localized to slightly more than half of a structure length. Longer extensions to the full length of the structures are seen only in a few isolated cases, far fewer than in Ver2. This may be due to less successful hydration of the structures in Ver3, leading to the formation of air bubbles and hydrophobic uncoated regions that are later repelled by growing axons. The same samples were then immunostained, and results are shown in Figure 4.18. The occupancy of the-trap shaped structures is present in both Ver2 and Ver3, however, as explained above, it is difficult to evaluate the efficacy of each of the designs with the method of immunostaining.

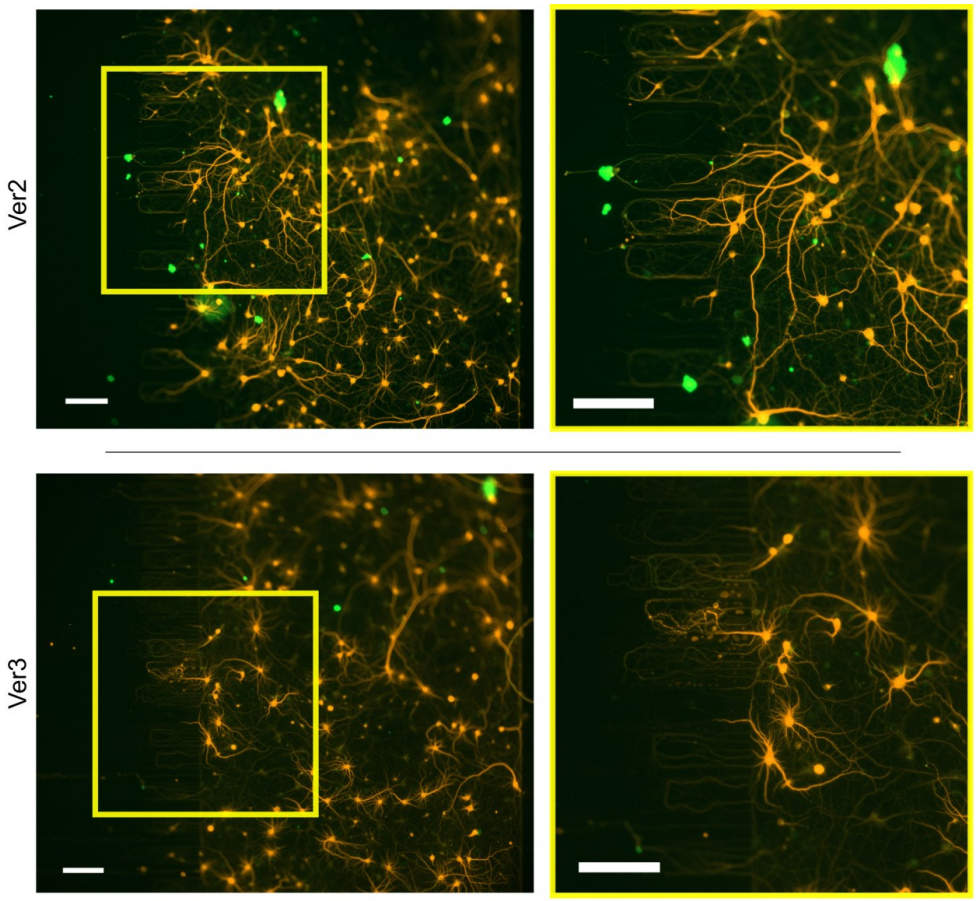

Figure 4.18 – Fluorescence micrographs of immunostained cortical neurons at DIV 23 after removal of microfluidic devices. Sample Ver2 and Ver3; original image (left) and magnified square-labeled area of trap shapes occupied by axons (right). Immunostaining: MAP2 (orange) and NFH (green). Scale bars: 200 µm.

4.3 Conclusions and Outlook

Two major challenges were addressed in this chapter: (1) successful cell culture development and maintenance in a closed comp-µFluidic system, and (2) design modification to improve unidirectional axon growth in the connecting microchannels. After a thorough examination of the possible difficulties causing the unequal distribution of cells in the cell chambers, several approaches have been considered. The primarily proposed **additional** and **wider** chambers offer a limited solution (see section 4.1.2.2) but significantly alter the original comp-µFluidic design. Thus, a more technical approach was considered with the goal of maintaining the original closed design of a device. A specific cell seeding procedure was developed and selected as the most optimal solution to the problem at hand. This gave me the opportunity to further investigate the internal microfluidic structure modifications to improve the unidirectionality of the device. Axonal growth was observed in two sets of shape designs called **Axon-Guiding** and **Axon-Trap** shapes. The focus of these modifications (explained in sections 4.2.1 and 4.2.2) was to create a microenvironment that would successfully guide axons in the desired direction and prevent axons from the opposite compartment from reaching the microchannels. The shapes of the axon traps showed a better potential in dealing with the described task, with the Ver2 design giving the quantitatively best results compared to the control and the Ver3 design, in the sets of samples observed. The limitations of using immunocytochemistry techniques in closed microfluidic systems made it difficult to fully evaluate the efficacy of the proposed structures. Further investigation in this direction would provide more clarity on the exact differences between Ver2 and Ver3 trap shapes.

Chapter 5

Neuronal Extracellular Activity Measurements in Comp-µFluidic-MEA Hybrid System

Implementation of a comp-µFluidic device with a microelectrode array enables a new level of possibilities when it comes to investigation of *in vitro* neuronal networks. The structure of comp-µFluidics provides a controllable microenvironment for cell culture development and growth, while an MEA serves as a means of detecting the spontaneous or induced activity of neurons. The confined space of microchannels creates a high resistance that causes the amplification of detected extracellular action potentials traveling along the axon. The basis of recording configuration and data processing is discussed in the first section of this chapter (see section 5.1), followed by the results of the obtained recordings in different comp-µFluidic-MEA devices with variation in microchannel lengths and device assembly procedures. The points of interest I focused on were: **(1)** analysis of spike shapes occurring at different days of recording and the position along the microchannel (see section 5.2); **(2)** the amplification effect caused by the confined microchannel space (see section 5.3); **(3)** signal propagation velocities observed in proposed devices (see section 5.4).

5.1 Detection of Axonal Action Potentials Within Microchannels

5.1.1 Recording Configuration of In Vitro Experiments

The BioMAS configuration for recording neuronal activity is shown in Figure 2.8 and described in detail in section 2.4.1. In an iMEA200 layout, electrodes are arranged in an 8×8 grid with 200 µm interelectrode spacing. Centrally structured microchannels divide the MEA into left (*L*-) and right (*R*-) compartments. Electrically functionalized microchannels contain two, four or six electrodes each, depending on the microchannel length used for a given device – SHORT, MEDIUM and LONG, respectively (see section 3.1.1, Figure 3.1). In the case of a 16×4 electrode grid in the r16MEA layout, all microchannels are electrically active, with four recording electrodes per microchannel (see section 3.1.1, Figure 3.2). As described in section 4.1.3, axon extension is expected to be from receiving to emitting side of the asymmetric axon-diode microchannel structure that connect left and right µFluidic compartments. Due to the microchannel amplification effect (see section 1.3.3 and results discussed in the upcoming section 5.3), recordings from electrodes within microchannels are characterized by a good SNR while recordings from electrodes located in cell body compartments rarely show any visible activity. This is mainly due to the poor sealing resistance between the cells and the recording interface, as well as the nature of cell distribution and density in each individual cell culture.

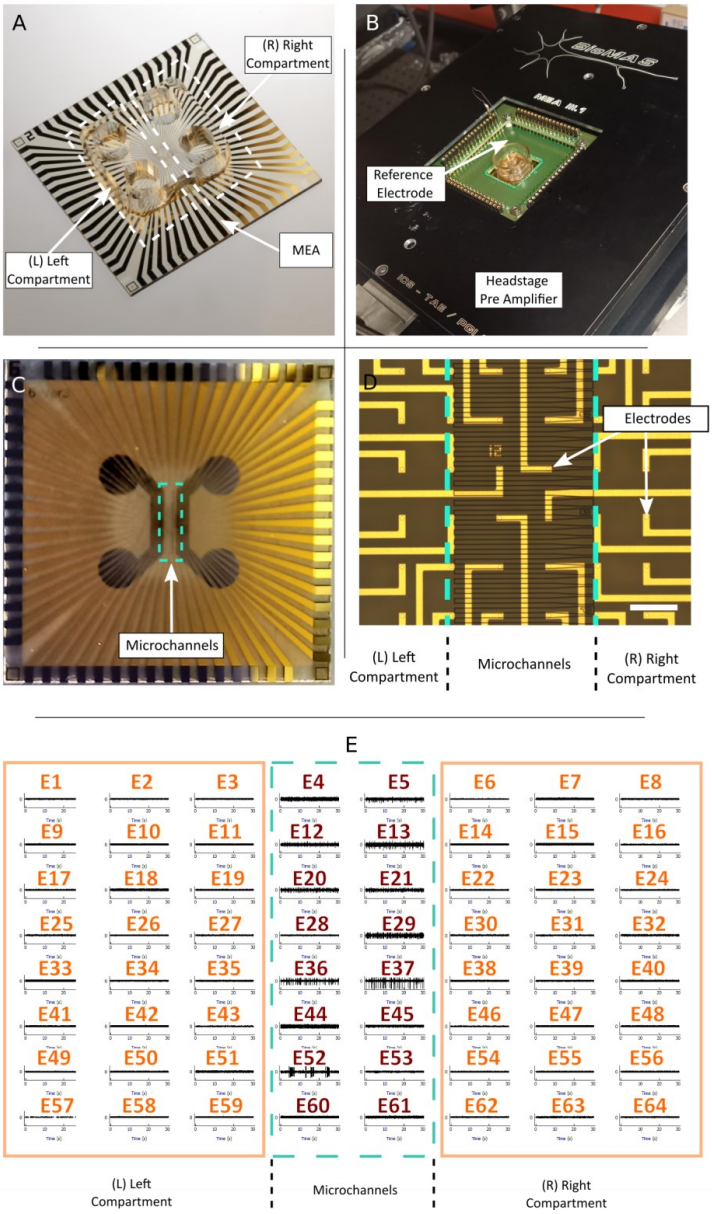

Figure 5.1 – Configuration of a recording device and signals recorded from an MEA structured with short microchannels on top. (A) A comp-µFluidic-MEA hybrid device. **(B)** A device configured in a preamplifier headstage, together with an Ag/AgCl reference electrode placed in one of the chambers. **(C)** The left and right compartments are interconnected by asymmetric axon-diode microchannels. **(D)** A recording area of an MEA with 64 electrodes, arranged in an 8 × 8 grid and 200 µm apart. Each electrically active microchannel contains two electrodes. **(E)** The electrophysiological activity recorded with BioMAS. Electrodes are labeled by numbers. Scale bar: 200 µm.

Cortical and striatal embryonic neurons are cultured in the comp-µFluidic-MEA hybrid system as previously described in section 4.1.2.3. Neurons are cultured and grown to maturity at an approximate density of 1500 cells/mm^2. Spontaneous network activity typically occurs after DIV 14 and has been successfully maintained until DIV 35 in some samples. Recordings are performed from DIV 14, DIV 21, and depending on cell culture, DIV 25, 28, 29, and 35. Measurements are performed at 10 and 50 kHz sampling rates, depending on the desired analysis of a given measurement. For spike shape analysis, a 10 kHz sampling rate was sufficient to obtain data for further analysis. In the case of calculating signal propagation velocities, it was necessary to use a 50 kHz sampling rate to ensure good temporal resolution of a recording.

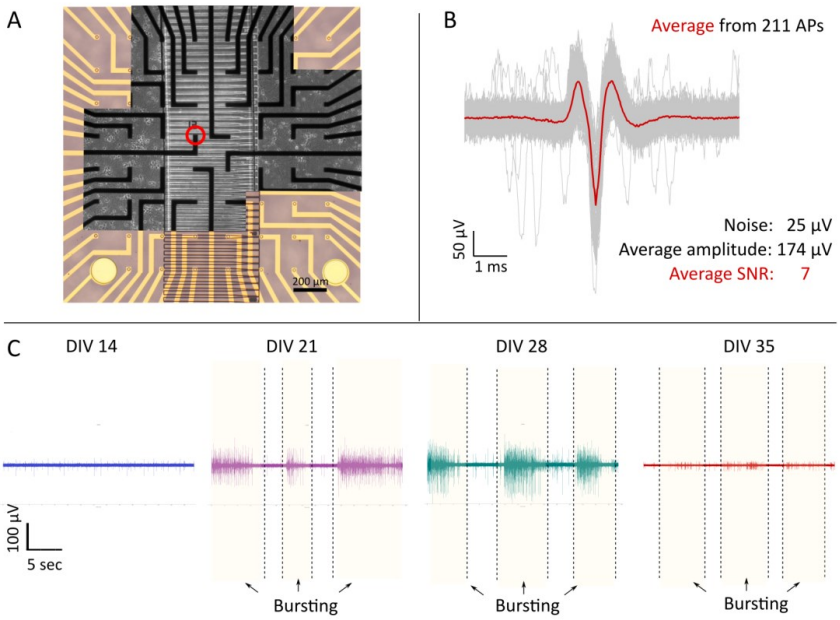

Figure 5.2 – Spontaneous activity recording in a cortico-striatal co-culture. (A) Phase-contrast micrographs of a cortico-striatal co-culture at DIV 14 connected by short axon-diode microchannels. Images are combined with an MEA for easier orientation. The red circle shows electrode E28, which recorded axonal EAPs. **(B)** The averaged EAP (red) from 211 individual EAPs (gray) recorded at E28. **(C)** Time traces of neuronal recordings at different stages of culture maturity. Characteristic bursting activity is evident from DIV 21.

Co-culture connectivity was established from DIV 14 and fully developed by DIV 21. This was confirmed by recording EAPs within the microchannels and synchronous bursting patterns (Figure 5.2 (C)). Figure 5.3 shows the positions of the electrically active microchannels. The electrode numbering corresponds to the numbering used for an 8×8 grid MEA, but in the

following text this will be simplified by referring to the number of observed electrically active microchannel (row). A raster plot (Figure 5.3, right) shows the electrophysiological activity of the cortico-striatal co-culture seeded in an **ir**reversibly **b**onded (**IRB**) device with short microchannels.

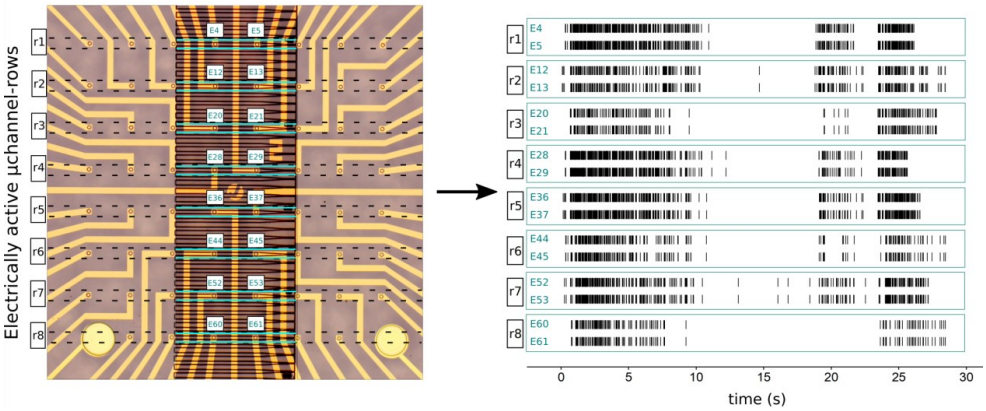

Figure 5.3 – Raster plot example of a developing co-culture in an IRB device at DIV 21. MEA sketch (on the left) with highlighted electrically active microchannels (in turquoise solid lines) containing two electrodes from each electrode row. Row numbers are shown with the prefix **"r"**; electrode numbering starts with the prefix **"E"** and corresponds to the 8 × 8 grid MEA numbering. Example of a raster plot (on the right) with data sets grouped in two by two in each electrically active microchannel.

Detailed raster plots are presented in Figure 5.4. Each plot shows consecutive 30 second recordings. At DIV 14, recording was possible in six out of eight microchannels. The lack of synchronicity of the occurring EAPs indicates that the connectivity in the whole cell culture is not yet strong. At DIV 21, bursting activity with high synchronicity is present on different time scales within all eight electrically active microchannels, suggesting a well-established connection between the two chambers. Continuous connectivity is present in the co-culture until DIV 35. As the cells age, the bursting activity gradually decreases its synchronicity through the developed network. At DIV 35, there is also the first decrease in the number of active microchannels, indicating progressive cell death and loss of network connectivity.

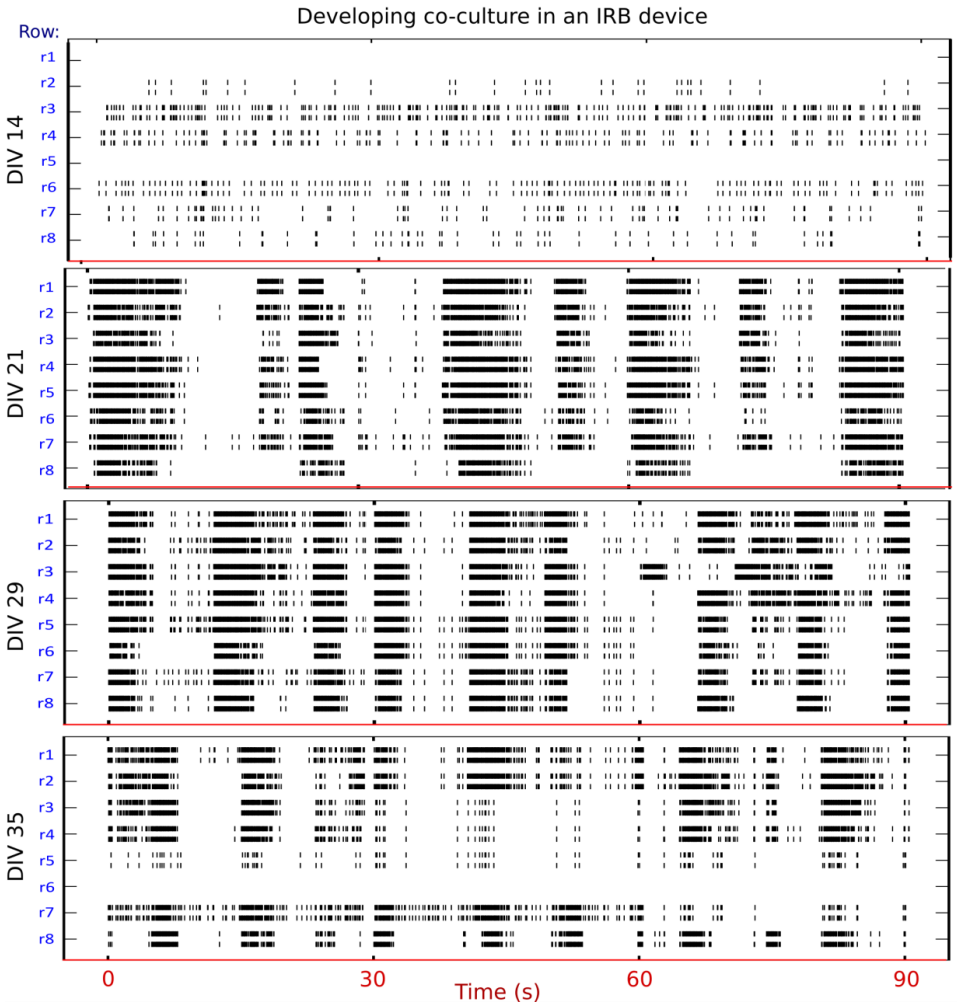

Figure 5.4 – **Raster plot of a cortico-striatal co-culture. DIV 14** shows a gradual development of co-culture connectivity that matures at **DIV 21** with synchronous patterns among microchannels in several different timescales. Maturing co-culture gradually loses bursting synchronicity. The connectivity of the chambers shows electrophysiological activity until DIV 35. Synchronous bursting is still present at various time scales at **DIV 29**, while its decrease is more visible and prominent at **DIV 35**.

5.1.2 Spontaneous Activity Confirms That Co-Culture is Connected

To confirm chamber connectivity, network synchrony was measured. The network spike rate was estimated from a sum of binary spike trains convolved by Gaussian kernel with a width of 3 s and a standard deviation of 0.5 s. Convolution of the summed binary traces allows the generation of a smooth collective trace for cleaner network profile estimates. Network burst peaks were identified from the convolved network rate trace using a soft prominence threshold of median + standard deviation (Figure 5.5 (B)).

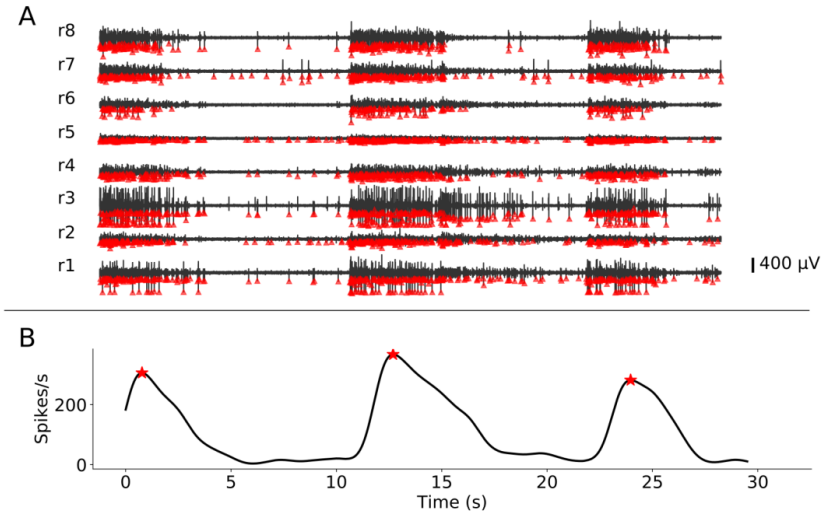

Figure 5.5 – Synchronous bursting between electrically active microchannels at DIV 29 confirms the connectivity of the two culture compartments. (A) Time trace of burst activity in separate rows recorded at the same electrode position. **(B)** Convolution of the merged binary traces with burst peaks marked with a red star.

Because of the expected predominant forward directionality, it is assumed that the axonal spike synchrony reflects the synchronization of the left (parent) subcompartment and therefore does not depend on the length of the microchannel. Therefore, the data sets for different microchannel lengths of a total of 9 cultures were pooled to evaluate the overall culture synchrony and its maturation over time. Figure 5.6 compares the bursting activity of each analyzed culture over time. The overall burst rate of less than 0.1 Hz falls into the category of slow oscillations well documented for homogeneous *in vitro* networks (Neske, 2016). This suggests that local morphological separation of microchannels does not alter the synchronization of the network.

The generation and persistence of propagating burst patterns suggest that two subcompartments were directly connected and synchronized, as the signal would not persist without connections. In addition, the burst rate and the maximum within-burst rate followed a course similar to that of homogeneous cultures sampled by MEAs (Chiappalone et al., 2006). Starting with relatively sparse activity (Figure 5.4), the network progressed into the bursting regime, peaking at DIV 29, followed by a decrease in both burst rates and within-burst spiking at DIV 35 (Figure 5.6). The increase in within-burst rate in the 14-29 DIV range may be due to both increased synchrony between channels, as burst peaks become more defined, and increased firing rates within channels, likely due to the engagement of multiple neurons as they are recruited into the synchrony of the network. The final decrease in burst rate and maximum burst frequency marks the peak of network maturation through plasticity processes such as synaptic pruning (Faust et al., 2021; Antonello et al., 2022). Overall, the results suggest that the network follows similar maturation patterns, indicating the non-invasiveness of the proposed comp-µFluidic-MEA hybrid construct to pursue questions in the context of co-culture networks.

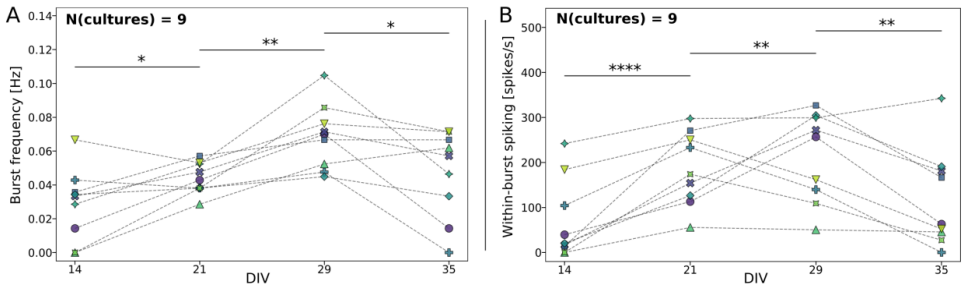

Figure 5.6 – Synchronization of subcompartments observed by bursting frequencies. (A) Bursting frequencies over time analyzed in a total of nine cultures. The bursting rate of <0.1Hz oscillates through divided DIV measurements with a similar pattern in all analyzed samples. Peak bursting rate is detected at DIV 29. Paired t-test: $p_{(DIV14/DIV21)}$ = 0.0260; $p_{(DIV21/DIV29)}$ = 0.0033; $p_{(DIV29/DIV35)}$ = 0.0317 **(B)** The within-burst bursting rate increases during the first four weeks of culture maturation, followed by a decline detected at DIV 35, representing a fading activity in overmature culture. Paired t-test: $p_{(DIV14/DIV21)}$ = 0.0007; $p_{(DIV21/DIV29)}$ = 0.0081; $p_{(DIV29/DIV35)}$ = 0.0050.

5.2 Analysis of Extracellular Action Potential (EAP) Footprint Shapes

Electrophysiological recordings were analyzed in two different comp-µFluidic-MEA systems: **(1)** MEA devices with axon-diode microchannels of different lengths (short, medium, and long) and **(2)** r16MEA devices with a total of 16 axon-diode microchannels and a fixed medium microchannel length. Each of these categories was observed under two conditions with respect to the assembly method of the final device: **(a)** **r**eversible **b**onding (**RB**), and **(b)** **ir**reversible APTES **b**onding (**IRB**), between the MEA surface and the PDMS microfluidics on top. The reason for this variation is the expectation of better sealing of cells in the case of IRB samples, which could potentially result in a different variance in spike shape occurrence and distribution along the microchannel. Data was collected from several separate samples on different DIVs, starting from DIV 14 to DIV 29. The distribution and occurrence of shapes were observed in the total number of electrodes showing recorded neuronal activity. It is important to note that spontaneous activity was not observed in all electrically active microchannels, so the number of electrodes observed may vary from sample to sample. However, this variation is not significantly different, so I decided to consider them as comparable.

5.2.1 EAP Shape Templates for Spike Classification Analysis

5.4.3.1 Typical shapes of extracellular action potentials

Unlike intracellularly recorded action potentials, extracellular recordings occur in a variety and complexity of spike shapes. A commonly observed feature of extracellularly recorded signals is the appearance of a prominent negative peak. The full shape can vary from **monophasic**, **diphasic**, **triphasic** to more complex **multiphasic**. This has been observed in many *in vivo* studies (Anastassiou et al., 2015; Trainito et al., 2019; Sun et al., 2021). However, due to the difference in recording methodology, findings from these types of studies are not applicable to the analysis in 2D neuronal extracellular recordings.

In vitro extracellularly recorded action potentials were not fully understood and thoroughly characterized until the publication by Hierlemann's group in 2015 (Lewandowska et al., 2015). Most previous publications were limited in resolution for closer analysis of spike waveforms

due to the number and size of channels or recording electrodes, until Lewandowska et al. implemented complementary metal-oxide-semiconductor (CMOS)-based high-density MEAs (HDMEAs) in combination with a compartmentalized microfluidic device containing microchannels for axonal isolation and extracellular recording. Their publication presents, for the first time, a complete overview of the action potential waveform evolution along the microchannel, as well as during culture development, recorded from the unmyelinated axons of cortical neurons derived from primary rat neurons. The exact nature of the experimentally observed EAPs is still not fully understood, except for the previously reported clear distinction between spike shapes originating from the soma and axonal compartments (Lewandowska et al., 2015; Deligkaris et al., 2016). Since all my electrophysiological experiments are performed on rat primary cortical neurons, I found their publications crucial to validate the results and experiments presented in this thesis.

According to their thorough investigation of EAPs recorded with HDMEAs, both groups describe **somatic EAPs** as broad monophasic or broad biphasic shape with a predominantly negative first peak followed by a smaller positive peak. The typical shape of **axonal EAPs** is shown to be *triphasic* with the larger positive peak before the main negative peak, or a narrow symmetrical triphasic shape (Deligkaris et al., 2016). Lewandowska et al. additionally attribute a *bi-/triphasic axonal signal* consisting of a large positive peak followed by a large negative peak, and in some cases a third much smaller positive peak. In addition to their study, they investigate the origins of more complicated waveforms that occur in older cultures and show that they appear to be a combination of two or more individual signals from different axons. The typical axonal action potential waveforms described have also been recognized in recordings from my experimental setup. Somatic-like shapes were occasionally recorded inside and outside the microchannels, but without a more thorough investigation of the EAP origins it is not possible to claim that these spikes are certainly somatic. The remainder of the commonly occurring waveforms correspond closely to findings cited in the aforementioned literature.

5.4.3.2 Spike Shape Templates for Classification of Recorded Action Potentials

I divided the prototype waveforms into a total of six separate shape types (Figure 5.7). ***Type 1*** (**T1**) *biphasic shape* closely resembles previously reported extracellular **somatic** EAPs. ***Type 2*** (**T2**) and ***type 3*** (**T3**) are described as axonal EAPs in a study by Lewandowska, where the positive and negative phases have similar amplitude values, and the negative phase is sometimes followed by a very small third positive spike. In the following text, both types will be referred to as **biphasic** shape. The following three variations of the **triphasic shape** are what are commonly reported as classic neuritic EAPs. They consist of sharp and prominent negative phases accompanied by **symmetrical** positive phases in ***type 4*** (**T4**), or **asymmetrical** positive phases found in ***type 5*** (**T5**) and ***type 6*** (**T6**). The occurrence of *somatic-like* spike shapes (T1) cannot be fully understood and explained from the available data sets and methods used in the presented experiments. Therefore, it is necessary to consider the possibility that the characterization of this type of shape as purely somatic may be wrong. They are reminiscent

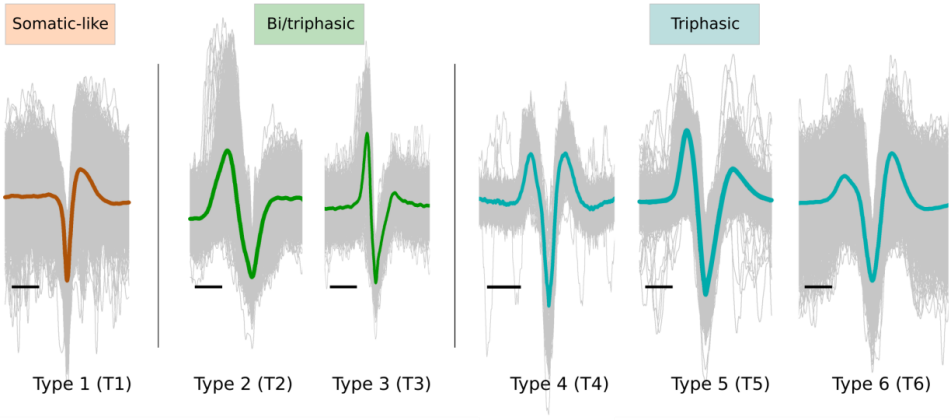

Figure 5.7 – Typical shapes of axonal extracellular action potentials. The biphasic shape *Type 1* (**T1**) is similar to what is assumed to be the somatic EAP shape, although this shape has been observed in microchannels. *Types 2* **(T2)** and *Type 3* (**T3**) are bi/triphasic shapes with similar amplitude values of the (first) positive and negative phases. More typical triphasic shapes, distinguished by a very prominent negative phase and symmetric or asymmetric positive phases, are *Type 4* **(T4)**, *Type 5* **(T5)** *and Type 6* **(T6)**, respectively. Scale bar: 1 ms.

by shape characteristics of previously reported EAPs derived from soma, but somas are less likely to occur in small confined spaces of microchannels. Further investigation would provide a clearer picture of the origin of this shape type. However, in future text, the characterized shape type will be reffered to as **somatic-like** spike shape.

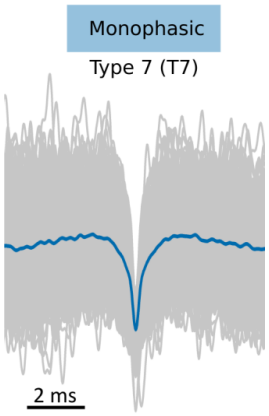

Figure 5.8 – Monophasic *Type 7* (T7) shape detected by Peak-finder algorithm.

Besides the most common extracellular spike shapes known from the literature, a more specific spike shape has caught my attention. Its occurrence happens to be very specifically positioned near the receiving or emitting side of the microchannels. This signal could only be detected by the peak-finder algorithm (see sections 2.4.3 and the following 5.2.2). Being monophasic in shape and relatively small in peak-to-peak amplitude, none of the proposed shape type templates correspond to a successful match. Therefore, I decided to recognize it as a separate, seventh monophasic shape type (Figure 5.8), in further text designated as **monophasic *type 7*** (**T7**).

Finally, all detected action potentials with more than three phases and/or more complex shapes are grouped into **complex** shape type or ***type 8*** **(T8)**, with some examples shown in Figure 5.9.

Similar complex shapes were also reported by Lewandovska et al. (2015) and explained as the result of superposition of different action potentials recorded from the same electrode. The origin of the superpositioned spikes is not easy to deduce, but some understanding can be gained by assuming the simultaneous excitation of different neuronal cells.

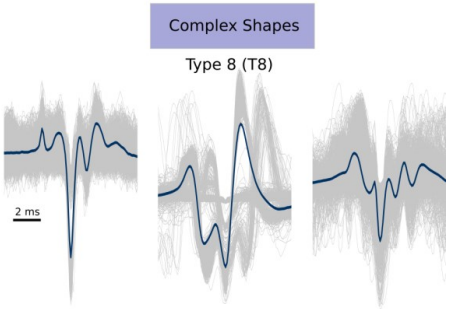

Figure 5.9 – Complex shapes, referred to as *Type 8* (T8) detected by the Peak-Finder algorithm. The origins of these complex spike shapes can occur as a superposition of different spike shapes detected by the same electrode. Scale bar: 2 ms.

5.2.2 Data Processing for Spike Detection and Shape Classification

For a comprehensive analysis and classification of waveform shapes, data for each microchannel length were observed separately on each DIV. The analysis is based on spontaneous neuronal activity only, as no stimulation was applied. Due to the complexity of implementing spike sorting algorithms on recordings from non-commercial recording devices, I decided to simplify the approach in a reasonable way. The analysis pipeline was discussed with and developed by a colleague PhD student, Bogdana Čepkenović. The identification and classification of spike shapes is performed as follows:

1) First, the raw electrode data are processed with band-pass filtering (100-4000 Hz). The criterion for identifying spikes in the filtered data is the detection of events with negative peak height greater than four or five times the standard deviation of the trace median. The spike width criterion is set to a duration of 0.5 ms, and spikes were considered as isolated firing events if they were separated by at least 2 ms window.

2) Recordings are viewed sequentially along each microchannel with the expectation of detecting propagating EAPs originating from the same axon. The electrode with the most spikes found was considered as a reference. To ensure spike correlation between consecutive electrodes, the custom-built algorithm identifies spikes in surrounding electrodes as the closest corresponding spikes in the [-10, +10] ms time window around the reference electrode's spike.

3) The Peak-Finder algorithm then combines all the waveforms found from each electrode individually and aligns their waveforms around the global minimum of the signal. The average waveform is a **spike-triggered average footprint** (**STA;** intoduced by Deligkaris et al., in 2016.)

4) These STA footprints (Figure 5.10 (D)) are further manually compared with the EAP shape templates described in the section above and classified into corresponding shape types.

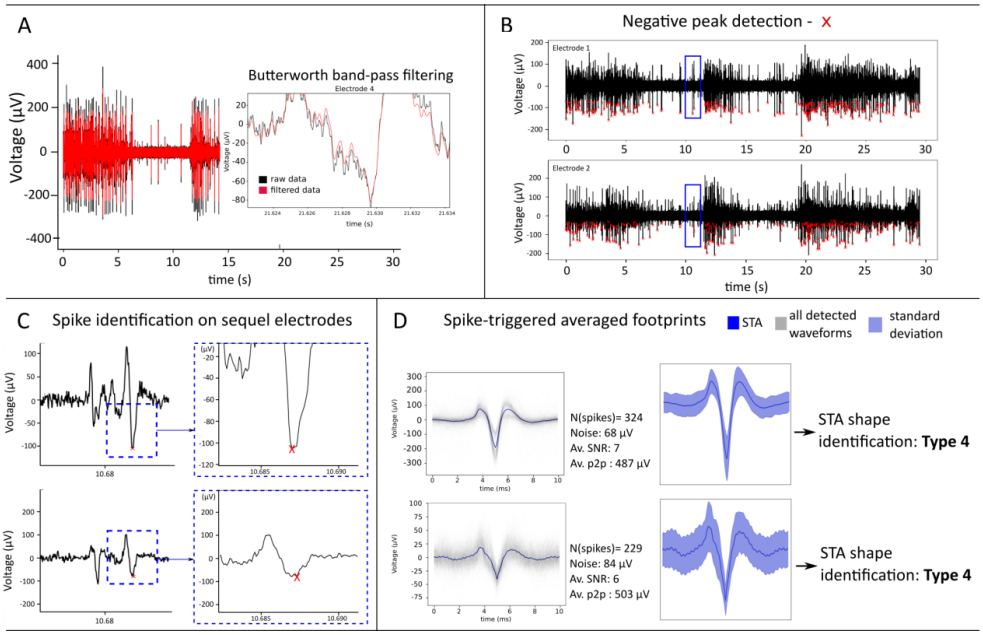

Figure 5.10 – **Data processing workflow for EAP detection and spike shape sorting analysis. (A)** Raw data is filtered by a Butterworth band-pass filter with 100 Hz low and 4 kHz high cut frequencies. **(B)** A custom written Python algorithm detects peaks according to a specified order of criteria. **(C)** An electrode with the highest number of detected peaks serves as a reference electrode for peak detection in adjacent electrodes. **(D)** Detected waveforms are aligned to the negative peak and an STA (spike triggered average) footprint is generated for each recording electrode.

However, the approach described has some disadvantages and limitations that should be considered when interpreting the results. One of the most prominent limitations is that the algorithm yields only one STA footprint per electrode, which is often a great simplification of the actual reality. Due to the relatively large cross-sectional area (45-90 µm^2), it is reasonable to expect that more than one axon may grow through the microchannel. This is expected also according to previously reported findings from Wang et al. in 2012 when they showed that the cross-section area of 12 µm^2 can be occupied by at least 12 axons. Their measurements of microchannel resistivity before and after cell culture showed maximum of 7 units recorded, with a typical axonal diameter of 0.2-0.5 µm (Bartlett and Banker, 1984; Shepherd and Harris, 1998; Jinno et al., 2007). In my experimental setup, this is also suggested by the complexity of some recordings, where several different shapes are detected on the time trace of the same electrode. Thus, the algorithm is blind to a number of simultaneously recorded EAPs and limits the result to the spike shape that corresponds to the most common spikes on the reference electrode. However, this simplification is still acceptable for studying trends along the

microchannel. One of the advantages of the applied method lies precisely in this approach to spike identification along the microchannels. Namely, in recordings where the SNR is lower than 4, it is difficult to identify real spikes without the algorithm that recognizes them according to the recordings on a referent electrode. A single criterion with a threshold of 5 × STDEV of the background noise would filter out these spikes without detection. Changing the criterion to a lower multiplication of STDEV than 4 or 5 results in defining false spikes from the noise. Therefore, the only way to detect spikes in these recordings is to use the spike-triggered averaging method.

5.2.3 Distribution of STA Footprints along Microchannels

To classify the spikes, the STA footprints were matched to previously defined spike shape templates. As reported in a study by Lewandowska et al. (2015), the shapes of the spikes tend to change along the microchannel length. The following two subsections analyze the distribution of evaluated STA footprints on electrode positions along microchannels.

5.2.3.1 Along Axon Diode microchannels of Different Lengths

A detailed description of the device designs used in this part is given in section 3.1.1. The MEA layout of an 8 × 8 grid of electrodes combined with microchannels of different lengths results in a total of eight electrically active microchannels with two, four or six electrodes in each of these microchannels. Two different types of device assembly were used in this work: reversible (RB) and irreversible (IRB), as previously described in section 3.2.3. Samples were divided into groups based on microchannel length and device assembly method. The number of samples in each group varied due to the unpredictable success of maintaining cultured cells. To quantify and compare the difference between groups, I measure the success of each sample in the experiment by the final *activity yield* of a device, which is the percentage of electrically active microchannels that recorded axonal action potentials. This measure is compared between RB and IRB samples in each microchannel length group across DIVs when experiments took place. In Table 5.1 I provide a detailed overview of all samples included in further analysis. The total number of electrically functional microchannels is calculated by multiplying the number of MEAs by eight, which is the same number of electrode rows in each sample. As shown, the

most obvious difference appears between RB and IRB samples in each microchannel length group. In each group, IRB samples have much higher activity yield during the whole cell culture maintenance. It should be noted that the number of MEAs used is not the same between samples. However, the difference of one MEA in each observed comparison does not have a significant effect on the final yield differences, as the yield in IRB samples would remain higher even if the total number of RB active microchannels were scaled to the same number of MEAs. This suggests that the IRB samples showed a more compact usability of each device, while the RB samples made it more difficult to maintain the stability of the neuronal network through microchannels. Over time, the activity yield gradually decreased in all samples. This is expected as the culture ages and cells overcrowd the culture space, reducing the viability of the established networks. Cell culture in IRB samples was successfully maintained and recorded until DIV 35, while only one RB sample (long µchannels) showed spontaneous activity until DIV 30. These initial observations suggest that the difference in assembly method may have an impact on the shape of recorded signals, which I will observe in more detail in the following sections.

Sample specifications			Activity yield of recording microchannels					
µChannel length	N(MEAs)	Device assembly	DIV14	DIV21	DIV28	DIV29	DIV30	DIV35
long (L)	4	RB	78%	50%	41%	×	25%	×
	3	IRB	92%	79%	×	79%	×	67%
medium (M)	5	RB	53%	20%	×	×	×	×
	4	IRB	81%	75%	×	72%	×	59%
short (S)	4	RB	53%	72%	28%	×	×	×
	3	IRB	88%	100%	×	88%	×	71%

Table 5.1 – Activity yield of recording microchannels. The comparison of activities between samples is presented as the percentage of electrically functional microchannels actively recording over time. A different number of MEAs is observed for each sample. Samples are grouped according to microchannel length and device assembly procedure. In all microchannel lengths, IRB samples show the highest success rate of activity over time, with maximum activity yield of 100 % in three IRB comp-µFluidic-MEA devices with short microchannels at DIV 21, and with all three lengths recording up to DIV 35.

Effect of Device Assembly Approach on Spike Shape Occurrence

In this section, I will observe the effects of assembly approach on the occurrence of spike shape in axon diode microchannels. As described in the previous section 3.2.3, reversible (RB) and irreversible (IRB) methods were introduced to find the most optimal approach to assemble the final comp-µFluidic-MEA device. The reversible binding is suitable to ensure the reusability of MEAs, while the irreversible APTES bonding provides a more robust system with potentially improved cell-electrode coupling.

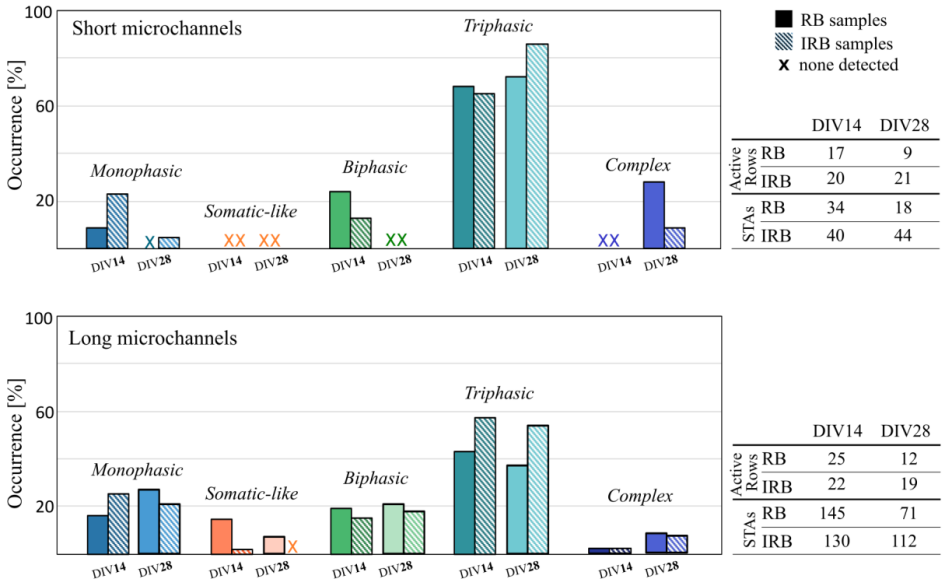

		DIV14	DIV28
Active Rows	RB	17	9
	IRB	20	21
STAs	RB	34	18
	IRB	40	44

		DIV14	DIV28
Active Rows	RB	25	12
	IRB	22	19
STAs	RB	145	71
	IRB	130	112

Figure 5.11 – STA waveform trends occurring in short and long microchannels detected on DIV 14 and 28 in reversibly (RB) and irreversibly (IRB) assembled devices. Each spike shape is compared at DIV 14 and 28, in short (top bar plot) and long (bottom bar plot) microchannels. Tables on the right show the exact number of active microchannel rows that were recorded and the total number of STAs taken for data analysis.

To observe the change in spike shape occurrence, I compare the percentage of each spike shape on DIV 14 and DIV 28. Figure 5.11 shows a comparison of detected spikes in RB and IRB devices in short and long microchannels. Each set of observed samples had a different number of STA footprints that were considered for analysis due to the variation of electrically active microchannels (rows) recording EAPs. An additional table in Figure 5.11 gives a numeric overview of analyzed STAs in each group of samples. There is a noticeable decrease in the number of detected STAs in both sets of RB samples over time, while the detection of STAs increases slightly in both IRB samples. The occurrence of the *triphasic shape* is most prominent

in both data sets, while the other shapes occur more frequently along long microchannels. The highest occurrence of triphasic shape is also expected, as these are the most common shapes occurring in extracellular axonal recordings reported in previous studies (Lewandowska et al., 2015). *Biphasic shapes* fall into the same category as previously reported extracellular axon signals. However, their occurrence changes only slightly over time in long microchannels (~20%). The same shape is present only at DIV 14 when recorded with short microchannels. The reason for this difference may lie in the length of the microchannel and the maturity of the axon, resulting in a specific spike shape depending on the axon segment captured by the recording electrode inside the microchannel. Another interesting observation is a trend in the occurrence of *monophasic spike shape*. It is more frequent in long microchannels, up to 22% in RB samples at DIV 28, while its occurrence is less than 10% in short microchannels in the RB samples. A more detailed overview of this phenomenon will be discussed in the following section.

The total occurrence of spike shapes in the IRB samples is shown in Figure 5.12. Activity was recorded on four days: DIV 14, 21, 29, and 35. The number of samples observed remained constant over time, with variations in activity yield as described in Table 5.1. All three microchannel lengths recorded the vast majority of triphasic spike shapes regardless of the maturity of the cell culture. The monophasic shape was present in all three samples at DIV 14. The frequency of this shape decreased and remained low in the short and medium microchannel lengths, while in the long microchannel it occurred ~20% of the time even in older cultures. A more detailed analysis of its occurrence in these samples is discussed in the following sections. Somatic-like shapes were not detected or were detected less than 6 % of the time. Complex shapes were detected less than 10% of the time, except in the case of medium length microchannels at DIV 35 (20%). The biphasic shape marked with green bars is a common axonal spike shape, interestingly detected less often in short microchannels.

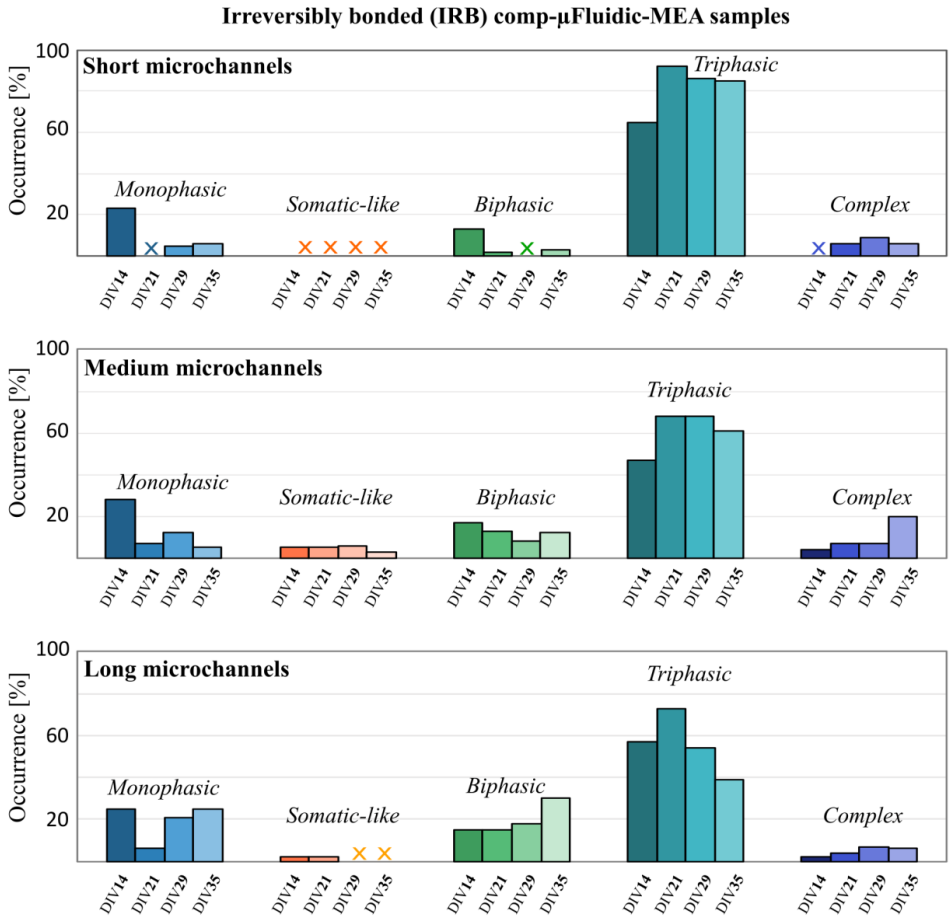

Figure 5.12 – STA waveforms occurring trends over time in irreversibly assembled devices (IRB) of short, medium, and long microchannels. The trend was followed from DIV 14 to DIV 35. All three microchannels recorded the highest number of triphasic shaped spikes and the lowest number of somatic-like spikes.

Observing the distribution of spike shapes along the microchannels

Having obtained a general picture of the overall occurrence of each spike shape, I am interested in describing their distribution along the microchannels as a function of recording electrode positions. The MEA layout with an 8 × 8 electrode grid is already described in section 3.1.1, with different microchannel lengths covering a sequence of electrodes in each row. The electrode position numbers are considered along a grid line from E1 to E8, with different positions covered by each of the microchannel lengths.

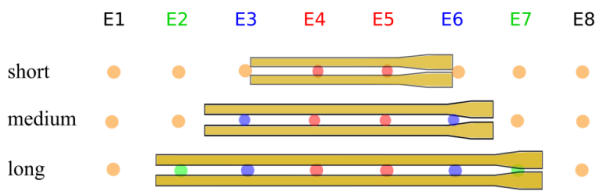

Figure 5.13 – Electrode numbering along the electrically active microchannels. The numbering corresponds to the iMEA200 with an 8 × 8 grid electrode layout. Electrodes within microchannels are colored to guide the eye to the appropriate electrode numbering.

Figure 5.13 illustrates the position of the electrodes along the electrically active microchannels of different lengths. This numbering is used throughout the text to describe trends in spike shape.

Spike Shapes along Long Microchannels

For a more detailed overview of the spike shape distribution, I observed each recorded DIV separately with paired RB and IRB samples. In Figure 5.14 I present results from DIV 14 and DIV 21, while the full overview of their occurrence on each DIV (14-35) is given in additional Figure C.1 . A total of four RB and three IRB devices were tracked in this experiment.

An approximation of the spike shape evolution along the microchannels must be taken with caution due to the limited and different number of recorded STAs on each observed DIV (see Table 5.1 for the microchannel activity yield in each sample and DIV). At DIV 14, the cell culture is not yet fully mature, but the first activity can be detected. It is interesting to note a slight difference between two types of assembly even at this early stage of cell culture development (Figure 5.14, top stacked bar plots). Namely, there is a higher occurrence of somatic-like waveforms in RB samples (total 14% (RB) vs. 2% (IRB)), while monophasic waveforms are more frequent in IRB samples (total 25% (IRB) vs. 16% (RB)). Only one week later, at DIV 21, there is a significant change in the distribution of shapes in these two samples (Figure 5.14, bottom stacked bar plots). The monophasic shape represents 29% of all recorded STAs in the RB samples and only 6% in the IRB samples. At the same time, the triphasic shape occurs only 38% of the time in RB and more frequently 73% of the time in IRB samples.

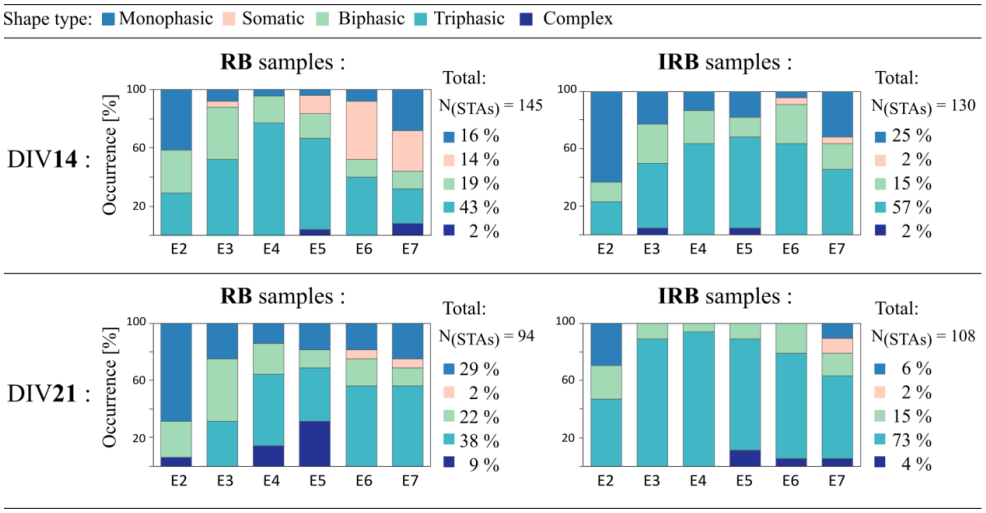

Figure 5.14 – Percentage occurrence and distribution of EAP spike shapes along the long microchannels. Analysis in reversibly (RB) and irreversibly (IRB) binding MEA-microfluidics device assemblies on DIV 14 (top stacked bar plots) and DIV 21 (bottom stacked bar plots). Electrode numbering corresponds to electrode positions found within the observed microchannel length. Spike shape legend is at the top of the figure.

One of the most obvious differences between the two groups is the distribution and occurrence of the monophasic (T7) shape. In the case of RB devices, STAs footprints corresponding to this shape were found at every electrode position within the microchannel, with a total occurrence of 29%, while the IRB devices recorded this type of shape only at E2 and E7, positions found at each end of the microchannel, with a total occurrence of only 6%. Triphasic shapes also show a marked difference depending on the assembly strategy. Electrodes within RB samples recorded 38% of triphasic spike shapes, while IRB samples recorded a total of 73% of triphasic spike shapes. On the other hand, the occurrence of somatic (T1) and complex (T8) types is approximately equal and very low regardless of the device binding type.

Spike Shape Evolution Trend in Single Long Microchannel

The microchannel system itself provides a unique environment in each sample observed, with the possibility of containing multiple axons. The cell culture density may also vary from sample to sample, making it more difficult to get a consistent picture and expectation of spike shape evolution over time at each electrode position. A similar observation has already been

reported by (Pan et al., 2012) where they observe that axons initially tend to grow first along the edges of microchannels and then fill the central area of the tunnel. They use this pattern of axonal growth to explain differences in spike shapes, the recording of multiple axons at the same electrode, or why sometimes no signal is recorded. The ability to examine recordings in individual microchannels also provides valuable insight into spike evolution trends. Figure 5.15 shows an example of an electrically active microchannel in RB and IRB samples that successfully recorded axonal activity. Spike shape evolution is observed along six adjacent electrodes over 30 DIVs for RB and 35 DIVs for IRB samples.

In contrast to the observations of Hierlermann's group (Lewandowska et al., 2015), spikes in **RB sample** on the first day of recording (shown in Figure 5.15 (B), at DIV 14) do not have identical shapes, but rather differ from each other at almost all electrode positions. The first recording electrode E2 records a small amplitude monophasic shape that changes to a triphasic shape in the following three electrodes (E3: *Type 5*; E4: *Type 4*; E5: *Type 4*). The STA shape at the electrode E6 resembles a somatic-like spike shape (*Type 1*), although it can be speculated whether the electrode at this distance from the exit could record a somatic EAP. From the available data, it is difficult to make this assumption with certainty, so the interpretation of this spike shape should be taken with caution. The last electrode position E7, located in the narrowing part of the microchannel, records a "classical" axonal asymmetric triphasic shape with a most prominent negative phase followed by a larger second positive phase (*Type 6*). However, the results presented from an **IRB sample** show a more uniform spike shape propagating along the microchannel at DIV 14. The first electrode position E2 records a low-amplitude monophasic shape, but all subsequent adjacent electrodes record one of the proposed triphasic shape types (E3: *Type 6*; E4: *Type 4*; E5: *Type 4*; E6: *Type 5*; E7: *Type 4*). More interesting differences can be seen across the time scale. The RB sample shows less variation in spike shape change over time. Electrode positions E2 and E3 maintain the same shape types over time, with a slight decrease in amplitude in the case of the triphasic *Type5* shape at position E3. In subsequent adjacent electrodes, the change is gradual and synchronous, from triphasic *Type 5* or *Type 4* to less complex bi/triphasic *Type 2* and *Type 3* shapes. The EAP amplitudes do not change significantly with time but have a larger value in the middle part of the observed microchannel of the RB sample. In contrast, the illustrated example from an IRB sample shows a more dramatic change in spikes, both in shape and amplitude (Figure 5.15 (C)). At DIV 14, the axon most likely does not have a successful coupling

at E2, resulting in the recording of a low amplitude monophasic shape *Type 7*. The rest of the electrodes show typical axonal activity of triphasic shapes, transitioning from asymmetric *Type 5* (electrode position E3) to symmetric *Type 4* (electrode positions E4, E5) to the final asymmetric *Type 6* shape (on E6, E7) and a decrease in amplitude. A unique feature in this case is a drastic change in the spike shapes detected in the following DIVs. The transitions that occur

are different from those in the previously described RB sample and in the publication mentioned. Namely, at DIV 21 a very narrow signal of asymmetric (E2, E3, E4, E5, E7: *Type 6*; E6: *Type 5*) triphasic shapes are recorded, with a decrease of amplitude in the middle of the microchannel. At DIV 29, amplitudes are uniform along the microchannel (~ 50 µV) with a significant increase at the very narrow end of the emitting side (~ 200 µV). On the last day of

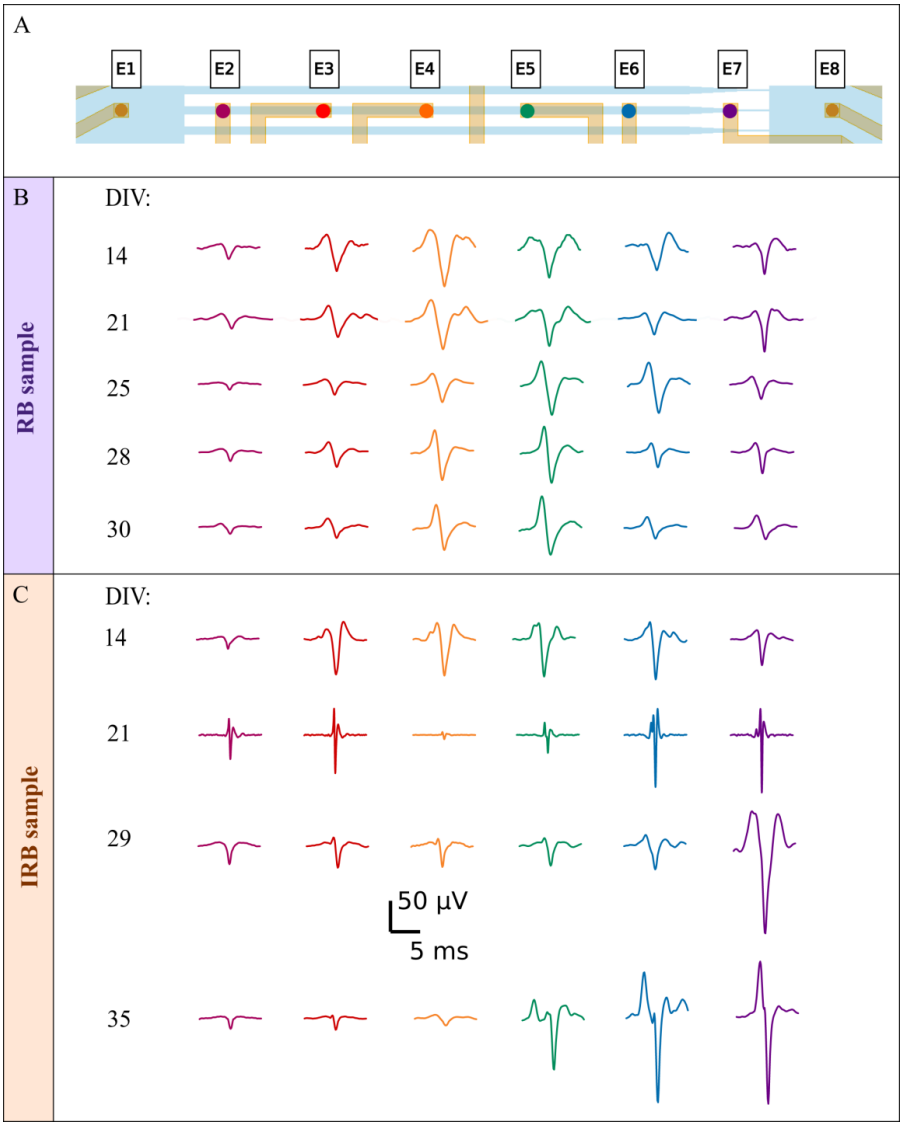

Figure 5.15 – Map of spike shape evolution in long microchannels recorded in RB and IRB devices. **(A)** Microchannel sketch with electrode position labels. The color of the electrode corresponds to the color of the recorded spikes below. **(B)** Reversibly assembled device recording. **(C)** Irreversibly assembled device recorded spikes vary in shape and amplitude.

recording at DIV 35, the spikes show more complexity towards the emitting side of a microchannel. The nature of these *Type8* shapes cannot be explained with certainty, but it is suggested that superposition of adjacent spikes may occur, as shown in previous studies (Lewandowska et al., 2015).

Spike Shapes along Medium Microchannels

Medium microchannel RB samples had the least successful cell culture during these experiments. The starting number of five samples had a microchannel activity yield of 53%, which dropped to 20% in the following week of recording. Three IRB samples maintained a high yield of 81% active microchannels at DIV 14 and 75% at DIV 21 (Figure 5.16). Although the number of samples could not be maintained in maturing cultures, certain trends could still be observed. Somatic and complex forms were the least present in all cultures. RB samples did not record the presence of these shape types, which may be a consequence of less successfully developed neuronal networks. Nevertheless, triphasic shape types predominated in all observed experiments.

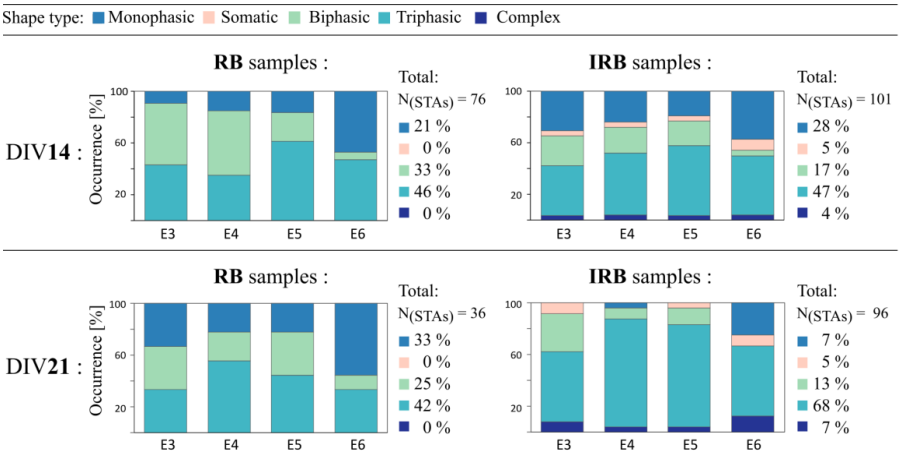

Figure 5.16 – Percentage occurrence and distribution of EAP spike shapes along the mid-length microchannels. Analysis in reversibly (RB) and irreversibly (IRB) binding MEA-microfluidics device assemblies on DIV 14 (top stacked bar plots) and DIV 21 (bottom stacked bar plots). Electrode numbering corresponds to electrode positions found within the observed microchannel length. The spike shape legend is shown at the top of the figure.

Spike Shape Evolution Trend in Single Medium Microchannel

When observing a randomly selected single microchannel, the picture is different from what could be observed in long microchannels (Figure 5.17). A significant difference between the two samples is that the spike amplitudes in the IRB sample have more than 4 times higher peak-to-peak amplitudes. These gain effects are discussed in more detail in section 5.3.1. In terms of spike shape evolution, RB samples show a consistent shape across the recording DIVs, with a significant decrease in spike amplitudes (Figure 5.17 (B). In IRB samples, spike shapes remain consistent throughout the cell culture development and tend to become more irregular as the cell culture matures (Figure 5.17 (C), DIV 29 and 35).

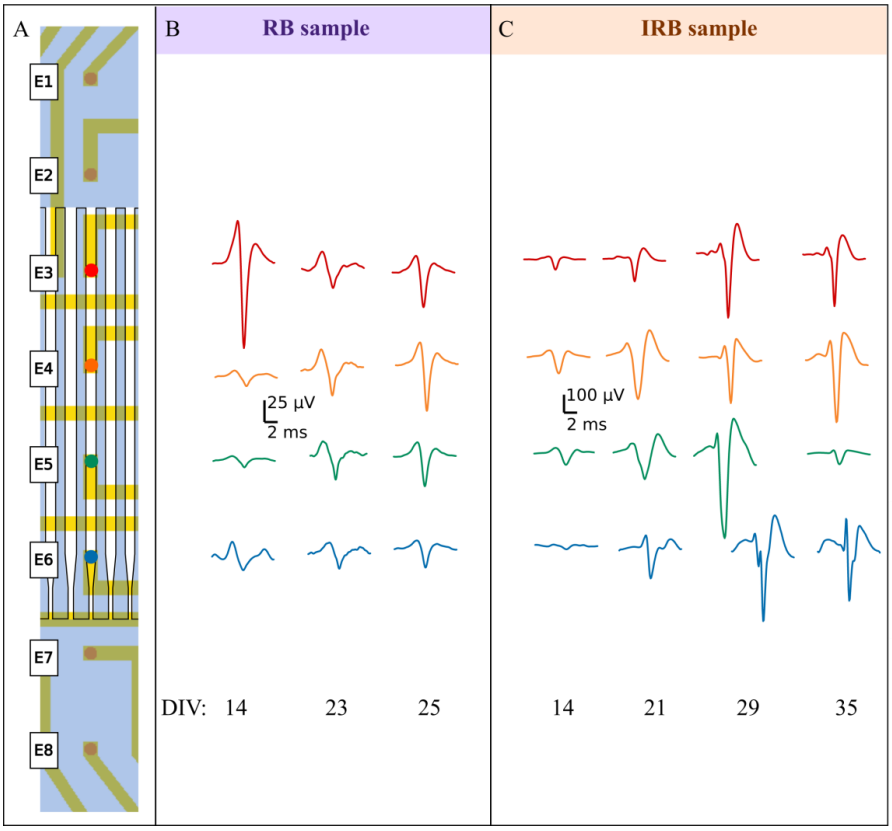

Figure 5.17 – Map of spike shape evolution in medium microchannels recorded in RB and IRB devices. **(A)** Microchannel sketch with electrode position labels. The color of the electrode corresponds to the color of the recorded spikes below. **(B)** Reversibly assembled device recording. **(C)** Irreversibly assembled device recorded spikes vary in shape and amplitude.

Spike Shapes along Short Microchannels

For the short microchannel samples, five RB and three IRB samples were run in experiments. The higher activity yield in IRB samples was observed at both DIVs, consistent with the previously described microchannel lengths. RB microchannels showed 53% activity at DIV 14 and 72% at DIV 21, while IRB samples showed 88% and 100% activity at the respective DIVs. Interestingly, all five spike shapes were identified within the RB sample group, while the IRB recordings predominantly showed the triphasic spike shape (Figure 5.18). The highest variance of shapes is present in the RB sample at DIV 21, when all shapes were recognized during the sorting process. Complex shape *Type 8* was detected in both types of samples at DIV 21.

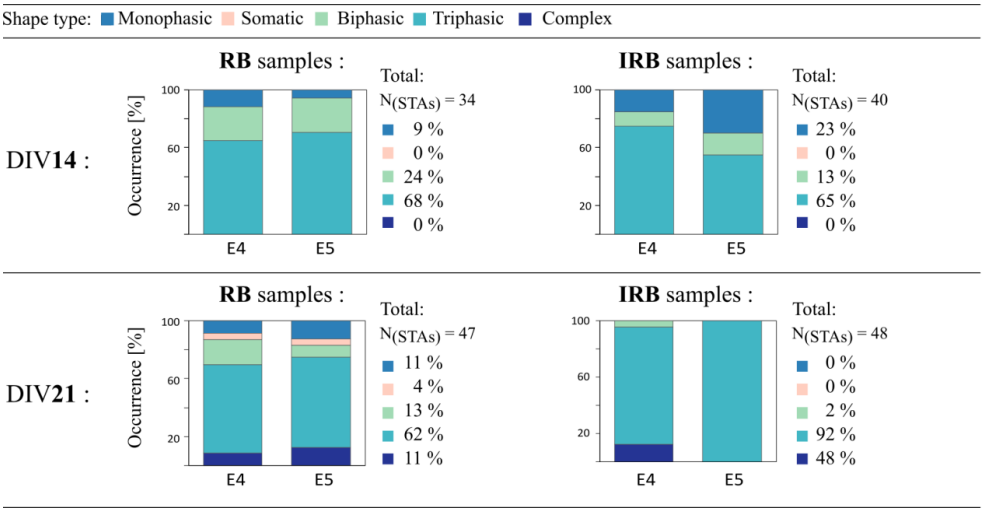

Figure 5.18 – Percentage occurrence and distribution of EAP spike shapes along the short length microchannels. Analysis in reversibly (RB) and irreversibly (IRB) binding MEA-microfluidics device assemblies on DIV 14 (top stacked bar plots) and DIV 21 (bottom stacked bar plots). Electrode numbering corresponds to electrode positions found within the observed microchannel length. The spike shape legend is shown at the top of the figure.

Spike Shape Evolution Trend in Single Short Microchannel

Figure 5.19 shows the evolution of spike waveforms on different DIVs in a single observed microchannel. The RB sample showed activity at DIV 14, 21, and 28, while the IRB sample showed activity up to DIV 35. Spike shapes show a more irregular trend in spike shape change than described above for other microchannel lengths. The shape remains consistent within the observed DIV, and changes with time. This may be due to the detection of spikes

originating from different axons growing through the same electrically functional microchannel. The complex waveform recorded in the IRB sample at DIV 21 confirms that two or more axons are conducting the signal, which combine and superimpose to give a complex pentaphasic spike shape. These pentaphasic shapes have already been described by Lewandowska et al. (2015).

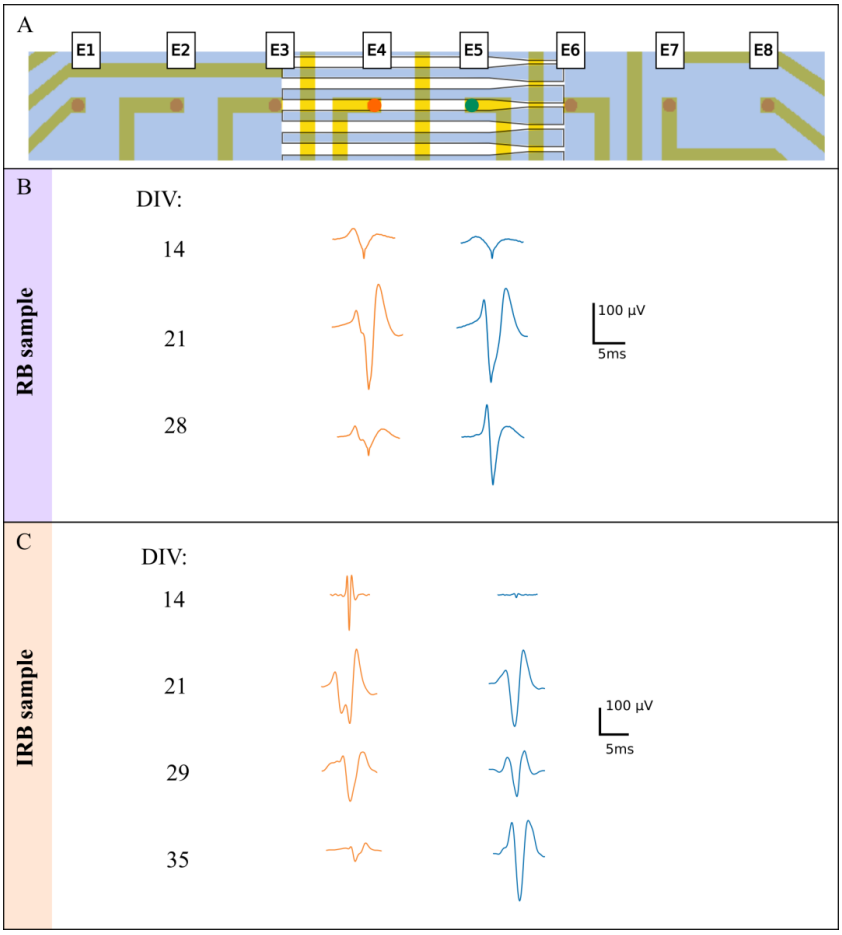

Figure 5.19 – Map of spike shape evolution in short microchannels recorded in RB and IRB devices. **(A)** Microchannel sketch with electrode position labels. The color of the electrode corresponds to the color of the recorded spikes below. **(B)** Reversibly assembled device recording. **(C)** Irreversibly assembled device recorded spikes vary in shape and amplitude.

5.2.3.2 Along Microchannels in µFluidic-r16MEA System

In the µFluidic -r16MEA system, the number of electrically active microchannels is 16 with a constant length of 864 µm and four electrodes in each microchannel. Neuronal cultures were maintained until DIV 29 in reversibly (RB) assembled systems and until DIV 26 in irreversibly (IRB) assembled systems. Spontaneous activity could not be recorded continuously through DIVs from all cultured samples. The number of samples varies over time, so I will discuss a sum of all active microchannels from different individual cultures and their activities in subsequent DIVs.

STA spike shapes occurrences along the microchannels

The RB µFluidic-r16MEA device recorded spontaneous neuronal activity from DIV 14 to DIV 29. The total number of RB samples observed was four (at DIV 14), decreasing to three (at DIV 18-22), two (at DIV 26), and finally one (at DIV 29). Since the number of active microchannels also varies from sample to sample, a reference for comparing the data sets is the total number of STAs observed at each DIV. A comparison of total spike shape occurrences between RB and IRB samples is shown in Figure 5.20. Both types of devices show a similar trend in the total percentage of spike shapes over time. Monophasic *Type 7* shape is more present at DIV 14 than in other recording days. Somatic-like *Type 1* shapes were detected least in both groups of samples. The complexity of detected spikes increases with time but remains below 20% of detected spikes in both RB and IRB. Biphasic *Type 2/3* and triphasic *Type 4/5/6* remain the most frequently detected shapes, as in previously described samples with axon diode

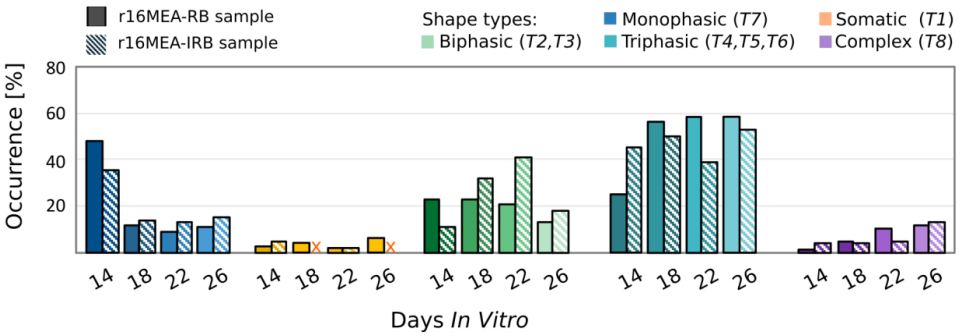

Figure 5.20 – Comparison of total occurrences (in %) of each spike shape in all recorded DIVs in r16MEA-RB and r16MEA-IRB samples. Bars are grouped by spike shape with designated colors. A graph shows trends in the change in spike shape occurrence over time DIV 14-26 by comparing RB (solid color bars) and IRB (dashed bars).

microchannels of different lengths. The activity of the IRB samples could be recorded from DIV 14 to DIV 26. The initial number of samples was four (at DIV 14), decreasing to two (at DIV 18-22), and finally to one active culture sample (at DIV 26). Nevertheless, the yield of microchannel recordings from active cultures was at least 60% and in most cases over 75%.

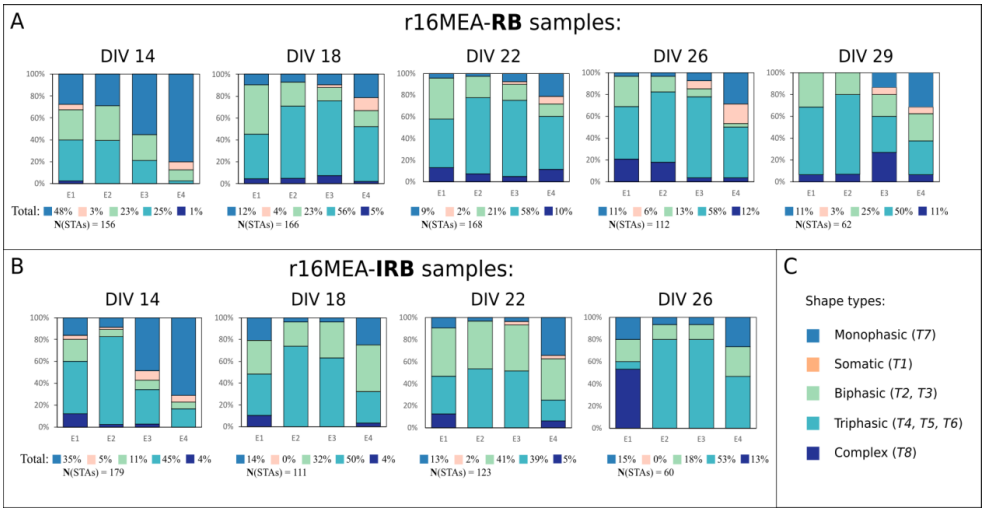

Figure 5.21 – STA shapes distribution along r16MEA microchannels at different DIVs. (A) Spike shapes distribution in RB samples at DIV 14-29. **(B)** Spike shape distribution in IRB samples at DIV 14-26. **(C)** Spike shape color legend, corresponding to percentage bars in (A) and (B) plots.

Figure 5.21 shows a detailed observation of the distribution and occurrence of STA shapes at each electrode position along the microchannel in RB and in IRB samples. The most striking observation is the almost reciprocal change in the occurrence of monophasic and triphasic shapes. At DIV 14, monophasic *Type 7* shape is the most present with 48% (RB) and 35% (IRB) total occurrence, while its number decreases to 11% (RB) and 15% (IRB) at the last recording day of each group. In contrast, the triphasic forms have a significant increase in occurrence in the RB samples, from 25% (at DIV 14) to 58% (at DIV 26), while the IRB samples have a less pronounced increase from the beginning of recording, from 45% (at DIV 14) to 53% (at DIV 26). This is consistent with the expectation of a gradual strengthening of neuronal co-culture connectivity. The monophasic shape predominance at DIV 14 indicates lower axonal density within the microchannels and less successful sealing of axons to the electrode surface. The observed results are highly consistent with previously presented trends in samples with axon diode microchannels. Triphasic shapes are the most common in both samples at all DIVs, and complex shapes are the least common, with a slight increase in occurrence in maturing cell cultures.

Spike Shape Evolution Trend in µFluidic-r16MEA Microchannel

Figure 5.22 shows the spike shape evolution along a microchannel in each of the samples analyzed. Both microchannels are in row 8 of the r16MEA which is the central position of the

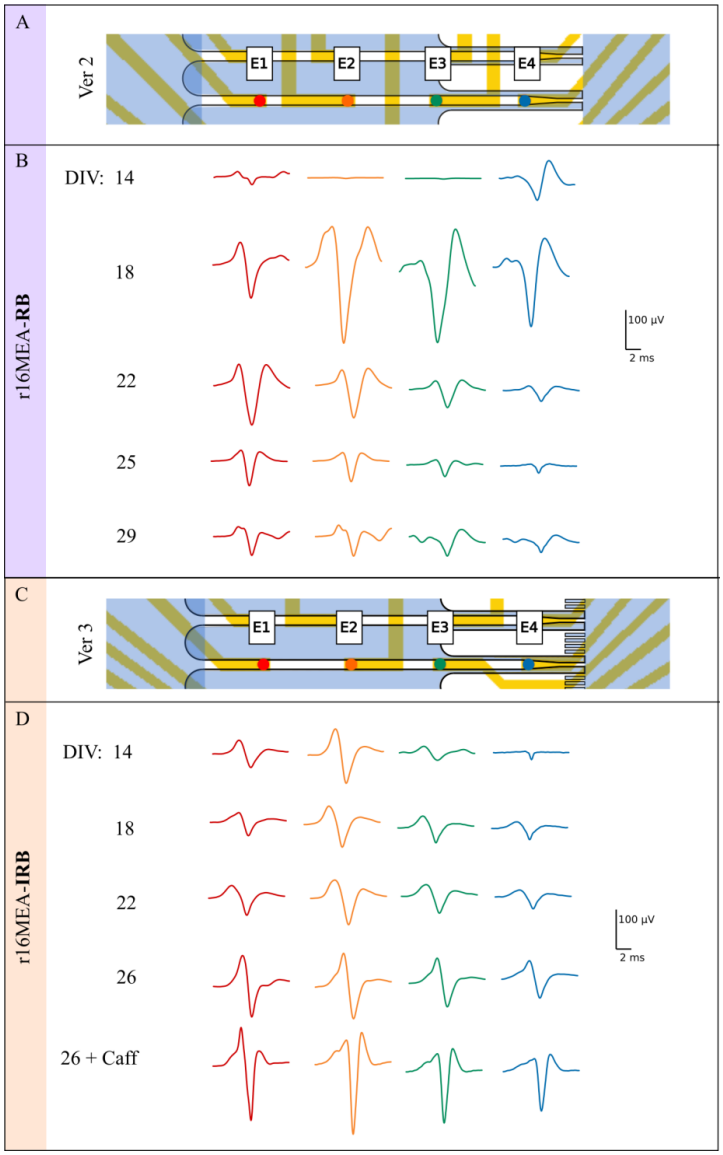

Figure 5.22 – Spike shape evolution in RB and IRB µFluidic-r16MEA. (A) A sketch of a microchannel in the RB sample with Ver2 trap shape structures. **(B)** Spike shape evolution in the RB sample from DIV 14 to DIV 29. **(C)** A sketch of a microchannel in the IRB sample with Ver3 trap shape structures. **(D)** Spike shape evolution in the IRB sample microchannel from DIV 14 to DIV 26 and final addition of 8mM caffeine.

device. The results obtained from these specific microchannels provide insight into the predictability of spike shapes, but less predictability of the amplitudes of the same spikes. What can be observed in DIV 14 is that there is an inconsistency in the shapes of the detected STAs along the microchannel. In both samples, this situation changes starting from DIV 18. While the IRB sample shows a consistent set of recorded shapes, the RB sample maintains a variety of detected shapes along the microchannel. However, this changes in a maturing culture, with a noticeable consistency of STA shapes along the microchannel. The amplification

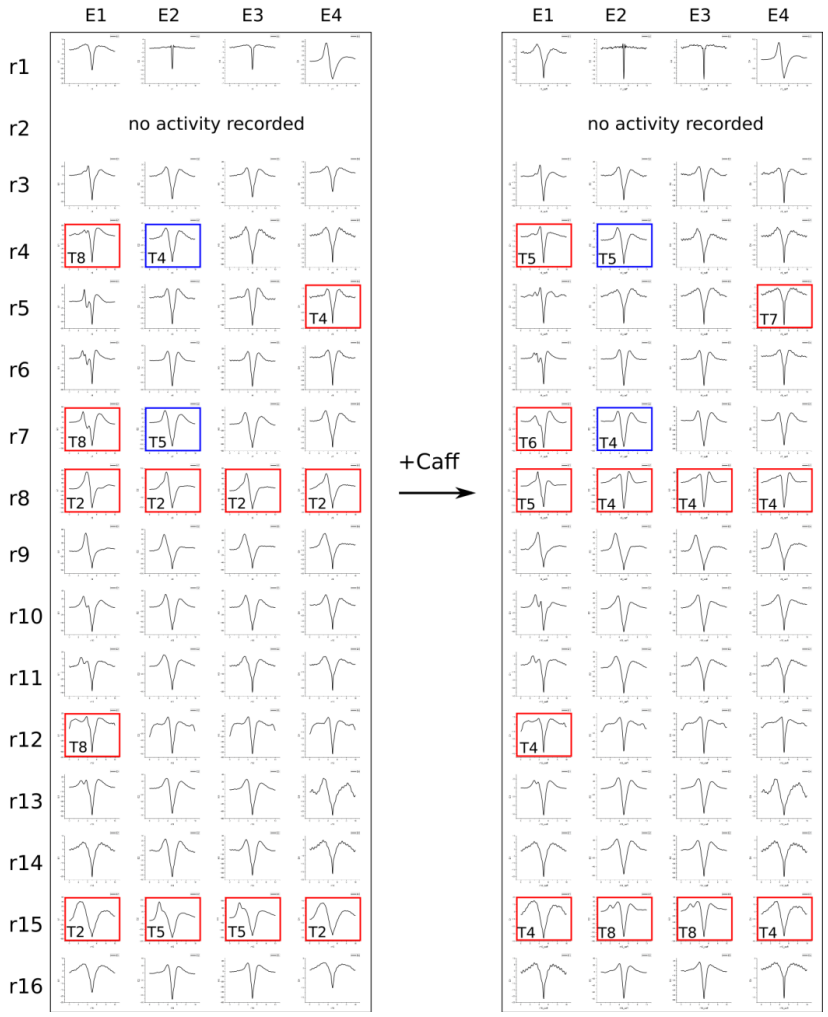

Figure 5.23 – IRB sample at DIV 26 *spike shape change* upon caffeine addition. A total of 14 electrodes detected a different STA upon addition of 8mM caffeine. The change is complete in only two rows: r8 and r15. In blue rectangles are shapes that did not change significantly, i.e. remained within the same group of triphasic shapes. The red rectangles are shapes that underwent a visible change in shape by also belonging to different groups of spike signals.

of the signal in the RB-µFluidic-r16MEA is most prominent at DIV 18, whereas the IRB-µFluidic-r16MEA has a gradual increase in spike amplitudes over time.

Another interesting observation is a change in spike shape upon addition of caffeine (8 mM) in one of the IRB samples at DIV 26. I was curious about the overall effect of caffeine on the whole culture, and Figure 5.23 gives a comprehensive picture of the results. Out of a total of 60 active electrodes (r16MEA activity yield 94%), 14 show a change in STA shape upon addition of caffeine. Only two of these STAs (E2 in r4 and E2 in r7, marked with blue rectangles) undergo only a slight change, where the recorded shape belongs to the same shape group. All other STAs (12 detected in total) change their shape upon the addition of caffeine (marked with red rectangles). A detailed observation of the activity trace shows that spike shapes recorded before the addition of caffeine are also present after its addition. The STAs detected after caffeine addition are usually not present in the previous recording of the same electrode. This suggests that caffeine may have induced activity in previously silent neurons, or increased activity in cells whose signals were not previously dominant. Either way, these results suggest that neurons tend to form bundles of axons that pass through the same microchannel. Since the detection of spikes is not neuron specific, this may lead to the presented effect of *spike shape change* on the same electrode.

5.3 Microchannels as Axonal Amplifiers

The signal amplification effect is one of the main advantages of the µFluidic-MEA hybrid system developed in this thesis. The theoretical background of this phenomenon is explained in section 1.3.3. In the following sections, I observe the amplification effect in axon diode shaped microchannels of three different lengths in µFluidic-MEA and in the µFluidic-r16MEA device.

5.3.1 Amplification Trends Along Microchannels

Amplification trends are observed as the change in **peak-to-peak** (**p2p**) amplitudes of detected spikes along the microchannel at a given DIV. Median value of all detected amplitudes at specific electrode positions are taken for analysis. Median p2p values are then normalized to

the maximum value within each microchannel. Although the results of each microchannel may differ from each other, as already confirmed by Wang et al. (2012) and recognized in the experiments performed, certain trends could be detected when cultures were observed separately. Therefore, I performed an analysis where each µFluidic-MEA device with cell culture was observed individually. Median amplitudes were averaged at each electrode position, resulting in a unique amplification trend for each sample.

The method of device assembly did not show a significant influence on the amplification trend and was therefore ignored for this question. A more significant influence seems to be the length of the microchannels and especially the electrode distance from the receiving and emitting side of the microchannels. As the most representative data set, I chose DIV 14, where the number of samples and active microchannels was the highest (a total of 17 MEAs; 107 active microchannels). Figure 5.24 depicts the amplification trends of each MEA sample as a function of the microchannel length and the electrode distances from the receiving (left) or emitting (right) side of the microchannel. All samples show either increasing or decreasing signal amplification. The trends are more apparent in samples with a greater number of active microchannels. At DIV 14, all short microchannels (five cultures) show a predominantly ascending trend with the highest spike amplitudes at electrode position E5, closer to the emitting side of the microchannel. In the medium microchannels (five cultures), descending trends with the highest amplitudes start at the electrode position E3, while ascending trends amplify the signal at positions E5 or E6. The last group of samples with long microchannels

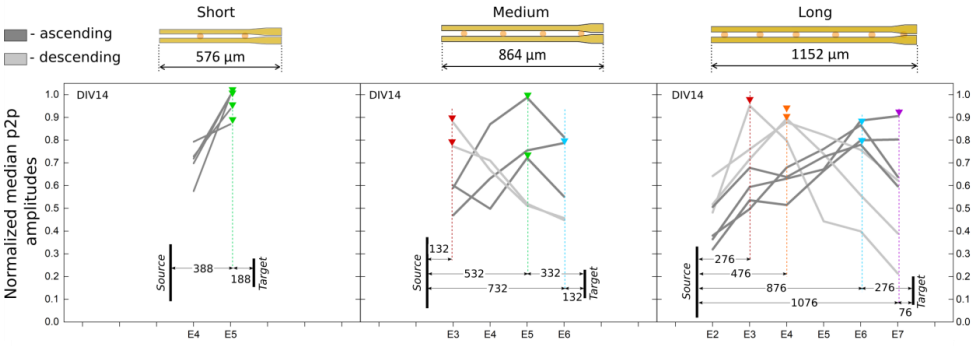

Figure 5.24 – Signal amplification trends in short, medium, and long microchannels at DIV 14. Sketches of corresponding microchannels show full lengths and electrode positions. Graphs are listed in the same order as sketches above. Trends are given as averaged normalized median p2p amplitude values for each sample with more than three active microchannels. Trends are shown as ascending (dark gray) or descending (light gray). Triangle shapes guide the eye to the highest peaks and correspond to electrode positions by color. All distances relative to the receiving or emitting side are given in µm scale.

(seven cultures) amplifies the signal at E3 or E4 in descending trends and at E6 or E7 in ascending trends.

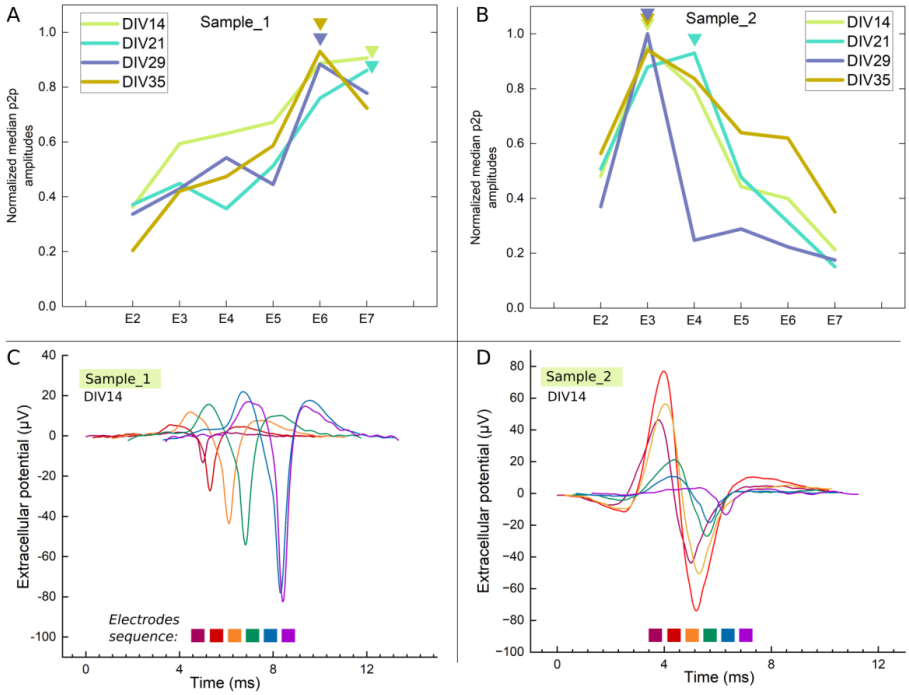

Figure 5.25 – Amplification trends over time in long microchannel samples. (**A**) The ascending amplification trend in sample_1 follows the main course over time. The highest amplitudes are recorded in the last two electrodes, near the emitting side of the channel. (**B**) The descending trend of sample_2 is maintained over time. The highest amplification occurs at positions E3 and E4. (**C-D**) Amplification of the corresponding action potentials at DIV 14 are shown in the lower plots. Spikes are colored according to the order of the recording electrode: E2 (dark red), E3 (red), E4 (orange), E5 (green), E6 (blue), E7 (purple).

I then examined individual samples with ascending and one with descending trends in the following days: DIV 14, 21, 29, and 35 (Figure 5.25) in long microchannels. The amplification trends do not change their course in either sample, i.e. they are always either ascending or descending in all DIVs. The only obvious change is the shift position where the highest amplitudes are detected. For the ascending trend (*sample*_1), the amplification takes place at the last electrode position E7 at DIV 14 and 21 and then changes to E6 at DIV 29 and 35 (Figure 5.25 (A)). In the case of the descending trend (*sample*_2), the highest amplitudes are detected at E3, except at DIV 21 when it moves to E4 (Figure 5.25 (B)). The causes of these changes cannot be understood from the available data. One can only assume that the morphological development of neurons in combination with a given environment allows a dynamic nature of the axon-electrode contact that causes the shift.

However, the position of the highest peak differs from the expectations derived from a publication by Wang et al. in 2012. In their study, they defined the amplification position relative to the distance of the electrode from the entrance of the microchannel. According to their simulation and practical experiments, the amplitudes increase when the length of the microchannel is less than 200 µm. In all cases with longer microchannels, the amplitudes decrease after 200 µm due to signal attenuation and reach the maximum amplitude at 129 µm distance from the entrance that corresponds to the second electrode position of their device. However, this is not entirely the case in the results I present. In most cases presented, the amplification occurs at one of the two electrodes closest to either side of the microchannel. In the case of long microchannels, the third electrode may also take on the role of recording the largest amplitude, even though the shortest distance to the end of the microchannel is 476 µm. However, the geometry and dimensions of the microchannel used in their study differs from the one used in this thesis, and factors such as the size of an axonal diameter can also introduce the difference in results.

Irreversibly Bonded (IRB) Device Influences Neuronal Signal Amplification

The microchannel amplification effect is expected to occur and has been demonstrated in all microchannel length variations. Besides its position of occurrence, another important aspect of interest is the amplitude values and their total occurrence with respect to the microchannel length. In this case, the analysis is performed over the total number of detected spikes and their peak-to-peak amplitudes. This is a more comprehensive determination of the actual amplitude values, as it considers all detected spikes, not just the p2p amplitude of the estimated STA footprints. My main interest in this aspect is the comparison of amplitude values and their distribution between two main groups of samples (IRB and RB) and later between the different microchannel lengths. Here, I present only the results from DIV 21, when the culture reaches full maturation and network bursting synchrony.

In Figure 5.26, overlapping histograms show visible differences in the amplitude distribution of the total number of spikes analyzed from each group. Most of the amplitudes in the RB samples fall into the small amplitude range (< 0.2 mV) with 84% of the total occurrence. At the same time, large amplitudes (> 0.6 mV) occur in only 1% of the total. IRB samples show a

difference with 61% of small amplitudes and 7% of large amplitudes. 32% of IRB and 16% of RB spikes fall into the medium amplitude range (0.2 mV < x < 0.6 mV). Despite the obvious differences in the occurrence of large amplitudes, the highest peaks are recorded in the RB devices (Figure 5.26, purple rug).

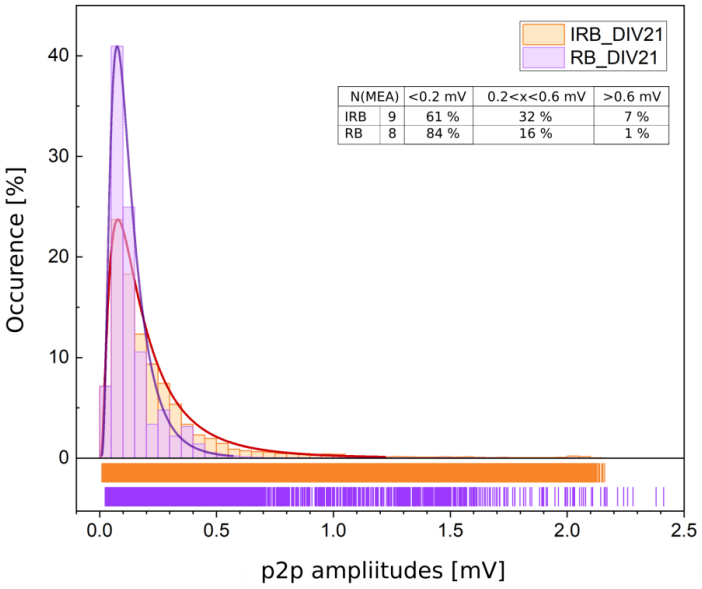

Figure 5.26 – Peak-to-peak amplitude distribution in irreversibly and reversibly assembled µFluidic-MEA hybrids at DIV 21. Comparison of IRB and RB sample groups shows that there is a difference in amplitude distribution between these sample groups. Bin size: 50 (scaled 0.05).

The next question is how are the amplitudes distributed among groups of different microchannel lengths?

Figure 5.27 shows the effect of microchannel length along with the difference in assembly procedure. However, the number of samples analyzed varies significantly in some data sets and requires caution in the absolute interpretation of the results presented. Interesting phenomena are observed: most amplitudes larger than 0.2 mV in both groups of samples happen to be recorded in MEAs with short microchannels. Up to 54% of all recorded spikes in IRB devices with short microchannels have amplitudes larger than 0.2 mV, of which 14% of total belong to very large amplitudes (> 0.6 mV). At the same time, in all three groups of RB

devices, more than 70% of the values fall in the range of small amplitudes (< 0.2 mV). However, short microchannels give a better percentage gain with spike amplitudes larger than 0.2 mV.

These observations lead to the conclusion that the most successful amplification effect is within the short microchannels and moreover in IRB devices. The effect of short microchannels has the most successful outcome in terms of signal amplification due to the attenuation of the signal recorded in longer microchannels.

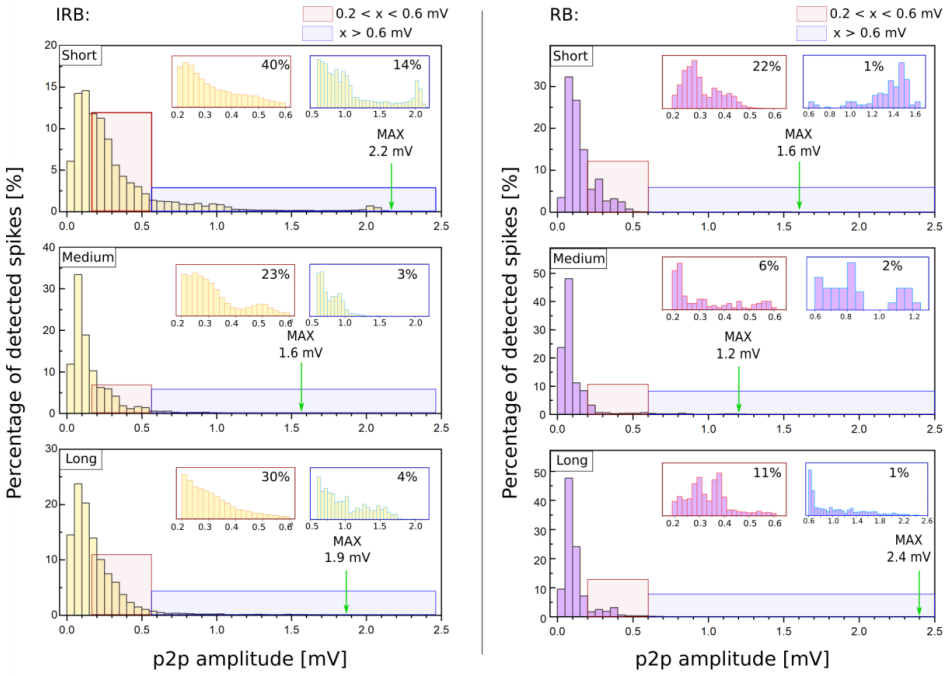

Figure 5.27 – Peak-to-peak amplitude distribution histograms in different microchannel lengths at DIV21, observed in IRB (left) and RB (right) samples. Red rectangles contain the distribution of peak-to-peak amplitudes in the range 0.2-0.6 mV, and blue rectangles contain amplitudes greater than 0.6mV.

Spike Shapes Show Unique Groups of Peak-to-Peak Amplitude Values

When it comes to amplitudes, another question arises: what is the relationship trend between spike shapes and p2p amplitudes?

A comparison of the p2p amplitudes of each spike shape (T1-T8) is shown in Figure 5.28. The box plot colors refer to the spike shape groups as follows: *monophasic* (blue), *somatic-like*

(orange), *biphasic* (green), *triphasic* (turquoise), and *complex* (purple). Peak-to-peak median amplitude values are analyzed from all microchannel lengths, regardless of device assembly type. The most prominent amplitude ranges are present in the triphasic and complex spike shapes.

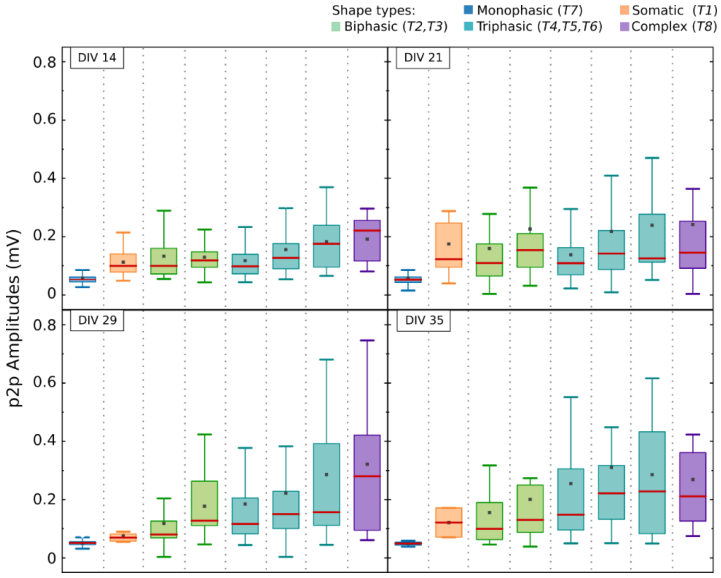

Figure 5.28 – **Peak-to-peak amplitudes as a function of spike shape type.** Box plots show the p2p amplitude distribution of each spike shape in DIV 14, 21, 29, and 35. Outliers are not included in the final figure to facilitate understanding of the results. The colors of the box plots correspond to the spike shapes, as indicated in the legend. **Median**: red line; **mean**: dark gray squares.

These trends are more apparent in Figure 5.29, where box plots are grouped for each spike shape over time. The monophasic shape (T7) keeps the amplitude range constant over time, below 100 µV, and is the smallest in amplitude of all the shape groups compared. This is an interesting observation that should be seen in close connection with the presented distribution of these shapes along the microchannels. In fact, the monophasic shape occurs mostly at the beginning or at the end of the recording microchannel. The small amplitudes indicate a lack of successful axon coupling to the recording electrode. This agrees with the microscopic observation of Pan et al. (2012) who reported that axons tend to grow first along the edges of the microchannels and then fill the central area. Similar observations have also been published by Habibey et al. (2017), confirming the reproducibility of this effect due to the nature of the microenvironment. The consequence is that axons may not encounter all subsequent electrodes, which explains why there is a difference in spike shapes and their

amplitudes, or why sometimes no signal is recorded. All other shapes show a larger span of amplitudes with an increasing trend as the culture matures. All three types of triphasic shapes (*Type 4/5/6*) follow a similar trend of gradually increasing amplitude ranges.

An interesting relationship between the occurrence of each spike shape and amplitude ranges is also observed. Since the triphasic shape is the most common shape during the mature phase of cell activity, it is also reasonable to expect greater variation in amplitude range over time. However, a complex shape is not as present in the detected activities, but the amplitude ranges are as large as for the triphasic shape. The cause of this effect is difficult to predict without a more focused and detailed examination of the nature of the spikes themselves. The study by Lewandowska et al. (2015) has shown the complexity of these spikes and their unique way of structuring from separate spike shape aggregates.

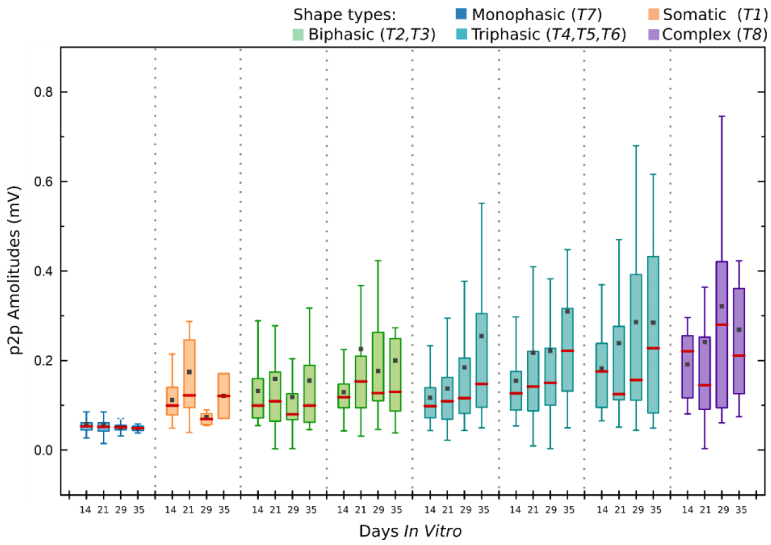

Figure 5.29 — Peak-to-peak amplitude changes in each spike shape over time. The following plot of amplitudes shows a difference in the dynamics of change in each spike shape. The monophasic shape shows uniformity in amplitudes over time. Other shapes show variation, with a tendency toward an expanded set of recorded values and a gradual increase in the median (red line) over time.

5.3.2 Amplification Trends Along Microchannels in r16MEA

All six µFluidic-r16MEA samples analyzed gave different results than would be expected based on previously presented results. In contrast to MEAs with axon-diode microchannel designs,

r16MEAs show descending amplification in all cultures regardless of the type of binding (Figure 5.31). The largest peak amplitudes are recorded on the first or second electrode. The descending trend persists over time as observed in the previous section. Peak-to-peak amplitudes between the two groups of samples are compared as the final percentage occurrence within each data set of the median p2p values of all detected spikes at DIV 21 (Figure 5.30). Similar to the results shown in Figure 5.26, µFluidic-r16MEA samples show a similar trend of amplification effect between two observed sample groups. Namely, RB devices recorded action potentials up to 3.1 mV, while the largest detected spike in IRB samples was around 0.6 mV. However, this is difficult to interpret due to the small number of individual cultures in each dataset group and the limited observation of amplitude span when considering median p2p values instead of full p2p datasets.

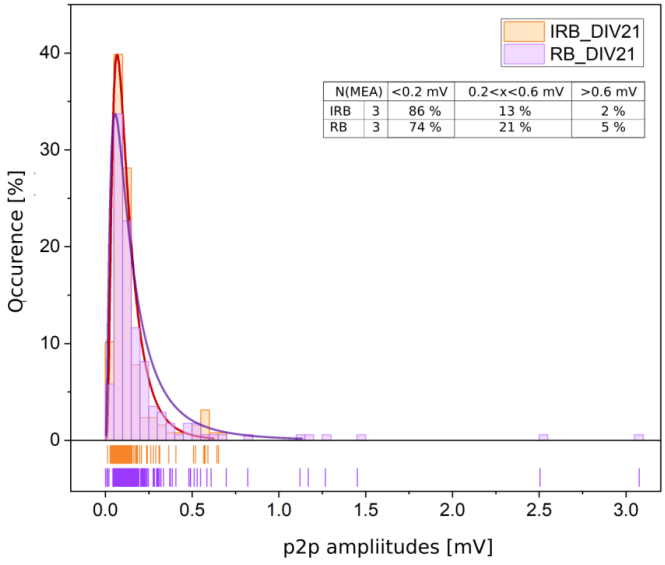

Figure 5.30 – Median peak-to-peak amplitudes distribution in irreversibly and reversibly assembled µFl-r16MEA-hybrids. Peak-to-peak amplitudes are compared within three main groups of values indicated in the table. Bin size: 50 (scaled 0.05).

An interesting difference between recordings within microchannels in µFluidic-MEA and µFluidic-r16MEA is that the latter have exclusively shown a descending trend of spike amplification. One assumption that could lead to such a result is the different geometric shape within the microchannels. In the case of axon diodes, the intermicrochannel distance is 25 µm, and in the case of axon-traps this distance is 85 µm. This increased intermicrochannel space allows for better sealing of the PDMS microchannel structures, resulting in a more stable

cellular microenvironment. As a result, growing axons have a system of microchannels with less variance and the recording provides a more stable and predictable amplification trend. The position of the maximum peak values is similar to the distance reported and predicted by Wang et al. (2012). The position of the electrodes relative to the entrance of the microchannel is 132 µm and 332 µm for the first and second electrodes, respectively. In their study, the critical distances were 129 µm in the experimental setup and 236 µm in the simulation for a 1 mm long, 1 µm high, and 20 µm wide microchannel.

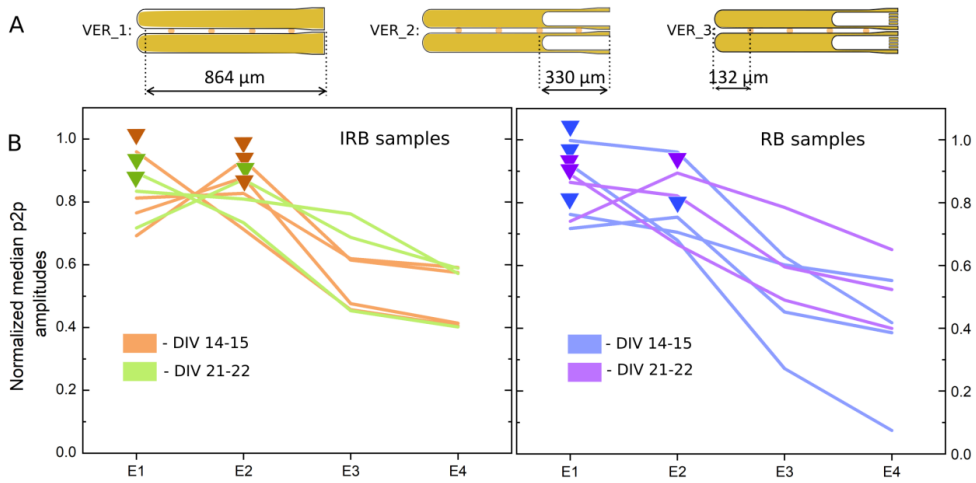

Figure 5.31 – Amplification trends in IRB and RB µFuidic-r16MEA samples at DIVs 14/15 and 21/22. **(A)** Sketches of microchannel designs used in combination with r16MEAs. **(B)** Amplification trends observed in seven IRB (left graph) and seven RB (right graph) samples over time. Triangles indicate the highest peaks in each sample. All observed recordings showed a descending trend with the highest peak in the first half of the microchannel.

With respect to the amplitudes of each spike shape over time, the results show some differences compared to µFluidic-MEA devices. In contrast to the analyzed axon diode microchannel recordings, the triphasic (T4 and T5) shapes show constant amplitude ranges over time. The monophasic (T7) shape shows a constant, although significantly smaller, p2p amplitude range over time, up to 20 µV. The relationship between their amplitude and their distribution along the microchannel is consistent with the previously described patterns. Their occurrence is mostly at the edges of the microchannels, where the axons tend to grow along the edges and the axon-electrode coupling is not as good as in the middle of the microchannel.

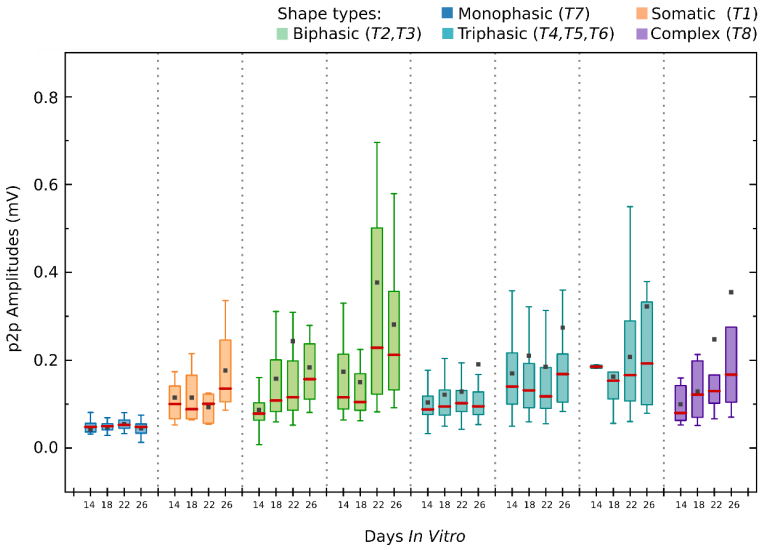

Figure 5.32 – Peak-to-peak amplitude changes in each spike shape over time in µFluidic-r16MEA samples. The following plot of amplitudes shows a difference in change dynamics in each spike shape. The monophasic shape shows uniformity in amplitudes over time. Other shapes show more variation, possibly due to the uneven number of samples observed.

5.4 Propagation Velocities

Several research groups have adopted the approach of coupled µFluidic-MEA platforms to mimic various neuronal circuits *in vitro* (Taylor et al., 2005; Bradley J. Dworak, 2009; Park et al., 2009; Berdichevsky et al., 2010; Shi et al., 2010; Habibey et al., 2022). The non-invasive recording system makes it a suitable choice for deeper investigation and understanding of axonal properties and their information processing (Taylor et al., 2003, 2005). Controlling the position of individual axons with microfluidic microchannels offers great potential for biomedical research, drug screening and medical applications for axonal regeneration after injury (FitzGerald et al., 2009; Hosmane et al., 2011). Electrodes outside of microchannels record almost exclusively from larger cell bodies. This configuration is used to grow coupled neural networks that are connected via predefined axonal growth pathways. Axonal information processing has been a major topic of interest in neuroscience, and this device highly enables it. The precise electric coupling of axons and electrodes within microchannel structures enables the recording of action potential propagation velocities. In previous studies,

these velocities were estimated to be between 0.18 and 1.14 m/s (Bradley J. Dworak, 2009). These results were used to validate and analyze the findings of this thesis.

5.4.1 Signal Propagation Velocity

How is Signal Propagation Velocity Measured with This Device?

High-level brain functions develop through successful and specific communication between neuronal networks. *In vitro*, a predefined and controlled microenvironment of axonal growth can mimic the complex nature of intercommunication between certain subregions of the brain. Understanding the directionality and velocity of signal propagation is a major challenge in comprehending neuronal networks. The purpose of the axon diode microchannel design in this thesis is to support the natural unidirectional communication of cortical and striatal sub-regions in the mammalian brain. The focus of this thesis is predominantly on the spontaneous activity of cortico-striatal co-culture. Electrical stimulation of the cells was not performed in this study due to previously reported possible interference of stimulation strength on axonal conduction (Shimba et al., 2015). Spontaneous activity is typically first observed at DIV 14 after plating the cells. The recordings were mainly conducted within microchannels, unlike other similar studies where recordings were also possible outside this area. The microchannels increase sealing resistance, resulting in voltage amplification (FitzGerald et al., 2008; Dworak and Wheeler, 2009; Pan et al., 2014). This is also described in more detail in section 1.3.3.

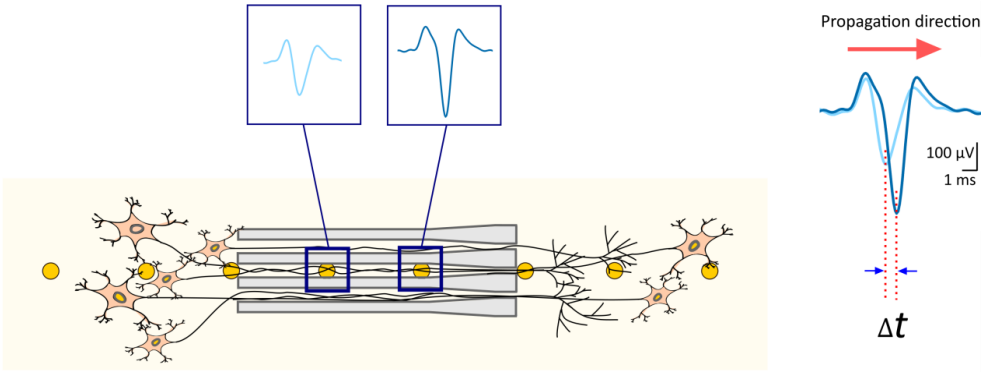

Figure 5.33 – Illustration of axonal signal propagation along the microchannel. Neurons extend their axons directed by the axon diode microchannels. The electrodes are evenly distributed with an inter-distance of 200 µm. For simplicity, only one electrically active microchannel is depicted. Electrodes within the microchannel (framed in dark blue) detect the traveling axonal action potential. The detected waveforms are framed in rectangles above the corresponding electrodes. On the right is a view of a pair of spikes in relation to each other. A time delay between the two is apparent, allowing for the deduction of the direction of signal propagation.

Figure 5.34 (A) shows that electrophysiological signals on electrodes within microchannels have significantly higher amplitudes, while electrodes located in compartments show no visible signals. This demonstrates the effect being discussed. When electrodes are placed in sequence, signals recorded within microchannels can be used to determine the direction of signal propagation by detecting conduction delays. The temporal difference between the negative amplitudes of correlated signals is defined as the time needed for the same spike to cross the distance between two electrodes (see Figure 5.33).

As the electrode distance is predefined, it is possible to calculate the propagating speed of the observed action potential is possible using the following equation:

$$v = \frac{s}{\Delta t} \tag{5.1}$$

where the propagation velocity ($\boldsymbol{v}$) is calculated as the ratio between the electrode distance ($\boldsymbol{s}$), in this case, a constant 200 µm and the time ($\Delta \boldsymbol{t}$) it takes for the action potential to travel that distance.

Figure 5.34 (B) shows that spikes from sequel electrodes E36 and E37 occur almost simultaneously. Figure 5.34 (C) displays spike pairs with a very short time delay, indicating that they occur due to the propagation of action potentials on axons. However, not all recorded signals have a corresponding match in the adjacent electrode. This phenomenon was previously reported by Wheeler's group (Pan et al., 2011), who suggested that some axons in a microchannel may be isolated from an electrode, resulting in the failure to record a traveling signal. Additionally, a single electrode often records a variety of spike shapes and amplitudes, indicating that multiple axons are present in the microchannel. Spike pair amplitudes can vary significantly due to the position of the axon within the electrically active microchannel. Figure 5.33 illustrates this phenomenon, where the amplitude difference between paired spikes can reach up to 200 µV. Therefore, spike pairs are distinguished based on waveform similarity and temporal proximity. The turquoise-framed spikes have triphasic shapes with a prominent first positive phase, a salient negative phase, and a small amplitude positive phase at the end. The time delay between negative phases and the order of their occurrence indicates that the spike is traveling in the expected direction, from left to right. The purple-framed second spike pair illustrates a different case. The waveform is also triphasic, but with the third phase larger in amplitude than the first phase. The time difference between negative phases in this pair of

spikes suggests that the propagation is in the opposite direction than expected, from right to left. These inequalities lead to the conclusion that the action potential originates from a different axon. There is a slight distortion between the waveforms of the spike pair labeled purple. The waveform recorded on electrode E37 has a wider shape than its pair due to the existing hump notable on the right side of the shape. The cause of this occurrence is uncertain, but one possibility is the superposition of two different spikes, as previously described by Hierlemann's group (Lewandowska et al., 2015).

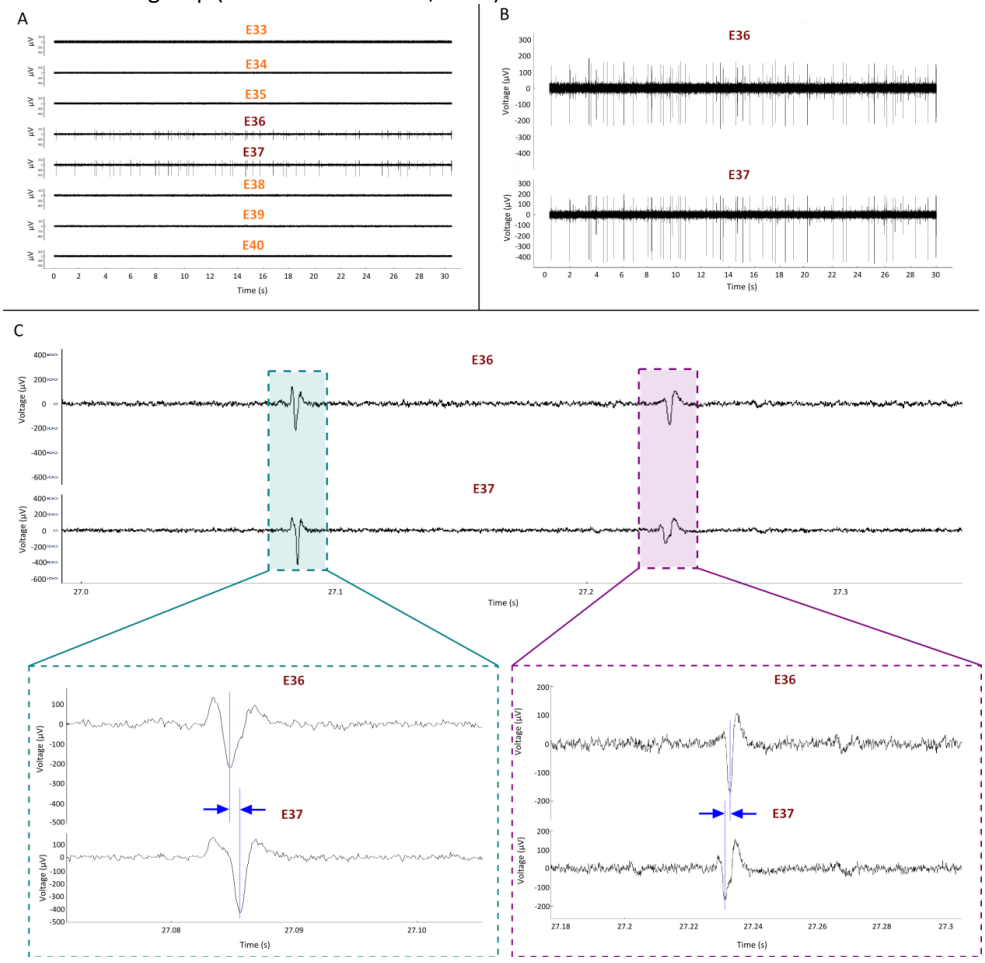

Figure 5.34 – Propagating signals recorded within the microchannel. (A) Electrodes E36 and E37, located within the microchannel, showed notably higher action potential amplitudes compared to electrodes outside the microchannel. **(B)** The signals from electrodes E36 and E37 were nearly simultaneous. **(C)** The top panel displays an enlarged view of spike pairs on electrodes E36 and E37. Two spike pairs are indicated by the frames. The bottom panel shows the same spike pairs and indicates the temporal difference between each pair (labeled with blue arrows). The pair framed in turquoise color depicts positive signal propagation, with the action potential propagating from the left to the right compartment as expected. The pair framed in purple depicts propagation in the opposite direction.

5.4.2 Spike Detection and Direction of Signal Propagation

In the following sections, the results of signal propagation analysis obtained by the µFluidic-MEA hybrid devices presented in this thesis will be presented. To account for a large amount of noise on some recording electrodes, parameters for spike detection had to be modified. The modifications were discussed with and introduced in the analysis algorithm by a colleague PhD student, Bogdana Čepkenović. The criterion for spike detection was set at a rigorous threshold of 30 or 40 µV, depending on the individual case. This approach reduces the number of detected spikes but improves the quality of the analyzed data. This is accomplished by focusing solely on amplified spikes with well-defined negative peak form. Figure 5.35 presents a

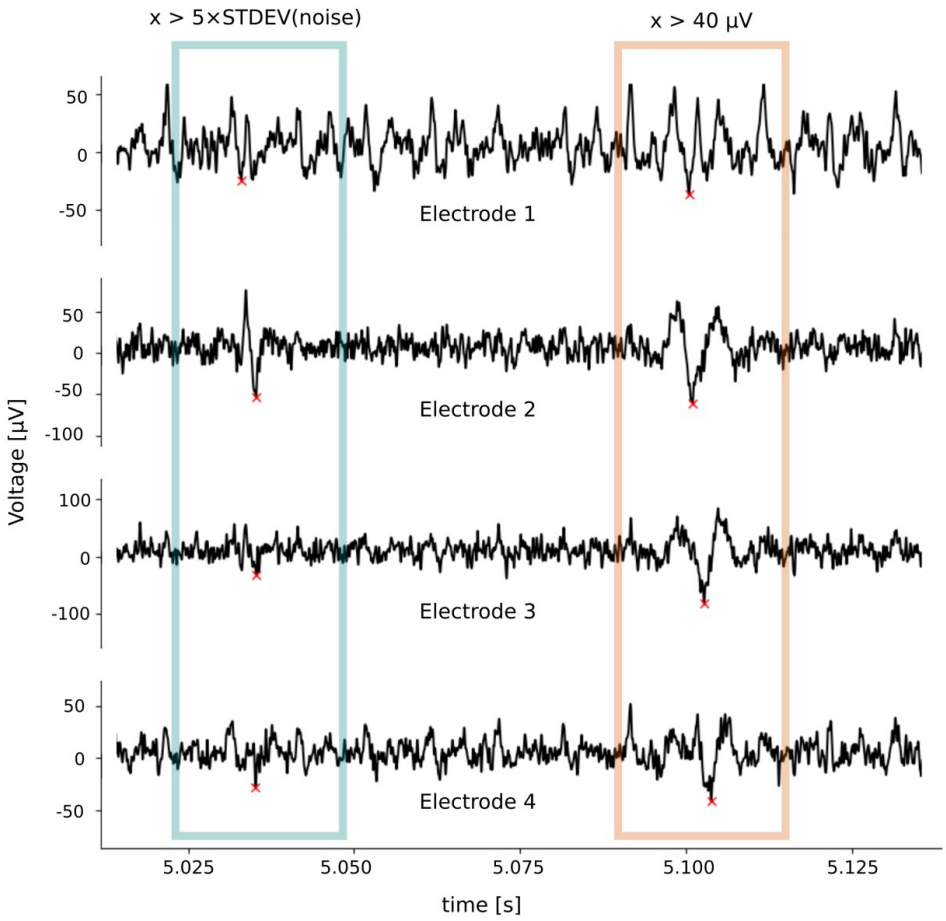

Figure 5.35 – Spike detection criteria affect the quality of pulled data for signal propagation analysis. Setting the threshold to 5×STDEV (noise) often detects unreliable paired spikes throughout the microchannel (blue rectangle). The new criterion, which focuses on spikes above 40 µV (or 30 µV in some recordings), provides a more reliable set of spike pairs for propagation analysis (orange rectangle).

recording that illustrates the difference in detection selectivity depending on the parameters chosen for recognizing action potential spike forms. In both cases, the referent electrode is positioned at E2, and spikes on adjacent electrodes are referenced to the spikes found on this electrode. When setting the parameters to a threshold of 5 × STDEV (noise), both spikes are detected. However, when limiting x to > 40µV, only the spike in the orange rectangle is visible. The spikes on E2 are well-defined and would be classified as *Type 3* (blue) and *Type 4* (orange) spike shapes. However, the situation on adjacent electrodes is not the same in both cases, as the assigned spikes in the rest of the electrodes are not well-defined in a blue rectangle. The distorted shapes indicate that the peaks are more likely to be due to noise rather than actual spikes. Therefore, the spike detected on the E2 electrode is likely an isolated event from an axon that is not in close proximity to adjacent electrodes within the microchannel. By adjusting the threshold to 40 µV, events like this are excluded, and the focus is solely on spikes that have a recognizable shape on all recording electrodes.

Sampling Rate and Velocity Expectance

The sampling rate for signal propagation analysis was set at 50 kHz, providing a higher temporal resolution than in the case of recordings used for spike-shape analysis. This results in a theoretical temporal delay of 0.02 ms between two paired spikes on adjacent electrodes. Any time delay shorter than this was considered invalid and ignored by the analysis algorithm. Based on the given conditions, this device can detect a maximum propagation velocity of 10 m/s.

5.4.2.1 Possible Directions of Signal Propagation

Recorded samples revealed three types of propagation direction, all three illustrated in Figure 5.36: **forward** (orthodromic), **backward** (antidromic), and **atypical** (ortho- and antidromic at the same spike pairing sequence). The origins of all three types will be discussed in the following paragraphs, as they are important in understanding the nature of neuronal networks and their possible controllability. Further adjustments in selection criteria were introduced to distinguish between these directions of propagation.

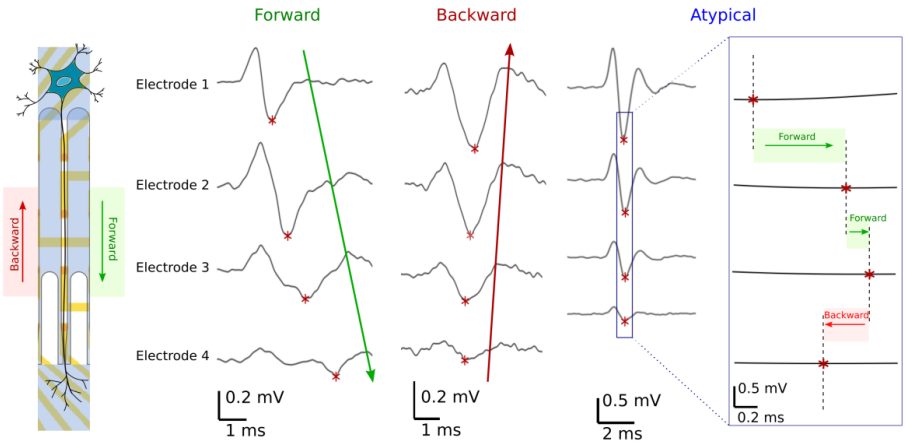

Figure 5.36 – Three possible directions of signal propagation. The expected direction of propagation is from the left to the right compartment with respect to the axon diode orientation. Backward propagation can also occur due to various reasons. The spike train exhibits both forward and backward directions, which is an atypical directionality.

Forward Direction of Signal Propagation

The second criterion introduced narrows the analysis to spike-pairs that propagate in a forward direction along the entire microchannel within the expected time resolution defined by the recording's sampling rate. Spike trains with at least one spike-pair propagating in the opposite direction or with a time delay below the set temporal resolution were excluded from further analysis. The analysis was conducted on only a portion of the total number of detected spikes. Additionally, this approach shows promise in defining the activity of individual axons. As previously mentioned, axons tend to form bundles when growing along the microchannel, making it challenging to distinguish the individual activity of one axon. This is also why some detected spikes do not have a corresponding spike pair on adjacent electrodes. However, if spike pairs are detected on all adjacent electrodes and they propagate in the same direction, it is highly probable that the detected propagation event is associated with a specific axonal activity. This criterion further reduced the number of spikes analyzed, as illustrated in Figure 5.37.

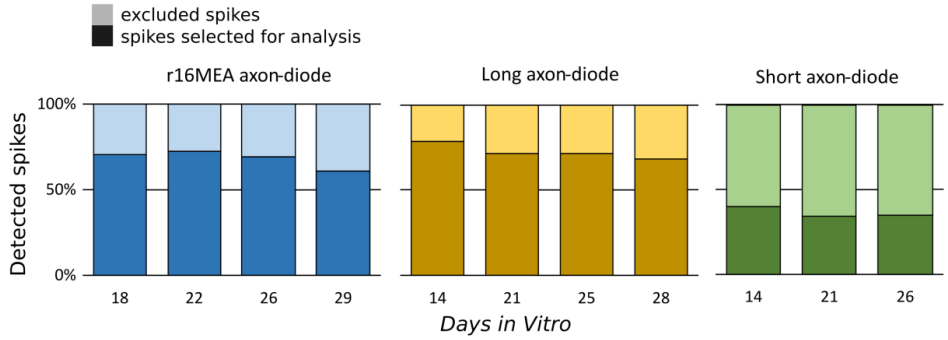

Figure 5.37 – The use of specific selection criteria reduces the initial number of detected spikes. Dark and bright bars represent selected and excluded spikes, respectively. The figure shows one sample from each of the signified groups: µFluidic-r16MEA, µFluidic-MEA-long, and µFluidic-MEA-short microchannels.

The figure shows the ratio of selected spikes for further analysis (dark bars) to excluded spike-pairs due to non-fulfillment of the given conditions (light bars). Additionally, the figure displays one co-culture from each group: µFluidic-r16MEA (blue), µFluidic-MEA with long axon-diodes (yellow), and µFluidic-MEA with short axon-diodes (green). The ratio remains consistent over time within each sample, indicating stable network activity and signal propagation directionality. It is worth noting that for short axon-diodes, the number of excluded spike-pairs is greater than the number of forward-propagating pairs. These excluded pairs originate from either back-propagating pairs or pairs with a time delay below 0.02 ms.

Backward Direction of Propagation

As previously described by Taylor et al. (2003), axon-diode microchannels offer limited unidirectionality for axonal growth. Axons can grow along microchannels from both subcompartments of a device, allowing for backward propagation of the signal. The constriction at the end of the channel decreases the likelihood of axonal growth in the opposite direction. However, propagating events are still detected in this direction. It is important to consider other potential causes of backward propagation. In a recent 2021 publication, Aguiar's group investigated possible causes of backward propagation (Mateus et al., 2021), including ephaptic coupling, axon regrowth, axo-axonal coupling, and antidromic conduction caused by spontaneous activation in distal parts of the axon. They concluded that

antidromic conduction is the most frequent cause of backward propagation of action potentials. This significantly changes the course of understanding on how information flows in *in vitro* neuronal cultures. As pointed out by the authors, this study suggests that unidirectional axonal growth may not necessarily lead to unidirectional information flow.

The author notes that many attempts have been made to acquire the microenvironment with the purpose of improving the unidirectionality of axonal growth (Aebersold et al., 2016; Holloway et al., 2021; Habibey et al., 2022), including a part of this thesis. This passage discusses the challenge of identifying the origin of backward propagating signals in dual-compartment systems with co-cultured neuronal networks. To address this challenge, a detailed examination is necessary. Therefore, quantifying only the backward propagating signals cannot be used as a reliable criterion for analyzing the proposed unidirectionality of the device. Regardless of their nature of origin, backward propagating signals were detected in all axon diode microchannel lengths. Figure 5.38 (i, iii, iv, v) illustrates possible causes of backward propagation detection.

Atypical Direction of Propagation

Spike-pairs of reverse propagation direction were occasionally recorded in only one part of the microchannel, while the rest of the paired spikes maintained the orthodromic direction (Figure 5.36). This phenomenon could only be observed in microchannels containing more than two electrodes. However, this occurrence contradicts the assumption that the axon elongates through the entire microchannel. It is challenging to substantiate such an occurrence based on the available data. This irregular spike propagation may be caused by incorrect spike-pairing due to the analysis algorithm, or waveform distortion leading to inaccurate detection of the negative peak. The exclusion of these spike-pairs has reduced the number of actual spikes analyzed for signal propagation velocities. Figure 5.38 (b, f) illustrates possible causes of backward propagation detection.

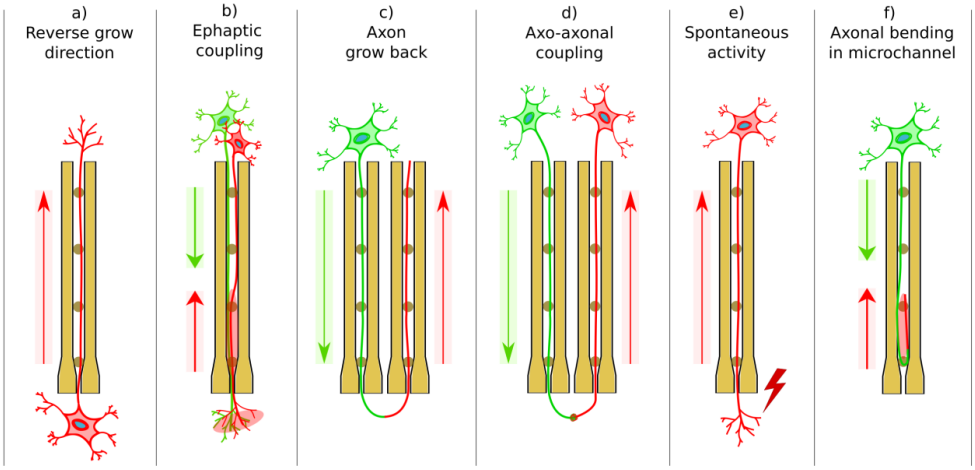

Figure 5.38 – Schematic of the possible causes for backward and atypical propagation. Neurons are color-coded based on their propagation direction: red for backward and green for forward. Arrows of the same colors indicate the direction of propagation and the region of the microchannel where it occurs. Six possible scenarios that can result in back-propagating signals in a part or along the entire microchannel are presented from left to right.: **(a)** axonal extension in the opposite direction (reverse growth direction); **(b)** nonsynaptic electrical coupling (ephaptic coupling); **(c)** axon growth back to the same compartment after full extension to the other compartment ('U'-turn); **(d)** axo-axonal coupling caused by electrical synapse and/or gap junction; **(e)** spontaneous activation in the distal regions of the axon; **(f)** bending of the axon due to a change in microchannel geometry. The figure was adapted from (Mateus et al., 2021).

5.4.3 Signal Propagation Velocities Along the Microchannels

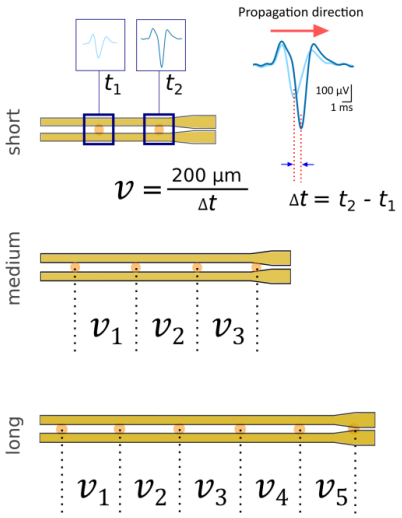

Figure 5.39 – Propagation velocities were observed between each pair of adjacent electrodes. The distance between electrodes was constant at 200 µm. Time delays were measured as the time differences between spike pairs in adjacent electrodes.

Section 5.4.1 explains that signal propagation velocity is defined by the time delay of spike-pairs detected on two successive electrodes of known distance. To understand possible changes in velocities along the axon, propagation was observed in portions by measuring the velocity between each two adjacent electrodes within the microchannel. Figure 5.39 shows the velocity sequences for each microchannel length.

Spike time stamps are determined as the time points where the negative peak reaches its maximum amplitude. The temporal resolution for calculating signal propagation velocity depends on the sample rate of the analyzed recording and is set to 50 kHz. This means that the highest theoretically possible propagation velocity that can be measured with this device is 10 m/s. Although the device offers high temporal resolution and the possibility of axonal isolation, it is important to note that axons are unlikely to grow in a straight line over the recording electrodes. This can make it challenging to obtain accurate results on the velocity of the traveling action potential. However, by considering the predicted approximation, the device provides an opportunity to understand the electrophysiological behavior of neuronal networks.

5.4.3.1 Signal Propagation Velocities Along Long Microchannels

After applying all the described conditions for detecting orthodromic propagating spike pairs, I observed a significant reduction in the number of detected spikes. This reduction had an impact on the final number of cell cultures with a sufficient number of microchannels to provide satisfactory recordings. The number of active microchannels in the cultures varied

over time. Therefore, I decided to focus on presenting the results of only one cell culture that showed consistent activity up to DIV 28 (Figure 5.40).

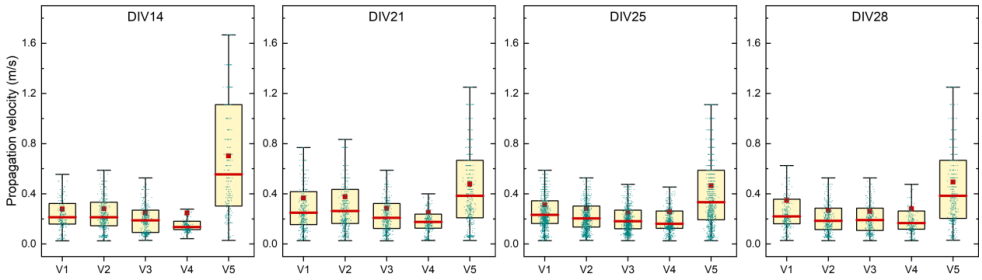

Figure 5.40 – The distribution of propagation velocities along the long microchannel. The box plots illustrate the velocity distribution in specific regions of the microchannel over time. Green dots represent the data points of each velocity position plotted over the box plots. Median values are presented by red lines, and mean values are shown by dark red squares for each set of data.

The number of active microchannels remained consistent throughout the recording period, with at least 50% activity yield on all days. Specifically, there were four active microchannels at DIV 14, eight at DIV 21 and DIV 25, and six at the final DIV 28. The velocities remained constant along the microchannel and over time, with a sudden change occurring between electrodes E6 and E7, where V5 was recorded. This trend is consistent over time, suggesting that the geometry of the microchannel can influence the propagating signal velocity. The last electrode (E7) is positioned at the narrowing part of the emitting side of the microchannel. The narrowed channel may serve as an axonal straightener, as the environment is confined and leaves very little freedom for axonal meandric growth. By straightening this part of the axon, the distance that it passes from E6 to E7 is shorter, and closer to the actual electrode distance. This may lead to a decrease in conduction delays, and an overall increase of measured velocity (V5).

The complete tabular presentation of measured velocities along the microchannels over time is given in Table D.1.

5.4.3.2 Signal Propagation Velocities Along Medium Microchannels

The microchannels in the µFluidic-r16MEA devices are designed and sized to match the medium axon-diode microchannels. The cell cultures and overall microchannel activity were

more successful compared to cultures in traditional µFluidic-MEA devices. Therefore, I present the results from these updated and improved devices (Fig. 5.41).

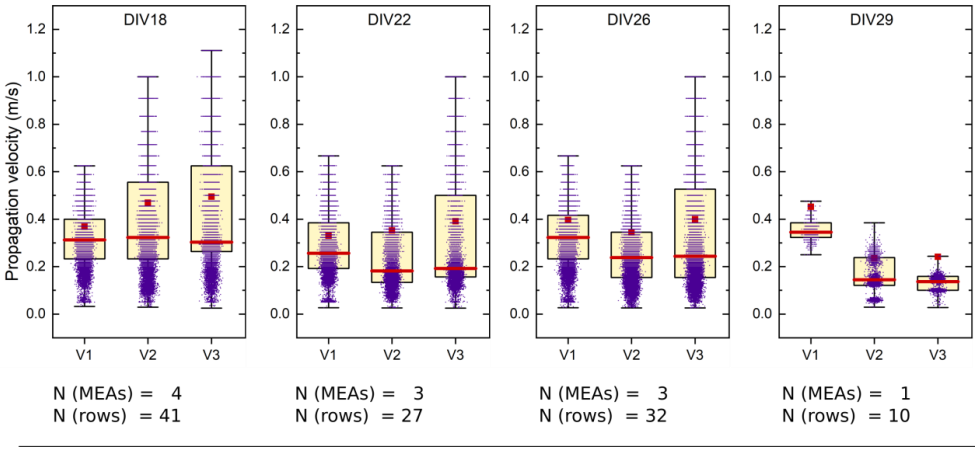

Figure 5.41 – Propagation velocities distribution in µFluidic-r16MEAs over time. Each recordable DIV had a different number of cultures and electrically active microchannels. The box plots illustrate the distribution of velocities in specific parts of the medium-sized microchannel length. The purple dots over the box plots represent the data points of each recording.

Each microchannel has four recording electrodes, enabling the detection of three sequential spike-pairs or three propagation velocities along the axon: V1, V2, and V3. The number of active microchannels per DIV is: 41 for DIV 18, 27 for DIV 22, and 32 for DIV 26. Data sets are combined and analyzed with respect to the velocity position and DIV at which the recording was taken. Unlike the previously presented results from the long microchannels, there is no evident increase in median velocity values at the narrowing part of the microchannels. The distance of the last recording electrode from the microchannel exit is 56 µm longer than in the case of long microchannel (exact distances depicted in Figure 5.24 in section 5.3.1). Velocities remain in constant range over time. DIV 29 shows a different distribution of values with a drop in values V2 and V3. However, this is a presentation of only one cell culture that remained active until DIV 29.

The complete tabular presentation of measured velocities along the microchannels over time is given in Table D.2.

5.4.3.3 Signal Propagation Velocities Along Short Microchannels

A total of four cell cultures were observed from DIV 14, with a total of 14 active microchannels for data analysis. The number of active cultures decreased at DIV 26 and DIV 28 due to the maturing of the cells. When it comes to short microchannels, an interesting effect is observed in the initial day of recording. Analyzed propagation velocities are higher than in previously analyzed samples, with median values reaching 1.7 m/s (*Q1*: 0.3; *Q3*: 3.3) (Figure 5.42 (A)). These values then decrease in the following days, with values of 0.5 m/s (*Q1*: 0.2; *Q3*: 1.7).

A Results with theoretically possible outcome

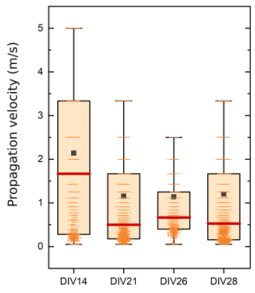

	DIV14	DIV21	DIV26	DIV28
Median	1.7	0.5	0.7	0.5
Q1 | Q3:	0.3 | 3.3	0.2 | 1.7	0.4 | 1.3	0.2 | 1.7
Mean ± SD	2.1 ± 1.9	1.2 ± 1.4	1.1 ± 1.2	1.2 ± 1.4

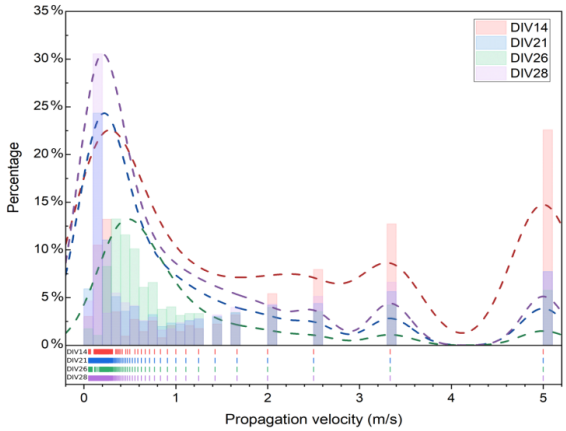

B Results with electrophysiologicaly possible outcome

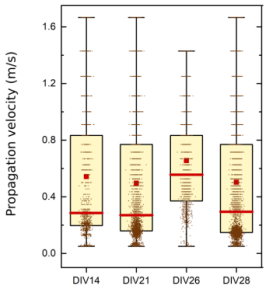

	DIV14	DIV21	DIV26	DIV28
Median	0.3	0.3	0.6	0.3
Q1 | Q3:	0.2 | 0.8	0.2 | 0.8	0.4 | 0.8	0.1 | 0.8
Mean ± SD	0.5 ± 0.5	0.5 ± 0.5	0.7 ± 0.4	0.5 ± 0.5

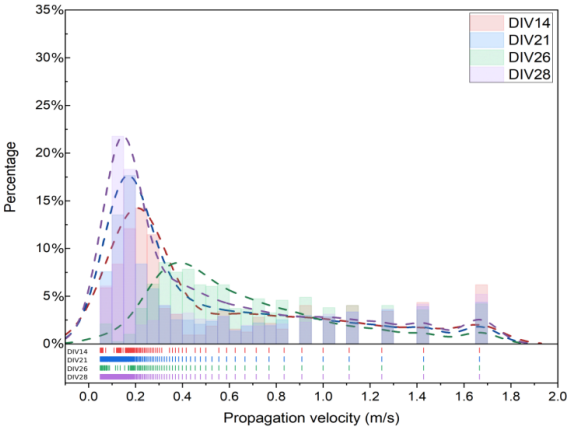

Figure 5.42 – Distribution of propagation velocities along short microchannels. (A) The available datasets showed a highly non-uniform distribution of velocities, with a significant number of very large velocity values ranging up to 5 m/s. **(B)** The same set of results was analyzed again, excluding values higher than 2 m/s, which were considered highly unlikely electrophysiological events under the given conditions.

Mean values of the same data set reach up to 2.1±1.9 m/s, at DIV14. These values suggest that many spike pairs are at the edge of time delay detection resolution, which is why I decided to exclude all spike pairs with conduction delay equal to or smaller than 0.1 ms. Although action potentials can have high speed values *in vivo*, it is very unlikely to expect this under electrophysiological conditions of unmyelinated axons of primary rat neurons. Corresponding results are presented in Figure 5.42 (B). Median velocities have more consistent values, as listed in the table in the same figure, resulting in 0.3 m/s propagation velocities and rise to 0.6 m/s at DIV 26.

5.4.3.4 *Signal Propagation Velocities in The Central Region of Microchannels*

Next, I observe the propagation velocities in the central region of microchannels, regardless of microchannel length. I chose to observe this part of the microchannel as it is expected that the recording electrodes are uniformly covered by axons. The median values of gathered data are listed in the table in Figure 5.43. Combined data suggests that the velocity range in this region has small changes over time.

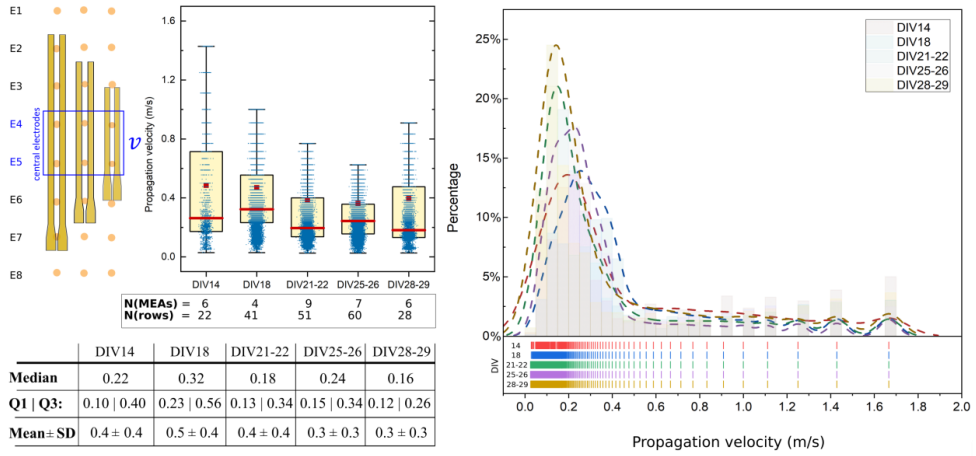

	DIV14	DIV18	DIV21-22	DIV25-26	DIV28-29
Median	0.22	0.32	0.18	0.24	0.16
Q1 | Q3:	0.10 | 0.40	0.23 | 0.56	0.13 | 0.34	0.15 | 0.34	0.12 | 0.26
Mean± SD	0.4 ± 0.4	0.5 ± 0.4	0.4 ± 0.4	0.3 ± 0.3	0.3 ± 0.3

Figure 5.43 – The distribution of propagation velocities in the central region of each microchannel length. The sketch on the left shows the central electrodes within each microchannel length. The data sets were obtained from all available recordings in each DIV range. The blue dots over the box plots represent the data points of each recording. The number of active cell cultures (MEAs) and recordable electrically active microchannels (rows) are listed beneath each corresponding box plot.

5.5 Conclusions and Outlook

A more detailed examination of the electrophysiological connectivity between co-cultures was conducted in this chapter. The observed co-culture connectivity was confirmed by measuring the overall slow oscillations, which are typical for homogeneous in vitro networks (Neske, 2016). This suggests that the microenvironmental manipulation of cell growth does not impact the network synchrony. However, the total microchannel activity yield demonstrated a dependence on the final device assembly method. The irreversible bonding process resulted in a more compact and stable usability of each device, in comparison to the reversible assembly method, which exhibited unstable neuronal network connectivity over time. The improved sealing of axons to the electrodes by APTES treatment for irreversible device assembly may be a contributing factor to this outcome.

The spike shapes were analyzed by classifying the recorded spike-triggered averaged shapes into eight different shape types. All types have been previously reported (Lewandowska et al., 2015; Deligkaris et al., 2016), except for the *monophasic* type (T7), which was recognized and classified in this analysis. The distribution of shapes along the microchannels is dependent on the device assembly approach and the length of the microchannels. In general, the variety of occurring spike shapes is larger in longer microchannels compared to shorter microchannels and in reversible (RB) compared to irreversible (IRB) assembled devices. Nevertheless, the most frequently occurring spike shapes fall under the category of biphasic (~20%) and triphasic (~50% to ~90%), in accordance with previously described shape types by aforementioned research groups. The distribution of the newly recognized monophasic shape exhibits a unique trend in relation to the observed position of the electrode within the microchannel and cell culture maturity. Its occurrence is most prominent at the beginning of the cell culture activity (at DIV 14) and is recorded mostly at the boundary electrodes inside the microchannels (electrode positions E2 and E7 in long microchannels). The amplitude of this shape is usually below 0.1 mV and remains constant over time, while all other shapes show more dynamic change of amplitudes over time. The cause of this phenomenon can be linked to previously reported microscopic observations by Pan et al. (2012) who described a tendency for axonal growth along the walls in the boundary microchannel area. The sealing of the axons and electrodes is less successful in this area, resulting in less defined shape and lower amplitude spikes being recorded.

The amplification of the signals was in accordance with previous findings (FitzGerald et al., 2008), but with a different spatial pattern than described by Pan et al. (2012). A unique ascending or descending trend of amplification is characteristic of each individual sample observed separately. The trend of amplification remains the same over time with possible occasional shifts between adjacent electrodes with the largest p2p value recorded. This indicates only slight changes in the dynamics of axon movement over time and its constant relationship with the surrounding microenvironment. However, the type of device assembly influences the amplification effect of the recording microchannels in a µFluidic-MEA device. The improved contact between axon and electrode in IRB samples provides a larger number of spike amplitudes above 0.2 mV than in RB samples. In both types of assembly, the majority of spikes with medium and large amplitudes are detected within short microchannels. The only explanation for this phenomenon is the attenuation of the signal when measured with longer microchannels.

The electrode sequence within microchannels allows the measurement of signal propagation velocities of an observed culture. This has already been investigated in similar µFluidic-MEA systems (Bradley J. Dworak, 2009) and serves as an established tool for better understanding of neuronal network information processing. The successful unidirectionality of the axon-diode microchannels reported by Taylor et al. (2003) could not be replicated, necessitating the inclusion of all three (forward, backward, and atypical) propagation directions in the analysis. The detected velocities are consistent with previously published values by Bradley J. Dworak and range between 0.14 and 0.56 m/s median values. A change in velocities is not significant along medium-length microchannels, while an increase is detected in the last electrode sequence within long microchannels. This suggests a possible effect of the narrowing microstructure on the emitting side of the microchannel, where the last recording electrode is placed. One probable reason is that the axons become straightened in this section, while they have more space to meander in the rest of the microchannel area. Further detailed examinations of this phenomenon would be required to gain a more comprehensive understanding of this change.

Conclusions and Outlook

The mystery of the brain and its mechanisms of function have been a source of fascination for scientists from diverse fields for centuries. The advancement of technology has played a pivotal role in addressing the challenges and providing insights into the enigmatic nature of the brain. The comprehension of the information processing between neuronal cells reveals the mechanisms of brain function, thereby paving the way for the discovery of novel therapeutic approaches for the treatment of various diseases and illnesses. One of the methodologies employed in the manipulation of in vitro neuronal networks with microfluidic microchannels is presented in this thesis in a comprehensive manner, accompanied by a detailed characterisation.

Although this technique has been employed since the 1970s, the advent of new technology offers promising avenues for enhancing the microfluidic system, potentially leading to more straightforward and dependable applications. In this thesis, I have utilized compartmentalized microfluidic devices assembled on top of an MEA with pre-existing microchannels. This innovative approach of direct microchannel structuring on top of the recording device has not been previously documented in the literature. A photosensitive polymer, HD-8820, was utilized for this purpose, as a stable and biocompatible material that is often employed for the creation of micron-scale patterns with controlled side-wall profiles. Two primary groups of hybrid devices were developed: µFluidic-iMEA200 and µFluidic-r16MEA. The initial set of devices was constructed with three distinct microchannel lengths, while the second set featured a doubled number of electrically active microchannels with a constant length. The r16MEA's design variation was concentrated in the subcompartments, with the introduction of axon-guiding shapes on the receiving side and axon-trap shapes on the emitting side of the microchannels.

The optimization of hybrid-device use was contingent upon the successful placement of primary neuronal cells for uniform distribution of axons crossing the recording platform. Approaches such as additional and wide chambers were introduced as potential solutions to the creation of uniform network connectivity, but were not considered for the final use of the hybrid devices. Instead, an optimized seeding technique was developed with the objective of maintaining the structural integrity of the microfluidic. The results of immunocytochemistry

of the prepared cultures in different microfluidic designs revealed that the previously reported high unidirectionality of the original axon-diode microchannels could not be reproduced. The reason for such results may be connected to the experimental setup itself and slight differences in microchannel dimensions used in this thesis compared to those developed by Taylor et al. Improvements were achieved by limiting the number of electrically active microchannels and introducing axon-trap shapes. A quantitative immunocytochemical analysis indicated that the Ver2 design exhibited the most promising effect in reducing the number of axons growing through the microchannels in the opposite direction. Further investigation, including a larger number of samples and qualitative analysis of immunocytochemical results, is necessary for a clear and reliable comparison of the proposed designs.

This thesis addresses three main topics related to extracellular activity of neuronal co-culture: (1) action potential waveform shape analysis, (2) amplification effect of microchannels, and (3) signal propagation directionality and velocity. Extracellular action potential shape analysis is based on the classification of spike-triggered averaged waveforms into eight categories of unique shapes. The most prevalent shape observed in all samples, regardless of the day of the recording, was a group of triphasic spike shapes. The device assembly approach (RB vs. IRB) influenced the overall distribution of shapes along the long microchannels. This was most evident in the occurrence of the small-amplitude monophasic shape, which was predominantly detected on the first and last electrodes within the microchannel and was more prevalent in RB samples. The observed phenomenon may be attributed to the differential sealing of cells to the recording surface when comparing the RB and IRB device assembly approaches. This indicates that for more accurate spike shape analysis, the IRB approach should be employed, as it provides a more stable and compact environment for the development of *in vitro* neuronal networks. The assembly type also exhibits a comparable outcome with regard to the amplification effect. A greater number of spike amplitudes above 0.2 mV is observed in IRB samples than in RB samples. The length of the microchannel also affects the results, with shorter microchannels demonstrating the most effective amplification, while the signal becomes attenuated in the other lengths. The signal propagation velocity can be measured with all microchannel lengths, but only in sequences, by calculating the velocity of spike pairs between each pair of electrodes. This implies that the long microchannels measure a total of five separate velocities, which are then averaged to obtain the final value. However, the geometry of the microchannel and the position of the electrodes in the long

microchannel affect the individual velocities between each detected spike pair. The propagation velocity value significantly increases towards the end of the long microchannel, where the last recording electrode is found at the narrowing part of the microchannel. This is a significant finding, as it provides insight into the axonal dynamics in confined spaces, where the geometry must be considered in order to understand the results. The median values fall within the range of previously reported results by other research groups.

In conclusion, a novel set of adaptations was introduced and tested in this thesis, resulting in successful electrophysiological analysis of neuronal co-cultured networks that could be validated by previously published findings. As reported by Lewandovska et al., the most frequently observed EAP waveform is triphasic in nature. In addition to the same shapes recognized in this thesis, a monophasic shape has been identified and described, offering valuable insight into axonal dynamics within the recording microchannel. The impact of microchannel asymmetrical geometry and the newly introduced irreversible device assembly provide important directions for further development and use of these devices. Furthermore, it has been demonstrated that in contrast to the design developed by Peyrin et al., the µFluidic-r16MEA divided microchannel layout provides a more stable and reliable microenvironment with reproducible trends of axon potential amplification. Collectively, these incremental advances create a set of possibilities that bring us closer to understanding all known and unknown mysteries of the brain.

References

Abbott, J., Ye, T., Krenek, K., Gertner, R. S., Wu, W., Jung, H. S., et al. (2020). **Extracellular recording of direct synaptic signals with a CMOS-nanoelectrode array**. *Lab Chip* 20, 3239–3248. doi: 10.1039/d0lc00553c

Abbott, L. F. (1999). **Lapicque's introduction of the integrate-and-fire model neuron (1907)**. *Brain Res Bull* 50, 303–304. doi: 10.1016/S0361-9230(99)00161-6

Aebersold, M. J., Dermutz, H., Forró, C., Weydert, S., Thompson-Steckel, G., Vörös, J., et al. (2016). **"Brains on a chip": Towards engineered neural networks.** *TrAC Trends in Analytical Chemistry* 78, 60–69. doi: 10.1016/J.TRAC.2016.01.025

Alt, K. W., Jeunesse, C., Buitrago-Tellez, C. H., Wachter, R., Boes, E., and Pichler, S. L. (1997). **Evidence for stone age cranial surgery**. *Nature* 387, 360. doi: 10.1038/387360a0

Anastassiou, C. A., Perin, R., Buzsáki, G., Markram, H., Koch, C., and Anastassiou, C. A. (2015). **Cell type-and activity-dependent extracellular correlates of intracellular spiking**. *J Neurophysiol* 114, 608–623. doi: 10.1152/jn.00628.2014.-Despite

Anastassiou, C., Buzsáki, G., and Koch, C. (2013). "**Biophysics of extracellular spikes," in *Principles of Neural Coding***, eds. R. Quian Quiroga and S. Panzeri (Boca Raton, FL: CRC Press Taylor & Francis Group), 15–37.

Antonello, P. C., Varley, T. F., Beggs, J., Porcionatto, M., Sporns, O., and Faber, J. (2022). **Self-organization of in vitro neuronal assemblies drives to complex network topology**. *Elife* 11. doi: 10.7554/ELIFE.74921

Aumiller, G. D., Chandross, E. A., Tomlinson, W. J., and Weber, H. P. (1974). **Submicrometer resolution replication of relief patterns for integrated optics**. *J Appl Phys* 45, 4557. doi: 10.1063/1.1663087

Bakkum, D. J., Frey, U., Radivojevic, M., Russell, T. L., Müller, J., Fiscella, M., et al. (2013). **Tracking axonal action potential propagation on a high-density microelectrode array across hundreds of sites**. *Nat Commun* 4, 2181. doi: 10.1038/ncomms3181

Bartlett, W. P., and Banker, G. A. (1984). **An electron microscopic study of the development of axons and dendrites by hippocampal neurons in culture. I. Cells Which Develop Without Intercellular Contacts**. *The Journal of Neuroscience* 4, 1944–1953. doi: 10.1523/JNEUROSCI.04-08-01944.1984

Bashir, A., Awan, T. I., Tehseen, A., Tahir, M. B., and Ijaz, M. (2020). **"Interfaces and surfaces,"** in *Chemistry of Nanomaterials*, (Elsevier), 51–87. doi: 10.1016/B978-0-12-818908-5.00003-2

Bear, M. F., Connors, B. W., and Paradiso, M. A. (2015). ***Neuroscience: Exploring the brain***., 4th ed., eds. E. Lupash, E. Connoly, B. Dilernia, and P. Williams. Philadelphia (PA): Lippincott Williams & Wilkins.

Bear, M. F., Connors, B. W., and Paradiso, M. A. (2015)a. **Neurons and Glia**. In: *Neuroscience: Exploring the brain*. 4th ed., eds. Lupash, E., Connoly, E., Dilernia, B., and Williams, P., fourth edition, Lippincott Williams & Wilkins, Philadelphia (PA), Chapter 2, p. 29 ff. ISBN 978-0-7817-7817-6

Bear, M. F., Connors, B. W., and Paradiso, M. A. (2015)b. **The Neuronal Membrane at Rest**. In: *Neuroscience: Exploring the brain*. 4th ed., eds. Lupash, E., Connoly, E., Dilernia, B., and Williams, P., Lippincott Williams & Wilkins, Philadelphia (PA),, Chapter 3, p. 66-70 ff. ISBN 978-0-7817-7817-6

Bear, M. F., Connors, B. W., and Paradiso, M. A. (2015)c. **The Neuronal Membrane at Rest**. In: *Neuroscience: Exploring the brain*. 4th ed., eds. Lupash, E., Connoly, E., Dilernia, B., and Williams, P., Lippincott Williams & Wilkins, Philadelphia (PA), Chapter 3, p. 71-72 ff. ISBN 978-0-7817-7817-6

Bear, M. F., Connors, B. W., and Paradiso, M. A. (2015)d. **The Action Potential**. In: *Neuroscience: Exploring the brain*. 4th ed., eds. Lupash, E., Connoly, E., Dilernia, B., and Williams, P., Lippincott Williams & Wilkins, Philadelphia (PA), Chapter 4, p. 100 ff. ISBN 978-0-7817-7817-6

Bear, M. F., Connors, B. W., and Paradiso, M. A. (2015)e. **The Action Potential**. In: *Neuroscience: Exploring the brain*. 4th ed., eds. Lupash, E., Connoly, E., Dilernia, B., and Williams, P., Lippincott Williams & Wilkins, Philadelphia (PA), Chapter 4, p. 84 ff. ISBN 978-0-7817-7817-6

Bear, M. F., Connors, B. W., and Paradiso, M. A. (2015)f. **Synaptic Transmission**. In: *Neuroscience: Exploring the brain*. 4th ed., eds. Lupash, E., Connoly, E., Dilernia, B., and Williams, P., Lippincott Williams & Wilkins, Philadelphia (PA), Chapter 5, p. 110-120 ff. ISBN 978-0-7817-7817-6

Bear, M. F., Connors, B. W., and Paradiso, M. A. (2015)g. **The Action Potential**. In: *Neuroscience: Exploring the brain*. 4th ed., eds. Lupash, E., Connoly, E., Dilernia, B., and Williams, P., Lippincott Williams & Wilkins, Philadelphia (PA), Chapter 4, p. 92 ff. ISBN 978-0-7817-7817-6

Benjamin Kacerovsky, J., and Murai, K. K. (2016). **Stargazing: Monitoring subcellular dynamics of brain astrocytes**. *Neuroscience* 323, 84–95. doi: 10.1016/J.NEUROSCIENCE.2015.07.007

Berdichevsky, Y., Staley, K. J., and Yarmush, M. L. (2010). **Building and manipulating neural pathways with microfluidics**. *Lab Chip* 10, 999–1004. doi: 10.1039/b922365g

Bezanilla, F., and Armstrong, C. M. (1977). **Inactivation of the sodium channel. I. Sodium current experiments**. *Journal of General Physiology* 70, 549–566. doi: 10.1085/jgp.70.5.549

Boppart, S. A., Wheeler, B. C., and Wallace, C. S. (1992). **A Flexible Perforated Microelectrode Array for Extended Neural Recordings**. *IEEE Trans Biomed Eng* 39, 37–42. doi: 10.1109/10.108125

Bradley J. Dworak, B. C. W. (2009). **Novel MEA Platform with PDMS microtunnels enables detection of action potential propagation from isolated axons in culture**. *Lab Chip* 9, 404–410. doi: 10.1039/b806689b.Novel

Brofiga, M., Pisano, M., Raiteri, R., and Massobrio, P. (2021). **On the road to the brain-on-a-chip: a review on strategies, methods, and applications**. *J Neural Eng* 18, 041005. doi: 10.1088/1741-2552/AC15E4

Brooks, C. M., and Eccles, J. C. (1947). **Electrical investigation of the monosynaptic pathway through the spinal cord.** *J Neurophysiol* 10, 251–273. doi: 10.1152/jn.1947.10.4.251

Buzsáki, G., Penttonen, M., Nádasdy, Z., and Bragin, A. (1996). **Pattern and inhibition-dependent invasion of pyramidal cell dendrites by fast spikes in the hippocampus in vivo**. *Proceedings of the National Academy of Sciences* 93, 9921–9925. doi: 10.1073/PNAS.93.18.9921

Campenot (1977). **Local control of neurite development by nerve growth factor.** *Proceedings of the National Academy of Sciences* 74, 4516–4519. doi: 10.1073/pnas.74.10.4516

Castagnola, E., Maiolo, L., Maggiolini, E., Minotti, A., Marrani, M., Maita, F., et al. (2015). **PEDOT-CNT-Coated Low-Impedance, Ultra-Flexible, and Brain-Conformable Micro-ECoG Arrays**. *IEEE Transactions on Neural Systems and Rehabilitation Engineering* 23, 342–350. doi: 10.1109/TNSRE.2014.2342880

Chandler, W. K., and Meves, H. (1970). **Evidence for two types of sodium conductance in axons perfused with sodium fluoride solution**. *J Physiol* 211, 653–678. doi: 10.1113/JPHYSIOL.1970.SP009298

Chang, J. C., Brewer, G. J., and Wheeler, B. C. (2000). **Microelectrode Array Recordings of Patterned Hippocampal Neurons for Four Weeks**. *Biomedical Microdevices 2000 2:4* 2, 245–253. doi: 10.1023/A:1009946920296

Chiappalone, M., Bove, M., Vato, A., Tedesco, M., and Martinoia, S. (2006). **Dissociated cortical networks show spontaneously correlated activity patterns during in vitro development**. *Brain Res* 1093, 41–53. doi: 10.1016/J.BRAINRES.2006.03.049

Clark, J., and Plonsey, R. (1968). **The Extracellular Potential Field of the Single Active Nerve Fiber in a Volume Conductor**. *Biophys J* 8, 842. doi: 10.1016/S0006-3495(68)86524-5

Connors, B. W., and Long, M. a. (2004). **Electrical synapses in the mammalian brain**. *Annu Rev Neurosci* 27, 393–418. doi: 10.1146/annurev.neuro.26.041002.131128

Coquinco, A., Kojic, L., Wen, W., Wang, Y. T., Jeon, N. L., Milnerwood, A. J., et al. (2014). **A microfluidic based in vitro model of synaptic competition**. *Molecular and Cellular Neuroscience*. doi: 10.1016/j.mcn.2014.03.001

Czeschik, A., Offenhäusser, A., and Wolfrum, B. (2014). **Fabrication of MEA-based nanocavity sensor arrays for extracellular recording of action potentials**. *physica status solidi (a)* 211, 1462–1466. doi: 10.1002/PSSA.201330365

Czeschik, A., Rinklin, P., Derra, U., Ullmann, S., Holik, P., Steltenkamp, S., et al. (2015). **Nanostructured cavity devices for extracellular stimulation of HL-1 cells**. *Nanoscale* 7, 9275–9281. doi: 10.1039/C5NR01690H

Dayan, P., and Abbott, L. F. (2005). ***Theoretical Neuroscience***., 1st Edn. Cambrige (MA): MIT Press. ISBN: 0-262-04199-5

Debanne, D. (2004). **Information processing in the axon**. *Nat Rev Neurosci* 5, 304–316. doi: 10.1038/nrn1397

del Campo, A., and Greiner, C. (2007). **SU-8: a photoresist for high-aspect-ratio and 3D submicron lithography**. *Journal of Micromechanics and Microengineering* 17, R81. doi: 10.1088/0960-1317/17/6/R01

Deligkaris, K., Bullmann, T., and Frey, U. (2016). **Extracellularly recorded somatic and neuritic signal shapes and classification algorithms for high-density microelectrode array electrophysiology**. *Front Neurosci* 10, 421. doi: 10.3389/FNINS.2016.00421/BIBTEX

Donaldson, I. M. (2009). **The Treatise of man (De homine) by René Descartes**. *J R Coll Physicians Edinb* 39, 375–376. doi: 10.4997/JRCPE.2009.418

Duffy, D. C., McDonald, J. C., Schueller, O. J. A., and Whitesides, G. M. (1998). **Rapid prototyping of microfluidic systems in poly(dimethylsiloxane).** *Anal Chem* 70, 4974–4984. doi: 10.1021/ac980656z

Dworak, B. J., and Wheeler, B. C. (2009). **Novel MEA platform with PDMS microtunnels enables the detection of action potential propagation from isolated axons in culture**. *Lab Chip* 9, 404–410. doi: 10.1039/B806689B

Ecken, H., Ingebrandt, S., Krause, M., Richter, D., Hara, M., and Offenhäusser, A. (2003). **64-Channel extended gate electrode arrays for extracellular signal recording**. *Electrochim Acta* 48, 3355–3362. doi: 10.1016/S0013-4686(03)00405-5

Eick, S. (2009). **Extracellular Stimulation of Individual Electrogenic Cells with Micro-Scaled Electrodes**. *Fakultaet fuer Elektrotechnik und Informationstechnik* PhD. doi: nbn:de:hbz:82-opus-31710

Erickson, J., Tooker, A., Tai, Y. C., and Pine, J. (2008). **Caged neuron MEA: a system for long-term investigation of cultured neural network connectivity**. *J Neurosci Methods* 175, 1–16. doi: 10.1016/J.JNEUMETH.2008.07.023

Fatt, P. (1957). **Electric potentials occurring around a neurone during its antidromic activation**. *J Neurophysiol* 20, 27–60. doi: 10.1152/jn.1957.20.1.27

Faust, T. E., Gunner, G., and Schafer, D. P. (2021). **Mechanisms governing activity-dependent synaptic pruning in the developing mammalian CNS**. *Nat Rev Neurosci.* 22, 657-673. doi: 10.1038/s41583-021-00507-y

FitzGerald, J. J., Lacour, S. P., McMahon, S. B., and Fawcett, J. W. (2008). **Microchannels as axonal amplifiers**. *IEEE Trans Biomed Eng* 55, 1136–1146. doi: 10.1109/TBME.2007.909533

FitzGerald, J. J., Lacour, S. P., McMahon, S. B., and Fawcett, J. W. (2009**). Microchannel electrodes for recording and stimulation: In vitro evaluation**. *IEEE Trans Biomed Eng* 56, 1524–1534. doi: 10.1109/TBME.2009.2013960

Foremny, K., Konerding, W. S., Behrens, A., Baumhoff, P., Froriep, U. P., Kral, A., et al. (2021). **Carbon-Nanotube-Coated Surface Electrodes for Cortical Recordings In Vivo**. *Nanomaterials 2021, Vol. 11, Page 1029* 11, 1029. doi: 10.3390/NANO11041029

Fotovvati, B., Namdari, N., and Dehghanghadikolaei, A. (2019). **On Coating Techniques for Surface Protection: A Review**. *Journal of Manufacturing and Materials Processing 2019, Vol. 3, Page 28* 3, 28. doi: 10.3390/JMMP3010028

Fromherz, P. (2003). **Semiconductor chips with ion channels, nerve cells and brain**. *Physica E Low Dimens Syst Nanostruct* 16, 24–34. doi: 10.1016/S1386-9477(02)00578-7

Garcia-Lopez, P., Garcia-Marin, V., and Freire, M. (2010). **The histological slides and drawings of Cajal**. *Front Neuroanat* 4, 1–16. doi: 10.3389/neuro.05.009.2010

Gold, C., Henze, D. a., Koch, C., and Buzsáki, G. (2006). **On the origin of the extracellular action potential waveform: A modeling study**. *J Neurophysiol* 95, 3113–3128. doi: 10.1152/jn.00979.2005

Gotro, J. (2017). **Polymers in Electronics Part Seven: Redistribution Layers for Fan-Out Wafer Level Packaging.** Available at: https://polymerinnovationblog.com/polymers-electronics-part-seven-redistribution-layers-fan-wafer-level-packaging/

Gross, G. W. (1979). **Simultaneous Single Unit Recording in vitro with a Photoetched Laser Deinsulated Gold Multimicroelectrode Surface**. *IEEE Trans Biomed Eng* BME-26, 273–279. doi: 10.1109/TBME.1979.326402

Guo, J., Yuan, J., and Chan, M. (2012). **Modeling of the cell-electrode interface noise for microelectrode arrays**. *IEEE Trans Biomed Circuits Syst* 6, 605–613. doi: 10.1109/TBCAS.2012.2189569

Habibey, R., Latifi, S., Mousavi, H., Pesce, M., Arab-Tehrany, E., and Blau, A. (2017). **A multielectrode array microchannel platform reveals both transient and slow changes in axonal conduction velocity**. *Sci Rep* 7, 1–14. doi: 10.1038/s41598-017-09033-3

Habibey, R., Rojo Arias, J. E., Striebel, J., and Busskamp, V. (2022). **Microfluidics for Neuronal Cell and Circuit Engineering**. *Chem Rev* 122, 14842–14880. doi: 10.1021/acs.chemrev.2c00212

Hamill, O. P., Marty, a., Neher, E., Sakmann, B., and Sigworth, F. J. (1981). **Improved patch-clamp techniques for high-resolution current recording from cells and cell-free membrane patches**. *Pflugers Arch* 391, 85–100. doi: 10.1007/BF00656997

Hansel, D., Mato, G., and Meunier, C. (1993). **Phase Dynamics for Weakly Coupled Hodgkin-Huxley Neurons**. *Europhys Lett* 23, 367. doi: 10.1209/0295-5075/23/5/011

Heim, M., Rousseau, L., Reculusa, S., Urbanova, V., Mazzocco, C., Joucla, S., et al. (2012a). **Combined macro-/mesoporous microelectrode arrays for low-noise extracellular recording of neural networks**. *J Neurophysiol* 108, 1793–1803. doi: 10.1152/jn.00711.2011

Heim, M., Yvert, B., and Kuhn, A. (2012b). **Nanostructuration strategies to enhance microelectrode array (MEA) performance for neuronal recording and stimulation**. *J Physiol Paris* 106, 137–145. doi: 10.1016/j.jphysparis.2011.10.001

Henze, D. A., Borhegyi, Z., Csicsvari, J., Mamiya, A., Harris, K. D., and Buzsáki, G. (2000). **Intracellular features predicted by extracellular recordings in the hippocampus in vivo**. *J Neurophysiol* 84, 390–400. doi: 10.1152/jn.2000.84.1.390

Hierlemann, A., Frey, U., Hafizovic, S., and Heer, F. (2011**). Growing cells atop microelectronic chips: Interfacing electrogenic cells in vitro with CMOS-based microelectrode arrays**. *Proceedings of the IEEE* 99, 252–284. doi: 10.1109/JPROC.2010.2066532

Hodgkin, A. L., and Huxley, A. F. (1952). **A quantitative description of membrane current and its application to conduction and excitation in nerve**. *J Physiol* 117, 500–544. doi: 10.1113/jphysiol.1952.sp004764

Hofmann, B., Kätelhön, E., Schottdorf, M., Offenhäusser, A., and Wolfrum, B. (2011). **Nanocavity electrode array for recording from electrogenic cells**. *Lab Chip* 11, 1054–1058. doi: 10.1039/c0lc00582g

Holloway, P. M., Willaime-Morawek, S., Siow, R., Barber, M., Owens, R. M., Sharma, A. D., et al. (2021). **Advances in microfluidic in vitro systems for neurological disease modeling**. *J Neurosci Res* 99, 1276–1307. doi: 10.1002/JNR.24794

Hosmane, S., Fournier, A., Wright, R., Rajbhandari, L., Siddique, R., Yang, I. H., et al. (2011). **Valve-based microfluidic compression platform: single axon injury and regrowth**. *Lab Chip* 11, 3888–3895. doi: 10.1039/C1LC20549H

Huxley, A. (2002). **From overshoot to voltage clamp**. *Trends Neurosci*. 25, 553–558. doi: 10.1016/S0166-2236(02)02280-4

Ingebrandt, S., Yeung, C. K., Krause, M., and Offenhäusser, A. (2005). **Neuron-transistor coupling: Interpretation of individual extracellular recorded signals**. *European Biophysics Journal* 34, 144–154. doi: 10.1007/S00249-004-0437-9/FIGURES/7

Jaeger, R. C. (2002). ***Introduction to Microelectronic Fabrication***., 2nd ed, eds. G. W. Neudeck and R. F. Pierret. New Jersey: Prentince Hall. ISBN: 0-201-44494-7

Jinno, S., Klausberger, T., Marton, L. F., Dalezios, Y., David, J., Roberts, B., et al. (2007). **Neuronal Diversity in GABAergic Long-Range Projections from the Hippocampus**. *The Journal of Neuroscience* 27, 8790-880. doi: 10.1523/JNEUROSCI.1847-07.2007

Kandel, E. R., Schwartz, J. H., Jessel, T. M., Siegelbaum, S. A., and Hudspeth, A. J. (2013)a. **Nerve Cells, Neural Circuitry, and Behavior**. In: *Principles of Neural Science*. eds. Kandel, E., Schwartz, J., Jessell, T., Siegelbaum, S., Hudspeth, A. J., fifth edition, McGraw-Hill, New York (NY), Chapter 2, p. 21 ff. ISBN: 978-0-07-181001-2

Kandel, E. R., Schwartz, J. H., Jessel, T. M., Siegelbaum, S. A., and Hudspeth, A. J. (2013)b. **Ion Channels**. In: *Principles of Neural Science*. 5th ed., eds. Kandel, E., Schwartz, J., Jessell, T., Siegelbaum, S., Hudspeth, A. J., McGraw-Hill, New York (NY), Chapter 5, p. 100-102 ff. ISBN: 978-0-07-181001-2

Kandel, E. R., Schwartz, J. H., Jessel, T. M., Siegelbaum, S. A., and Hudspeth, A. J. (2013)c. **Propagated Signaling: The Action Potential**. In: *Principles of Neural Science*. 5th ed., eds. Kandel, E., Schwartz, J., Jessell, T., Siegelbaum, S., Hudspeth, A. J., McGraw-Hill, New York (NY), Chapter 7, p. 139-146 ff. ISBN: 978-0-07-181001-2

Kandel, E. R., Schwartz, J. H., Jessel, T. M., Siegelbaum, S. A., and Hudspeth, A. J. (2013)d. **Propagated Signaling: The Action Potential**. In: *Principles of Neural Science*. 5th ed., eds. Kandel, E., Schwartz, J., Jessell, T., Siegelbaum, S., Hudspeth, A. J., McGraw-Hill, New York (NY), Chapter 7, p. 158 ff. ISBN: 978-0-07-181001-2

Kandel, E. R., Schwartz, J. H., Jessel, T. M., Siegelbaum, S. A., and Hudspeth, A. J. (2013)e. **Overview of Synaptic Transmission.**. In: *Principles of Neural Science*. 5th ed., eds. Kandel, E., Schwartz, J., Jessell, T., Siegelbaum, S., Hudspeth, A. J., McGraw-Hill, New York (NY), Chapter 8, p. 175-178 ff. ISBN: 978-0-07-181001-2

Keren, L. B., and Hanein, Y. (2012). **Carbon nanotube based multi electrode arrays for neuronal interfacing: Progress and prospects**. *Front Neural Circuits* 0, 122. doi: 10.3389/FNCIR.2012.00122/BIBTEX

Kim, L., Toh, Y. C., Voldman, J., and Yu, H. (2007). **A practical guide to microfluidic perfusion culture of adherent mammalian cells**. *Lab Chip* 7, 681–694. doi: 10.1039/B704602B

Kim, R., Joo, S., Jung, H., Hong, N., and Nam, Y. (2014**). Recent trends in microelectrode array technology for in vitro neural interface platform**. *Biomed Eng Lett* 4, 129–141. doi: 10.1007/s13534-014-0130-6

Kimpinski, K., Campenot, R. B., and Mearow, K. (1997). **Effects of the neurotrophins nerve growth factor, neurotrophin-3, and brain-derived neurotrophic factor (BDNF) on neurite growth from adult sensory neurons in compartmented cultures**. *J Neurobiol* 33, 395–410. doi: 10.1002/(SICI)1097-4695(199710)33:4<395::AID-NEU5>3.0.CO;2-5

Kireev, D. (2017). **Graphene devices for extracellular measurements**. RWTH Aachen University. Available at: https://publications.rwth-aachen.de/record/709103 (Accessed April 15, 2024).

Krause, M., Ingebrandt, S., Richter, D., Denyer, M., Scholl, M., Sprössler, C., et al. (2000). **Extended gate electrode arrays for extracellular signal recordings**. *Sens Actuators B Chem* 70, 101–107. doi: 10.1016/S0925-4005(00)00568-2

Lewandowska, M. K., Bakkum, D. J., Rompani, S. B., and Hierlemann, A. (2015**). Recording Large Extracellular Spikes in Microchannels along Many Axonal Sites from Individual Neurons**. *PLoS One* 10, e0118514. doi: 10.1371/journal.pone.0118514

Li, W., Xu, Z., Huang, J., Lin, X., Luo, R., Chen, C.-H., et al. (2014). **NeuroArray: a universal interface for patterning and interrogating neural circuitry with single cell resolution**. *Sci Rep* 4, 4784. doi: 10.1038/srep04784

Llinás, R. R. (2003). **The contribution of Santiago Ramon y Cajal to functional neuroscience**. *Nat Rev Neurosci* 4, 77–80. doi: 10.1038/nrn1011

Lopes, C. D. F., Mateus, J. C., and Aguiar, P. (2018). **Interfacing Microfluidics with Microelectrode Arrays for Studying Neuronal Communication and Axonal Signal Propagation**. *Journal of Visualized Experiments*. doi: 10.3791/58878

Lu, X., Kim-Han, J. S., O'Malley, K. L., and Sakiyama-Elbert, S. E. (2012). **A microdevice platform for visualizing mitochondrial transport in aligned dopaminergic axons**. *J Neurosci Methods* 209, 35–39. doi: 10.1016/j.jneumeth.2012.05.021

Manz, A., Becker, H. (1998). *Microsystem Technology in Chemistry and Life Sciences*. Eds. A. de Meijere, K. N. Houk, J.-M. Lehn, S. V. Ley, J. Thiem, B. M. Trost, F. Vögtle, H. Yamamoto. Springer-Verlag Berlin Heidelberg New York.

Masuda, S., Washizu, M., and Nanba, T. (1989**). Novel Method Of Cell Fusion In Field Constriction Area In Fluid Integrated Circuit**. *IEEE Trans Ind Appl* 25, 732–737. doi: 10.1109/28.31255

Mata, A., Fleischman, A. J., and Roy, S. (2005). **Characterization of Polydimethylsiloxane (PDMS) Properties for Biomedical Micro/Nanosystems.** *Biomed Microdevices* 7, 281–293. doi: 10.1007/S10544-005-6070-2/METRICS

Mateus, J. C., Lopes, C. D. F., Aroso, M., Costa, A. R., Gerós, A., Meneses, J., et al. (2021). **Bidirectional flow of action potentials in axons drives activity dynamics in neuronal cultures.** *J Neural Eng* 18, 066045. doi: 10.1088/1741-2552/AC41DB

Meunier, C., and Segev, I. (2002). **Playing the Devil's advocate: Is the Hodgkin-Huxley model useful?** *Trends Neurosci* 25, 558–563. doi: 10.1016/S0166-2236(02)02278-6

Millet, L. J., and Gillette, M. U. (2012). **New perspectives on neuronal development via microfluidic environments**. *Trends Neurosci* 35, 752–761. doi: 10.1016/J.TINS.2012.09.001

Miranda, I., Souza, A., Sousa, P., Ribeiro, J., Castanheira, E. M. S., Lima, R., et al. (2021**). Properties and Applications of PDMS for Biomedical Engineering: A Review**. *Journal of Functional Biomaterials 2022, Vol. 13, Page 2* 13, 2. doi: 10.3390/JFB13010002

Nam, Y., and Wheeler, B. C. (2011). **In Vitro Microelectrode Array Technology and Neural Recordings**. *Crit Rev Biomed Eng* 39, 45–62. doi: 10.1051/epjap/2012110475

Neske, G. T. (2016**). The slow oscillation in cortical and thalamic networks: Mechanisms and functions**. *Front Neural Circuits* 9, 172130. doi: 10.3389/FNCIR.2015.00088/BIBTEX

Neto, E., Alves, C. J., Sousa, D. M., Alencastre, I. S., Lourenço, A. H., Leitão, L., et al. (2014**). Sensory neurons and osteoblasts: close partners in a microfluidic platform**. *Integr. Biol.* 6, 586–595. doi: 10.1039/C4IB00035H

Neto, E., Leitão, L., Sousa, D. M., Alves, C. J., Alencastre, I. S., Aguiar, P., et al. (2016). **Compartmentalized Microfluidic Platforms: The Unrivaled Breakthrough of In Vitro Tools for Neurobiological Research**. *The Journal of Neuroscience* 36, 11573–11584. doi: 10.1523/JNEUROSCI.1748-16.2016

Nishimura, M., Toba, M., Matsuie, N., Motobe, T., and Ohe, M. (2015). **Evaluation of fan-out wafer level package using 200 °c curable positive-tone photodefinable polybenzoxazoles**. *IEEE CPMT Symposium Japan 2015: Packaging is Everywhere, ICSJ 2015*, 25–28. doi: 10.1109/ICSJ.2015.7357351

Novak, J. L., and Wheeler, B. C. (1986). **Recording from the Aplysia Abdominal Ganglion with a Planar Microelectrode Array**. *IEEE Trans Biomed Eng* BME-33, 196–202. doi: 10.1109/TBME.1986.325891

Pan, L., Alagapan, S., Franca, E., Brewer, G. J., and Bruce, C. (2012). **Propagation of Action Potential Activity in a Predefined Microtunnel Neural Network**. *J Neural Eng.* 8, 1–20. doi: 10.1088/1741-2560/8/4/046031.

Pan, L., Alagapan, S., Franca, E., DeMarse, T., Brewer, G. J., and Wheeler, B. C. (2014). **Large extracellular spikes recordable from axons in microtunnels**. *IEEE Trans Neural Syst Rehabil Eng* 22, 453–9. doi: 10.1109/TNSRE.2013.2289911

Park, J., Kim, S., Park, S. I., Choe, Y., Li, J., and Han, A. (2014**). A Microchip for Quantitative Analysis of CNS Axon Growth under Localized Biomolecular Treatments**. *J Neurosci Methods* 221, 166–174. doi: 10.1016/J.JNEUMETH.2013.09.018

Park, J., Koito, H., Li, J., and Han, A. (2009). **Microfluidic compartmentalized co-culture platform for CNS axon myelination research**. *Biomed Microdevices* 11, 1145–1153. doi: 10.1007/s10544-009-9331-7

Park, J. W., Vahidi, B., Taylor, A. M., Rhee, S. W., and Jeon, N. L. (2006). **Microfluidic culture platform for neuroscience research**. *Nat Protoc*. doi: 10.1038/nprot.2006.316

Perl, A., Reinhoudt, D. N., and Huskens, J. (2009). **Microcontact Printing: Limitations and Achievements**. *Advanced Materials* 21, 2257–2268. doi: 10.1002/ADMA.200801864

Peyrin, J.-M., Deleglise, B., Saias, L., Vignes, M., Gougis, P., Magnifico, S., et al. (2011). **Axon diodes for the reconstruction of oriented neuronal networks in microfluidic chambers**. *Lab Chip* 11, 3663. doi: 10.1039/c1lc20014c

Piccolino, M. (2002**). Fifty years of the Hodgkin-Huxley era**. *Trends Neurosci* 25, 552–553. doi: 10.1016/S0166-2236(02)02276-2

Pickard, R. S. (1979). **A review of printed circuit microelectrodes and their production**. *J Neurosci Methods* 1, 301–318. doi: 10.1016/0165-0270(79)90019-0

Pine, J. (1980). **Recording action potentials from cultured neurons with extracellular microcircuit electrodes**. *J Neurosci Methods* 2, 19–31. doi: 10.1016/0165-0270(80)90042-4

Posts, R. (2020). **Wafer Dies: Microelectronic Device Fabrication & Packaging; Polyimides (PI) & Polybenzoxazoles (PBO): Advanced Dielectric Polymers for Wafer Bumping & Wafer Level Packaging**. Available at: https://waferdies.com/polyimides-pi-and-polybenzoxazoles-pbo-advanced-dielectric-polymers-for-wafer-bumping-wafer-level-packaging/

Process Guide: **HD-8820 Aqueous Positive PBO** (2009). *HD MicroSystems*. Available at; https://www.yumpu.com/en/document/read/2066736/hd-8820-aqueous-positive-polyimide-hd-microsystems

Process Guide: **NANO SU-8 Negative Tone Photoresist** (2014). *MicroChem*. Available at: http://www.microchem.com/pdf/SU8_50-100.pdf

Raj M, K., and Chakraborty, S. (2020**). PDMS microfluidics: A mini review**. *J Appl Polym Sci* 137, 48958. doi: 10.1002/APP.48958

Rapp, M., Yarom, Y., and Segev, I. (1996). **Modeling back propagating action potential in weakly excitable dendrites of neocortical pyramidal cells**. *Proc Natl Acad Sci U S A* 93, 11985–11990. doi: 10.1073/pnas.93.21.11985

Sackmann, E. K., Fulton, A. L., and Beebe, D. J. (2014). **The present and future role of microfluidics in biomedical research**. *Nature 2014 507:7491* 507, 181–189. doi: 10.1038/nature13118

Sakai, K., Shimba, K., Kotani, K., and Jimbo, Y. (2017). **A co-culture microtunnel technique demonstrating a significant contribution of unmyelinated Schwann cells to the acceleration of axonal conduction in Schwann cell-regulated peripheral nerve development**. *Integr. Biol.* 9, 678–686. doi: 10.1039/C7IB00051K

Sakmann, B., and Neher, E. (1984). **Patch clamp techniques for studying ionic channels in excitable membranes**. *Annu Rev Physiol*. 46, 455–472. doi: 10.1146/annurev.ph.46.030184.002323

Sakmann, B., and Stuart, G. J. (1994**). Active propagation of somatic action potentials into neocortical pyrimidal cell dendrites**. *Nature* 367, 69–72. doi: 10.1038/367069a0

Seidl, a. H. (2014). **Regulation of conduction time along axons**. *Neuroscience* 276, 126–134. doi: 10.1016/j.neuroscience.2013.06.047

Seshan, Krishna. (2002). ***Handbook of thin-film deposition processes and techniques: principles, methods, equipment and applications***. Noyes Publications/William Andrew Pub.

Shakeri, A., Khan, S., and Didar, T. F. (2021). **Conventional and emerging strategies for the fabrication and functionalization of PDMS-based microfluidic devices**. *Lab Chip* 21, 3053–3075. doi: 10.1039/D1LC00288K

Shepherd, G. M. G., and Harris, K. M. (1998). **Three-Dimensional Structure and Composition of CA33CA1 Axons in Rat Hippocampal Slices: Implications for Presynaptic Connectivity and Compartmentalization**. *J. Neurosci.* 18(20), 8300-10. doi: 10.1523/JNEUROSCI.18-20-08300.1998.

Shi, P., Nedelec, S., Wichterle, H., and Kam, L. C. (2010). **Combined microfluidics/protein patterning platform for pharmacological interrogation of axon pathfinding**. *Lab Chip* 10, 1005–1010. doi: 10.1039/B922143C

Shimba, K., Kotani, K., and Jimbo, Y. (2021). **Microfabricated Device to Record Axonal Conduction under Pharmacological Treatment for Functional Evaluation of Axon Ion Channel**. *IEEE Trans Biomed Eng* 68, 3574–3581. doi: 10.1109/TBME.2021.3078473

Shimba, K., Sakai, K., Isomura, T., Kotani, K., and Jimbo, Y. (2015). **Axonal conduction slowing induced by spontaneous bursting activity in cortical neurons cultured in a microtunnel device**. *Integrative Biology (United Kingdom)* 7, 64–72. doi: 10.1039/c4ib00223g

Sim, J. Y., Haney, M. P., Park, S. Il, McCall, J. G., and Jeong, J.-W. (2017). **Microfluidic neural probes: in vivo tools for advancing neuroscience**. *Lab Chip* 17, 1406–1435. doi: 10.1039/C7LC00103G

Spira, M. E., and Hai, A. (2013). **Multi-electrode array technologies for neuroscience and cardiology**. *Nat Nanotechnol* 8, 83–94. doi: 10.1038/nnano.2012.265

Sun, S. H., Almasi, A., Yunzab, M., Zehra, S., Hicks, D. G., Kameneva, T., et al. (2021). **Analysis of extracellular spike waveforms and associated receptive fields of neurons in cat primary visual cortex**. *J Physiol* 599, 2211–2238. doi: 10.1113/JP281404

Takeuchi, A., Nakafutami, S., Tani, H., Mori, M., Takayama, Y., Moriguchi, H., et al. (2011). **Device for co-culture of sympathetic neurons and cardiomyocytes using microfabrication**. *Lab Chip* 11, 2268–2275. doi: 10.1039/C0LC00327A

Taylor, A. M., Blurton-Jones, M., Rhee, S. W., Cribbs, D. H., Cotman, C. W., and Jeon, N. L. (2005). **A microfluidic culture platform for CNS axonal injury, regeneration and transport**. *Nat Methods* 2, 599–605. doi: 10.1038/nmeth777

Taylor, A. M., Rhee, S. W., Tu, C. H., Cribbs, D. H., Cotman, C. W., and Jeon, N. L. (2003). **Microfluidic Multicompartment Device for Neuroscience Research**. *Langmuir* 19, 1551–1556. doi: 10.1021/la026417v

Terzuolo, C. A., and Araki, T. (1961). **An analysis of intra- versus extracellular potential changes associated with activity of single spinal motoneurons**. *Ann N Y Acad Sci* 94, 547–558. doi: 10.1111/j.1749-6632.1961.tb35558.x

Thomas, C. a., Springer, P. a., Loeb, G. E., Berwald-Netter, Y., and Okun, L. M. (1972). **A miniature microelectrode array to monitor the bioelectric activity of cultured cells**. *Exp Cell Res* 74, 61–66. doi: 10.1016/0014-4827(72)90481-8

Toepke, M. W., and Beebe, D. J. (2006). **PDMS absorption of small molecules and consequences in microfluidic applications**. *Lab Chip* 6, 1484–1486. doi: 10.1039/B612140C

Toma, K., Kano, H., and Offenhäusser, A. (2014). **Label-free measurement of cell-electrode cleft gap distance with high spatial resolution surface plasmon microscopy**. *ACS Nano* 8, 12612–12619. doi: 10.1021/nn505521e

Trainito, C., von Nicolai, C., Miller, E. K., and Siegel, M. (2019). **Extracellular Spike Waveform Dissociates Four Functionally Distinct Cell Classes in Primate Cortex**. *Current Biology* 29, 2973-2982.e5. doi: 10.1016/j.cub.2019.07.051

Van Den Berg, A., Craighead, H., Yang, P., Young, E. W. K., and Beebe, D. J. (2010). **Fundamentals of microfluidic cell culture in controlled microenvironments**. *Chem Soc Rev* 39, 1036–1048. doi: 10.1039/B909900J

Virchow, R. (1854). **Ueber das ausgebreitete Vorkommen einer dem Nervenmark analogen Substanz in den thierischen Geweben**. *Archiv für Pathologische Anatomie und Physiologie und für Klinische Medicin* 6, 562–572. doi: 10.1007/BF02116709

Virlogeux, A., Moutaux, E., Christaller, W., Genoux, A., Bruyère, J., Fino, E., et al. (2018). **Reconstituting Corticostriatal Network on-a-Chip Reveals the Contribution of the Presynaptic Compartment to Huntington's Disease**. *Cell Rep* 22, 110–122. doi: 10.1016/j.celrep.2017.12.013

Wang, L., Riss, M., Buitrago, J. O., and Claverol-Tinturé, E. (2012). **Biophysics of microchannel-enabled neuron–electrode interface**s. *J. Neural Eng* 9, 26010–14. doi: 10.1088/1741-2560/9/2/026010

Weidlich, S. D. (2017). **Nanoscale 3D structures towards improved cell-chip coupling on microelectrode arrays**. RWTH Aachen University. doi: 10.18154/RWTH-2017-10442

Whitesides, G. M. (2006). **The origins and the future of microfluidics**. *Nature* 442, 368–373. doi: 10.1038/nature05058

Wrobel, G., Höller, M., Ingebrandt, S., Dieluweit, S., Sommerhage, F., Bochem, H. P., et al. (2007). **Transmission electron microscopy study of the cellsensor interface**. *J R Soc Interface* 5, 213–222. doi: 10.1098/RSIF.2007.1094

Xia, Y., and Whitesides, G. M. (1998). **Soft Lithography**. *Annu. Rev. Mater. Sci.* 28, 153-84. doi: 10.1002/(SICI)1521-3773(19980316)37:5<550::AID-ANIE550>3.0.CO;2-G

Yun, S. H., Cabrera, L. M., Song, J. W., Futai, N., Tung, Y. C., Smith, G. D., et al. (2007). **Characterization and resolution of evaporation-mediated osmolality shifts that constrain microfluidic cell culture in poly(dimethylsiloxane) devices**. *Anal Chem* 79(3), 1126–1134. doi: 10.1021/ac061990v

Acknowledgements

I remember myself at the beginning of the PhD journey. It seemed like a clear and straightforward path, but little did I know that one courageous step into unknown scientific questions could have such a big impact on my entire life! And now, at the end of that journey, I cannot see it apart from the whole mosaic of life and see how it reshaped my days, my thoughts, my expectations, and even myself. There were many challenges to be faced along the way, but I'm so grateful for the journey and all that I've learned. Sometimes I felt like I was all alone, but most of the time I had so much support from so many people. I would like to take this opportunity to thank them all for being there for me.

First and foremost, I would like to thank you Prof. Dr. Andreas Offenhäusser for giving me the opportunity to start this journey, for your supervision and all the scientific discussions. I am deeply grateful to you for your unwavering trust in me despite my many doubts about myself and the difficult times caused by various unpredictable circumstances in my life. Your sincere encouragement and willingness to understand my difficulties was one of the forces that kept me going.

Prof. Dr.-Ing. Laura De Laporte, thank you kindly for your willingness to be the second examiner of my thesis.

My special thanks go to my colleague, but also a very good friend, PhD student Bogdana Čepkenović. Dear Bogdana, I appreciate your willingness to help so much. Scientific discussions with you were always on the point and I learned a lot from you. Your selfless help with Python script and data analysis finally pushed me out of a dead end and made it possible for me to continue, step by step, towards this goal. Thank you for your patience, for the sacrifice of your time and energy, and thank you for our friendship, despite all the differences and contrasts. It's good to have you here in Jülich! :)

My thanks also go to the unstoppable team of technicians at the IBI-3 Institute who were involved in my thesis, with special thanks to Tina Breuer: for diligent work with cells and keeping the labs in the best order; Marko Banzet: for help with the fabrication of MEAs and SU-8 molds; Michael Prömpers: for genuinely good spirit in the lab and kindness in every conversation and request for help.

I would also like to thank my colleagues and other students who were part of our institute and created a unique working atmosphere that I will always remember. These include Viviana (your patience and honest support make you a valued colleague), Dmitry (even for a short time, I enjoyed working with you, and learned so much), Timm (your spirit is unforgettable, and music jam sessions are something I will always remember), Chris (savior with all those carpools), Gabi, Marc, and Lucas (shall we continue

our workouts??), Vanessa, Esther, Jamal, Frano, Bohdan, Pegah, Kagithri, Corinna, Dominik, Erfan, Mattis, Johannes, Ann, Ekaterina, Lei, Susanne and many more.

Other people who I dare to call friends now, after such a long journey, also stood by my side… Thank you Kaća, Snežana, Val, Rudi, Anastasia, Marina, Vladimir… So many good memories were created with you!

My deer Rudi ;), your support and encouragement made all the difference in the last days of completing this thesis. Thank you for believing in me.

Finally, I would like to thank my family. Dear Mom and Dad, I know you would be proud of me. Dear aunts and uncles, sisters and brothers, I am always proud of our bond and the love we have for each other. Despite the distances and circumstances of life, I know that you are always by my side, supporting me, sending me love, holding me up. A special thank you to my dear brother Alek: you remember! It was difficult! And you were so supportive, so selflessly willing to jump in and solve problems! I cannot express how much I appreciate that! I hope you feel my gratitude and I pray to God for you! But also, thank you for always making me smile and laugh at times when I needed it so much. My dear little brother, I love you!

And of course, my dear dog Medi… What could you know… Little furry creature, we have been through so much together… Thank you for always being by my side.

Taking a moment to sit down and write this last section has brought me so many fond memories and has touched my heart deeply. Finally, I am truly grateful for this journey, dear God, thank you for giving me the strength and will to endure.

Appendices

Appendix A

Cleanroom fabrication recipes

In the following section, the concise recipes for fabrication of the iMEA200/r16MEA, SU-8 molds, and PDMS Comp-µFluidic devices are listed.

A1 Microelectrode Arrays Cleanroom Fabrication

Metallization

MEAs were structured on a 4" quartz wafer in an ISO 1 cleanroom at the Helmholtz Nanoelectronic Facility (HNF) in Forschungszentrum Jülich.

- **Dehydration**: wafer heat 150℃ on a hotplate for at least 5-10 minutes;
- **Spin-coating**: LOR-3B, 3000 rpm, with ramp, closed lid, 5 mL, dispersed around the whole wafer;
- **Soft bake**: 150℃, 5 minutes, hotplate;
- **Spin-coating**: AZ nLOF-2020, 3000 rpm, with ramp, closed lid, 3mL;
- **Soft bake**: 100℃, 2 minutes, hotplate;
- **Exposure**: i-line (350 nm UV), 55 mJ/cm^2;
- **Post-exposure bake**: 110℃, 1 minute, hotplate;
- **Development**: AZ 326 MIF for 35 seconds;
- **Washing**: water cascade, drying with N_2 gun;
- **e-beam assisted evaporation**: (10/100 nm) Ti/Au;
  deposition rates 0.3/0.5 nm/s (Ti/Au)
- **Lift off**: acetone, at least 12 hours, followed by AZ MIF-36, 10 minutes

Passivation

- **Dehydration**: wafer heat 150℃ on a hotplate for at least 5-10 minutes
- **Spin-coating**: adhesion promoter VM-652 (always use a fresh one), 3000 rpm, closed lid, 3 mL;
- **Spin-coating**: HD-8820, 5000 rpm, closed lid, 3-4 mL, disperse directly from the previously defrosted bottle, and remove any bubbles, 45 seconds;
- **Slow soft bake**: proximity hotplate set to 120℃,
  - Wafer moves slowly down on the supporting pins from initial height of 10 mm with 0.1 mm/s speed
  - Annealing for minutes when it reaches the hotplate surface
- **Exposure**: i-line, 400 mJ/cm^2;
- **Development**: AZ MIF-326 double puddle, each lasting 60 seconds with constantly shaking and rotation the wafers;
- **Washing**: water cascade, drying with N_2 gun;
- **Hard bake in a convection furnace**:
  - Start: room temperature, N_2 atmosphere;
  - Ramping up to 200℃ with a speed of 4 ℃ /min;
  - Hold the 200℃ for 30 minutes;
  - Ramping up to 350℃ with a speed of 2.5 ℃/min;
  - Hold the 350℃ for 30 minutes;
  - Gradual cool down to room temperature with the speed of 4℃/min;

Microchannel Structuring on Top of MEA

- **Dehydration**: wafer heat 150℃ on a hotplate for at least 5-10 minutes, or the process is continued right after the passivation layer hard bake with a partial cool down time;
- **Spin-coating**: HD-8820, 2500 rpm, closed lid, 45 seconds;
- **Continue the same steps listed in the previous paragraph.**

Reagent	Supplier
VM-652	HD Microsystems
HD-8820	HD Microsystems
LOR-3B	MicroChem Corp.
AZ nLOF-2020	MicroChem Corp.
AZ-5214e	MicroChem GmbH
AZ 326 MIF	MicroChem GmbH

Table A.1 – List of chemicals used in the cleanroom for the microelectrode array fabrication process.

A2 SU-8 Mold Cleanroom Fabrication Steps

The desired mold is constructed in a two-layer process on a 0.6 mm thick, 4" silicon wafer.

The 1st SU-8 layer

- **Dehydration**: wafer heat 150℃ on a hotplate for at least 5-10 minutes;
- **Spin-coating**: SU-8 2005, 5000 rpm, closed lid, 45 seconds;
- **Soft bake**: hotplate, 95℃, 150 seconds;
- **Exposure**: hard contact, 7.0 mW/cm^2, 9 seconds (63 mJ/ cm^2);
- **Post-exposure bake:** hotplate, 95℃, 150 seconds;
- **Development**: two step development in the same mr-Dev 600 (30s/15s) with the isopropanol rinsing step in between;
- **Washing:** rinsing with IPA, drying with N_2 gun;
- **Hard bake in a convection furnace:**
  - 200℃ for 30 minutes with 20 L/min nitrogen purge;
  - Gradual cool down to the room temperature;
- **Cleaning**: acetone, followed by isopropanol in ultrasonic bath (low to medium power) for removing any possible residual of SU-8

The 2nd SU-8 Layer

- **Dehydration**: wafer heat 150℃ on a hotplate for at least 5-10 minutes;
- **Spin-coating**: adhesion promoter SU-8 2001, 3000 rpm, open lid, 3.5 mL;
- **Soft bake**: hotplate, 95℃, 1 minute;

- **Spin-coating:** SU-8 2050 / SU-8 2100, 2000 rpm (5 seconds at 500 rpm, followed by acceleration of 100 rpm/second), closed lid, disperse directly from the bottle (approx. 3-4 mL, remove any bubbles), 35s;
- **Cleaning:** clean the bottom of the wafer from any SU-8 residues, and manually remove the resist from the alignment markers;
- **Soft bake:** perform on a hotplate in two steps: 65℃ for 2 minutes, 95℃, for 10 minutes;
- **Exposure:** filter out wavelengths <365 nm, hard contact, 7.0 mW/cm^2, 9 seconds (63 mJ/ cm^2);
- **Post-exposure bake:** two step bake on a hotplate:
  - 1st gradual increase to 65℃ for 8 minutes;
  - hold for 5 minutes;
  - 2nd gradual increase to 95℃ for 8 minutes;
  - Hold for 12 minutes;
  - Gradual cool down to at least 50℃;
- **Development**: two step development in the same mr-Dev 600, smooth wafer waving and rotating, with the isopropanol rinsing step in between; time depends on SU-8 viscosity:
  - SU-8 2050: 5min/2min;
  - SU-8 2100: 15min/5min;
- **Continue the same steps** listed for the 1st SU-8 layer (washing, hard bake, cleaning).

Reagent	Supplier
SU-8 2001	Microchemicals
SU-8 2005	Microchemicals
SU-8 2050	Microchemicals
SU-8 2100	Microchemicals
MR-dev600	Micro Resist Technology GmbH

Table A.2 – List of chemicals used in the cleanroom for the SU-8 molds fabrication process.

A3 PDMS Comp-µFluidic Structures Fabrication

- **PDMS preparation**: mix base and curing agent (10:1), degas overnight in a freezer at -20℃;
- **SU-8 molds hydrophobicity increase**: clean mold is incubated in 2% SDS for 15 minutes;
- **Mold clamp** in a custom-made Teflon holders;
- **Pour PDMS mix**: degassed mix is brought to the room temperature and spread over, starting from the center of the mold (remove any bubbles with a clean and sharp pipette tip);
- **The Teflon holder with the SU-8 mold and PDMS over** it is placed in a flat container covered with foil (top and under, to avoid sticking of the leaked SU-8 to the container surface)
- **PDMS Curing:** at 60℃ for at least 12 hours
- **PDMS removal from the mold:** careful manual removal is recommended in the direction of the microchannel narrowing, to avoid the rupture of the structures;
- **Individual device punching:** each device is separated by a 14 mm diameter circular steel puncher, and seeding champers are created in each device by a 3.5 diameter biopsy puncher;
- **Cleaning:**
  - acetone, medium ultrasonic bath, 3 minutes;
  - isopropanol, medium ultrasonic bath, 3 minutes;
  - rinsing in absolute ethanol, followed by 70% ethanol, and finally milli-Q water
  - drying with an N2 gun.

A4 Final µFluidic-MEA Device Assembly Protocol

Irreversible assembly: MEAs and PDMS comp-µFluidic devices are cleaned before the final device assembly. Connecting surfaces are treated with similar or the same parameters as follows:

- **Oxygen plasma surface activation**:
  - MEAs: 0.4 W, 0.8 mbar for 1 minute
  - PDMS comp-µFluidic devices: 0.7 W, 0.8 mbar for 1 minute;
- **APTES treatment of the bonding surfaces**:
  - Put devices on the Alu-foil covered flat surface, activated surfaces facing up;
  - Apply 30% aqueous APTES solution on the surfaces;
  - Cover the treated devices and incubate at RT for 10 minutes;
  - Thoroughly rinse the treated devices with Milli-Q water and dry with N_2 gun to remove any APTES excess from the surfaces;
- **Alignment of the bonding surfaces**: FinePlacer or manually under the microscope;
- **Dehydration**: Aligned hybrid-devices are heated at 110℃, hotplate for 10 minutes; the heat strengthens the bonding of two surfaces;
- **Hydration of microfluidics**: Milli-Q water is added into the microfluidic system, to prevent the loss of hydrophilicity.

Reversible assembly: MEAs and PDMS comp-µFluidic devices are aligned right after the cleaning step, and the next steps are applied in the following order:

- **Dehydration**: Aligned hybrid-devices are heated at 90℃ for 10 minutes;
- **Oxygen plasma activation**: 0.5 W, 0.8 mbar for 1 minute;
- **Hydration of microfluidics**: Milli-Q water is added into the microfluidic system, to prevent the loss of hydrophilicity.

Appendix B

Cell Culture Protocols

B1 Cortical and Striatal Rat Neurons

Isolation of cells

Isolation of cortical and striatal neurons from pregnant (E18) Wistar rats' embryonic cortices is performed in the following steps:

- Dissection of the cortex and digestion in 0.05% Trypsin for 10 minutes at 37℃ and 5% CO_2; swivel the suspension after 5 minutes of incubation;
- Transfer the cortices into a reaction tube containing:
  - Fresh Neurobasal medium
  - 1% (v/v) B27,
  - 0.5 mM L-glutamine,
  - 0.05 mg/mL gentamicin
- Three times wash with NB medium
- Mechanical dissociation with a 100-1000 µL pipette tip and settle for 1 minute
- Use the supernatant for dilution to appropriate cell density

Cell culture maintenance

Cells are seeded in Comp-µFluidic-MEA hybrid devices. Preparation of the devices prior to cell seeding is as follows:

- **Sterilization** under UV light for 1 hour
- **Coating of the microfluidics**: 20 µg/mL PLL in HBSS
- **Incubate** for 1 hour at 37℃

The exchange of medium is performed fully on a day after seeding (to remove cells that did not attach to the surface), and every third day half of the medium is exchanged (to avoid the disturbance of the cells attached in microchannel area). Freshly prepared medium is prepared in the following steps:

- Neurobasal medium (volume depends on a number of samples)
- 1% B27

- 0.25% L-glutamine
- 0.1% gentamicin

Substance	Add volume	Stock solution	Final concentration (v/v)
Neurobasal medium	10 mL	—	—
B27 supplement	100 µL	—	1%
L-glutamine	25 µL	200 mM	0.25%
gentamicin	10 µL	50 mg/mL	0.10%

Table B.1 – Supplemented Neurobasal medium. The medium for embryonic cortical cells from rats was prepared by adding the listed substances with specified concentrations.

B2 Viability Assay

- Wash samples 2-3 times with preheated PBS
- Add cal-AM and EtHD in a 1:1000 dilution ratio after one time wash with the same solution
- Incubation, hotplate at 37℃ for 15 minutes
- Wash samples 2-3 times with PBS

Substance	Supplier
B27 supplement	Thermo Fisher Scientific
bovine serum albumin (BSA)	Sigma-Aldrich
calcein-AM	Thermo Fisher Scientific
Deionized water (MilliQ)	Millipore
EtHD	Thermo Fisher Scientific
gentamicin	Sigma-Aldrich
HBSS	Sigma-Aldrich
L-glutamine	Thermo Fisher Scientific
Neurobasal medium	Life Technologies
PLL	Sigma-Aldrich
Paraformaldehyde	Sigma-Aldrich
Triton X-100	Sigma-Aldrich
trypsin EDTA	Life Technologies

Table B.2 – List of substances used in cell culture maintenance and viability assays.

B3 Immunostaining Assay

- Rinse samples twice with preheated 1×PBS
- Cell fixation with pre-warmed 4% paraformaldehyde for 10 minutes
- Wash samples three times with PBS

- Permeabilization with 0.3% Triton X-100 in PBS for 10 minutes, at RT
- Rinse twice with 1×PBS
- Block unspecific protein binding sites with a blocking buffer (1% BSA and 0.3% Triton X-100 in PBS) for 30 minutes at RT
- Apply the primary antibody in a 0.5% blocking buffer overnight at 4℃
- Rinse samples three times with PBS
- Apply secondary antibody in a 0.5% blocking buffer and incubate for 3 hours in the dark, at RT
- Wash once with 1×PBS and rinse with Milli-Q water (prevents PBS crystallization on the samples)
- Apply the mounting medium solution and incubate overnight in dark, RT
- Put a clean glass coverslip on top of the sample, and store at 4℃
- Samples are ready for imaging

Antibody	Dillution	Supplier	Target
Chicken anti-Neurofilament Heavy Chain	1:1000	abcam	axons
Mouse anti-Neurofilament Heavy Chain	1:1000	Millipore	axons
Rabbit anti-MAP2	1:500	abcam	cortical neurons
Mouse anti-Tau-1	1:300	Sigma Aldrich	axons
Goat anti-chicken Alexa Fluor 546	1:500	Life Technologies	chicken antibodies
Goat anti-rabbit Alexa Fluor 546	1:500	Life Technologies	rabbit antibodies
Goat anti-rabbit Alexa Fluor 488	1:500	Life Technologies	rabbit antibodies
Goat anti-mouse Alexa Fluor 488	1:500	Life Technologies	mouse antibodies
Goat anti-mouse Alexa Fluor 633	1:500	Life Technologies	mouse antibodies

Table B.3 – Primary and secondary antibodies used for fluorescent immunocytochemistry. Antibodies are listed (1st column), followed by dilution prepared for each experiment (2nd column), the supplier of the reagent (3rd column), and the target for immunostaining (4th column).

Appendix C

Figure C.1 – **Spike shape occurrence along each microchannel length at DIV 14-35.** Upper panel shows the comparison of shape occurrences in RB samples of all three microchannel lengths, except for the medium microchannels at DIV 28, when recording was not possible. Lower panel presents trends observed in IRB samples.

Appendix D

		DIV14	DIV21	DIV25	DIV28
V1	Median	0.21	0.25	0.23	0.22
	Q1 | Q3:	0.16 | 0.32	0.15 | 0.42	0.16 | 0.34	0.16 | 0.36
	Mean ± SD	0.28 ± 0.25	0.37 ± 0.36	0.31 ± 0.27	0.35 ± 0.34
V2	Median	0.21	0.26	0.20	0.19
	Q1 | Q3:	0.14 | 0.33	0.16 | 0.43	0.14 | 0.30	0.12 | 0.29
	Mean ± SD	0.28 ± 0.25	0.38 ± 0.35	0.28 ± 0.28	0.27 ± 0.28
V3	Median	0.19	0.21	0.18	0.19
	Q1 | Q3:	0.09 | 0.27	0.12 | 0.32	0.12 | 0.27	0.11 | 0.29
	Mean ± SD	0.25 ± 0.26	0.28 ± 0.26	0.25 ± 0.25	0.26 ± 0.26
V4	Median	0.14	0.18	0.16	0.17
	Q1 | Q3:	0.11 | 0.18	0.13 | 0.24	0.13 | 0.26	0.12 | 0.26
	Mean ± SD	0.25 ± 0.32	0.25 ± 0.28	0.26 ± 0.28	0.28 ± 0.33
V5	Median	0.56	0.38	0.33	0.38
	Q1 | Q3:	0.30 | 1.11	0.21 | 0.67	0.19 | 0.56	0.20 | 0.67
	Mean ± SD	0.70 ± 0.48	0.48 ± 0.38	0.43 ± 0.34	0.49 ± 0.38

Table D.1 – Propagation velocities in µFluidic-iMEA200 long µchannels over time (m/s).

		DIV18	DIV22	DIV26	DIV29
V1	Median	0.31	0.26	0.32	0.34
	Q1 | Q3:	0.23 | 0.40	0.19 | 0.38	0.23 | 0.42	0.32 | 0.38
	Mean ± SD	0.37 ± 0.27	0.33 ± 0.26	0.40 ± 0.31	0.45 ± 0.33
V2	Median	0.32	0.18	0.24	0.14
	Q1 | Q3:	0.23 | 0.56	0.13 | 0.34	0.15 | 0.34	0.12 | 0.24
	Mean ± SD	0.47 ± 0.39	0.35 ± 0.39	0.34 ± 0.34	0.24 ± 0.30
V3	Median	0.30	0.19	0.24	0.14
	Q1 | Q3:	0.26 | 0.63	0.16 | 0.50	0.15 | 0.53	0.10 | 0.16
	Mean ± SD	0.50 ± 0.39	0.39 ± 0.40	0.40 ± 0.37	0.24 ± 0.33

Table D.2 – Propagation velocities in µFluidic-r16MEA µchannels over time (m/s).

Declaration of Authorship

I, Jelena Stevanović, declare that this thesis and the work presented in it are my own and has been generated by me as the result of my own original research.

I do solemnely swear that:

1. This work was done wholly or mainly while in candidature for the doctoral degree at this faculty and university;

2. Where any part of this thesis has previously been submitted for a degree or any other qualification at this university or any other institution, this has been clearly stated;

3. Where I have consulted the published work of others or myself, this is always clearly attributed;

4. Where I have quoted from the work of others or myself, the source is always given. This thesis is entirely my own work, with the exception of such quotations;

5. I have acknowledged all major sources of assistance;

6. Where the thesis is based on work done by myself jointly with others, I have made clear exactly what was done by others and what I have contributed myself;

7. None of this work has been published before submission.

Date: 28.04.2025

Signature: 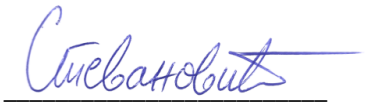

Band / Volume 282
Folding and structural studies of *saccharomyces cerevisiae* Phosphoglycerate Kinase
N. Bustorff (2024), xxvi, 126 pp
ISBN: 978-3-95806-754-7

Band / Volume 283
The role of cellular development in multicellular antiphage defense of *Streptomyces*
T. Luthe (2024), vi, 173 pp
ISBN: 978-3-95806-768-4

Band / Volume 284
Probing the Transformation from Transition Metal Complexes to Extended Two-Dimensional Nanostructures
D. Baranowski (2024), XII, 103 pp
ISBN: 978-3-95806-772-1

Band / Volume 285
Neutron Scattering
Lectures of the JCNS Laboratory Course held at Forschungszentrum Jülich and at the Heinz-Maier-Leibnitz Zentrum Garching
edited by S. Förster, K. Friese, M. Kruteva, S. Nandi, M. Zobel, R. Zorn (2024), ca. 365 pp
ISBN: 978-3-95806-774-5

Band / Volume 286
***Ab initio* investigation of intrinsic antiferromagnetic solitons**
Amal Jawdat Nayef Aldarawsheh (2024), xv, 164 pp
ISBN: 978-3-95806-785-1

Band / Volume 287
Understanding the dynamics of Plant-Bacteria-Bacteriophage interactions as a means to improve plant performance
S. H. Erdrich (2024), ix, 176 pp
ISBN: 978-3-95806-791-2

Band / Volume 288
Prediction of Magnetic Materials for Energy and Information Combining Data-Analytics and First-Principles Theory
R. Hilgers (2024), xv, 215 pp
ISBN: 978-3-95806-795-0

Band / Volume 289
Biodegradation and microbial upcycling of plastics
J. de Witt (2025), XVI, 259 pp
ISBN: 978-3-95806-804-9

Band / Volume 290
Practical Methods for Efficient Analytical Control in Superconducting Qubits
B. Li (2025), 202 pp
ISBN: 978-3-95806-807-0

Band / Volume 291
Ab initio investigation of topological magnetism in two-dimensional van der Waals heterostructures
N. Abuawwad (2025), xviii, 135 pp
ISBN: 978-3-95806-808-7

Band / Volume 292
Tolerance engineering of Pseudomonas for the efficient conversion and production of aldehydes
T. Lechtenberg (2025), XVI, 185 pp
ISBN: 978-3-95806-817-9

Band / Volume 293
Exploring the process window for production of itaconic, 2-hydroxyparaconic, and itatartaric acid with engineered *Ustilago* strains
P. Ernst (2025), x, 145 pp
ISBN: 978-3-95806-825-4

Band / Volume 294
Surface Plasmon Resonance Microscopy for the Characterization of Cell-Substrate Distances
J. Bednar (2025), xxiii, 187 pp
ISBN: 978-3-95806-830-8

Band / Volume 295
Microfluidic-MEA hybrid systems for electrophysiological recordings of neuronal co-cultures
J. Stevanović (2025), ix, 186 pp
ISBN: 978-3-95806-831-5

Weitere ***Schriften des Verlags im Forschungszentrum Jülich*** unter
http://wwwzb1.fz-juelich.de/verlagextern1/index.asp

Schlüsseltechnologien / Key Technologies
Band / Volume 295
ISBN 978-3-95806-831-5

Mitglied der Helmholtz-Gemeinschaft

JÜLICH
Forschungszentrum